Load prediction for a moored conical drillship in level unbroken ice: a discrete element and experimental investigation

by

Karl P. Lawrence

A thesis
presented to University of Waterloo
in fulfilment of the
thesis requirement for the degree of
Doctor of Philosophy
in
Civil Engineering

Waterloo, Ontario, Canada, 2009

Author Declaration

I hereby declare that I am the sole author of this thesis. This is a true copy of the thesis, including any required final revisions, as accepted by my examiners.

I understand that my thesis may be made electronically available to the public.

Abstract

This thesis is composed of theoretical, experimental, and numerical studies. In Part I, it discusses fundamental challenges of the discrete element method, provides a set of algorithms for addressing them, and presents performance gains of an improved algorithm on a target computer platform. A new contact detection and force resolution algorithm based upon (i) the fast common-plane (FCP) algorithm, (ii) using axis-aligned bounding boxes (AABBs) to perform a proximity search, (iii) estimating the time of collision, and (iv) accurate resolution of contact points is presented. Benchmark simulations indicate an order of magnitude increase in performance is achievable for a relatively small number of elements. A new parallel discrete element algorithm is presented which combines the domain decomposition, object-oriented, and perfectly parallel strategies of parallelism to eliminate the drawbacks of parallel discrete element algorithms put forth by past studies. A significant speed-up is observed in comparison to past studies in trials conducted on a NUMA-based SMP computer.

In Part II, various applications of the discrete element method are reviewed, with an emphasis on ice-structure interaction. The conical design of the Kulluk drillship is of particular interest due to its success in operating in the Beaufort Sea from 1975-1993 and its subsequent purchase and recommission by Shell in 2006. Three previous experimental studies and a unique set of full-scale data measurements form the basis for comparison of a concurrent experimental and numerical investigation. The

results of a model scale experiment at the NRC-IOT are analyzed and presented, followed by results of the numerical simulations. A 1:40 scale replica of the Kulluk platform in level ice produces results which are consistent with past experiments and confirm expected trends as well as different regimes of results dependent on the ductile/brittle behavior of ice. The numerical setup models the full-scale platform in three dimensions with a 24-sided rigid conical structure, ice as an elastic brittle material with plate-bending elements, and platform mooring through the implementation of a spread mooring algorithm. Numerical results are in agreement with past results for ice thickness of less than 1.2m, confirming that the initial design goal of the Kulluk was achieved while still overestimating the loads in comparison to the full-scale data set. Two explanations are presented for the non-conformity of the experimental and numerical predictions to the full-scale data results.

Acknowledgements

The financial support from the University of Waterloo, NSERC, and the NRC which made this research possible is greatly appreciated. In the following paragraphs I will attempt to extend my gratitude for all those assisted me throughout my graduate career.

Dr. Leo Rothenburg, for his invaluable guidance, insightful discussions, and immeasurable encouragement. While being an excellent supervisor and mentor, he has exhibited a kindness and understanding that I will strive to carry with me in my future endeavors.

Dr. Michael Lau, my co-supervisor at the NRC, for initially proposing the problem discussed in the thesis, his instruction and assistance, and direction throughout the course of my study.

The examining committee, Dr. Wayne Brodland, Dr. Giovanni Cascante, Dr. Maurice Dusseault, and Dr. John McPhee, for your invaluable comments, suggestions, and training during my study.

Dr. Mark Knight, for his generosity, countless discussions, and enthusiastic approach

which allowed me to expand my interests into new and developing engineering techniques.

Dr. Graham Gladwell, for, first, the opportunity to study in an area not to distant from my thesis topic, and secondly, for the chance to learn from one of the foremost experts in the field.

The administrative and computer staff of the Department of Civil Engineering: Marguarite Knectel, Bonnie Neglia, Sandra Machan, Sara Bland, Shirley Springall, Alice Seviora, Ken Bowman, Kevin Rampersad and Mike Cocker; for their assistance and kindness on many, many occasions.

My fellow graduate students, specifically Alireza Bayat and Rizwan Younis, for their true friendship which will undoubtedly continue for many more years to come.

Finally, on a personal note, I wish to thank all of my family and friends who were so patient and supportive during my post-secondary education. In particular my long time girlfriend, recently turned wife, Colleen. I can only hope to reflect the support you have shown me over the years.

To my wife, Colleen

Contents

List of Tables

List of Figures

Common Notations

Lower Case

a	contact radius
b	beam width
g	gravity
h	ice thickness
h_f	ride-up height
k	spring stiffness
l_c	characteristic length
(r, θ, z)	cylindrical coordinates
u	displacement
(x, y, z)	cartesian coordinates

Upper Case

D	structure diameter at waterline
E	Young's modulus
F_h	horizontal force
F_v	vertical force
K	mooring stiffness
P	load distribution
S_0	cohesion

T	temperature

Greek

α	cone angle
γ	porosity
δ	distance of mutual approach
ϵ	strain
μ	friction coefficient
ν	
ρ	density
ρ_i	ice density
ρ_w	water density
σ	stress
σ_1, σ_3	principal stresses
σ_c	compressive strength
σ_f	flexural strength
σ_t	tensile strength
τ	shear stress

Nomenclature

3DEC	Three-dimensional Discrete Element Code, from Itasca
AABB	Axis-aligned bounding box
ACL	Arctec Canada Limited
AMI	Applied Mechanics Inc.
AOGA	Alaskan Oil and Gas Association
ASME	American Society of Mechanical Engineers
C-CORE	Centre for Cold Ocean Research
CCREL	Cold Regions Research and Engineering Laboratory
CHC	Canadian Hydraulics Centre
CP	Common plane
CPU	Computer processing unit
DDA	Discontinuous deformation analysis
DE	Discrete Element
DECICE	Discrete Element Code for studying Ice related problems

DEM	Discrete Element Method
DESS	Double sided spatial sorting
EGADS	Ethylene Glycol - Aliphatic Detergent - Sugar
FCP	Fast common plane
FPGA	Field programmable gate arrays
FPSO	Floating Production Storage and Offloading vessel
GBS	Gravity Base Structure
GJK	Gilbert-Johnson-Keerthi
HPC	High performance computing
HSVA	Hamburg Model Ship Basin, Germany
IAHR	International Association for Hydraulic Research
IIHR	Iowa Institute for Hydraulic Research
IUTAM	International Union for Theoretical and Applied Mechanics
MPI	Message Passing Interface
NBS	No Binary Search
NCSA	National Center for Supercomputing Applications
NCSU	North Carolina State University
NRC	National Research Council of Canada
NRC-IMD	NRC Institute for Marine Dynamics

NRC-IOT	NRC Institute of Ocean Technology
NUMA	Non-Uniform Memory Access
OMAE	Offshore Mechanics and Engineering
PERD	Program on Energy Research and Development
PGI	Portland Group Inc.
POAC	Port and Ocean Engineering under Arctic Conditions
RCB	recursive coordinate bisection
SGI	Silicon Graphics Inc.
SLM	Shortest link method
SMP	Symmetric Multi-Processor
TLS	Two-level search
UDEC	Universal Discrete Element Code, from Itasca

Chapter 1

Introduction

1.1 Background

The oil and gas industry is one of Canada's most economically stimulating businesses. It not only provides a major export entity but also creates countless jobs during the construction, operation, and decommission phases of a typical project. Canada has abundant quantities of crude oil reserves both on- and offshore which have been or are currently being developed (see Figure 1.1). Onshore activities account for much of the development but are mainly focused in Alberta, where technology is constantly evolving to extract the estimated 315 billion barrels of oil in the oil sand deposits. A typical drilling platform in Western Canada produces approximately 8 cubic meters of oil per day on average (per well).

Offshore deposits (see Figure 1.2) have been harvested at rates of up to 9000 cubic meters per day (Canadian Centre for Energy Information, 2004). Conservative estimates of the offshore reserves suggest approximately 1.6 billion barrels of oil and 3 trillion cubic feet of gas are waiting to be extracted (Wright, 2000). The largest offshore oil and gas project currently in operation in Canada is Hibernia, located 315 km

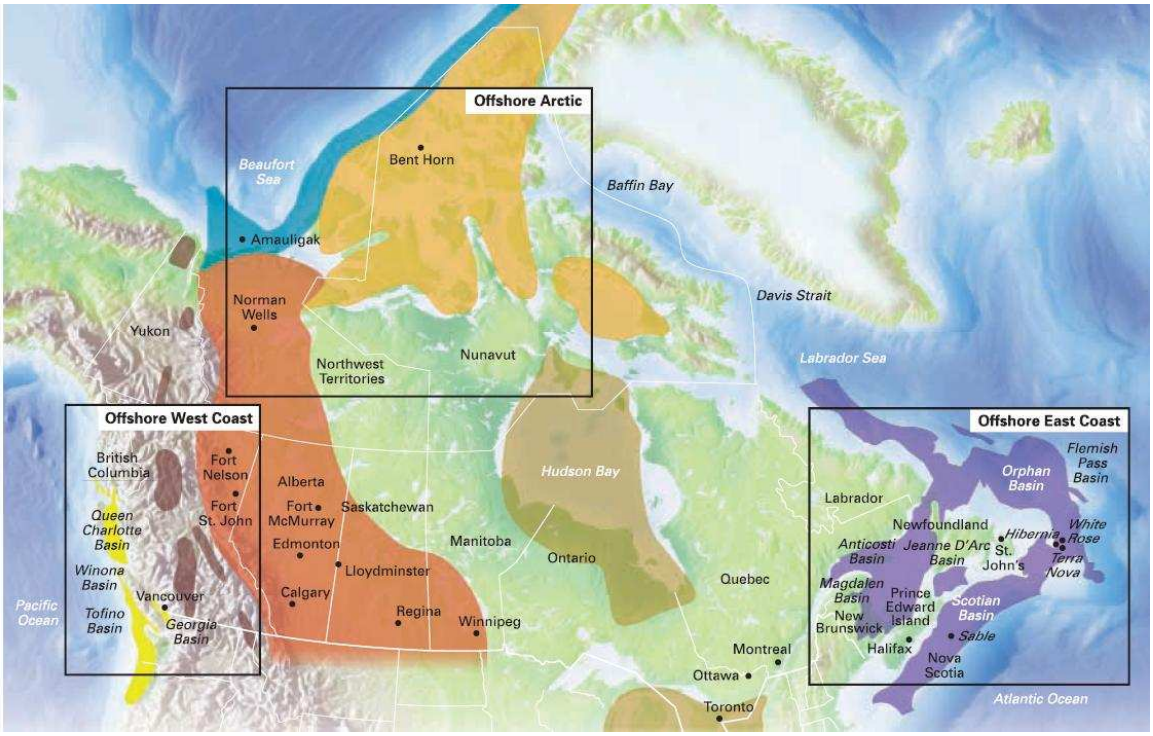

Figure 1.1: Map of Canada showing location of known crude oil deposits on- and offshore. (Canadian Centre for Energy Information, 2004)

Figure 1.2: Map of Eastern Canada showing location of known crude oil deposits offshore. (Canadian Centre for Energy Information, 2004)

east-southeast of St. John's, Newfoundland. This platform commenced operation in 1996 using a gravity-based structure (GBS) design in which the base of the platform rests on the ocean floor. The initial harvesting rate was 9000 cubic meters per day but has since slowed to 6000 cubic meters (150,000 barrels) per day as resources are depleted. Other current offshore developments are the Terra Nova (35km south-east of Hibernia) and White Rose projects (350km east of St. John's), which commenced operations in 2002 and 2005, respectively. Estimated oil reserves are 405 million barrels at the Terra Nova oilfield and 180 million barrels at the White Rose development. These projects utilize a floating production, storage, and offloading (FPSO) vessel.

Drilling platforms and barges off the east coast of Canada in the Arctic Ocean are subject to environmental challenges such as high winds, large waves, icebergs, and

pack ice. The GBS and FPSO structures have been specifically designed to withstand these factors. A key design requirement, for instance, of the Hibernia platform, was the ability to withstand the impact of a one-million-tonne iceberg with no damage.

As oil exploration moves further offshore to deeper water, floating platforms (Terra Nova, White Rose) are preferred over bottom-mounted structures (Hibernia) due to their cheaper construction costs and faster startup times. The dynamic response of fixed and moored platforms in various ice conditions and optimization of the platform geometry has been the topic of related research in the past two decades, with the bulk of the literature focused on conical-shaped drilling barges. These drillships offer a multi-directional resistance to ice and are subject, in most instances, to lower overall loads due to the dominant mode of ice failure (flexural or bending). Figure 1.3 displays the profile and plan views of upward- and downward-breaking conical structures and the resultant dominant failure mode when it is impacted by a level ice sheet. Upward- and downward-breaking fixed conical structures have been addressed in several experiments (Haynes et al., 1983; Wessels, 1984; Kato, 1986; Hirayama and Obara, 1986; Clough and Vinson, 1986; Maattanen, 1986; Lau et al., 1988; Lau and Williams, 1991) which have yielded empirical formulae for estimating peak horizontal and vertical loads. These loads are divided into three components: breaking, ride-up of the approaching ice sheet onto the structure, and clearing of the pieces around the structure. Inverting the structure, i.e., producing a downward-breaking fixed cone, has been shown to decrease the measured horizontal force by nearly 50% (Wessels, 1984) due to the absence of the ride-up component. Allowing the conical structure to undergo controlled displacements via an array of mooring cables produces an additional reduction of 50% in the observed horizontal force.

Downward-breaking conical drillships have also displayed distinct advantages over

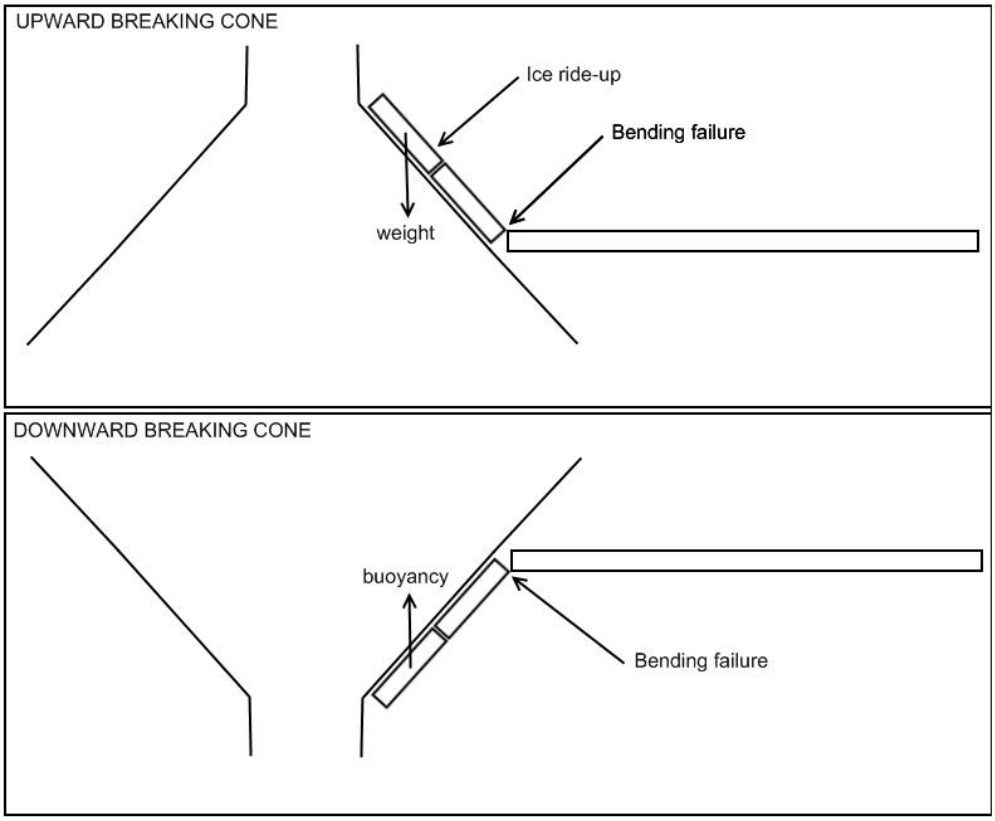

Figure 1.3: Conical structures and typical failure modes.

other vessels (Wright et al., 1998) when in operation. The most extensively studied ship of this kind is the "Kulluk", Inuvialuit for *thunder*, drilling barge, which operated in the ice-infested waters of the Beaufort Sea (see Figure 1.4) from the mid-1970s to the mid-1990s. The key design goals which motivated the conical shape and mooring were outlined by Wright (2000) and include:

1. minimizing ice forces by giving the ship a multi-directional resistance to ice
2. developing a base which would minimize ice forces and enhance the clearance of ice
3. developing a strong mooring which could resist large ice loads from pack ice
4. developing a submerged mooring system that would eliminate possible entanglement.

The conical shape of the drillship promotes fracturing of ice via bending, which significantly reduces the peak ice forces on the structure (implementing points 1-2). The downward-breaking design of the structure further promotes the submergence of the adjacent ice sheet as opposed to ride-up for upward-breaking conical ships, resulting in lower overall peak forces and enhanced clearing capabilities. The flare-out in hull design near the bottom of the structure prevents entanglement of the ice pieces with the mooring cables which, through a strong submerged mooring system, gives the structure an increased stability comparable to that of bottom-mounted structures but without the exorbitant costs.

The Kulluk facility, which included ice-breaker support, was extremely successful in extending operation of the drill rig an additional 30-60 days into the winter season. The revenue associated with this increase assuming a production rate of 80,000 barrels per day at $40 per barrel is approximately $100-200 million. After being idle for

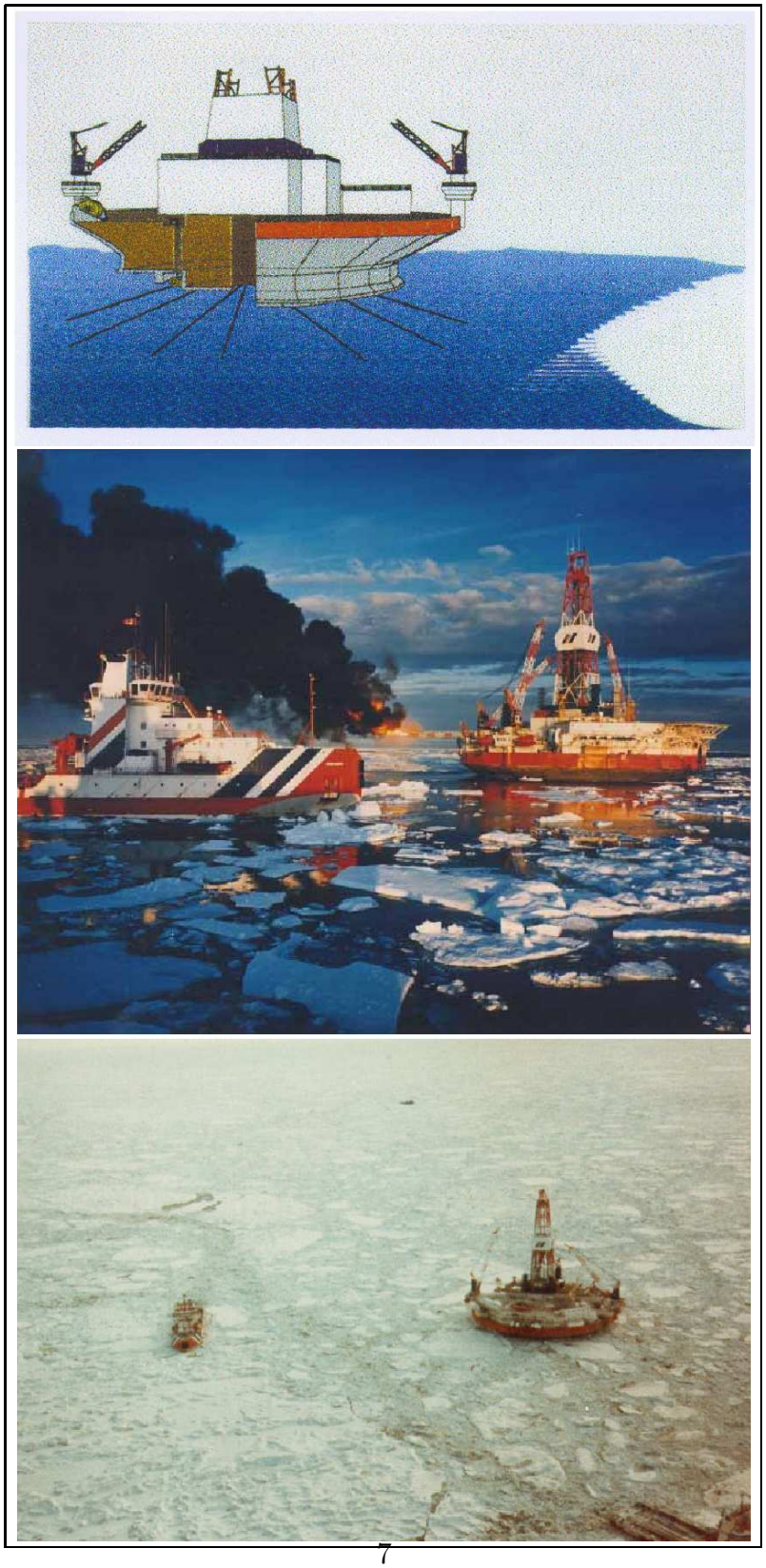

Figure 1.4: Schematic diagram of drillship Kulluk (top); the Kulluk operating in the Beaufort Sea at the Pitsiulak location (middle) testing for oil; the Kulluk drillship in ice-infested waters of the Beaufort Sea (bottom). Top/middle figures taken from Wright (2000). Bottom figure from Timco and Johnston (2002).

the 13-year period from 1993 to 2006, the Kulluk was still considered a state-of-the-art platform for oil and gas exploration. Consequently, Shell purchased the drillship from Gulf Canada and, after some refurbishment, sent it into the Beaufort Sea to drill three more wells at water depths up to 4000 meters.

1.2 Scope and Objectives

With the rapid advance of numerical techniques and computational hardware, numerical analysis has become a powerful simulation tool for modeling full-scale engineering problems. The discrete element method was developed to solve complex solid mechanics problems involving multiple interacting bodies undergoing fracturing, and it is particularly appropriate for cases in which contact behavior between adjacent ice blocks governs the interaction processes. However, a computational bottleneck, which is inherent in the method as the number and complexity of simulation elements increase, has slowed the growth of this numerical method.

The main objectives of this study are to:

(i) improve performance of the discrete element method through implementation of an improved contact detection algorithm;

(ii) develop a parallel algorithm for the DEM which performs well on multi-processor computers and achieves an adequate level of load-balancing;

(iii) implement a realistic mooring algorithm capable of simulating typical mooring systems for offshore vessels;

(iv) perform simulations in three-dimensions of a moored conical drillship with characteristics similar to that of the "Kulluk" in an effort to predict its dynamic load response in level, unbroken ice;

(v) compare the numerical results with existing model-scale experiments conducted at the NRC-IOT concurrent to this research, other model-scale experiments present in the literature, and full-scale observations.

Improved performance of the discrete element method allows for larger problem sets or finer detail of existing problem sets to be studied. While it will facilitate the current set of simulations, the importance of the results is applicable in any area utilizing the discrete element method to simulate the interaction of large numbers of particles.

The use of numerical methods for predicting peak ice loads on fixed and moored structures is a necessary tool for designers. Experiments of model scale structures in ice often produce varied or higher load results compared to the full-scale system as a consequence of the varying dynamics of the smaller scale systems. Numerical simulations offer a cheap (by comparison) and efficient alternative by which to investigate these problems. Moreover, the influence of inherent material properties which may not be addressed via experiment simulations may also be considered.

1.3 Approaches and Methodology

The Institute of Ocean Technology (IOT), a division of the National Research Council of Canada (NRC), is dedicated to the advancement of infrastructure and technology for ice-related engineering problems. To date, most of the contributions from this institution have been analytical, experimental, or empirical in nature. To complement these efforts, the IOT has recently initiated a strategy to pursue numerical modeling of ice-related problems using the discrete element method through this research.

Cundall (1971) first proposed the "distinct" element method as a means for simulating the behavior of jointed rocks. The details of the procedure were outlined in Cundall

and Strack (1978a, b), which was generalized in a subsequent paper by Williams et al. (1985), who presented the "discrete" element method (DEM). Since then, it has been applied to a wide range of problems via independent codes and commercial software. Applications of the discrete element method arise in mechanical, geotechnical and structural engineering and include, but are not limited to, simulations of particle motion, granular assemblies, ice-structure interaction, fracturing rocks, silo filling, impact problems, and so on (see for example Williams and O'Connor (1999), Lau et al. (2000), Han et al. (2000a,b), Hashash et al. (2005); Hashash (2006), Wait (2001)).

DECICE is an acronym for Discrete Element Code for ice-related problems. It is a commercial code, owned by Oceanic Consulting Group, currently in use by the NRC-IOT to study a variety of problems. The computer program was developed in 1986 by Applied Mechanics Inc. (Intera Technologies Inc., 1986) to solve complex solid mechanics problems (see Williams et al. (1985), Mustoe et al. (1987), Hocking et al. (1985c), Hocking et al. (1985a), Hocking et al. (1985b), Hocking et al. (1987)). DECICE simulations have been compared with model scale experimental tests conducted at the IOT in order to exhibit the power of accurate numerical modeling. Representative tests include an ice-sheet impacting a downward-sloping conical structure (bridge pier), performance of survival craft in an ice-infested environment, maneuvering of a ship in sea ice, ridge keel resistance during scouring, forces exerted by pack ice, and ice arch formation (see Schachter and Spencer (1994), McKenna (1997), Lau (1999, 2001, 2006), Lau et al. (2000); Lau and Re (2006); Lau et al. (2008)).

This research investigation is composed of theoretical, experimental, and numerical studies. The theoretical issues are at the forefront of discrete element modeling

as discussed in a review by Cundall and Hart (1992). In the paper, a list of beneficial developments which would add to the existing knowledge base of the discrete element method was suggested. The first two of the nine listed improvements are:

> 1. Robust and efficient algorithms for contact detection and updating (Cundall and Hart, 1992)

and

> 2. Development of data structures and algorithms suitable for parallel-processing machines (Cundall and Hart, 1992).

This constitutes the motivation between research objectives (i)-(ii) as discussed in the previous section.

In another report by Comfort et al. (1999) which evaluated model test experiments of moored structures in ice, it was suggested that the next step in understanding the complexities associated with ice-structure interaction were:

1. comparing the results with existing field data (a reference was made directly to the Kulluk drillship due to the wealth of information collected) and;
2. comparing the results with numerical modeling results which can be used to determine the effect of the different parameters.

A series of reports were published in the following years by Wright (1999, 2000) addressing the first issue, but relatively little has been achieved on the second. To the knowledge of the author, the only attempt at numerical simulations used a two-dimensional particle in cell method (see Barker et al. (2000b,a)) to achieve very rough estimates without modeling the true complexities of the system (such as the spread mooring system, the dynamic response, and the three-dimensional nature). The gap

in the literature put forth by Comfort et al. (1999) forms the basis of research objectives (iii)-(v).

In Part I of this thesis, the two fundamental issues discussed by Cundall and Hart (1992) are investigated. Algorithms relating to the discrete element method are studied across a wide range of research areas including computer graphics, computational geometry, and engineering. Although the application and requirements in each field are unique, the driving forces behind the need for algorithm development are the improvements listed above.

Part II of this thesis focuses on numerical simulations of the motivating problem, complemented with existing experimental and full-scale results. Experimental tests of a 1:40 model size drillship were conducted by the technical staff at the NRC-IOT under the supervision of Dr. Michael Lau concurrently to this work and the findings are reported herein. Similar experimental findings are also presented for comparison, as are the full-scale observations for the drillship. The full-scale results which were summarized in a series of reports by Wright (1999, 2000) represent an unparalleled source of data. At the time, the ice and performance monitoring was used to provide real-time information to onboard personnel who made decisions related to ice management and safety concerns. Three-dimensional simulations are conducted using the DECICE code for both a fixed and moored full-scale representation of the Kulluk drillship. A mooring algorithm is implemented into DECICE which is capable of simulating the actual mooring conditions present and recorded while in operation. The effect of numerical and physical parameters on the resulting interaction of the ship and ice are addressed by series of computer simulations.

1.4 Organization of the Thesis

This thesis consists of a total of nine chapters. The first chapter is introductory and discusses the motivation and methodology of the problem. Chapter 2 marks the beginning of Part I of the research and presents the mathematical formulation of the DEM within DECICE as well as a literature review of the DEM algorithm and its applications (including those using the DECICE algorithm) over the past three to four decades. DEM limitations are addressed which exhibit the requirement for a new contact detection algorithm within the DECICE code. Chapter 3 presents the algorithm improvement and results along with benchmark verification problems for the new contact detection scheme. The algorithm is developed specifically within the DECICE framework to minimize CPU resources with the use of modern data-storage techniques. This redevelopment of the original algorithms and data structures lead into an investigation of high-performance computing issues which are considered in Chapter 4 by the extension of DECICE to a multi-processor environment. Chapter 5 marks the transition to Part II of the research. The complete Kulluk model description as well as a review of relevant literature on ice-structure interaction is presented. The experimental findings obtained at the NRC-IOT are presented in Chapter 6. In Chapter 7, simulations involving a downward breaking moored conical drillship, similar to the Kulluk, in unbroken level ice are considered. Chapter 7 also outlines the incorporation of a new spread mooring algorithm following from Lau et al. (2005) into the DECICE code. Comparisons are made to existing experimental/measured results when available. The final chapter summarizes the contributions and results of the current research. Future work in the area is also proposed.

PART I. THEORETICAL CONTRIBUTIONS TO THE DISCRETE ELEMENT METHOD

Chapter 2

The Discrete Element Method

2.1 Introduction

This chapter presents the mathematical formulation of the DEM within DECICE as well as a literature review of the DEM algorithm and its applications over the past three to four decades. DEM limitations are addressed which exhibit the requirement for a new contact detection algorithm within the DECICE code.

2.2 History of the Discrete Element Method

Numerical techniques such as the finite difference, finite element, and boundary element methods were developed to model problems of continuum mechanics. The theory has been extended to jointed materials and elements allowing for models involving discontinuous media through the use of interface elements or "slide lines". Predetermined knowledge of the geometry (and interface characteristics) are required in these extensions, which lead to difficulties when the simulation should consider intersecting interfaces, the detection of new contacts, and large displacement/rotations. These continuum-based models are not particularly suited to studying granular/block

media such as soils, rocks, and ice floes, which involve multiple bodies which may interact with one another and undergo displacements, rotations, and fracturing.

The discrete element method is a numerical technique used to simulate the motion of systems involving a large number of particles or any other discontinuous media. It is similar to the finite element method but with the modification that individual elements are viewed as distinct entities. In a local element-by-element sense, it is still founded in continuum mechanics since each element or group of elements is governed by the laws of continuum mechanics. Continuum mechanics problems may be modeled with the DEM using techniques such as inter-element "locking" in which separation forces have an opposite signed counterpart which "lock" two or more elements together. The finite-element/difference techniques assume continuity and treat interacting objects as a special case. The DEM is based on the assumption that every discrete element has distinct boundaries which separate it from every other element and hence is directly applicable to problems involving discontinuous media.

Several numerical recipes in the literature fall under the heading of the discrete element method (see Figure 2.1). The first division is based upon the material representation of elements as rigid or deformable. When the deformation of a system is dependent on the movement of elements, as is the case for simulations of unconfined rock masses, the use of rigid elements is suitable. When this is not the case, element deformations should be addressed, typically using either of the following two methods. The first method involves sub-dividing elements into constant strain zones. The two-dimensional code UDEC (Itasca, 2003d) divides all blocks into multiple constant strain triangles as a means of representing internal deformations. When this method is used in conjunction with an explicit in-time numerical scheme, it is referred to as the "distinct" element method (following from Cundall (1971)). The second method

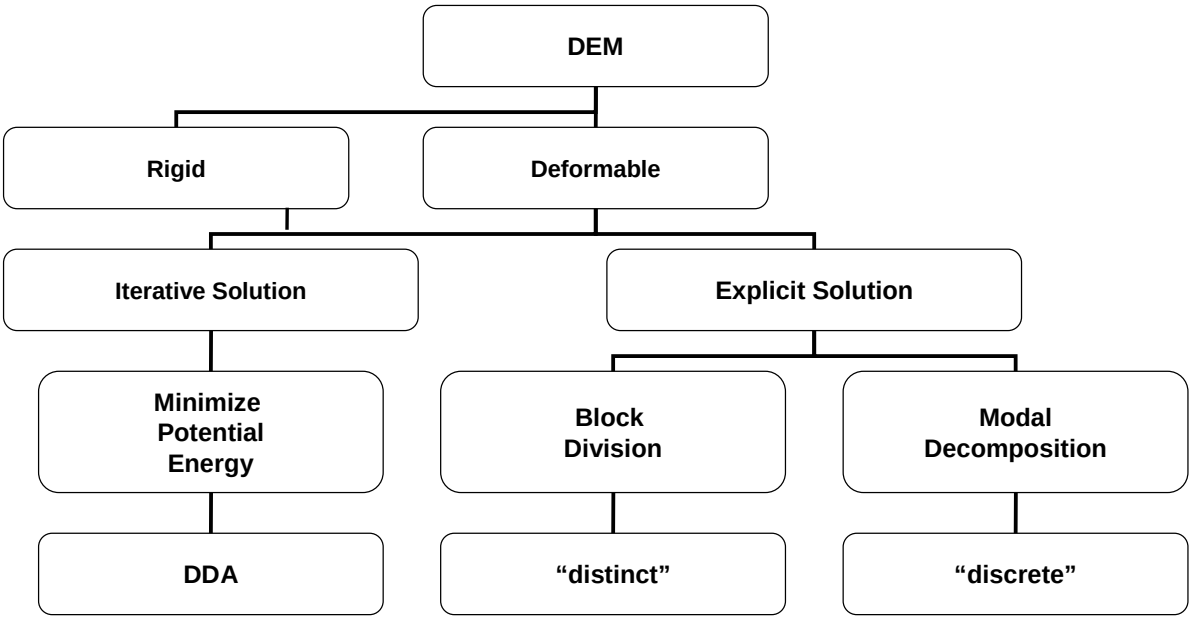

Figure 2.1: Branches of the discrete element method (DEM)

for representing deformable elements is to express the body as a superposition of modal shapes (not necessarily the eigenmodes; see Williams et al. (1987)). This was originally termed the “discrete” element method but has coalesced over the years with the “distinct” element method of Cundall to form the broader category term DEM. Simple deformation of complex shapes may be simulated more efficiently using the second method, since only a few modes are typically required as compared to a detailed subdivision of the element. The requirement of the superposition of modes, however, leads to difficulties in representing non-linear materials - a property more simply represented in the first method by assigning the appropriate constitutive relationship to the subdivisions.

A third distinction made within the area of discrete element methods which allow for rigid and deformable elements is discontinuous deformation analysis (DDA). It

was first introduced by Shi (1989) using the principle of minimum potential energy but may be derived in general using Hamilton's principle. Implicit iterations are used to solve a set of equilibrium displacement equations which minimize the potential energy. This is different than the methods discussed above which solve the equations of motion explicitly, requiring the dissipation of energy through some means of damping; care must be taken not to over-damp the system to the point where the true vibrations are removed. In DDA, no such artificial damping is required to dissipate energy, but the inherent numerical damping is often too large (since it grows proportionally to characteristic length scale) and must be reduced through other methods.

The particular branch of the DEM studied in this thesis follows from Williams et al. (1985). Since its conception, variations of the DEM have been applied to a wide range of problems via independent codes and commercial software such as those listed in Table 2.1: Most of these algorithms use either two-dimensional disks or

Code Name	Author	2D/3D	Elements
BALL	Cundall	2D	circular
TRUBALL	Cundall	3D	spherical
SDEC	F. Donze	2D	circular
YADE	F. Donze	3D	circular
EDEM	DEM Solutions Ltd	3D	spherical
ELFIN	Rockfield Software Ltd	2D/3D	Combined FE/DE
PFC	Itasca (2003b)	2D	circular
PFC3D	Itasca (2003c)	3D	spherical
UDEC	Itasca (2003d)	2D	polygonal
3DEC	Itasca (2003a)	3D	polyhedral
DBLOKS3D	Nezami et al. (2004)	3D	polyhedral
DECICE	Williams et al. (1987)	2D	polygonal
DECICE3D	Williams et al. (1987)	3D	polygonal

Table 2.1: Summary of existing independent codes and commercial software employing the DEM.

three-dimensional spheres in their discrete element formulation due to their simple

geometric representations (i.e., only location and radius are required). Studies have shown however that circular elements may fail to model the true dynamics of granular problems (Grest et al., 2001) and that a more realistic model of disjoint media would use polygonal (in 2D) and polyhedral (in 3D) elements. These element types are composed of vertices, edges, and faces which much be monitored during each calculation step to identify possible contacting elements. Inter-particle contacts must be resolved to prevent the penetration of one particle into another. Proper detection and resolution of these contacts is therefore much more complex than for circular elements, resulting is a computational bottleneck during this portion of the DE algorithm. For that reason, only DECICE3D, 3DEC and DBLOK3D make use of three-dimensional polyhedral elements in their discrete element schemes.

Separating forces may be calculated using either the "soft contact" or "hard contact" approach. In the hard contact approach, no interpenetration of elements is allowed and hence compatibility conditions must be enforced along the boundaries of contacting elements (see Cundall and Hart (1992)). In contrast, the soft contact approach permits the numerical (non-physical) interpenetration of approaching elements and calculates the separation force as a function of the penetration depth and/or overlap area between the two contacting elements.

In 1987, G. Hocking and his coworkers through Applied Mechanics Incorporated (Hocking et al., 1985c; Williams et al., 1985) created a Discrete Element Code for ICE-related problems. The computer program was developed using 8- (cuboids), 6- (wedges), and 4-noded (tetrahedrons) polyhedra (see Figure 2.2). Initial ice-related problems were verified using the DECICE code by Hocking et al. (1985c,a,b), and Worgan and Mustoe (1989).

In 1993, the National Research Council's Institute for Ocean Technology (NRC-IOT) acquired the right to use the software to model ice-related problems. Since then, the DECICE software has been upgraded and successfully used to model problems including ice loads on conical structures, jamming of floes at bridge piers, modeling of the mechanical behavior of ice rubble, pack ice stability and associated forces on offshore structures, rubble loads exerted on an inclined retaining wall, ridge keel resistance during seabed scouring, performance of a ship maneuvering in ice, characteristics leading to ice arch formation between bridge piers, and the performance of a survival craft in ice (see Schachter and Spencer (1994), McKenna (1997), Lau (1999, 2001, 2006), Lau et al. (2000); Lau and Re (2006); Lau et al. (2008)).

One of the purposes of this research is to improve the performance of the DEM within DECICE code. To accomplish this task, the particular formulation and solution scheme of the discrete element method within DECICE is outlined in the next section.

2.3 DECICE Method of Solution

2.3.1 Overview

In the following subsections, the solution procedure within DECICE is outlined. The goal is to transform the governing laws into a set of discretized equations for each type of element (tetrahedron, wedge, cuboid). These discretized equations are then solved by expressing the displacement field as a superposition of spatial/time-dependent functions. For small elastic displacements, translational and rotational motions are given by the zero frequency mode, and higher order modes describe the deformation. The number of modes required to describe the deformation of the elements differs

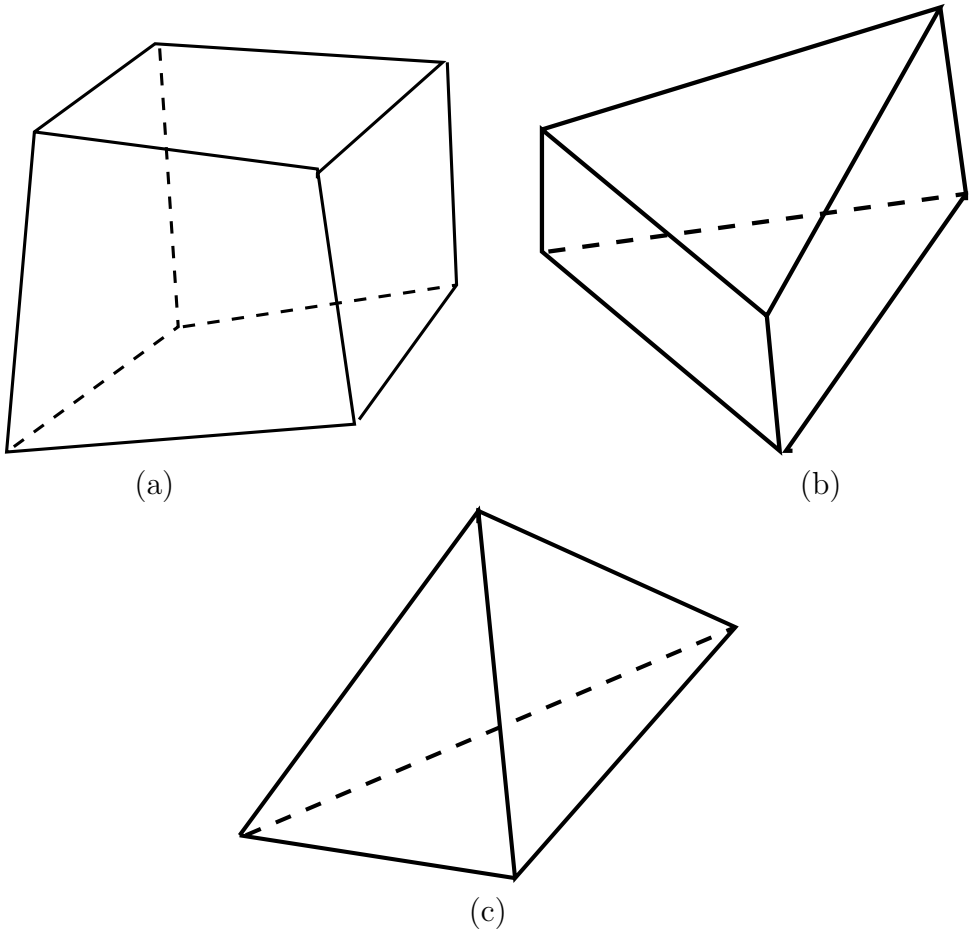

Figure 2.2: Allowable polyhedral elements within DECICE; (a) cuboids, (b) wedges, and (c) tetrahedrons.

depending on the order (number of nodes) of the element. The resultant equations for the natural modes may be decoupled and are in the familiar form of Euler's equation given by

$$\mathbf{M}\ddot{\xi} + \mathbf{C}\dot{\xi} + \mathbf{K}\xi = \mathbf{F} \tag{2.1}$$

where ξ is an unknown time-dependent function, dot refers to differentiation in time, $\mathbf{M}$ is the mass matrix, $\mathbf{C}$ is the damping matrix, $\mathbf{K}$ is the stiffness matrix, and $\mathbf{F}$ is the applied load. These equations are integrated using a second order central difference scheme given below:

$$\dot{\xi}_i = \mathbf{M}^{-1}(\mathbf{F}(t_i) - \mathbf{C}\dot{\xi}(t_{i-\frac{1}{2}}) - \mathbf{K}\xi(t_i) \tag{2.2}$$

$$\dot{\xi}(t_{i+\frac{1}{2}}) = \dot{\xi}(t_{i-\frac{1}{2}}) + \ddot{\xi}(t_i)\triangle t \tag{2.3}$$

$$\xi(t_{i+1}) = \xi(t_i) + \dot{\xi}(t_i)\triangle t \tag{2.4}$$

where $\triangle t$ is the time step and t_i is the current time. The velocity used in the damping term of the first equation must lag behind by half a time-step, since it is calculated using the acceleration in the second equation.

2.3.2 Governing equations and discretization

The governing equations of the discrete element method follow from conservation of mass and energy and the balance of momentum and moment of momentum. These equations mathematically describe the transient motion of a rigid or deformable body (element) when paired with a set of appropriate initial and boundary conditions. Within the formulation of DECICE, a non-inertial frame of reference is employed so that the total linear and angular momentum of the element is zero. A trial expansion representing the displacement vector for element i is written as

$$u_i(x, y, z, t) = \sum_{k=1}^{\infty} \phi_i^k(x, y, z)\xi^k(t) \tag{2.5}$$

so that the spatial and temporal variables are separated using the basis functions $\phi_i^k(x, y, z)$ and unknown time-dependent functions $\xi^k(t)$. Using Hamilton's principle the governing equations of motion and deformation can be written as

$$M^k \ddot{\xi} k = F_V^k + F_S^k - \int \phi_{i,j}^k \sigma_{ij} dV \tag{2.6}$$

where

$$M^k = \int_V \rho \phi_i^k \phi_i^k dV \tag{2.7}$$

is the mass matrix constructed using the basis functions,

$$F_V^k = \int_V \phi_i^k R_i dV \tag{2.8}$$

are body forces acting over the volume of each element,

$$F_S = \int_S \phi_i \sigma_{ij} n_j dS \tag{2.9}$$

are the surface/traction forces, ρ is the density, σ_{ij} is the stress tensor, n_j is the unit (outward) normal to S and R_i are body forces per unit volume. A finite number of basis functions, n, are then utilized to describe a linear displacement field in two and three dimensions as

$$u_i(x, y, z, t) = u_i^0(t) + e_{ijk}\Theta_j(t) r_k + \phi_i^m \xi^m(t) + \cdots + \phi_i^n \xi^n(t) \tag{2.10}$$

where $r = (x, y, z)$ is the position vector of any point P within the element in the moving frame of reference, $u_i^0(t)$ is the component of rigid body translation, $\Theta_i(t)$ are the components of rigid body rotation, and ϕ_i^k, $k = m$ to n, are the components of the expansion representing the displacement due to deformation. Rigid elements may be completely represented by the first two terms of (2.10). Assuming small relative displacements and a constant stress distribution σ_{ij} within each element a set of decoupled equations in the form of Euler's equation for the rigid body motion/deformation terms of (2.10) may be obtained and solved using the central difference scheme previously outlined. For more information on the numerical scheme refer to the original contributions of Hocking (1987), Mustoe (1992), or Intera Technologies Inc. (1986).

2.3.3 Applied loads

The total applied load on each element is the sum of all global and local forces acting on that element. These include

- body forces;
- buoyancy and water drag forces; and
- interaction forces.

Body forces are global forces and apply to all element centroids within a certain zone, buoyancy and water drag forces are calculated for those elements which displace a volume of water, and interaction forces are present when one element comes into contact with another to prevent interpenetration of elements, using the "soft contact" approach discussed earlier. The contact law which is implemented in DECICE is the common spring-dashpot model based on Hookian theory given by

$$F_n = k_n u_n + \beta \dot{u}_n \tag{2.11}$$

$$F_s = k_s u_s + \beta \dot{u}_s \tag{2.12}$$

where k_n (k_s) is the normal (shear) interaction stiffness, u_n (u_s) is the normal (shear) deformation, and F_n (F_s) is the calculated normal (shear) interaction force, and β is a damping parameter for the dashpot forces acting against the corresponding velocities ($\dot{u}_n$, $\dot{u}_s$). This law is commonly used in practice, since the linear dependence of the contact force on the calculated displacement is computationally very efficient.

2.3.4 Interaction and cracking

Two types of failure are permitted within DECICE. The first is the cracking of elements which are "locked" together and the second is the cracking of elements through their centroid (see Figure 2.3). Element locking is implemented via attractive inter-

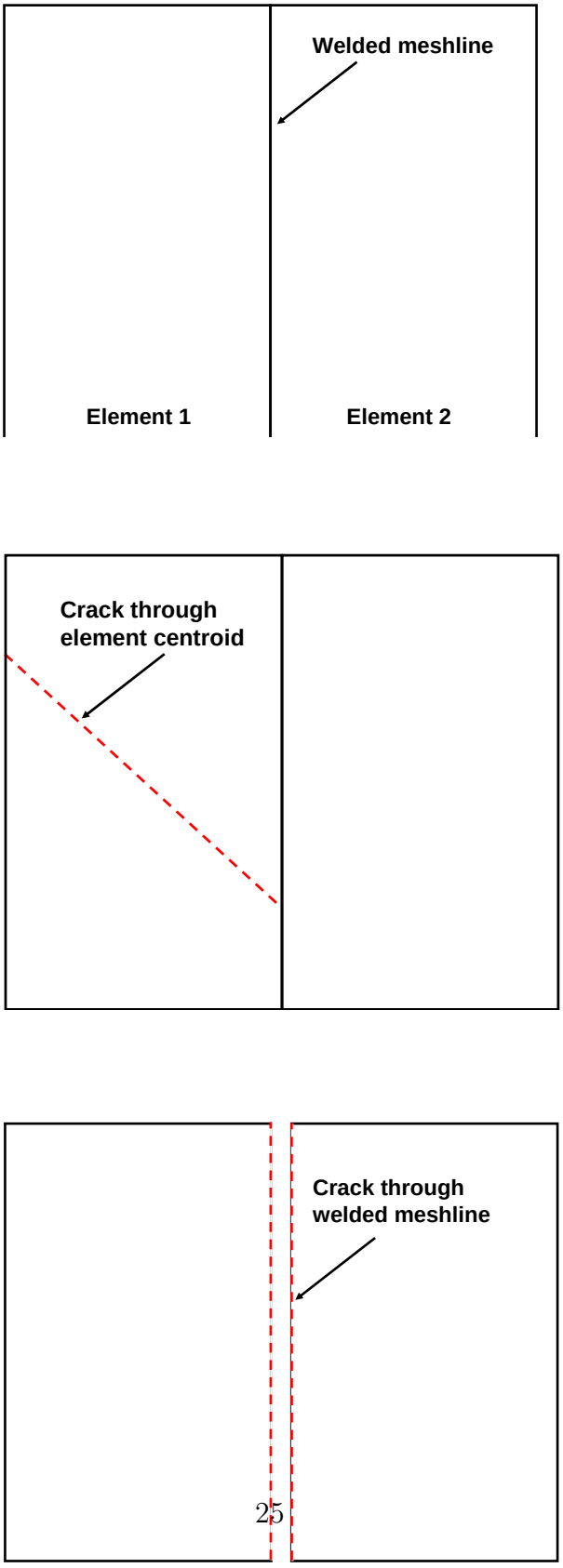

Figure 2.3: Two types of element fracturing permitted within DECICE

element contact forces which act to keep elements together as opposed to preventing interpenetration. Locking may be used in the DEM to model continuum-based features. Inter-element fracturing occurs along the common faces where elements are locked. The second type of permitted fracturing is intra-element fracturing. Elements are permitted to fracture through their centroid, but at any angle. Triangular and quadrilateral elements in two dimensions for instance may fracture into subsequent triangular and quadrilateral elements, and cuboids and wedges in three dimensions may fracture into subsequent cuboids and wedges. The only further stipulation is that three dimensional elements fracture through opposite faces. Fracturing of tetrahedral elements is therefore prohibited since tetrahedral elements do not have a clearly defined opposite face.

The three failure criteria implemented within DECICE are compressive (shear), tensile, and bending failure. The specifics, defined by the Mohr-Coulomb tension cutoff model, are described below for each of the three cases.

Compressive failure

First, the criteria for compressive (shear) failure along a plane is given by

$$|\tau| \geq S_0 + \mu\sigma \tag{2.13}$$

where σ and τ are the normal and shear stresses, μ is the coefficient of internal friction, and S_0 is the internal cohesion of the material which is either defined by user-input or calculated using the unconfined compressive strength σ_c as

$$S_0 = \sigma_c \frac{\sqrt{\mu^2 + 1} - \mu}{2}. \tag{2.14}$$

For intra-element cracking, this condition is rewritten in terms of the principle stresses as

$$\sigma_1 \geq \sigma_c + \sigma_3 \tan^2\left(\frac{\pi}{4} + \frac{\phi}{2}\right) \tag{2.15}$$

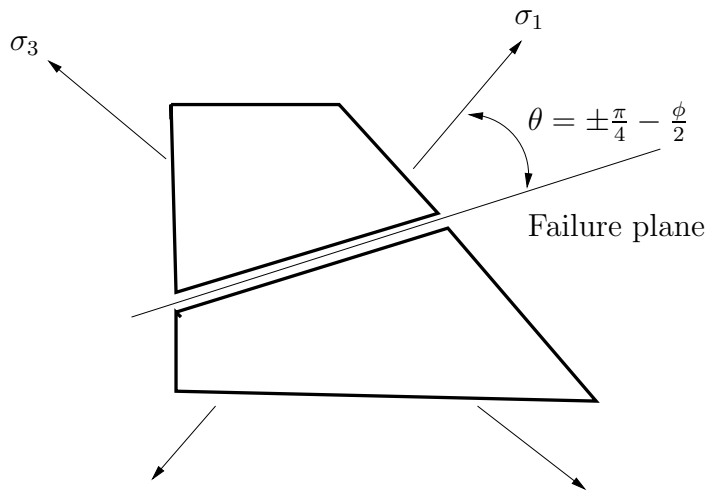

Figure 2.4: A two-dimensional sketch showing the plane of compressive failure.

where σ_1 and σ_3 are the maximum and minimum principle stresses, respectively, and ϕ is the internal friction angle defined by $\phi = \tan^{-1}(\mu)$. The result, in three dimensions, is that there are two allowable fracture planes which are perpendicular to the σ_1, σ_3-plane and form an angle of $\pm\left(\frac{\pi}{4} + \frac{\phi}{2}\right)$ with the positive σ_1-direction (see Figure 2.4).

Tensile failure

The criteria for tensile failure may be written as

$$\sigma_3 \geq \sigma_t \tag{2.16}$$

where σ_3 is the minimum principle stress and σ_c is the user prescribed tensile strength of the material. In two-dimensions, the intra-element fracture plane forms an angle of

$$\theta = \tan^{-1}\left(\frac{\sigma_1 - \sigma_x}{\tau_{xy}}\right) \tag{2.17}$$

with the positive x-axis. In three dimensions, the intra-element fracture plane is the plane passing though the centroid with the unit normal in the direction of σ_3 (see Figure 2.5).

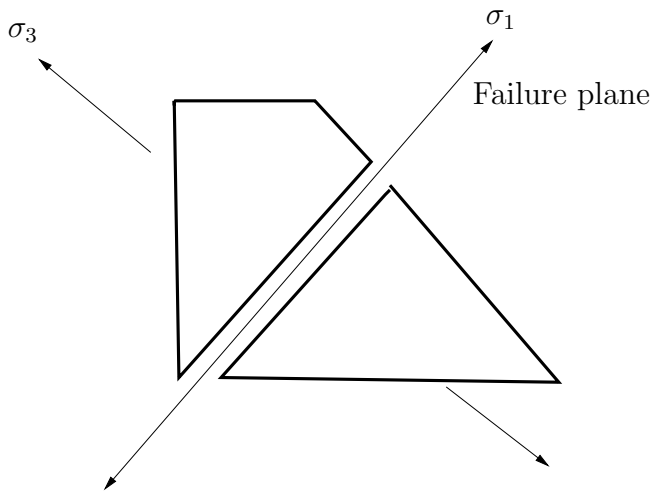

Figure 2.5: A two-dimensional sketch showing the plane of tension failure.

Bending failure

In order for bending failure to occur, beam or plate elements must be used. In two dimensions, the bending failure criteria is given by

$$\sigma_{\max} \geq \sigma_f \tag{2.18}$$

where σ_f is the flexural strength of the beam and $\sigma_{\max}$ is the maximum tensile fiber stress calculated from the sum of the beam bending stress σ_b and the tensile stresses σ_l along the axis of the beam. An analogous definition is used in three dimensions, with $\sigma_{\max}$ taken as the maximum tensile fiber stress calculated from the three-dimensional direct stresses and plate bending stresses. The plane of failure is perpendicular to the bending axis, as shown in Figure 2.6.

When elements fracture as a result of one of these three types of failure, further elements are generated. Kinetic energy must be preserved and strain energy must be released during the fracturing process. The release of strain energy over a single time-step would result in a numerical instability and thus the strain energy is

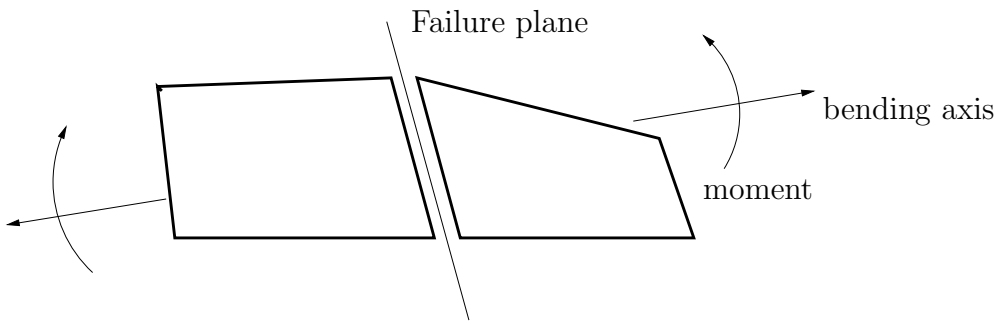

Figure 2.6: A two-dimensional sketch showing the plane of bending failure.

slowly released during several time-steps which follow the instantaneous fracture of the element.

2.3.5 Solution scheme

A computational flowchart of the dynamic explicit-explicit solution algorithm is depicted in Figure 2.7. The solution scheme consists of three steps:

1. calculating rigid body motion and deformation (via governing equations);

2. performing material dependent calculations (via constitutive equations);

3. performing update of system dependent variables.

In Stage 1, the rigid body motion is calculated using a central difference approximation of the time derivative in Sections 2.3.1-2.3.2. From the decoupled displacement and deformation terms the strain is calculated and then nodal velocities, v_i, and displacements, x_i, (as well as effective mass matrix terms, $\bar{M}_{ij}$, and moment of inertia terms, I_{ij}) are updated using

$$v_i^{n+\frac{1}{2}} = V_i^{n-\frac{1}{2}} + \dot{\epsilon}_{ij}^{n+\frac{1}{2}}(x_j^n - X_j^n) + e_{ijk}(x_k^n - X_k^n) \tag{2.19}$$

$$x_i^{n+1} = x_i^n + v_i^{n+\frac{1}{2}} \triangle t. \tag{2.20}$$

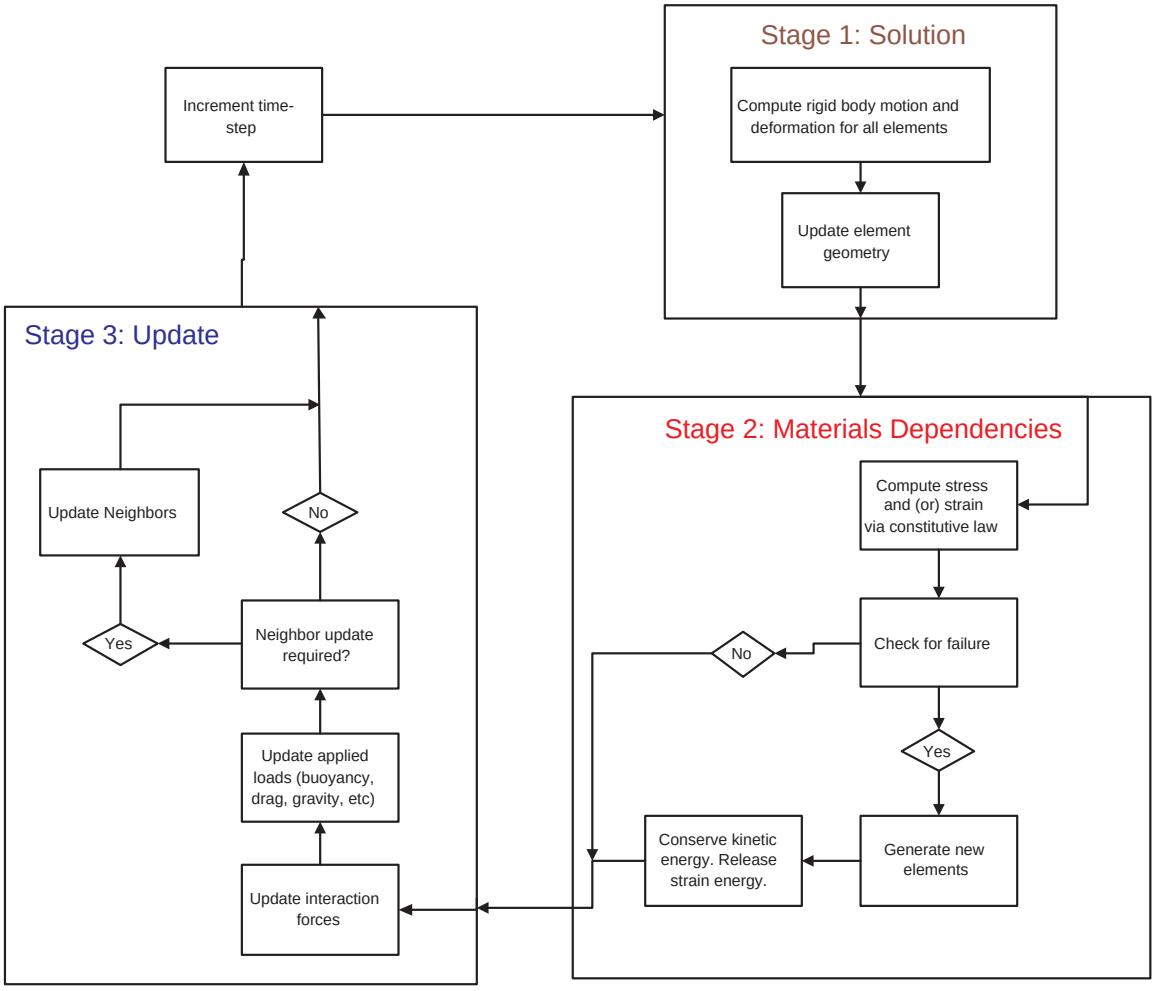

Figure 2.7: Flow chart depicting three stages of dynamic explicit-explicit solution scheme.

$$\bar{M}_{ij}^{n+1} = \bar{M}_{ij}^{n} + (\bar{M}_{kj}^{n}\dot{R}_{ik} + \bar{M}_{ik}^{n}\dot{R}_{jk})\triangle t \tag{2.21}$$

$$I_{ij}^{n+1} = I_{ij}^{n} + (I_{kj}^{n}\dot{R}_{ik} + I_{ik}^{n}\dot{R}_{jk})\triangle t \tag{2.22}$$

where $R_{ij} = T_{ij} - \delta_{ij}$, T_{ij} are the components of the stress dyadic, and δ_{ij} is the Kronecker delta function. This completes stage 1 of the calculations.

Since the strain for each element has been found in Stage 1, Stage 2 begins by determining the stress within each element using the particular constitutive law which has been specified. There are currently three allowable constitutive laws implemented: linear elasticity, elasto-plasticity, and visco-plasticity. The calculation scheme for each constitutive law is outlined below.

All three laws have in common that the incremental stress must be calculated and followed by the updating of the total element stress. The general algorithm may be written as

$$\triangle\sigma_{ij} = D_{ijkl}\triangle\epsilon_{kl} - D_{ijkl}H_{kl} \tag{2.23}$$

and

$$\sigma_{ij}^{n+1} = \sigma_{ij}^{n} + \triangle\sigma_{ij} + (\sigma_{kj}^{n}\dot{R}_{ik} + \sigma_{ik}\dot{R}_{jk})\triangle t, \tag{2.24}$$

where D_{ijkl} is the elastic stain-stress tensor and H_{kl} is a law-dependent function (zero for linear elasticity).

Once the elemental stress is calculated, each element is checked for failure using the criteria outlined in 2.3.4. Only one instance of failure can occur for each of the possible failure modes per time-step. This limitation could result in larger than expected loads/stresses in elements when elements which should fracture remain intact. During these failures, kinetic energy is preserved and the stresses are reduced in the cracked elements so that the normal and shear stresses across the plane of fracture

are zero.

Stage 3 is the final stage before incrementing the time-step where the interaction forces are updated. The relative velocity of an interacting node and face is calculated and transformed into a local coordinate system according to the normal and shear directions. The incremental interaction force is calculated as

$$\triangle f_i = k_{ij}^I(\triangle U_j + \beta \triangle \dot{U}_j) + \triangle \bar{f}_i \tag{2.25}$$

where $\triangle U_j$, $\triangle \dot{U}_j$ are the incremental displacement and velocities of the centroid of the elements, k_{ij}^I is the stiffness matrix of interaction coefficients, and $\triangle \bar{f}_i$ is the force correction vector for slippage and tensile separation. The total interaction force is then updated using

$$f_i^{n+1} = Q_{ij}(f_j^n + \triangle f_j) \tag{2.26}$$

where Q_{ij} is a coordinate transformation vector used to transform the incremental force from the local normal-shear aligned axis to the global axis.

The centroid forces F_i^n and moment sums P_i^n are then updated for each element involved in the interaction using

$$F_i^{n+1} = F_i^n \pm f_i^{n+1} \tag{2.27}$$

$$P_i^{n+1} = P_i^n \pm e_{ilm} f_l^{n+1}(x_m - X_m) \tag{2.28}$$

where the $\pm$ sign is necessary so that equal and opposite forces are simultaneously applied to each element. Finally, at the end of this stage the forces and moments resulting from any externally applied forces are updated. The time-step is incremented by $\triangle t$ and the three stages are repeated until the final time has been reached.

2.3.6 Stability criteria

The method of integration of the governing equations was first used by Byrne (1974) and the stability limitation on the time step $\triangle t$ was addressed by Belytschko et al. (1979). The entire numerical scheme is stable provided the time-step Δt is chosen as

$$\Delta t = \min\left(2\sqrt{\frac{n_c m}{k}}, 2\sqrt{\frac{m_d}{K}}, 2\sqrt{\frac{m_s}{G}}\right) \tag{2.29}$$

which represents the maximum natural frequency of an unconstrained element due to rigid body motion and deformation where $k = \max(k_s, k_n)$, m is the mass of the element, n_c is the maximum number of interactions on the element, K, G are the bulk and shear modulus, respectively, and m_d, m_s are the minimum direct and shear effective masses of the element. Details of the implementation and algorithms may be found in Intera Technologies Inc. (1986).

2.4 Literature Review

The application of the DEM in this thesis is ice-structure interaction but typical uses in other engineering fields are presented. Research relevant to algorithm improvement of the contact detection scheme of the DEM is then presented followed by a review of past ice-related DECICE simulations. The latter was originally presented in a conference paper prepared by the author (Lau et al., 2008). High performance computing considerations and relevant literature is intentionally removed from this section and are addressed in Chapter 4, which discusses parallel DE simulations.

2.4.1 Discrete Element Method - Application areas

Applications of the discrete element method arise in many engineering fields. Reviews which discuss example applications in environmental and geo-mechanical engineering are presented by Richards et al. (2004) and O'Sullivan et al. (2006). Specific particle

shapes have been applied to different types of problems. Discrete element methods which use polygonal representations have been used to study the behavior of rock masses in mining engineering by Cundall (1971, 1980); Hocking (1978) and problems in ice mechanics by Hocking et al. (1985c, 1987); Hocking (1987, 1993). Ellipsoidal elements have been used by Rothenburg and Bathurst (1991); Ting et al. (1993); Ng and Lin (1993); Ng (1994); Sawada and Pradham (1994); Lin et al. (1996); Lin and Manocha (1997) for problems involving particulate media such as sands and clays. The discussion which follows briefly outlines a few sample applications in the past decade and then discusses recent applications of the DECICE computer code.

The inherent properties and/or flow of discontinuous granular media are the subject of many studies. The compression of assemblies of clay particles is addressed by Yao and Anandarajah (2003), granular crushing under direct shear is simulated by Lobo-Guerrero and Vallejo (2005), and triaxial tests are modeled by Ng (2004). Properties of dense assemblies of particles including the angle of repose are modeled by Johnson and Williams (2002). Other studies address granular flow (Schwarz et al., 1998), granular ratcheting (Garcia-Rojo et al., 2004), silo filing (Holst et al., 1999; Sanad et al., 2001), shot peening (Han et al., 2000a,b), tumbling mills (Mishra, 2003a,b) and the flow of ore in ore passes (Nazeri, 2004).

The discrete element method has also been used extensively to study problem arising in rock, mining, and fracture mechanics. Nicot et al. (2001) uses the DEM to design retaining nets for stopping rock falls and Prochazka (2004) use it to simulate conditions in which bumps or rock bursts can occur in deep mines when accumulated potential energy is abruptly released. Problems involving the impact of missiles on concrete beams (Magnier and Donze, 1998), fracturing of reinforced concrete plates (Riera and Iturrioz, 1998), dynamic loading of concrete at high strain rates (Hentz

et al., 2004), and the dynamic fracturing of other geo-mechanical materials (Camborde et al., 2000) have also been addressed.

Six previous studies conducted at the NRC-IOT which utilized DECICE and are now presented to show the versatility of the code in modeling ice-related problems. This discussion is an excerpt of a conference paper prepared during the course of this research (Lau et al., 2008). Other notable simulations using DECICE not presented here were conducted by: Murray and Spencer (1997) to investigate the loads exerted on a moored tanker in pack ice; Hocking et al. (1985c,a,b), who presented a series of papers studying resultant forces due to ice ride-up, ice ridge cone interaction, large floe impacts with offshore structures, and ice ride-up on artificial islands with various side shapes and; Lau et al. (2000), Lau et al. (1999); Lau (1999), who presented papers studying various other ice-related problems ranging from ice-structure interaction in various conditions to breaking patterns and failure mechanisms.

Ice-cone interaction is a complex process that involves the interaction between the structure, the intact ice mass, and the broken ice fragments. A proper simulation of the interaction requires accurate modeling of failure modes, the cracking patterns, and the dynamics generated during the interaction. The original simulations performed by Lau (2001) used DECICE to model the interaction of an ice sheet with a 60° conical bridge pier (see Figure 2.8). The results were verified with model tests carried out in a test tank at the IOT. In each of the simulations, flexural failure was exhibited most frequently, with failure typically beginning with the formation of a major circumferential crack through the centroid of the adjacent ice elements just after contact. As time progressed, the moving ice-sheet pushed the fragmented pieces up and around the cone, which led to the formation of a rubble pile in front of the structure.

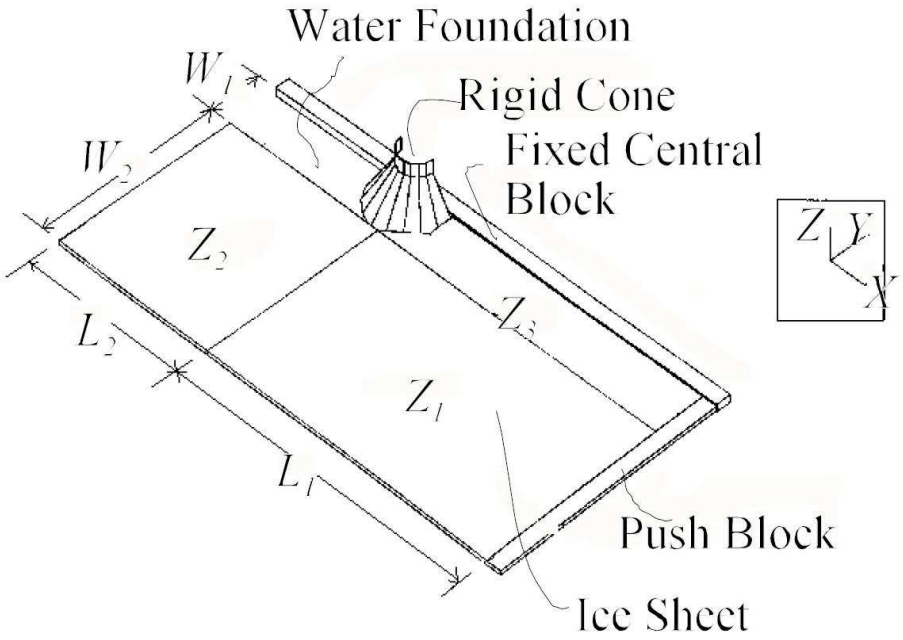

Figure 2.8: Ice-cone interaction model using DECICE.

The failure mode predicted by the numerical simulation differs from that observed in the model tests which involved "subsidiary" cracking, a stable pile-up of ice, and compressive shear failure, but was consistent with that observed around a full-scale conical structure, the Finnish Kemi I lighthouse in the Gulf of Bothnia (Hoikkanen, 1985), where test conditions were comparable. The numerical simulations slightly underestimated the peak force when flexural failure is dominant; despite this discrepancy in failure modes, the measured and predicted results are in good agreement.

The numerical simulations conducted by Lau (2006a) considered a 1:21 scale model of the Canadian icebreaker Terry Fox moving forward and turning in level ice. The results show the effects of ice conditions and ship motion on the computed forces and moments. Complementary model experimental tests conducted at the IOT (Lau and

Figure 2.9: Model test performed at NRC-IOT.

Derradji-Aouat, 2004) are shown in Figure 2.9. The interaction of the ship hull and leading ice edge consisted of the breaking of the ice followed by the submergence and subsequent clearing. These results are also typical of those observed in the model tests. In general, good agreement was observed between the numerical and experimental results at a curvature radius, R, of $R = 10$ and $R = 50$ meters.

During ice scouring, load which is exerted on the seabed by a floating ice feature depends on the ice feature characteristics, the driving force, and the seabed conditions. Modeling the ice feature as a single solid ice feature may be acceptable in the case of icebergs, but ice ridge keels may fail during interaction with the seabed and therefore limit the depth of scour and resultant load on the seabed. A preliminary investigation of the behavior of the ridge keel and seabed during scouring was presented in Lau and Re (2006).

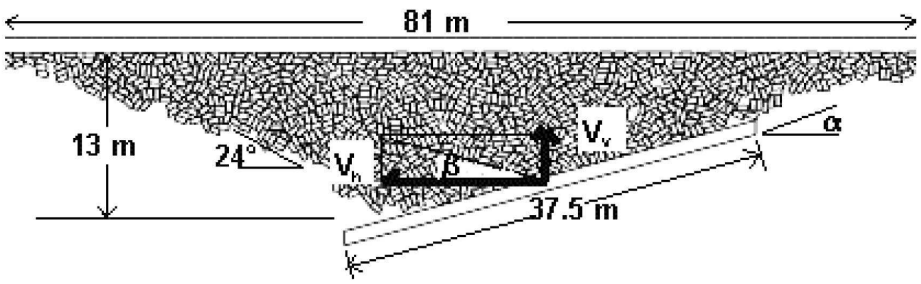

Figure 2.10: Geometry of ridge keel scouring problem.

The initial problem setup may be seen in Figure 2.10. The bottom plate was prescribed a velocity and the effect of the seabed inclination, trajectory angle, and ice-friction coefficient on the maximum nominal pressure was addressed. Ten simulations were conducted and indicate that the magnitude of pressure increases: (1) with increasing seabed plate penetration. The majority of stress was distributed on the leading area of the keel; (2) as the trajectory angle of the seabed increases as a result of the increasing confinement pressure; and (3) linearly with the coefficient of ice-friction.

The next ice-related problem studied with DECICE was focused on measuring/predicting performance of a totally enclosed motor-propelled survival craft (TEMPSC), which is used for emergency situations in harsh environments. The experimental scale model (see Lau (2006) for complete details) was constructed at the IOT and the numerical model (see Figure 2.11) was composed using DECICE. With reference to Figure 2.11, the numerical model consisted of a: (1) rigid moving ship; (2) free-floating pack ice; (3) rigid boundary; and (4) water foundation. A total of 24 simulations were conducted consisting of small and/or large ice floes and various other mechanical properties of ice. Interaction of smaller floes with the hull consisted of the floes being pushed aside or sliding under the hull whereas large floes were mainly pushed aside/ahead with a larger occurrence of accumulation in the front of the vessel in the

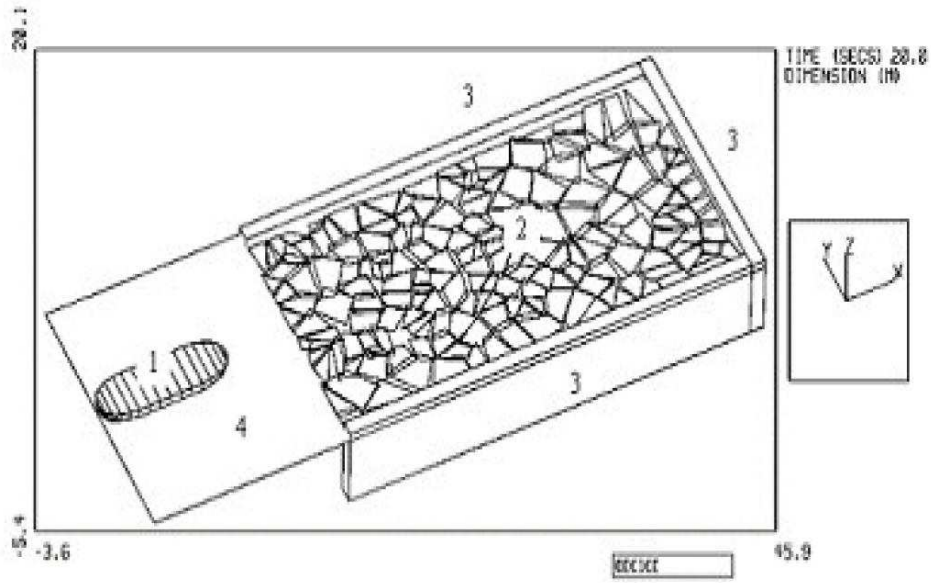

Figure 2.11: DECICE model of survival craft

latter case. The predicted versus measured resistance is in good agreement with the results even though the initial ice configuration differed from the experimental tests, as seen in Figure 2.12.

In pack ice, although floe splitting is observed for larger floes, the dominant mode of failure is floe buckling (vertical displacement of the edges). McKenna (1997) performed IOT-based experimental, analytical, and numerical tests (using DECICE) to investigate the effects of floe thickness, size, and ice density on the loads and subsequent failure modes exerted on by pack ice. A sample numerical simulation in which elements were generated to promote out of plane failure is shown in Figure 2.13. The numerical and experimental results were then used to develop an empirical relationship between all factors involved. The results indicate the transition between floe buckling and splitting occurs in the ice thickness range of 0.5-1.0 meter.

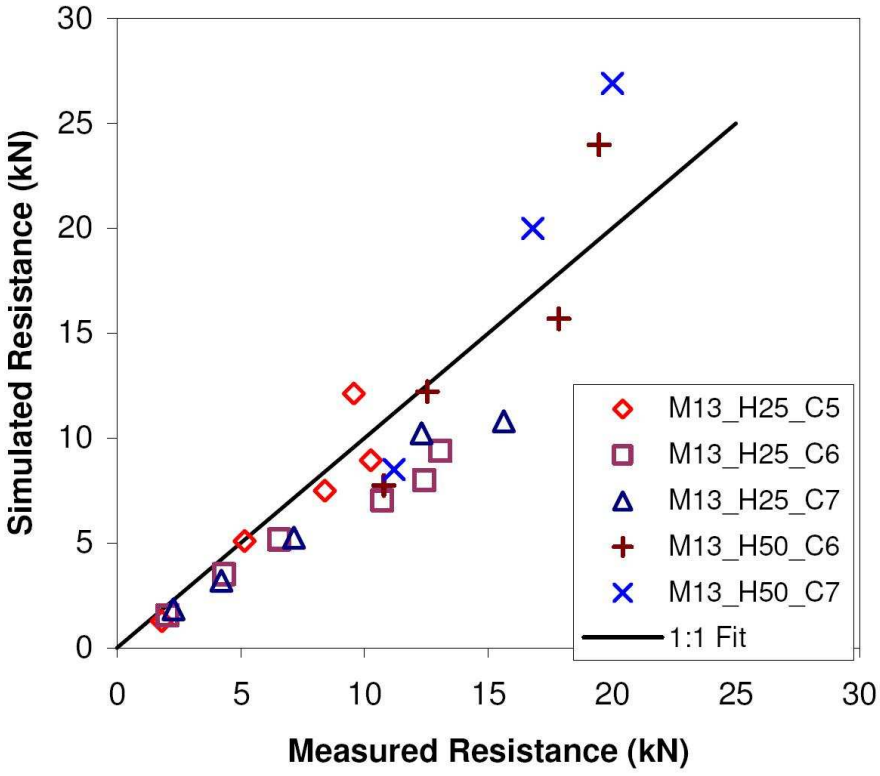

Figure 2.12: Predicted versus measured resistance.

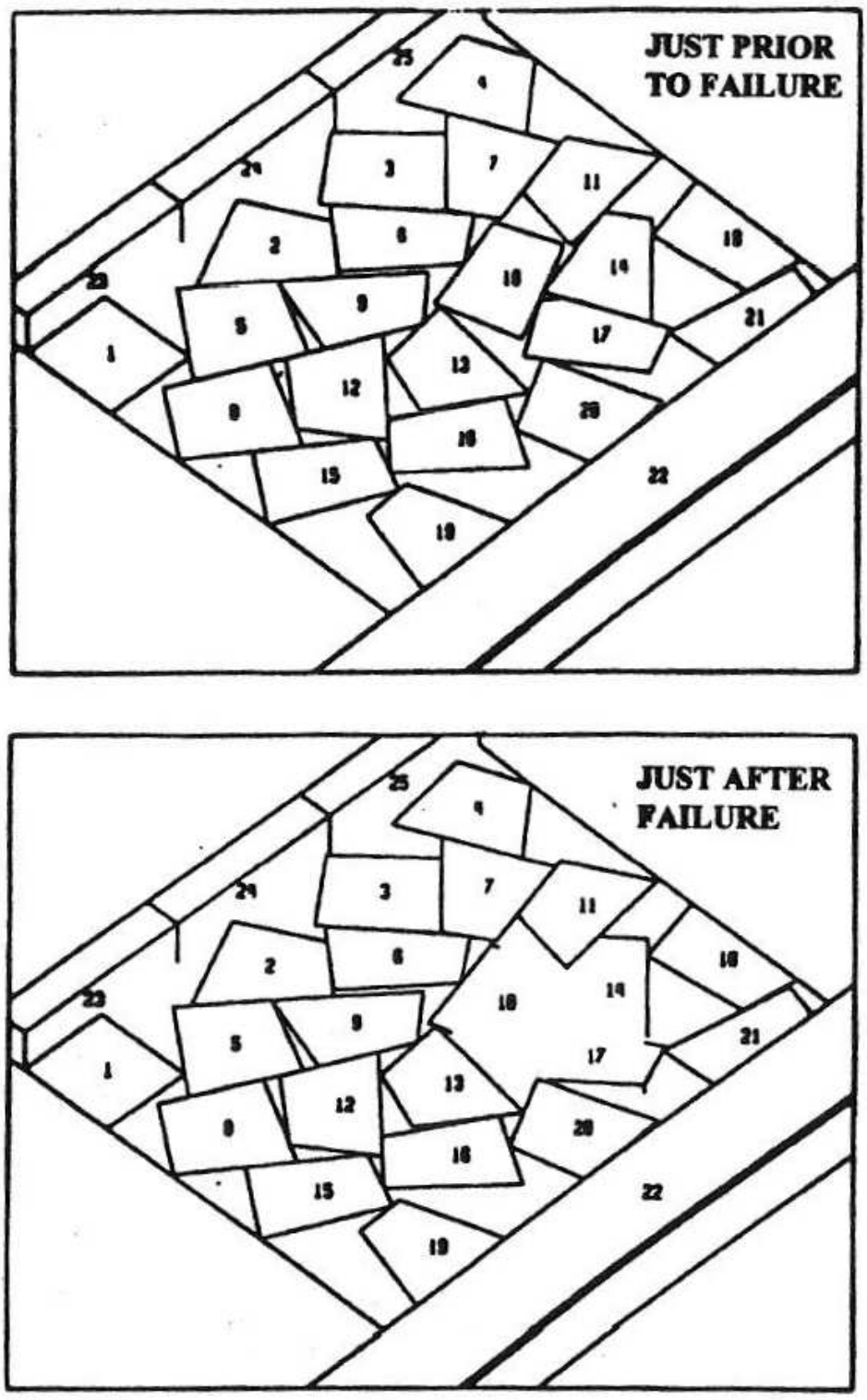

Figure 2.13: Floe ice bucking snapshots.

The final ice-related problem regards ice-arch formation and jamming on bridge piers. The purpose of the analysis was to develop a relationship between the critical ice concentration to floe size, pier spacing, and inter-floe friction. A total of 81 numerical simulations were conducted by Schachter and Spencer (1994) with the two-dimensional version of DECICE, in which each of the parameters was varied. A typical snapshot of the simulations is shown in Figure 2.14. An empirical formula was developed using the results to predict the critical concentration at which ice-arches will likely form. Concentrations above these critical curves would lead to stable arching while closer values would promote an unstable arch. The results compared well with the physical model of Calkins (1978) for a friction coefficient of 0.6.

2.4.2 Discrete Element Method - Contact detection

Since elements undergo displacements and rotations relative to one another, an algorithm must be developed to efficiently monitor all potential pairs of neighboring blocks. This stage of the DEM is referred to as "contact detection", and the next stage, in which the geometry of the two contacting elements is resolved, is referred to as "contact resolution".

The complexity of a 3D contact detection scheme is determined by the type of elements utilized. Three-dimensional spherical elements have been used to simplify the contact detection procedure in many geotechnical problems (Cundall, 1987; Liu et al., 1999; Zhang et al., 1997, 2001)). A sphere may be completely defined by specifying a center with radius and thus sphere-to-sphere contact is detected by comparing the distance between the center points to the sum of the radii. Elliptical elements have also been used in many DE schemes (Williams, 1992; Hogue, 1998; Mustoe et al., 2000; Wait, 2001; Johnson and Williams, 2004). However, using circular elements can result in incorrect modeling of systems of particles. For example, due to their

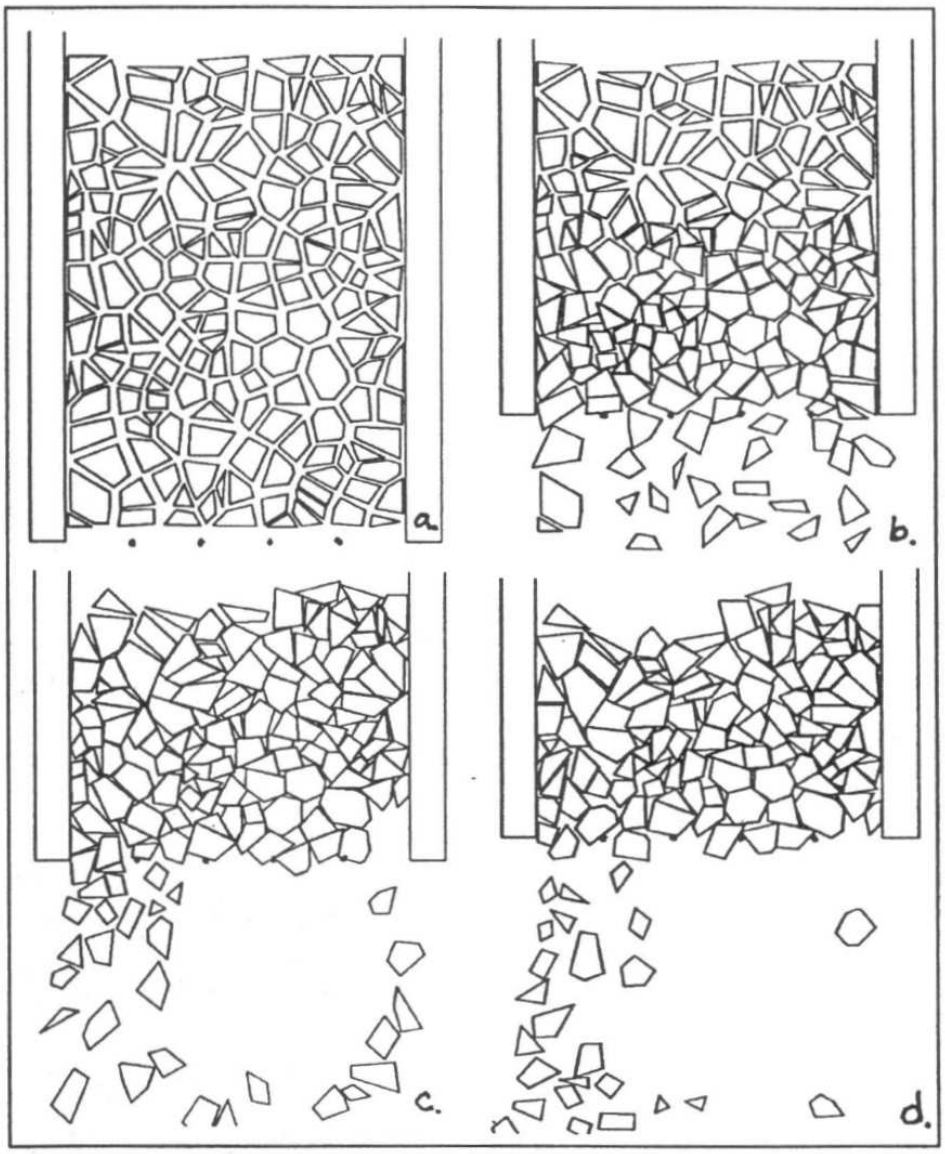

Figure 2.14: Snapshots of floe ice simulations.

smooth surfaces, spheres cannot interlock with one another, which is a property exhibited by many granular materials. Unlike real materials, Grest et al. (2001) showed that spheres tend to organize into dense groupings as the coefficient of friction decreases.

The extension of three-dimensional discrete element schemes to include polyhedral elements introduces additional difficulties since polyhedra consist of corner nodes, edges, and faces which may interact with one another in any feasible way. For example, two cuboids, A and B, consisting of eight corner nodes, twelve edges, and six faces, may interact in

$$N = (v_A + e_A + f_A) \cdot (v_B + e_B + f_B) = 676 \tag{2.30}$$

different ways, where v, e, and f represent the number of vertices, edges and faces for each element, respectively. A robust algorithm would check each of these possibilities, even though each contact type is not unique. All contacts between polyhedral elements may be reduced to one of two types:

(1) vertex-to-face; or

(2) edge-to-edge.

For instance, a vertex-to-vertex contact is a result of three or more vertex-to-face interactions at the same node. This reduces the number of possible contact to

$$N = v_A \cdot f_B + v_B \cdot f_A + e_A \cdot f_B + e_B \cdot f_A (= 240 \text{ for two cuboids.}) \tag{2.31}$$

This type of algorithm was originally implemented in DECICE. The added improvement which was included by the original authors in DECICE was the concept of a hidden node, edge, or face. That is, a node on element A cannot come into contact with a face which is on the opposite side of element B. This hidden node approach

further reduces the number of contact checks but it is still a rather robust and slow procedure which accounts for most of the simulation time within DECICE.

Cundall (1988) introduced an alternative approach which is implemented in the well-known software 3DEC ((Itasca, 2003a)). A contact detection algorithm is proposed that avoids element-to-element contact checks by defining a "common-plane" (CP) between each neighboring pair. The CP is figuratively defined as the plane which bisects the space between two polyhedra, or as the plane which maximizes the sum of the gaps in space to each element. Once the plane has been defined, the contact detection algorithm is then reduced to checking a series of vertex-to-face contacts, where the face in this case is the common-plane. The number of contact possibilities is reduced to

$$N = v_A + v_B (= 16 \text{ for two cuboids}). \tag{2.32}$$

The computational effort associated with positioning and orienting (through iterations) the CP rather than the robust algorithm addressed above, which must also be considered as part of the algorithm, was shown by Cundall (1988) to be linearly dependent on the number of vertices as

$$N \approx (4n + 1) \cdot (v_A + v_B) \tag{2.33}$$

where n is the number of iterations. These iterations are used to perturb a candidate plane about two arbitrary axes in either direction until a maximum gap is found. The overall efficiency of the algorithm in comparison to direct-testing is dependent on the number of iterations necessary to find the common-plane. Approximately 10 iterations would be equivalent to the minimum value of direct tests. In general, 9-30 iterations were required to set up a new contact if one did not previously exist between two elements, and 1-2 iterations if a contact has already been established in a previous time-step.

Nezami et al. (2004) presented the Fast Common Plane (FCP) algorithm which used geometrical considerations of the CP to limit the number of possible candidate planes. It was shown that the CP must lie within an envelope of space which is created by planes drawn midway between the closest vertices of the two elements and parallel to the corresponding adjacent faces (to be described in more detail in Chapter 3). If the perpendicular bisector of the line joining the two closest vertices is completely enclosed in the envelope of space, then this perpendicular bisector is the CP. Otherwise, the CP is the plane whose normal direction forms the smallest possible angle with the normal of the perpendicular bisector, and is completely contained within the envelope of space. After mathematical consideration, this stipulation yields a common-plane which is parallel to one or more of the six edges (three edges from each element) required to define the envelop space. Hence, by checking all of the edge-edge combinations, the CP may be defined. Iterations are required to position the plane, but the orientation, which required iterations in the original algorithm, proposed by Cundall (1988), is selected from the orientation of the candidate planes (the planes formed by edge-edge combinations). Three-dimensional simulations using their in house discrete element code, DBLOKS3D, yielded simulation times which were 12-40 times faster than the CP algorithm.

The shortest link method (SLM) was developed by the same team at the University of Illinois and presented by Nezami et al. (2006). It is based on defining the shortest Euclidean distance or "shortest link" using any two points on the two opposite elements. Once the shortest link is established, Nezami et al. (2006) show that the CP is the plane which perpendicularly bisects the shortest link between two elements. For the simulations conducted in the paper, the SLM was up to 17 times faster than the CP algorithm and nearly twice as fast as the FCP algorithm. Nezami

et al. (2006) provided an algorithm for computing the shortest link, but the same methodology has been studied vastly in the area of computer graphics/animation under the heading of closest point approaches. The added uniqueness of the SLM is mainly in its proposed relation to the CP algorithm.

The *closest point approach* is fundamental to many computational geometry algorithms. Lin and Canney (1991); Lin (1993); Lin and Manocha (1995, 1997) present an algorithm based on maintaining the closest features (vertices, edges, faces) of two elements which are not in contact (commonly referred to as the Lin-Canny algorithm). The robustness and simplicity of the Lin-Canney algorithm was improved in the V-clip algorithm (Mirtich, 1998), which could also handle the case where the polyhedra intersect. Both of these algorithms are based on the idea that the closest points must lie on features within the Voronoi regions of the opposing element. Assuming f is a feature (vertex, edge, or face), the Voronoi region of f is defined as the region outside of the polyhedron as close to f as to any other feature (Mirtich, 1998). The GJK algorithm (Gilbert et al., 1988) is a common alternative to the Lin-Canney algorithm and is based on computing the closest point on the convex hull of the Minkowski sum (or difference) using an iterative simplex procedure. The closest point on the Minkowski difference may be mapped back to give a pair of closest points on the two convex polyhedra. By determining these closest points the above algorithms are finding the *shortest link*, as was discussed by Nezami et al. (2006), who used the shortest link method as a means to define the CP.

The Lin-Canney and GJK algorithms were developed to determine the contact of smooth curves as well as non-convex polyhedra formed by a large number of nodes. DBLOKS3D from Nezami et al. (2006) was focused on elements consisting of multi-faceted polyhedra in order to realistically represent granular material (eg., gravel

particles modeled with 18-face polyhedra). Closest point or shortest link approaches are typically targeted towards these complex shapes since performance gains increase as the number of nodes (complexity of the elements) increase. The computational improvement associated with the application of these closest points approaches would not be fully realized within DECICE since the maximum number of nodes of a deformable element is small (only eight).

2.4.3 Discrete Element Method - Proximity search

The following algorithms are referred to as "contact" detection algorithms in their respective references but are more proximity search algorithms when applied to non-spherical elements. The No Binary Search (NBS) algorithm presented by Munjiza and Andrews (1998) is based on approximating discrete elements as spheres or disks for the purpose of contact detection. The algorithm uses a spatial decomposition of the approximated element domain to give a detection scheme which is linearly dependent on the number of elements and works well for problems with similar-sized objects.

Perkins and Williams (2001) present a double-sided spatial sorting (DESS) algorithm which is independent of varying object sizes. It yields better results than the NBS algorithm for less than 100,000 objects when the size ratios are greater than 8 to 1. The DESS algorithm is still based on using a bounding sphere, but the spatial decomposition and sorting sections are modified to increase performance.

The two-level search algorithm (TLS) of Zhao (2006) also uses bounding spheres in their proximity detection sequence. Pre-processing to determine the radius of the associated bounding spheres for each element is required and only possible due to the use of rigid (non-deforming) particles.

Using axis-aligned boxes, Cohen et al. (1995) presented another algorithm in the program I-COLLIDE for spatial sorting during this stage which is particularly applicable to polyhedral elements and dependent on the number of elements in the simulation. This axis-aligned bounding box (AABB) approach is the most applicable method for DECICE, since elements may deform and fracture, resulting in the need to recalculate bounding boxes.

2.5 Summary

This chapter presented a history and review of the discrete element method. It is a proven numerical strategy which has been implemented in DECICE to study problems in which ice interacts with a fixed or floating structure, as well as problems arising in other fields. The details of the algorithm are presented along with a review of the relevant literature. The contact detection algorithm which exists in DECICE is much less efficient than other algorithms which have been developed since its creation. In the chapters which follow, this algorithm is improved upon via both algorithmic and parallel redevelopment of the code.

Chapter 3

Algorithm Improvement

In this chapter, the implementation of a new contact detection/resolution scheme in DECICE is addressed. The new algorithm implements the idea of a "common plane" (CP) between elements, which was first introduced by Cundall (1988) and subsequently formed the basis of the algorithm used in 3DEC. The original CP algorithm uses iterations to position and orientate the plane between two neighboring elements, which limited the efficiency of the algorithm. Nezami et al. (2004) improved this algorithm via a geometrical interpretation of the problem, which limited the number of candidate planes and thus thus reduced the need for iterations to find the orientation of the plane (although iterations are still performed to position it). The FCP algorithm, as opposed to the SL algorithm, is chosen as the starting point for algorithmic improvement, since polyhedral elements are restricted to those consisting of 4, 6, and 8 nodes within DECICE. The SLM (similarly for the Lin-Canney and GJK algorithms (Gilbert et al., 1988; Lin and Canney, 1991) can result in a large number of iterations in several degenerate cases, which makes the FCP algorithm preferred for simpler geometries. A proximity detection scheme is also presented in this chapter.

3.1 Details of Implementation

The details of the CP and FCP algorithms mentioned in Chapter 2 are first expanded upon so that terminology used throughout the text is understood.

3.1.1 Original CP Algorithm

Cundall (1988) defined the CP as the plane which "maximizes the gap between the CP and the closest vertex". To define the CP, the signed distance is introduced as

$$d = \mathbf{n} \cdot (\mathbf{P} - \mathbf{P_0}) \tag{3.1}$$

where $\mathbf{n}$ and $\mathbf{P_0}$ are a normal and point which uniquely define the plane and $\mathbf{P}$ is any point in space. Any plane divides the space into a positive ($d > 0$) and negative

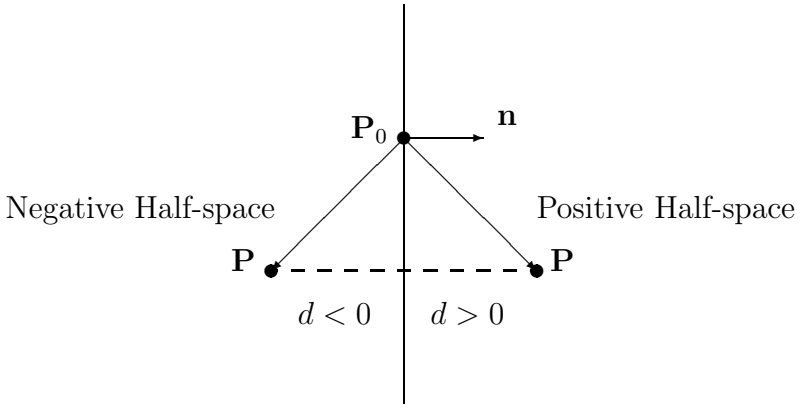

Figure 3.1: Plane separating positive and negative half-space.

($d < 0$) half-space (see Figure 3.1). The "distance" between the CP and a polyhedron A (see Figure 3.2) is then defined as

$$d_A = \begin{cases} \max(d_A^V) & \text{if} \quad d_A^C < 0 \\ \min(d_A^V) & \text{if} \quad d_A^C > 0. \end{cases} \tag{3.2}$$

where d_A^V is the signed distance (equation 3.1) over the vertices of the polyhedron and d_A^C is the signed distance of the center of mass of the element. That is, the distance

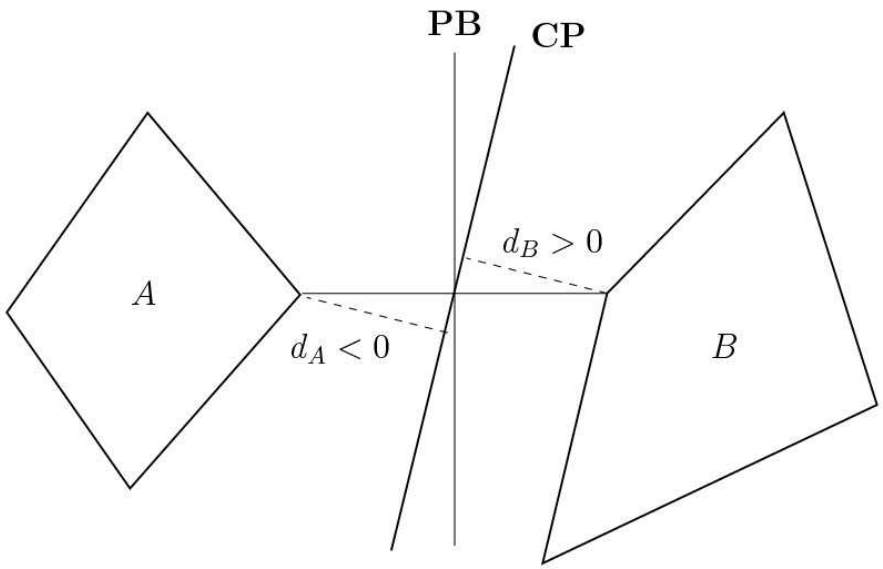

Figure 3.2: Configuration and notation for CP algorithm.

from a polyhedron to the CP is the maximum of the signed distance if the particles' centroid lies in the negative half-space and the minimum of the signed distance if the particles' centroid lies in the positive half-space. Without loss of generality, when considering the contact of any two elements, A and B, the CP is defined with the centroid of A in the negative half-space and the centroid of B in the positive half-space, so that the normal of the CP always points from A to B.

For two non-intersecting particles, the common plane CP is then defined as the plane which maximizes the gap $d_B - d_A$. If $d_B - d_A > \epsilon$, where ϵ is a user-defined tolerance, the particles are not in contact. For particles with $0 < d_B - d_A < \epsilon$, a CP is defined and monitored to determine when the two particles come into contact ($d_B - d_A < 0$).

To find the CP, Cundall (1988) presents an algorithm which iteratively positions

and orientates the plane. A reference point $\mathbf{M}$ is initially given as the midpoint between the centroids, with the direction given by the unit direction $\mathbf{n}$ along this line from the centroid of A to B. Iterations are performed to perturb the plane normal $\mathbf{n}$ by small angles in directions mutually orthogonal to $\mathbf{n}$. If either perturbation yields a larger gap, $d_B - d_A$, then this direction is taken as the new normal to the CP. The reference point is also iteratively updated during this procedure using

$$\mathbf{M} = \mathbf{M} + \left(\frac{d_A + d_B}{2} \right) \mathbf{n} \tag{3.3}$$

which is the midpoint of the vector joining the closest vertices (for blocks not in contact). This reference point also serves as the point at which the repelling force is applied when contact is established ($d_B - d_A < 0$). As a result, additional iterations are required during the mechanical cycle of the discrete element code to translate and rotate the contact point (or reference point $\mathbf{M}$) as well as to ensure it lies on the surface of both blocks.

To minimize the number of iterations during simulations, if a CP exists from a previous time step, then it is used as an initial guess for the CP instead of the vector along the line joining the centroids. This decreases the number of iterations, since particles are assumed to undergo small translations/rotations/deformations during a single time-step. Cundall reported that to determine the CP for the first time, approximately 9-30 iterations were required, but this reduces to 1-2 iterations if the CP is known from the previous time-step.

3.1.2 Fast CP Algorithm

Nezami et al. (2004) studied the geometry of the resultant plane from the original CP algorithm and were able to provide an algorithm which did not require iterations to find the orientation of the CP. Instead, it was proven that the CP is the plane

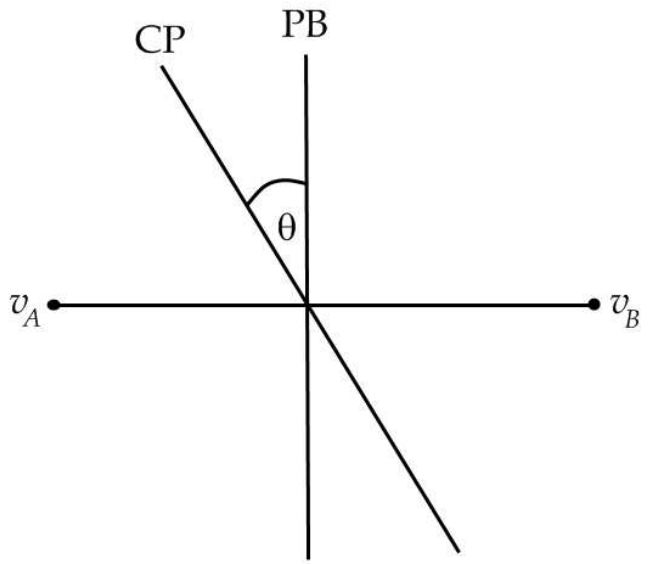

Figure 3.3: Two-dimensional view of CP, perpendicular bisector (PB) of line segment from v_A to v_B, and dihedral angle θ between the two planes.

which is located midway between the closest vertices of A and B (in terms of signed distance) and parallel to the plane chosen from a set of candidate planes. It was shown that the CP will minimize the dihedral angle, θ, between the perpendicular bisector of the line from the closest vertex of A, v_A to closest vertex of B, v_B (see Figure 3.3). Considering that each vertex has three adjacent edges, the orientation of the CP was chosen as the orientation from the following set of candidate planes which maximizes the gap $d_B - d_A$:

(i) the perpendicular bisector of the line from v_A to v_B

(ii) the plane passing through the midpoint of the line from v_A to v_B parallel to one of the adjacent faces of A or B

(iii) the plane passing through the midpoint of the line from v_A to v_B parallel to the plane formed by one edge from A and one edge from B

(iv) the plane passing through the midpoint of the line from v_A to v_B parallel to the plane formed by one edge from either A or B (which can be uniquely defined using the normal of the perpendicular bisector)

If the maximum gap $d_B - d_A$ over all vertices of A and B is greater than the gap given by the closest vertices to the perpendicular bisector, then the perpendicular bisector is the CP. If not, the 21 candidate planes given in (ii)-(iv) above are checked to see which yields the maximum gap. The midpoint of the two closest vertices is determined and the procedure is repeated. If at any time the gap exceeds the user-defined tolerance, ϵ, the iterations halt, since the two elements are not in contact. If at any time the gap is less than zero, iterations are stopped and an extra step is needed to separate the particles before determining the CP. It is imperative that this temporary separating distance be large enough to completely separate the particles but not so large that the geometry of the contact is changed. The maximum gap from the previous time-step is generally used to separate the particles in the direction of the corresponding previous CP normal. As a result, it is necessary in the FCP algorithm that proximity be established before true contact.

Simulations conducted by Nezami et al. (2004) suggest that the method is 12-40 times faster then the original CP algorithm, depending on the number of vertices and number of polyhedral elements.

3.1.3 New DECICE Algorithm

Contact detection within DECICE is composed of three nested steps. First, elements are sorted according to their physical location into regions of three-dimensional space. Rectangular regions with sides parallel to the three coordinate axes may be specified

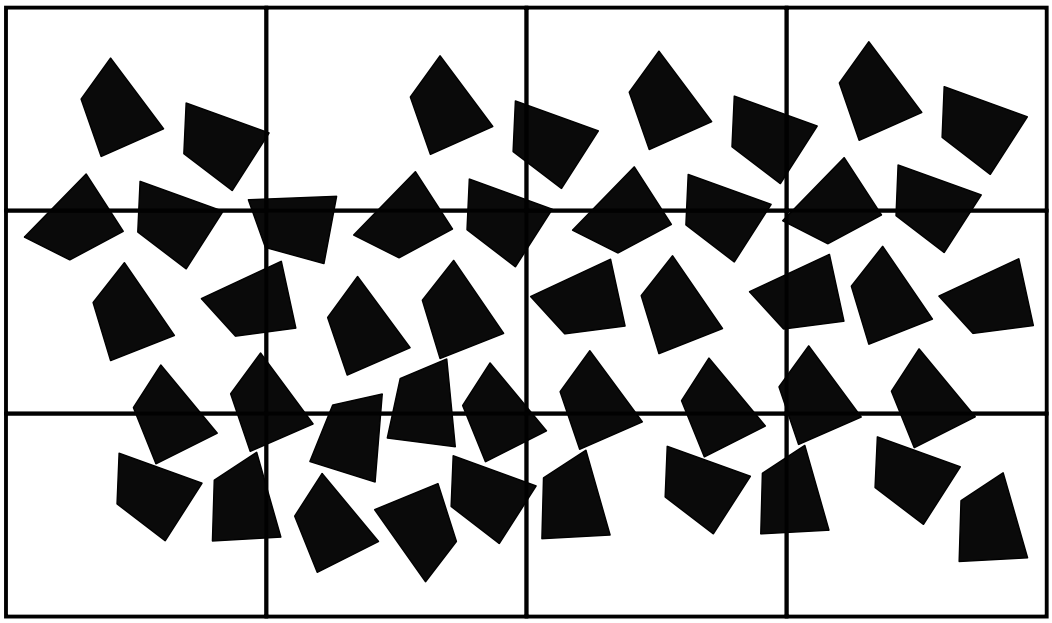

Figure 3.4: Spatial sorting of elements into rectangular regions.

to group elements which are geographically closer to one another into a series of potential contact lists (see Figure 3.4). These regions overlap each other by a distance of ϵ so that elements which are in different zones but just outside of potential contact are not excluded. As a distinct contact list is constructed for each zone, a potential contact pair may occur in more than one list. In this chapter, the spatial sorting step is not utilized nor are the effects of it included in the results presented. Rather, it is implemented with the knowledge that a parallel algorithm and associated load balancing study would follow. The method of dividing the three-dimensional space into rectangular regions to achieve load balancing across all processors is addressed in Chapter 4.

The contact list is traversed using axis-aligned bounding boxes (AABB) to perform a proximity check (see Figure 3.5) in the second step of the new algorithm. Nezami

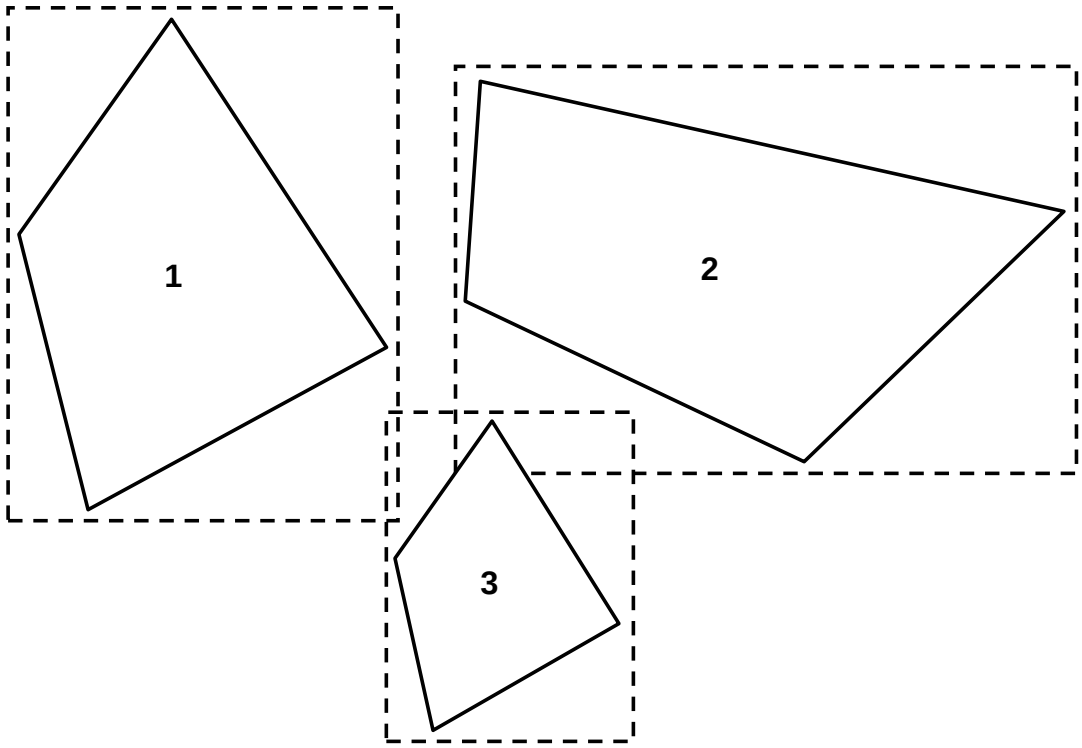

Figure 3.5: Proximity search using axis-aligned bounding boxes (AABBs). Element interaction between 1 and 2 is eliminated from the contact list since their AABBs do not intersect.

et al. (2006) is able to implement bounding spheres instead of AABBs, since their elements are rigid and thus the bounding spheres may be preprocessed. For deformable elements, it would be necessary to recalculate or update the bounding spheres at each time-step instead of comparing maximum coordinate values, as is the case for AABBs. If bounding boxes do not overlap within a tolerance, ϵ, then the contact pair is removed from the list. If overlap is detected, the pair remains in the list which will be used in the next stage of the algorithm. In contrast to the original contact detection algorithm within DECICE, multiple instances of corner-to-face and edge-to-face contact for a single pair of elements are not necessary. For instance, in the original algorithm it was necessary to loop over all nodes and edges of one element to check for contact with each face of the corresponding neighboring element. All that is required in this and the next stage of the new algorithm is a list of element-to-element interactions of the form (`IE1,IE2`) where `IE1, IE2` is the contact pair. Aside from multiple occurrences within zones, each candidate pair is checked only once, when the global element number `IE` is less than `IE2`.

Should contact still be possible after the first two stages, the FCP algorithm is implemented to further resolve the contact. Again the contact need only be checked if `IE` is less than `IE2`. All common planes will therefore have normals which partition `IE` in the negative half-space and `IE2` in the positive half-space. It is also important to note that although a reference point for the common plane $\mathbf{M}$ is determined, it is not used as the point of reaction for contact force application as in the original CP algorithm. This eliminates the requirement to calculate additional incremental translations and rotations of the reference point during the mechanical cycle and the need to ensure it lies on the surface of the contacting blocks. In practice, elements which are within distance of ϵ are stored as potential contacts in DECICE, where ϵ may be directly input but in general it is calculated as a fraction of the smallest edge

length.

The realization made by Nezami et al. (2006) that the common plane CP is the perpendicular bisector of the shortest link between two elements, has created a relationship between the idea of the common plane introduced by Cundall (1988) and other algorithms such as the GJK algorithm which derive from computational geometry. Another common practice associated with computational geometry is to approximate the time of collision between two elements. This approach may also be applied to the FCP algorithm. Although the distance along the shortest link between elements A and B is not known, their distance to a common plane CP, which mutually separates the two elements, is known. This, along with the relative velocities and accelerations towards the common plane, is utilized to estimate the time of collision. An estimate of the time of collision can further remove any unnecessary contact and force resolution calculations

Within DECICE, two tolerances are important in the contact detection scheme. First, the tolerance ϵ at which two elements are considered as potentially in contact, and secondly, the tolerance $\epsilon_0 \approx 0$ (zero in floating point arithmetic), which represents when a true contact is established and interaction forces are calculated. In many instances, elements which are separated by a distance ϵ may be traveling in opposite or parallel directions, especially in the case of a body force acting over a group of elements. As a result, the number of time-steps for the gap to change from ϵ to ϵ_0 could be quite large, resulting in unnecessarily lengthy calculations during the mechanical cycle.

At time t_i, for any two elements potentially in contact, the gap $(d_B - d_A)_{t_{i-1}}$ is known via a correct implementation of the FCP algorithm. At each time-step, the

reference point of the common plane is updated according to the relative motion of the two contacting elements during this time-step. The reference point is translated according to

$$\mathbf{M} = \mathbf{M} + \frac{(d_A + d_B)_{t_i}}{2}\mathbf{n} \tag{3.4}$$

where $\mathbf{n}$ is the normal to the CP. The incremental displacement normal to the CP is $\mathrm{d}_n = (d_B - d_A)_{t_i} - (d_B - d_A)_{t_{i-1}}$, or the change in gap over the current time-step. Two elements are approaching when $\mathrm{d}_n < 0$ (i.e., the gap in the current step is less than the gap in the previous step) and not approaching when $\mathrm{d}_n > 0$. The incremental velocities and accelerations towards the common plane may also be obtained by retaining details of previous time-steps. Since the relative motion is measured with respect to the normal direction to the CP, it is possible to derive collision time equations for the one-dimensional problem.

Two objects are in contact when the gap is ϵ_0. The time at which this gap occurs is referred to as the time of contact t_c. Assuming the path remains unaltered, the relative distance the elements have to travel in direction normal to the CP is $\mathrm{d}x_n = (d_B - d_A)_{t_i} - \epsilon_0$. The additional time required until contact, measured from the current time, $\Delta t_c = t_c - t_i$, may then be approximated as the solution of

$$(\Delta t_c)^2 \mathrm{d}\ddot{x}_n + (\Delta t_c)\mathrm{d}\dot{x}_n + \mathrm{d}x_n = 0 \tag{3.5}$$

or

$$\Delta t_c = \begin{cases} \frac{-\mathrm{d}\dot{x}_n + \sqrt{(\mathrm{d}\dot{x}_n)^2 - 4(\mathrm{d}\ddot{x}_n)(\mathrm{d}x_n)}}{2\mathrm{d}\ddot{x}_n} & \text{if } \mathrm{d}\ddot{x}_n \neq 0 \\ \frac{-\mathrm{d}x_n}{\mathrm{d}\dot{x}_n} & \text{if } \mathrm{d}\ddot{x}_n = 0 \end{cases} \tag{3.6}$$

where the single dot refers to relative velocities and two dots refer to relative acceleration towards the common plane. This scheme is only implemented when the bodies are separated and moving towards the CP. A positive gap $\mathrm{d}x_n > 0$ for approaching elements $\mathrm{d}\dot{x}_n < 0$ results in a positive Δt_c. If the acceleration is away from contact

(i.e., negative), $d\ddot{x}_n$ is considered zero in the equation 3.6, so that the time until collision is not over-estimated. The number of time-steps to collision, N_{t_c} is then

$$N_{t_c} = \frac{\Delta t_c}{\Delta t} \tag{3.7}$$

where Δt is the time-step within DECICE. With multiple bodies, interacting objects are likely to collide and change the path of one or more of the elements. Hence, in implementation, the time of collision is taken as a factor of magnitude less, or $N_{t_c}/10$.

Note that in the above analysis the relative displacement, velocity, and acceleration are with reference to the common plane, not the element centroids. Therefore, both translational and rotational movements are encompassed in the calculations, since both the CP position and orientation changes during the approach of two elements.

The updating of element contacts is triggered in two ways within DECICE. First, when the total translation and rotational motion exceeds user-defined limits ϵ, the contact detection scheme is called to update the contact arrays. After every time-step, the motion since the last update is calculated to determine if the contact arrays for the corresponding element and its neighbors should be updated. Second, there is a maximum number of time-steps N_u between successive neighbor updates. This latter method remains unaltered but is used as the instance to recalculate the approximate time of collision. In practice, for small time-steps, when a contact is first established, the approximate number of time-steps to collision $N_{t_c}/10$ is much larger than N_u. Thus, the criteria implemented within DECICE to approximate the number of time-steps until real time collision is

$$N_{\text{implement}} = \min(N_u, N_{t_c}/10) \tag{3.8}$$

When the number of steps until the approximate time of collision $N_{t_c}/10$ is greater than N_u, the potential contact of element A and B is neglected until the next update

of the contact arrays. In practice, this removes the requirement to access element and contact information and possibly resolve the contact geometry at intermediate time-steps between the current time-step and time of contact.

A schematic diagram of the new multi-phase contact detection algorithm is displayed in Figure 3.6. The procedure successively refines the contact detection/resolution

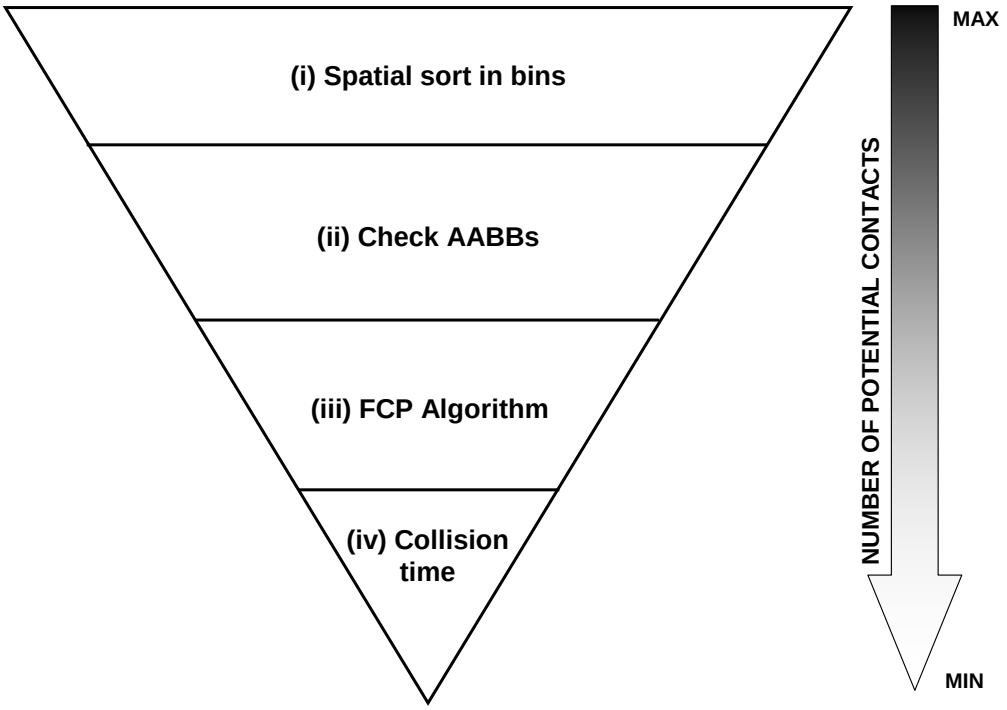

Figure 3.6: Schematic diagram of new contact detection algorithm consisting of: (i) spatial sorting; (ii) proximity detection using AABBs; (iii) contact detection using FCP algorithm; (iv) time of collision approximation.

scheme in the following manner: (i) spatial sorting elements into zones (not included in this chapter); (ii) proximity detection using AABBs of elemental contacts in the zone lists from step (i); (iii) contact detection using FCP algorithm over the refined list from step (ii); and (iv) time of collision approximation to remove the need for contact resolution during the mechanical cycle.

3.1.4 Implementation details

The code structure within DECICE was created to incorporate the key features of the original contact detection scheme. The arrays to store and retrieve data, as well as the procedure of contact detection/resolution and contact force updating, were all dependent on these arrays. By implementing the new contact detection algorithm, most of these arrays have become obsolete. The original algorithm required large storage arrays for possible vertex-face contacts and edge-face contacts for all potential contacts (as well directions, vertex, edge, and, face details, etc.). Using this scheme, a single element, A, may be checked multiple times with another element, B, requiring detailed calculations.

In contrast, the new algorithm implements an element-by-element approach to contact detection. To determine contact between two elements, the distance to the common plane is calculated for each element. If the elements intersect the common plane, then they are in contact. If they come within some user-defined tolerance ϵ, then they are flagged as potential contacts. The number of time-steps until collision is then approximated using equation (3.8) to further reduce the list of potential contacts. Resolution of the geometrical features of the contact (such as a face-to-face contact, vertex-to-face, edge-to-edge, edge-to-face, or vertex-to-edge) is not considered until a true contact has been established. This algorithm only requires storage of a list of potential element-to-element contacts, a CP normal, and a reference point. When a contact exists, the contact points and resultant forces as discussed in Section 3.6 must also be stored.

When using the CP/FCP algorithm, and in particular the implementation used herein involving non-rigid elements, it is important that true contacts (when elements intersect the CP) first be recognized as potential contacts (when they lie within a given

tolerance ϵ of the CP). This is essential in determining the direction of the corresponding contact force between two elements since the CP for elements in contact is found by temporarily separating these elements in a direction given by the CP from the previous time-step.

3.1.5 Contact force magnitude and resolution

Contact force laws are the subject of many discrete element studies (Mirghasemi et al., 1997; Williams and O'Connor, 1999; Perkins and Williams, 2001; Mishra, 2003a; Johnson and Williams, 2004). Both the magnitude of the repelling forces and the point(s) of application of the resulting forces have been debated. The magnitude of the force is typically chosen as proportional to some power of the penetration depth or area of contact. Mirghasemi et al. (1997) used assemblies of two-dimensional particles to show that the two different laws yielded similar behavior. A review of existing analytical contact laws was also presented, which includes the contact of two elastic spheres, a cylindrical punch with a semi-infinite half-space, and a right circular cone with an elastic half-space. The laws presented are

$$F_{\text{sph}} = \frac{2ED^2}{3(1-\nu^2)}\left(\frac{\delta}{D}\right)^{\frac{3}{2}} \tag{3.9}$$

$$F_{\text{cyl}} = \frac{E}{3(1-\nu^2)}d\delta \tag{3.10}$$

$$F_{\text{con}} = \frac{E}{3(1-\nu^2)}\frac{2\tan\beta}{\pi}\delta^2 \tag{3.11}$$

where E is the elastic modulus, ν is the Poisson ratio, D is the diameter of the spheres, d is the diameter of the cone, β is the half-angle of the cone, and δ is the penetration depth. When circular or spherical particles are utilized, the contact law is chosen to simulate the behavior of the sphere-to-sphere contact law. For polygonal particles, there is no explicit analytical relationship. Mirghasemi et al. (1997) reduced each of

the above laws to the form

$$F = \alpha \frac{E}{1-\nu^2} A \tag{3.12}$$

where A is the area of overlap of the two bodies ($\alpha = \sqrt{2}/4$ for spheres, $\alpha = 1$ for cylinders, and $\alpha = 2/\pi$ for cones). Since calculating the overlap area is more expensive (computationally) than using a linear law, they also approximated this law using $A = d\delta$, where d is a constant representing the diameter of the contact area.

Motivated by the results of Mirghasemi et al. (1997), it can be shown that the diameter of contact, assuming the bodies are rigid (and using the "soft" contact model) for each of the problems above, is

$$D_{sph} = \sqrt{2D\delta} \tag{3.13}$$

$$D_{cyl} = d \tag{3.14}$$

$$D_{con} = 2\delta \tan\beta. \tag{3.15}$$

Substitution of these formulae into the forces yields

$$F_{\text{sph}} = K^* \gamma D_{sph} \delta \tag{3.16}$$

$$F_{\text{cyl}} = K^* \gamma D_{cyl} \delta \tag{3.17}$$

$$F_{\text{con}} = K^* \gamma D_{con} \delta \tag{3.18}$$

or

$$F = K D_c \delta \tag{3.19}$$

where $K = \gamma K^*$, $K^* = E/(1-\nu^2)$, D_c is the diameter of contact, and $\gamma = \sqrt{2}/3$ for a sphere, $\gamma = 1$ for a cylinder, and $\gamma = 1/\pi$ for a cone. This contact law is the same as was proposed by Mirghasemi et al. (1997), where the area, instead of being calculated explicitly, is determined by approximating D_c in $A = D_c\delta$ (noting the different notation). This subsequently results in a linear contact law, since D_c is a constant

and yielded results which were similar to the same simulation in which the contact area was explicitly determined.

This analysis reduces three distinct contact geometries to the same law with three unique coefficients. The transition between these types of contacts and the corresponding value of γ is shown graphically in Figure 3.7. Since all geometries are

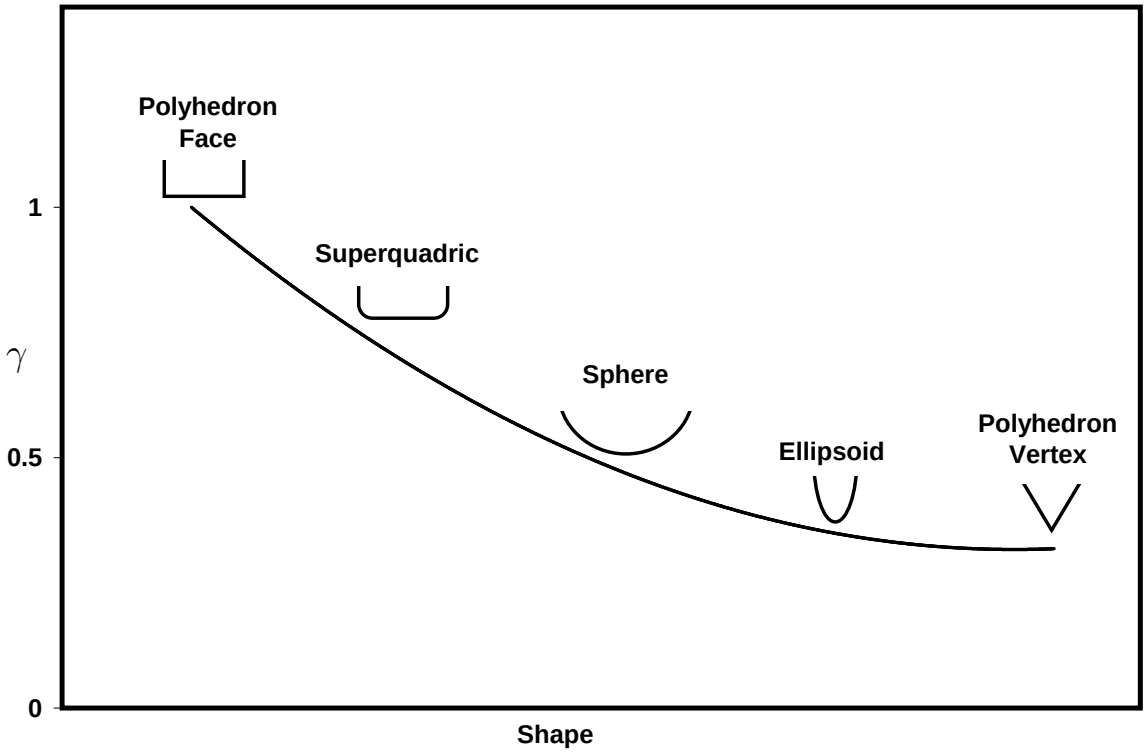

Figure 3.7: Transition of contact for radially symmetric geometries projected onto a two-dimensional plane.

radially symmetric, projecting each geometry in the contact region into two dimensions forms a polygonal face contact (from the cylindrical punch), a circular contact (from the sphere), and a polygonal vertex contact. The constant γ for each of these contact types is taken as $\gamma = 1$, $\sqrt{2}/3$ and $1/\pi$, respectively. It is not unreasonable

to assume, then, that this constant γ should evolve, as the curvature of the contact evolves from a polygonal face to a circle and finally to a vertex. Extrapolating to three dimensions (see Figure 3.7), the contact type evolves from a polyhedral face to a superquadric as the curvature near the vertices decreases. The next step in the evolution is to a spherical contact type as the radii of curvature near the vertices of the superquadric coalesce. As the spherical contact narrows, it forms a contact of an ellipsoid and finally, in the limiting case, the localized contact becomes that of a polyhedral vertex as the ellipse sharpens. The complete transition of contact types is explained in this graph as the value of γ decreases.

The second point which is often addressed is the point of application of the contact forces. Cundall and Strack (1978) uses the reference point during the positioning of the common plane as the point of application of the contact force but has to perform iterations during the mechanical cycle to enforce compatibility conditions. Mirghasemi et al. (1997) test different contact points on the surface of one of the particles or at the centroid of the overlap area as potential points of application. In the original version of DECICE, contact points were determined by node-to-face and edge-to-edge contact detection. That is, contact points are either a vertex of a polyhedron or lie along the edge of a polyhedron. This is notably different than what was employed in the original common plane algorithm and therefore an alternative procedure is employed in the new algorithm.

The reference point maintained during the contact detection stage is not used as the point of application of the contact force in this algorithm. A method similar to that used by Nezami et al. (2006) but consistent with the numerical algorithm of DECICE is utilized instead.

When contact between elements A and B is established (Figure 3.8(a)) through the multi-stage detection algorithm, the corresponding nodes of A and B which lie within a distance δ (taken as the stored gap $\delta = d_B - d_A$) (see Figure 3.8(b)-3.8(c)) from the common plane are projected onto the common plane (Figure 3.8(d)). On this plane, the projection of the nodes from A and the nodes of B each form a convex polygon (possibly reducing to a point or line). In the case where both reduce to a polygon, a modification of the algorithm presented by O'Rourke (1994) is used to determine the intersection of the convex polygons: they either intersect, one polygon is inside the other, or the polygons are disjoint. In the latter case, the particles are no longer in contact. If one polygon is completely inside the other, the nodes of the element which formed the projection of the polygon are taken as the contact points. If the two polygons intersect, then the corners of the convex hull of the intersection of both polygons (Figure 3.8(d)) are taken as contact points when projected back onto the elements A and B. When projected back onto the elements, this results in pairs of contact points (one on element A and one on element B) for each corner of the convex hull.

There are several cases in which one or both of the projections do not form a convex polygon on the common plane. If N_A and N_B are the number of points projected onto the common plane from elements A and B, respectively, then the contact point determination scheme is as follows:

i. $N_A = 1$ and $N_B = 1$ - vertex-to-vertex contact - the corresponding vertices on A and B are used as contact points;

ii. $N_A = 1$ and $N_B = 2$ - vertex-to-edge contact - the vertex of A is used as the contact point;

iii. $N_A = 1$ and $N_B > 2$ - vertex-to-face contact - the vertex of A is used;

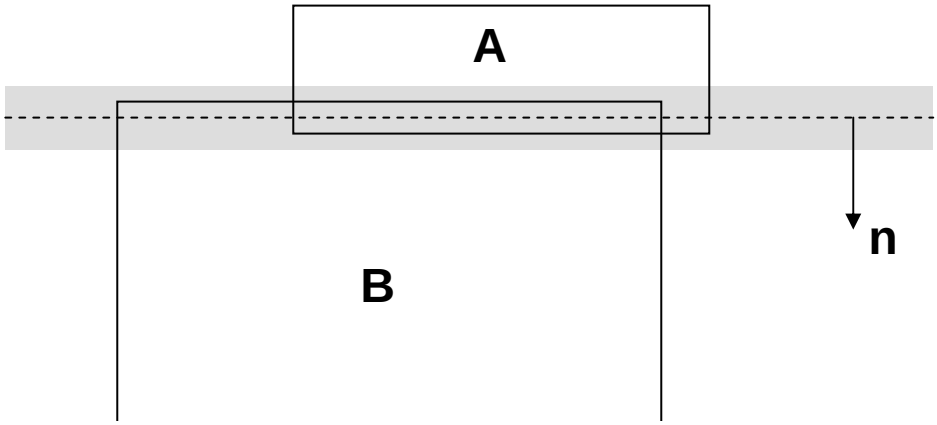

(a)

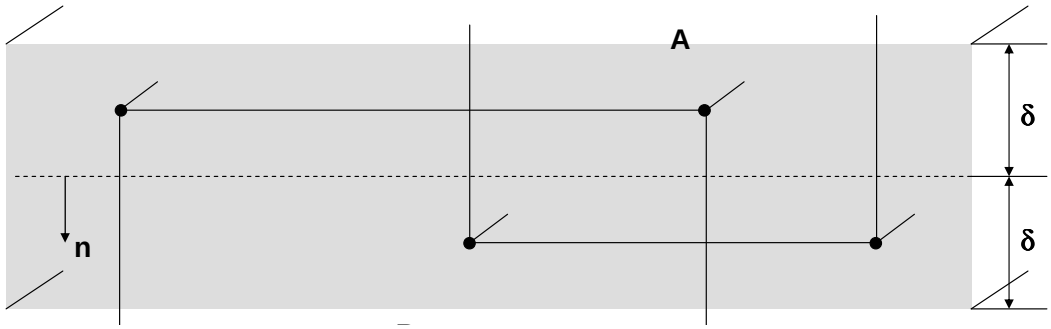

(b)

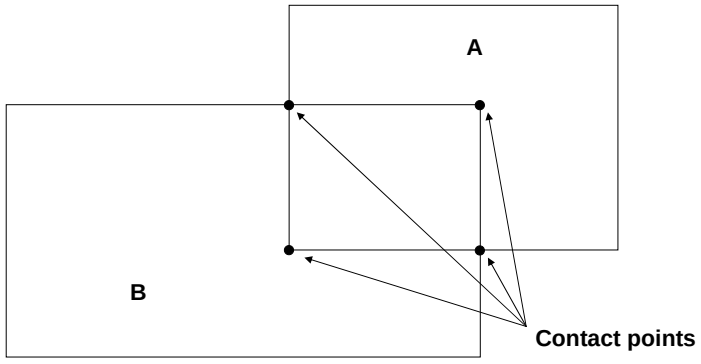

(c)

Figure 3.8: (a) Side view of blocks colliding and position of common plane with normal **n**; (b) scaled view of collision zone of two blocks. All nodes within a distance of δ to the common plane are projected onto the common plane; (c) projection of nodes onto common plane. The intersection of the two convex polygons yields the contact points.

iv. $N_A = 2$ and $N_B = 2$ - edge-to-edge contact - the closest point on the two lines segments is found and projected back onto A and B. If segments are parallel, endpoints of the segments are projected onto one another and the smallest overlap is taken;

v. $N_A = 2$ and $N_B > 2$ - edge-to-face contact - intersection of segment and convex polygon which is different depending on how many segment endpoints are outside the polygon;

vi. $N_A > 2$ and $N_B > 2$ - face-to-face contact - points of intersection of the two projected convex polygons.

The above descriptions may be mirrored for the remaining cases (for example, when $N_A = 2$ and $N_B = 1$). Using these contact points, the corresponding contact forces are then updated, as will be outlined shortly. One of the main reasons for selecting this type of contact resolution scheme is to maintain a similar set of contact points, as existed originally in DECICE. The contact points resulting from this resolution algorithm will correspond to either a vertex-to-face or edge-to-edge intersection.

With this algorithm and the analytical reductions performed above to reduce the contact force to $F = KA$, a reasoning behind using the traditional linear force-displacement law is proposed. For face contact, the value of γ is 1 and for vertex contact the value is $1/\pi \approx 1/3$. For an element to be in face contact, it must have at least 3 (maximum of 4 in DECICE) vertices within a small distance to the common plane, corresponding to a value of $\gamma = 1$. When this occurs in DECICE, each of the vertices is regarded as a contact point yielding a net contact force of at least $F = 3K\delta$ when using the linear contact model. In contrast, in vertex-to-face contact, the vertex is regarded as the contact point, producing a repelling force $F = K\delta$. The ratio of vertex-face to face-face contact force is 1/3, similar to the intended value of γ for

vertex contacts. The combination the findings of Mirghasemi et al. (1997) together with this implicit application of the parameter γ through multiple contact points in DECICE leads to the decision to maintain the use of a linear force-displacement relationship in this research.

This resolution of the contact geometry is performed at every-time step when two elements are in contact and thus minimal changes in the contact geometry due to rigid body motion and deformation are captured. In the case of face-to-face contact, the contact area may also be approximated using the area of intersection of the projected convex polygon, should it be necessary in the contact force-displacement relationship. This area is not utilized in this study.

Following from the above argument, contact forces are linearly resolved in the following manner at each contact point. The relative velocity of element B to element A is defined as

$$\Delta\dot{\mathbf{u}} = \dot{\mathbf{u}}_B - \dot{\mathbf{u}}_A + \omega_{\mathbf{A}} \times (\mathbf{C_i} - \mathbf{C_A}) - \omega_{\mathbf{B}} \times (\mathbf{C_i} - \mathbf{C_B}) \tag{3.20}$$

where $\dot{\mathbf{u}}_A$, $\dot{\mathbf{u}}_B$,$\omega_{\mathbf{A}}$, ω_B are the incremental translational and rotational velocity vectors at the centroid $(\mathbf{C_A}, \mathbf{C_B})$, respectively, and $\mathbf{C_i}$ are contact points. The incremental displacement are calculated as a product with the time-step Δt given by

$$\Delta\mathbf{u} = \mathbf{\Delta\dot{u}\Delta t} \tag{3.21}$$

This displacement vector is then resolved into normal and shear components to the common plane using

$$\Delta u_n = \Delta\mathbf{u} \cdot \mathbf{n} \tag{3.22}$$

$$\Delta u_{s_1,s_2} = \Delta\mathbf{u} \cdot \mathbf{s_1}, \mathbf{s_2} \tag{3.23}$$

where $\mathbf{n}$ is the normal to the common plane, and $\mathbf{s_1}, \mathbf{s_2}$ are two orthogonal shear directions in the common plane. The incremental element forces are then updated

using the procedure outlined in the Section 2.3.5.

3.2 Verification of Contact Scheme

Although differences may exist due to variations in force resolution in more complex problems, the fundamental behavior of the algorithm within DECICE should remain intact. Several benchmark problems are considered in this section to ensure the validity of the newly implemented contact detection scheme. First, individual contact types are addressed to show the correspondence between the original and new algorithms within DECICE, and then several benchmark problems are illustrated.

3.2.1 Contact type comparisons

Several control problems are set up in this section to verify that the old and new contact schemes within DECICE produce similar results. A series of numerical experiments are presented where one element is fixed and the other element is approaching and will come in contact. The orientation of the second element is prescribed so that the following contact types are encountered:

1. face-to-face;
2. edge-to-face;
3. vertex-to-face;
4. edge-to-edge.

The initial configuration for each type of contact is shown in Figure 3.9. The forces and displacements of the second block are monitored during the collision and presented in Figures 3.10-3.13 for each case. In each case, the force and velocity results match exactly which is due to the fact that the contact point resolution scheme in the

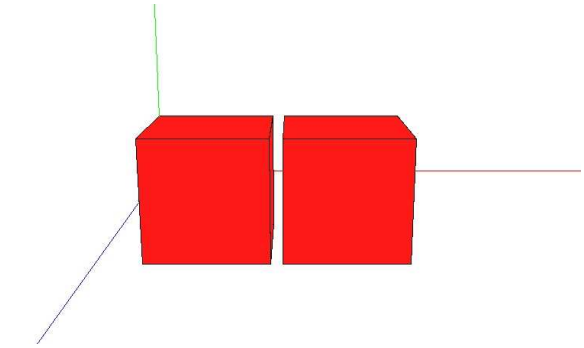

(a) Face-to-face contact.

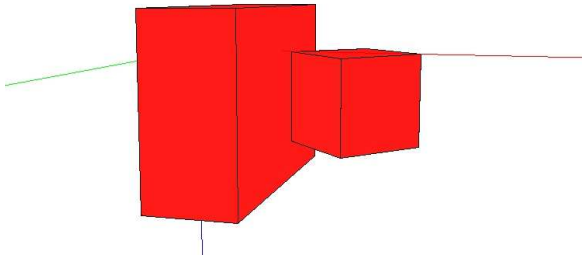

(b) Edge-to-face contact.

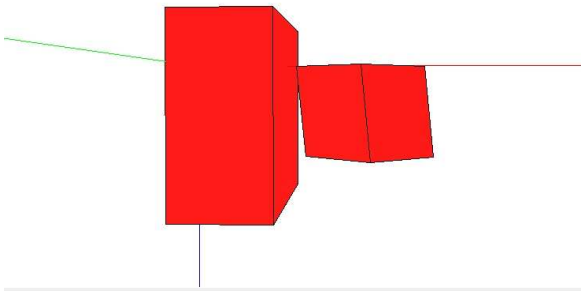

(c) Vertex-to-face contact.

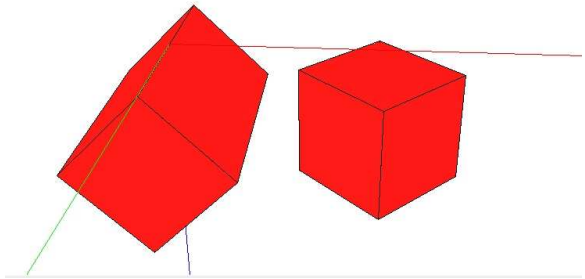

(d) Edge-to-edge contact.

Figure 3.9: Initial configuration of different contact types.

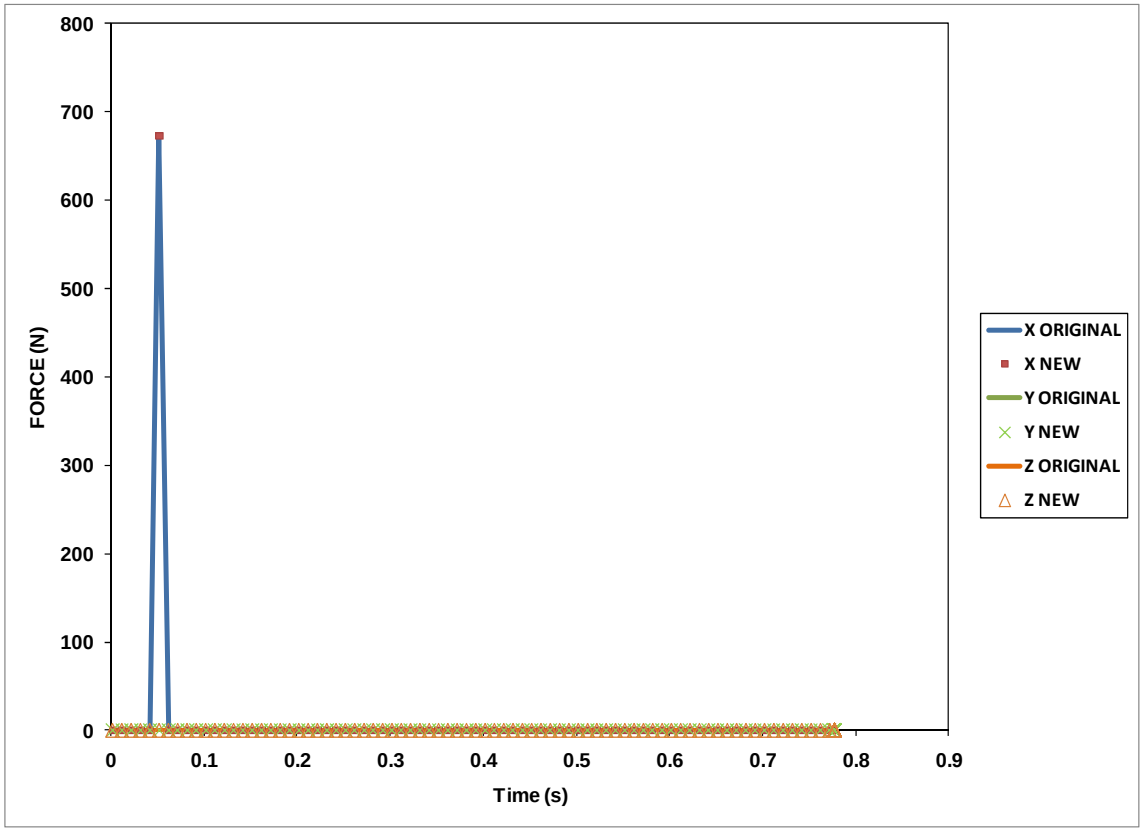

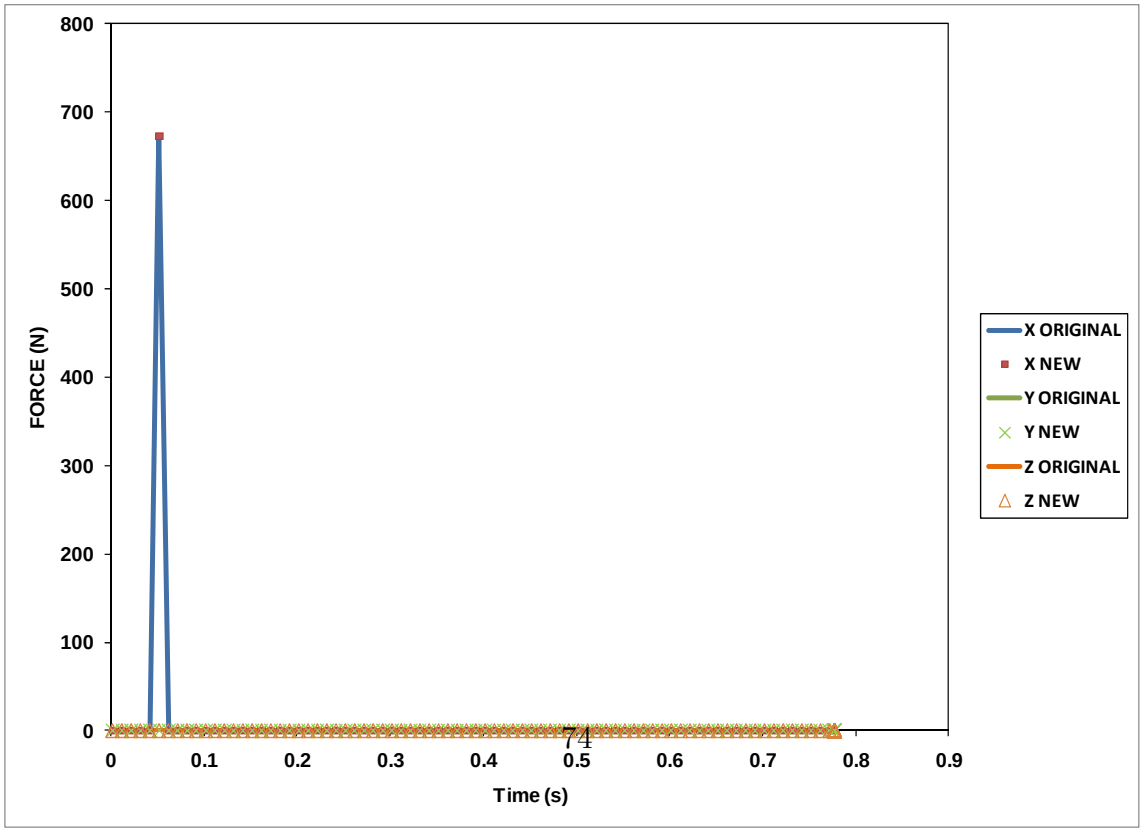

Figure 3.10: Forces and velocities when approaching block is configured for face-to-face contact.

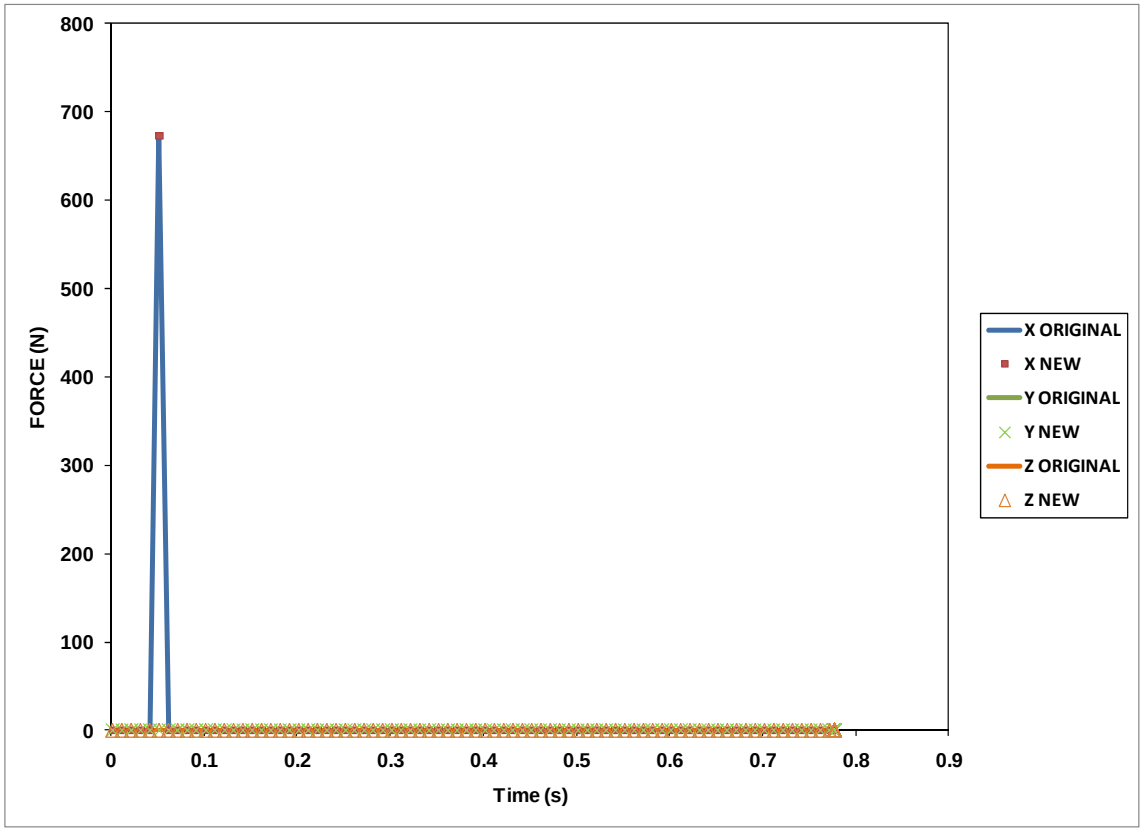

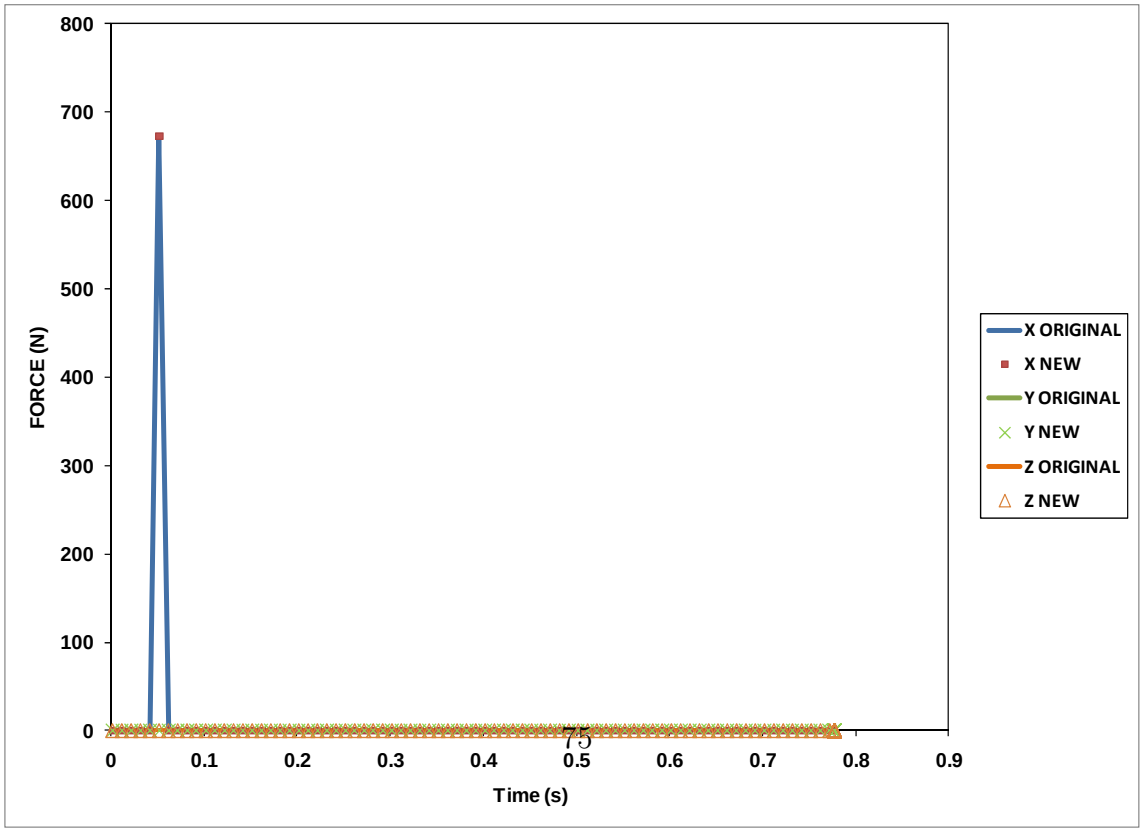

Figure 3.11: Forces and velocities when approaching block is configured for edge-to-face contact.

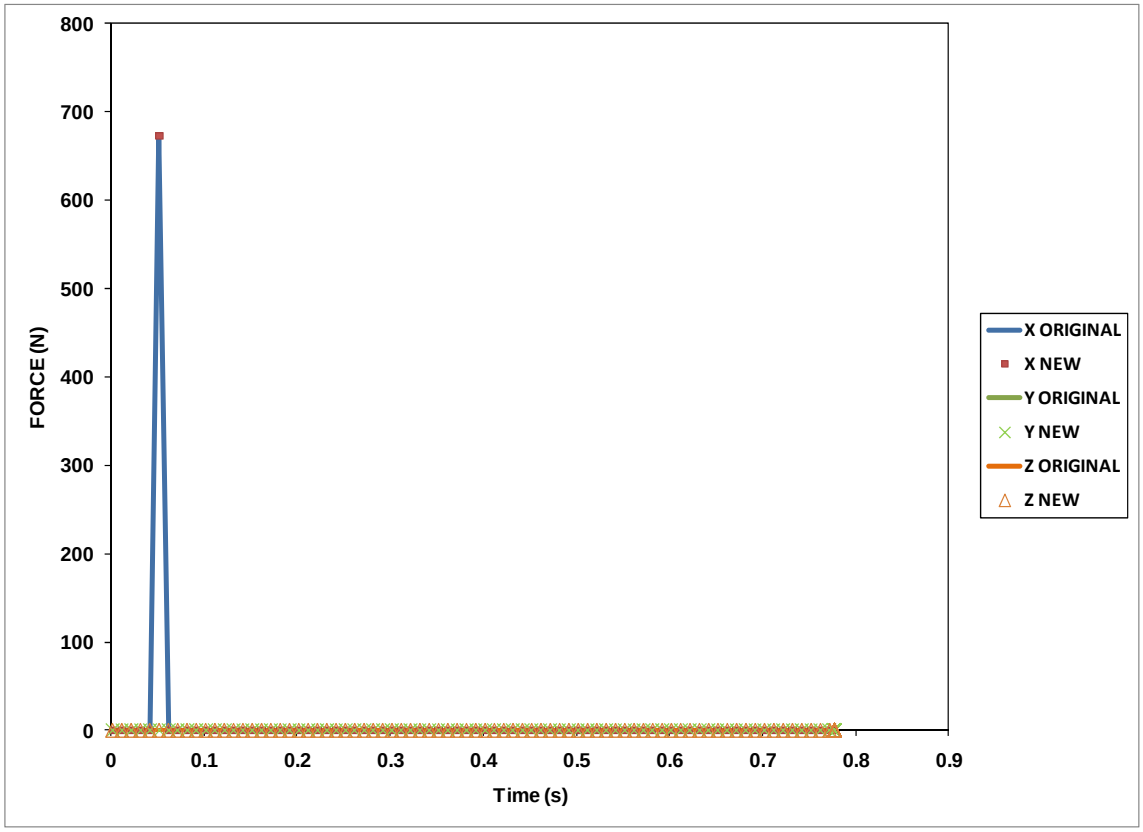

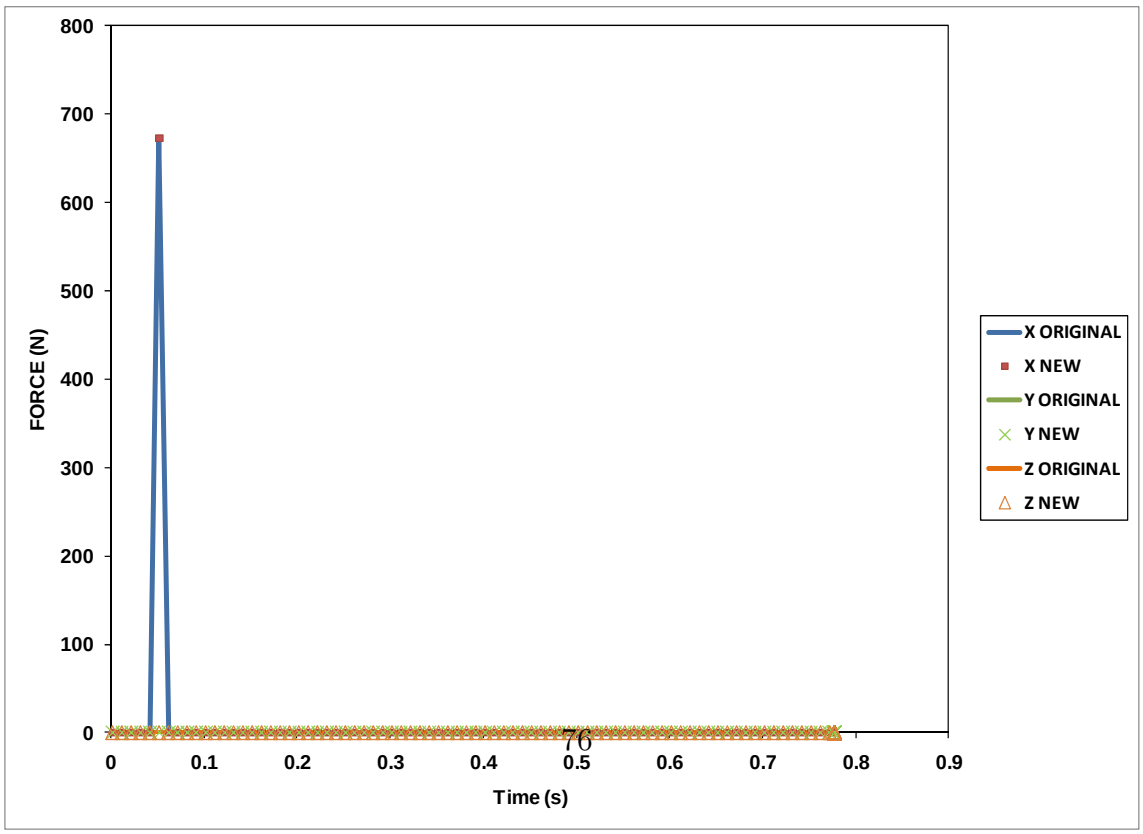

Figure 3.12: Forces and velocities when approaching block is configured for vertex-to-face contact.

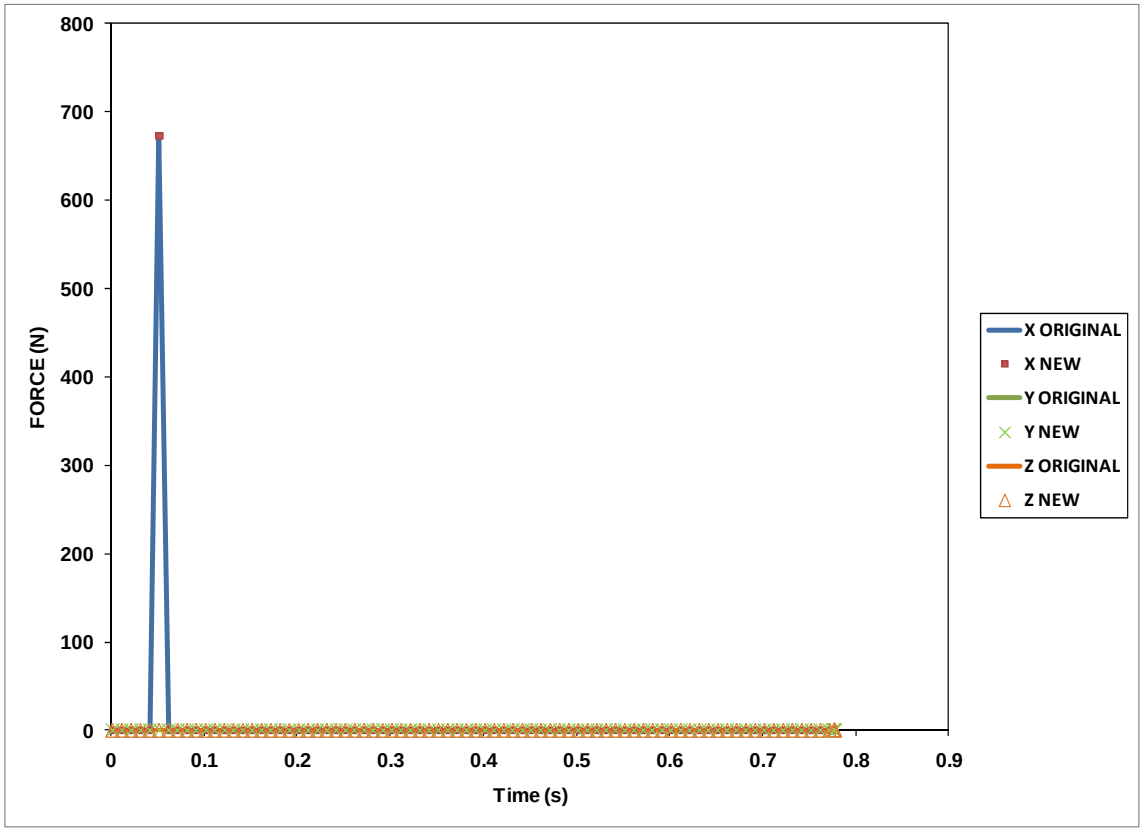

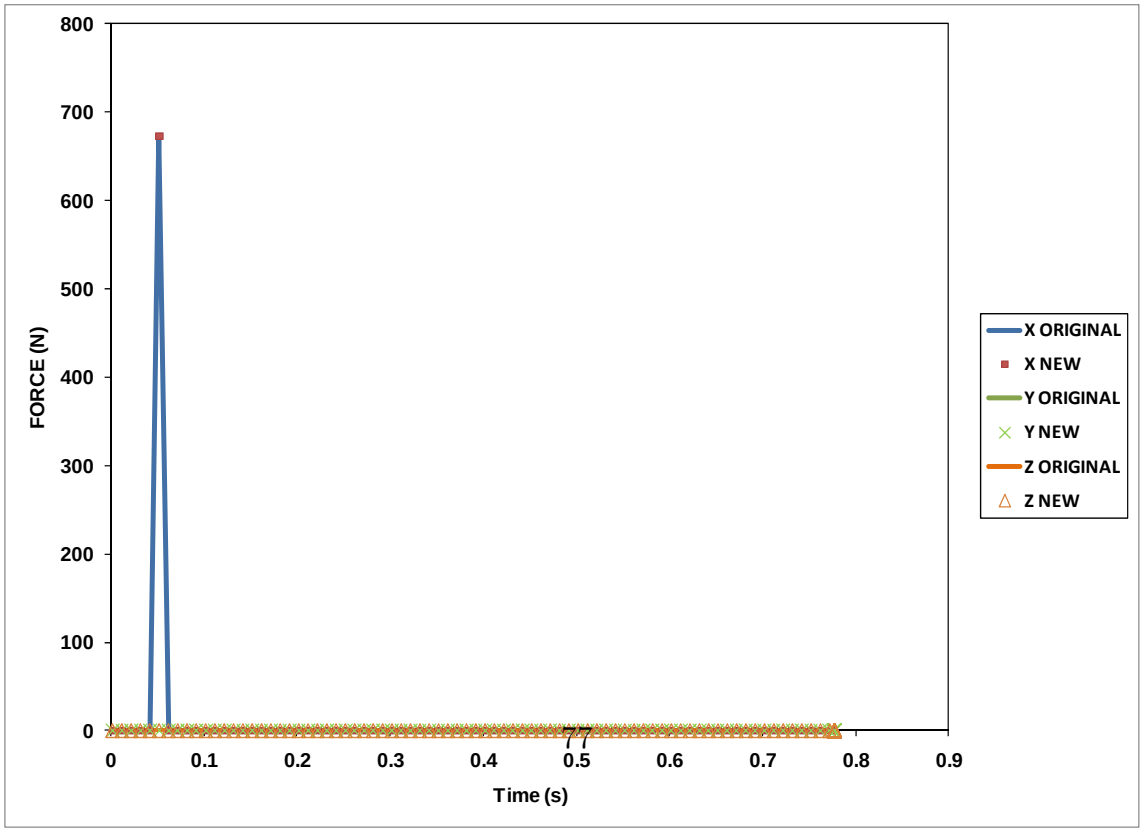

Figure 3.13: Forces and velocities when approaching block is configured for edge-to-edge contact.

Block A		Block B	
Measurement	Value	Measurement	Value
Velocity v	(-0.456,0,0)	Velocity v	(0.456,0,0)
Angular velocity ω	(0,2.18,0)	Angular velocity ω	(0,-2.18,0)
Moment of ω	(0,0.1667,0)	Moment of ω	(0,0.1667,0)

Table 3.1: The kinetic properties of blocks A and B after collision.

new algorithm, discussed in Section 3.1.5, produces points which are almost identical to the contact points utilized in the original DECICE algorithm.

3.2.2 3D dynamic collision of two cubes

Consider two unit cubes (1m $\times$ 1m $\times$ 1m) positioned in face-to-face contact at time $t = 0$, as shown in Figure 3.14. The centroids of cube A and B are at elevation $z = 0$m and $z = 0.5$m, respectively, so that the contact area is exactly half the area of the approaching faces. Initial velocities are $\mathbf{v}_A = (1, 0, 0)$ and $\mathbf{v}_B = (-1, 0, 0)$ meters per second. Since the initial linear and angular momentum is zero, the initial kinetic energy is given by

$$K_o = \frac{1}{2} m_A v_{Ax}^2 + \frac{1}{2} m_B v_{Bx}^2 = 1.0 \tag{3.24}$$

with $\rho_A = \rho_B = 1$. At time $t = t_f > 0$, the collision will have occurred and the block should be moving apart while kinetic energy is conserved. The expression for final kinetic energy is

$$K_f = \frac{1}{2} m_A v_A^2 + \frac{1}{2} m_B v_B^2 + \frac{1}{2} I \omega_A^2 + \frac{1}{2} I \omega_B^2 \tag{3.25}$$

A series of snapshots are shown in Figure 3.14. The time-step, automatically generated from equation (2.29), is 7.77×10^{-4}.

A plot of the velocity components of each element and the kinetic energy over the duration of the impact is shown in Figure 3.15-3.17. The details of the kinematics of the problem after impact for each block are shown in Table 3.1. The final kinetic

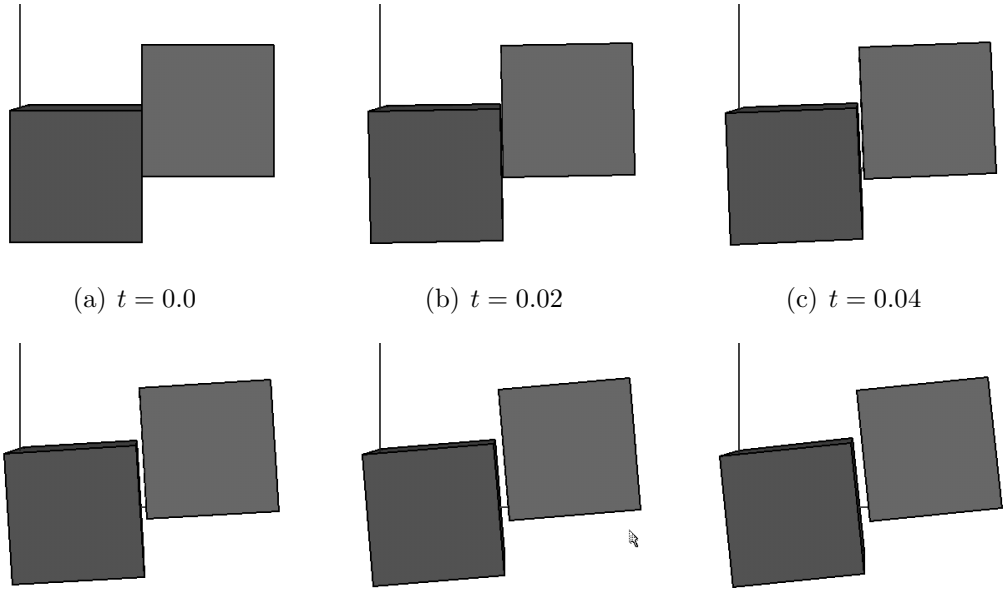

(a) $t = 0.0$ (b) $t = 0.02$ (c) $t = 0.04$

(d) $t = 0.06$ (e) $t = 0.08$ (f) $t = 0.10$

Figure 3.14: Snapshots of the collision of two approaching blocks.

energy and coefficient of restitution are as expected (=1.0) for the elastic collision.

3.2.3 Sliding of two elastic blocks

The geometry of this simulation is depicted in Figure 3.18. Two cubes resting on a large plate (see Figure 3.18) are both subject to a gravitational field given by $\mathbf{g} = (10, 0, -10)$ m/s^2. The coefficient of friction between element 2 (which is located further in the direction of increasing x-direction, see Figure 3.18) and the plate is larger than for element 1. The initial block separation is taken as 0.25 meters so that the expected time of collision may be calculated as $t = 0.267$ seconds.

The velocity profile of each block is plotted in Figure 3.19. Collision occurs between $t = 0.26$ and $t = 0.27$ seconds, as indicated by the sudden change in velocity. Snapshots of the simulation are given in Figure 3.20.

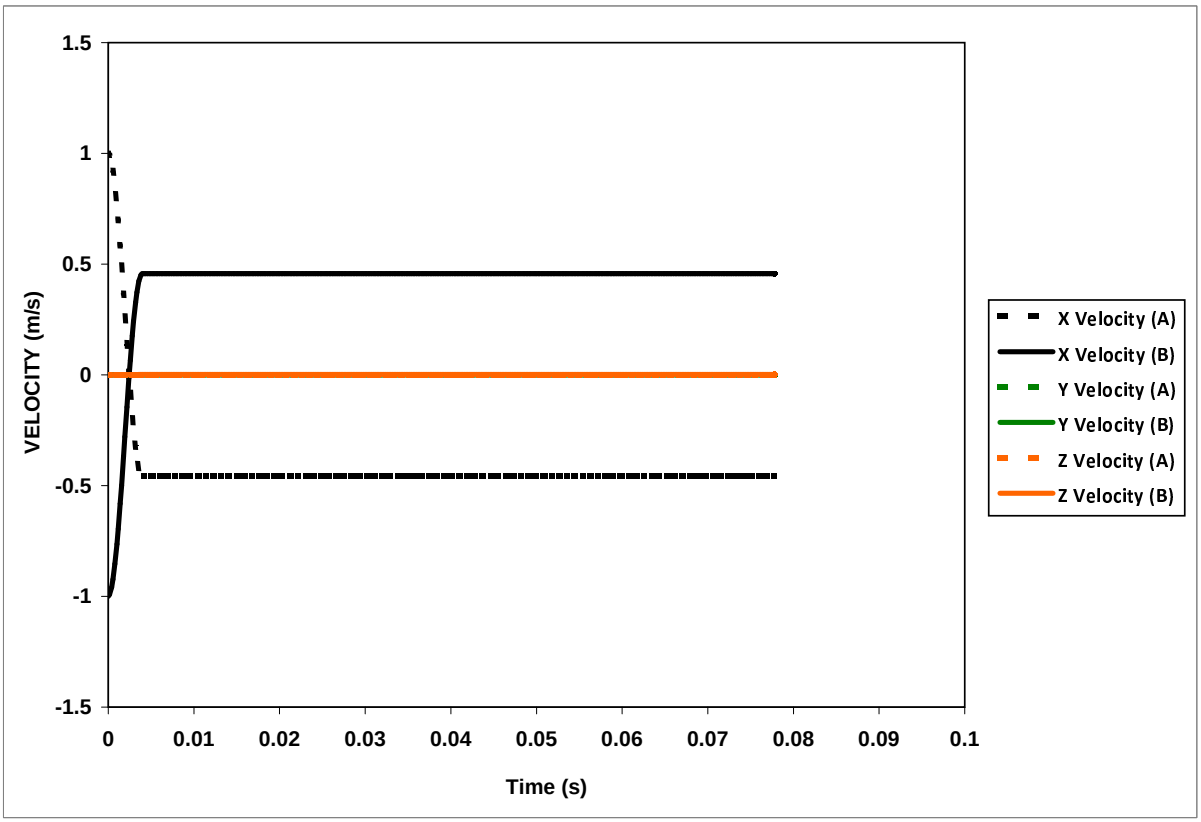

Figure 3.15: Velocity of blocks A and B during impact.

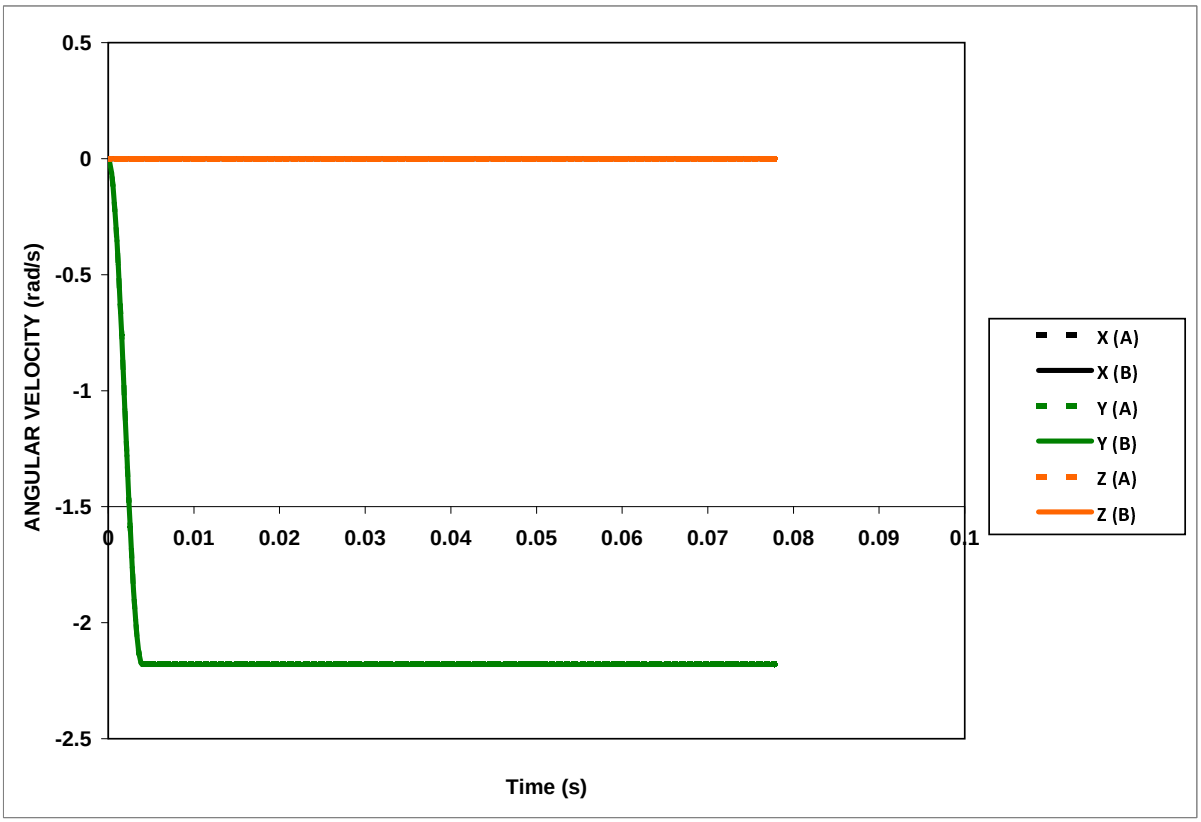

Figure 3.16: Angular velocity of blocks A and B during impact.

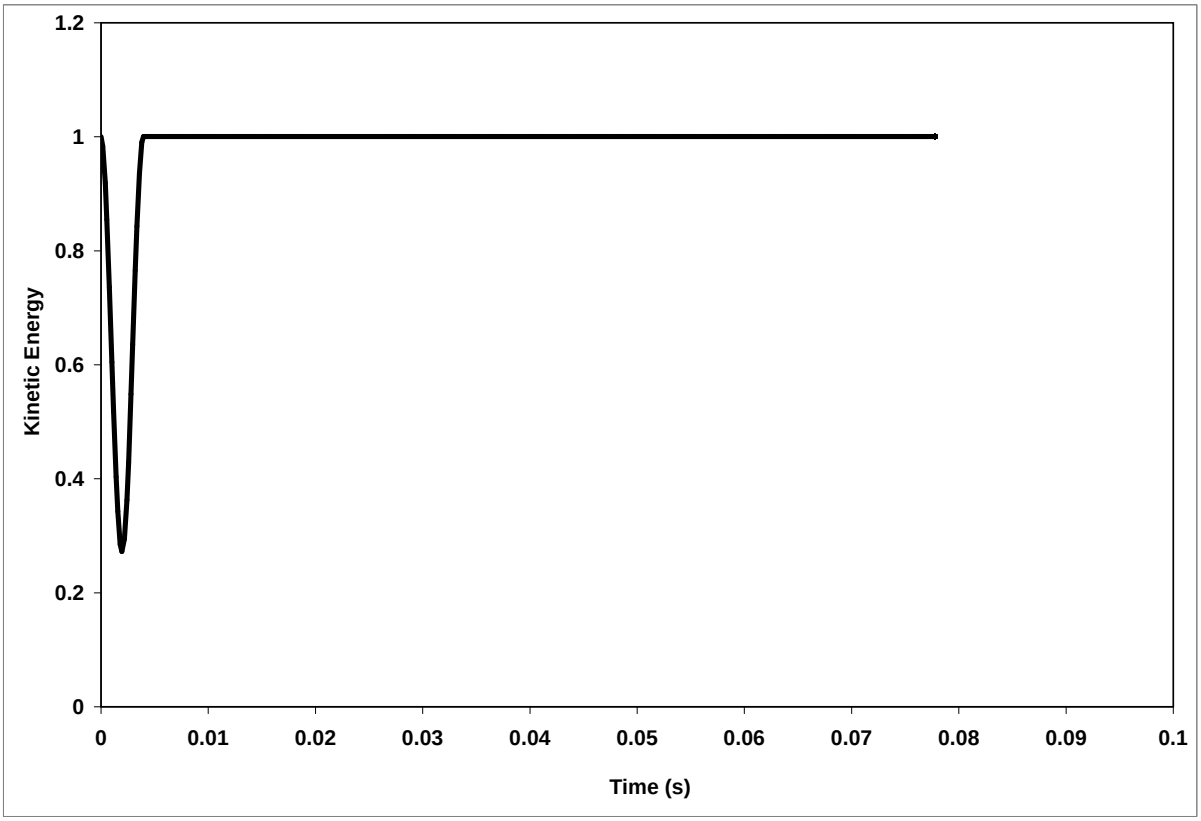

Figure 3.17: Kinetic energy during impact.

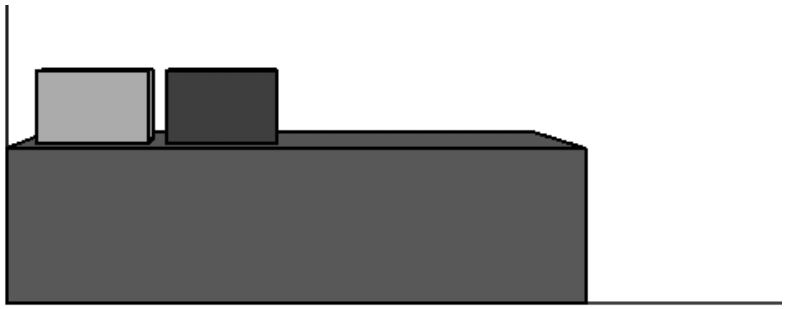

Figure 3.18: Initial geometry of the problem involving two elastic blocks, with different friction coefficients, sliding along a horizontal plane.

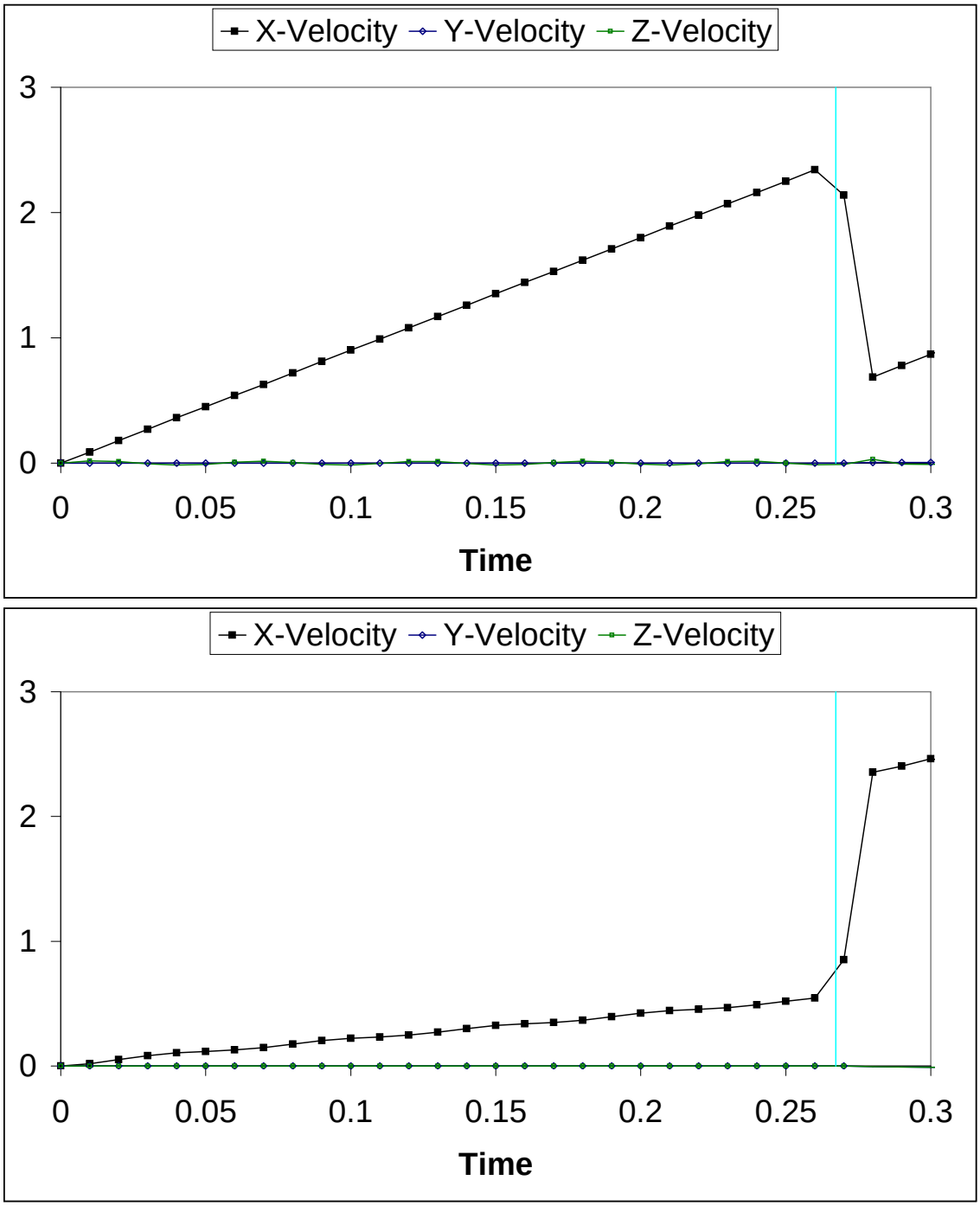

Figure 3.19: Velocities of blocks 1 (top) and (2) for the duration of the simulation involving sliding collision of two elastic blocks.

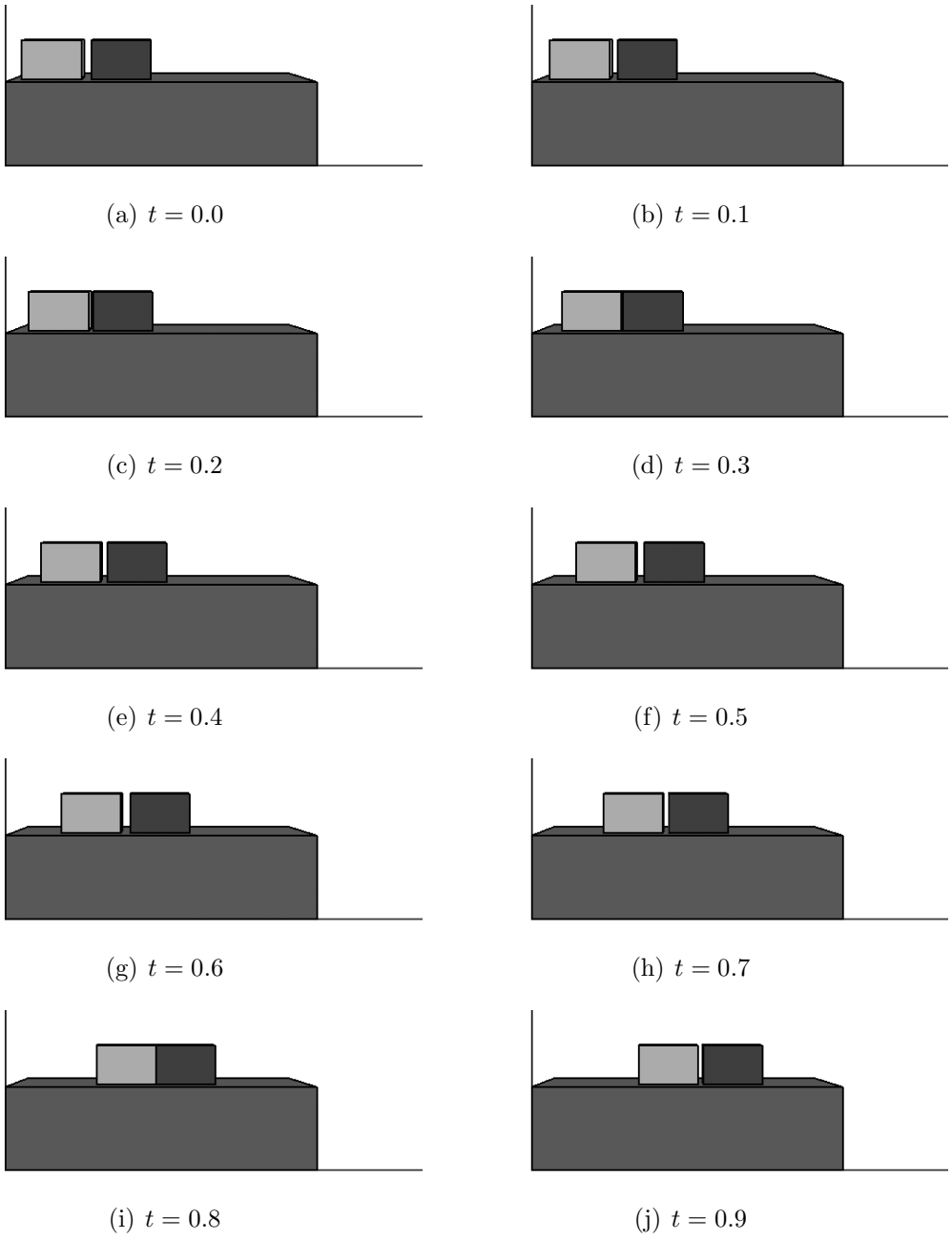

(a) $t = 0.0$ (b) $t = 0.1$

(c) $t = 0.2$ (d) $t = 0.3$

(e) $t = 0.4$ (f) $t = 0.5$

(g) $t = 0.6$ (h) $t = 0.7$

(i) $t = 0.8$ (j) $t = 0.9$

Figure 3.20: Simulation snapshots of two elastic blocks sliding under body forces with different friction coefficients with the bottom plate.

3.2.4 Sliding of elastic blocks on a friction plane

The geometry of this simulation is depicted in Figure 3.21. Three cubes are positioned

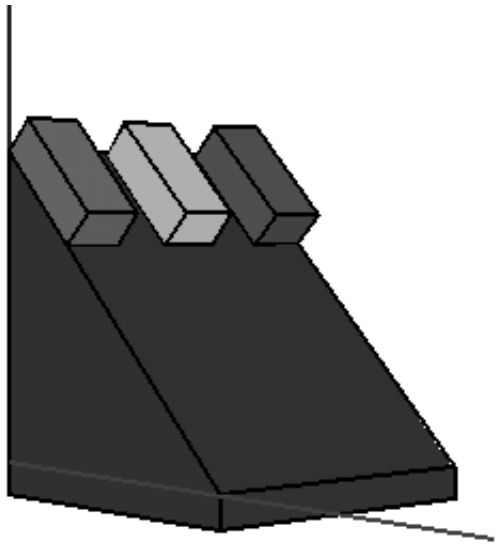

Figure 3.21: Initial configuration of blocks sliding on a friction plane.

on a friction plane inclined at an angle of 45 degrees to the horizontal and subject to gravity $g_z = -10$ m/s^2. The coefficient of friction of the three blocks is taken as $\mu = 0.1$, 0.5, and 1.0, which corresponds to a friction angle of 5.7, 25.6, and 45 degrees. The block with 45° friction angle is expected to remain fixed while the other two blocks accelerate down the friction plane. The velocity profiles of the three blocks are given in Figure 3.22 along with a series of snapshots in Figure 3.23. The point at which the block with friction coefficient $\mu = 0.1$ falls off the end of the friction plane is indicated by the kink in the z-velocity curve near $t = 0.65$ seconds.

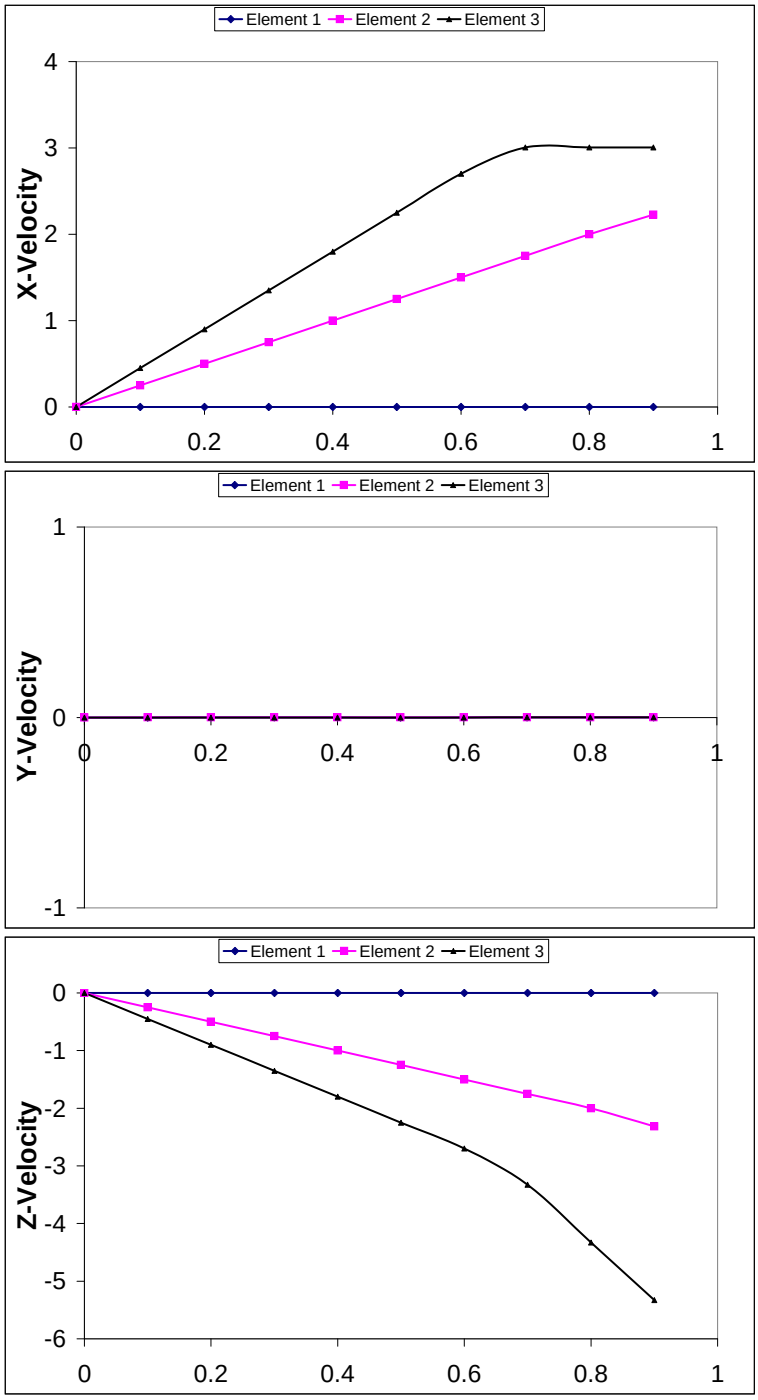

Figure 3.22: Velocity components of each of the elements for the duration of the simulation involving three blocks sliding down a 45° plane.

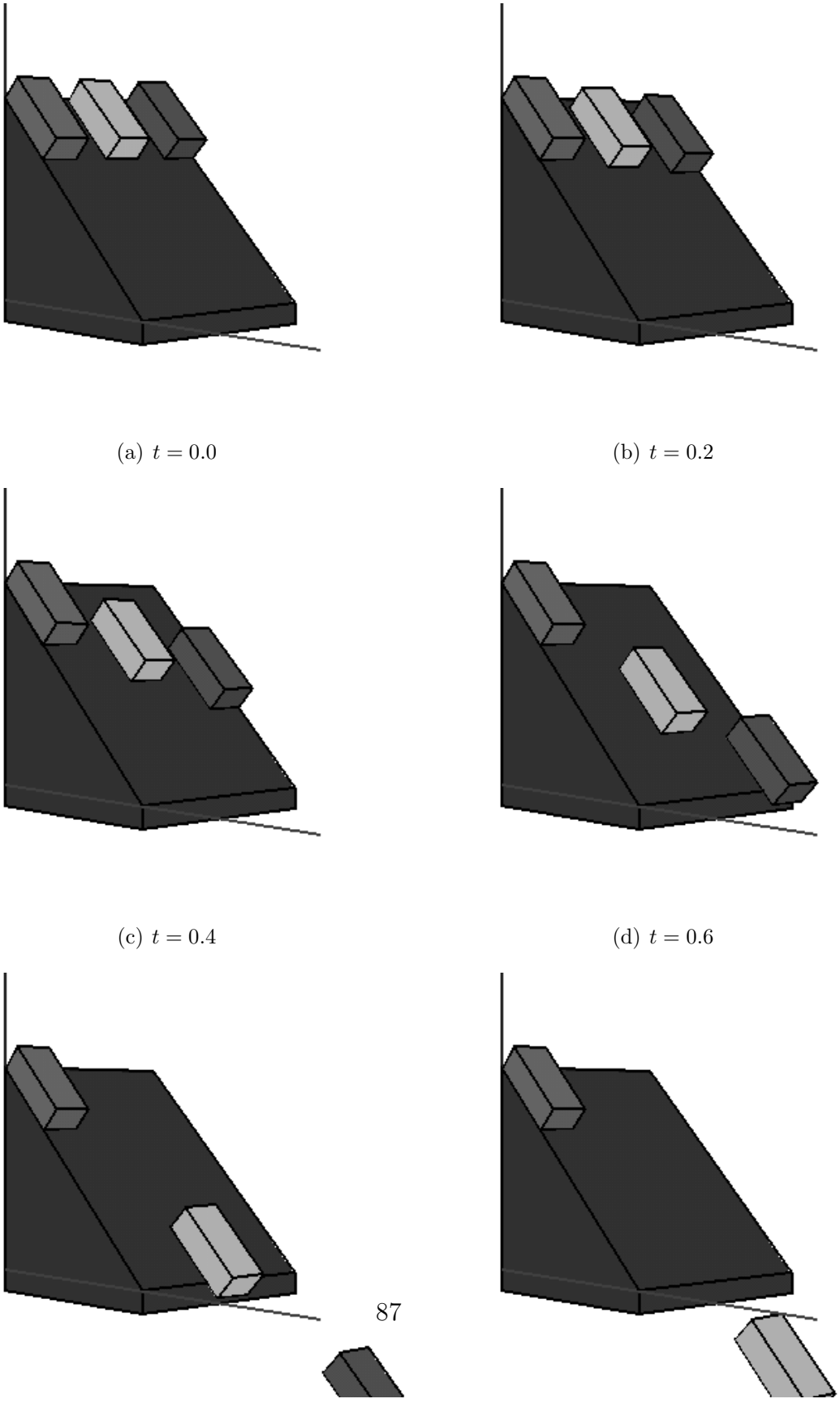

(a) $t = 0.0$ (b) $t = 0.2$

(c) $t = 0.4$ (d) $t = 0.6$

(e) $t = 0.8$ (f) $t = 1.0$

Figure 3.23: Snapshots for the duration of the simulation involving three blocks sliding down a 45° plane.

3.3 Results and Discussions

To determine the effect of the new algorithm on performance during the contact detection/resolution phase of DECICE, a simple model consisting of a 25cm by 20cm by 50 cm box (length by width by height). Cuboid elements (8-nodes) are randomly generated in the space above the box and slowly fill the box as they fall under the influence of gravity and rebound off the bottom plane. The average dimensions of the randomly generated elements are 2cm×2cm×2cm. The trials consisting of 100, 200, 300, 400, and 500 elements, with an automatically generated time-step of $\Delta t = 0.194 \times 10^{-6}$ (resulting from stability limits on deformation in Section 2.29), were conducted for times up to $t = 0.388$ seconds (two million time-steps). Note that the actual number of elements is five more than those listed above if the box base and four sides are included, but for the purpose of this study the number of randomly generated elements is referenced. The results of the before and after views of the trials can be seen in Figures 3.24-3.28. The results for execution time, approximate number of elements

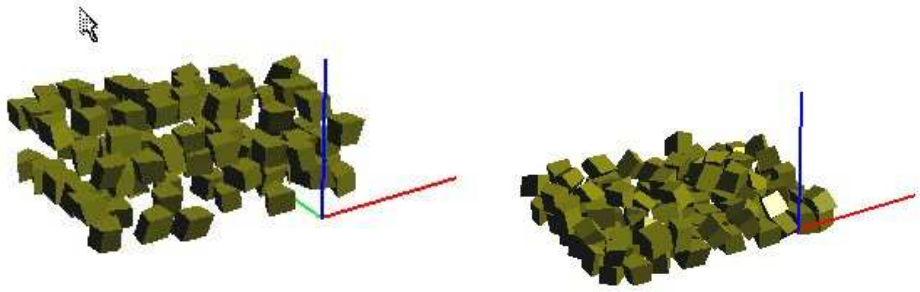

Figure 3.24: Before and after snapshots of 100 randomly-generated elements collecting in a box.

in contact at final time, and speed-up are given in Table 1 and depicted in Figure 3.29 for the various algorithms. For comparison purposes, simulations were also conducted using 3DEC. The random elements generated and output by DECICE were used to construct a corresponding input file for 3DEC for the five simulations considered. In

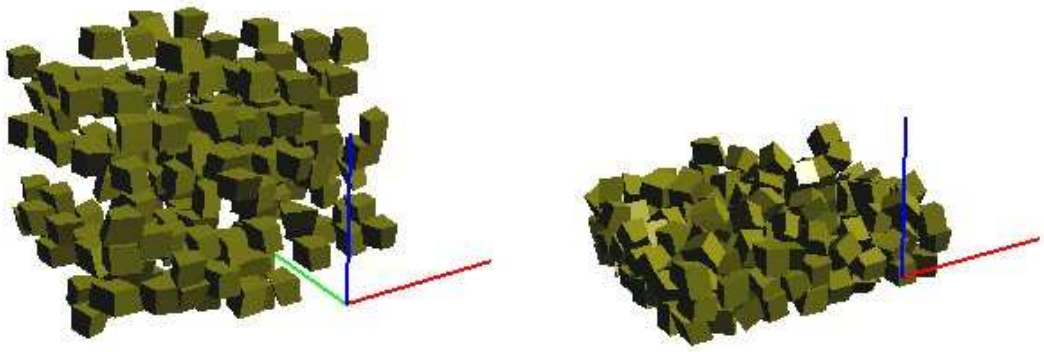

Figure 3.25: Before and after snapshots of 200 randomly-generated elements collecting in a box.

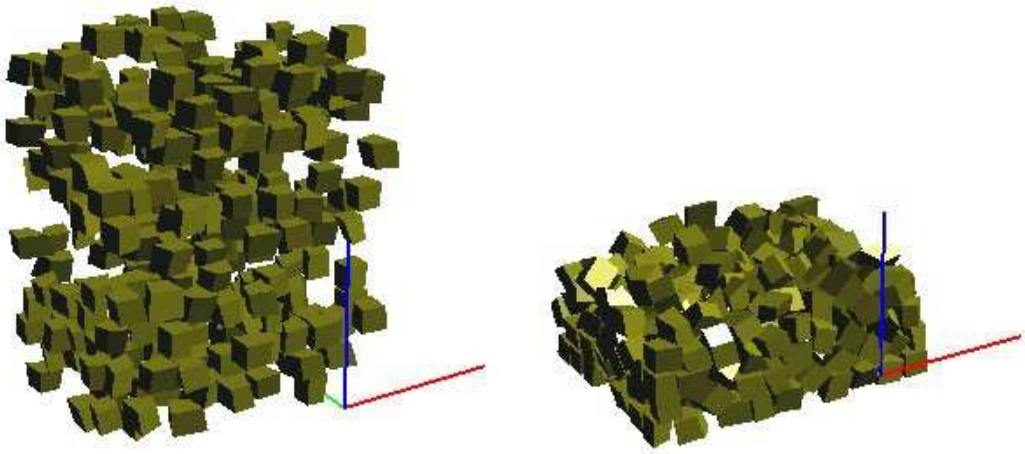

Figure 3.26: Before and after snapshots of 300 randomly-generated elements collecting in a box.

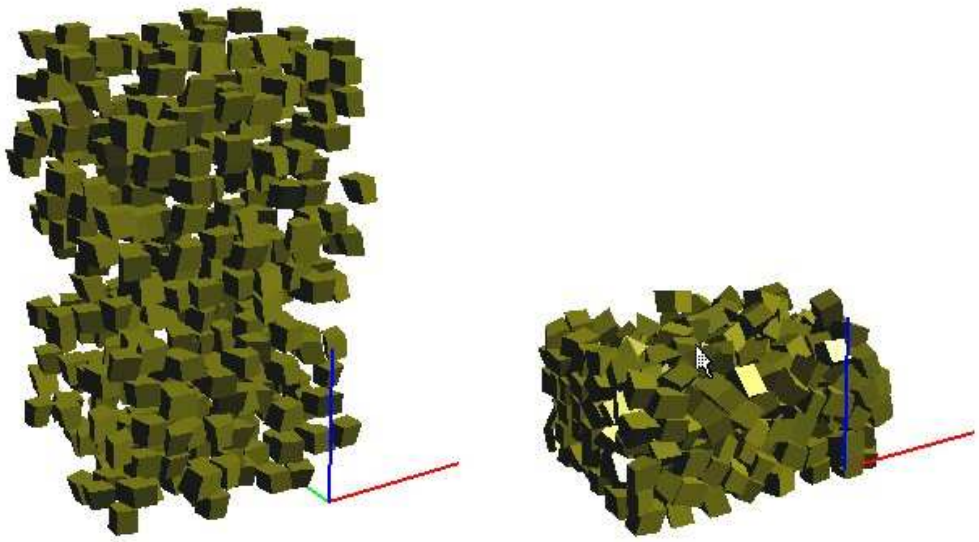

Figure 3.27: Before and after snapshots of 400 randomly-generated elements collecting in a box.

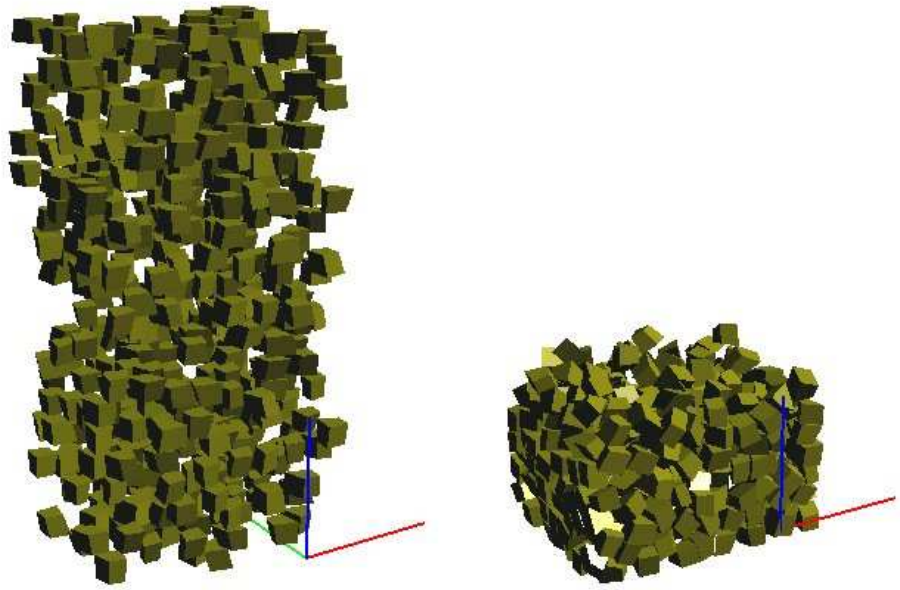

Figure 3.28: Before and after snapshots of 500 randomly-generated elements collecting in a box.

addition to the physical properties, the numerical properties such as the number of time-steps and increment were matched to those used in the DECICE simulations, since the algorithm within DECICE updates the CP reference point at every time-step. The same was achieved in 3DEC by setting the appropriate parameter, `nucp`, to 1 (the default value is 10). Assuming that the solution schemes for 3DEC and DECICE are comparable in terms of simulation time, the resulting simulation times should be dependent on the number of elements and/or contacts. Please note that the intention in using 3DEC is only to present simulation times for the matching problem, with associated numerical and physical parameters, which is originally simulated in DECICE. Further, DECICE simulations are conducted on a Linux based AMD-Opteron processor system, whereas 3DEC simulations are conducted on a different Windows-based PC with Intel processors. Both processor speeds are 2.4GHz. To ensure the comparison between DECICE and 3DEC performance results are comparable on the different hosts, DECICE was ported to the Windows environment and compiled with the same set of PGI compilers (Windows version). The model with 100 elements was then conducted and yielded a simulation time within 2.5% of the corresponding simulation on Linux (approximately 7 minutes). Hence, the effect of the different operating systems and computers on the measured performance is

Simulation	Elements(Contacts)	Old	3DEC	FCP	New	Speedup Ratio
1	100(326)	16973	18093	1794	1318	12.88
2	200(861)	50774	51608	3505	2560	19.83
3	300(1394)	86989	80944	5464	4180	20.81
4	400(1939)	132409	94654	7713	6192	21.38
5	500(2340)	154945	132997	9977	7389	20.96

Table 1: Simulation time (in seconds) and observed speed-up for simple box-filling problem.

assumed to be negligible.

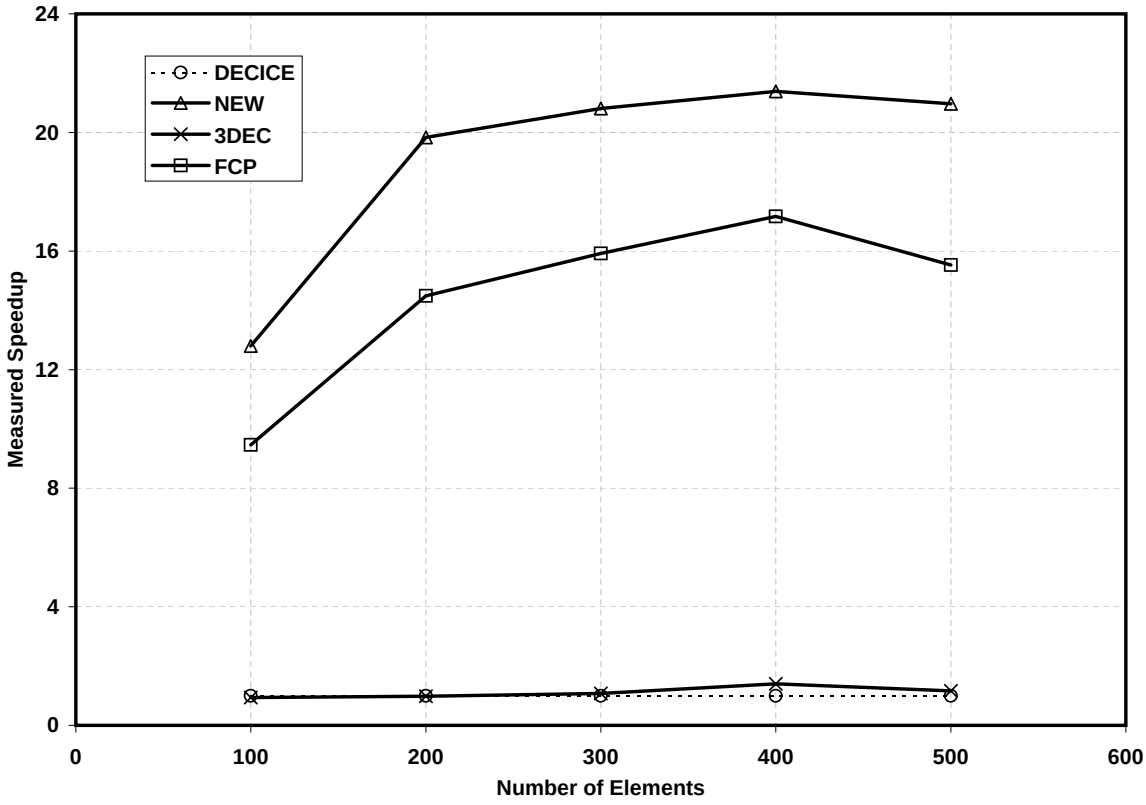

Figure 3.29: Observed speed-up in simulation time for simple box-filling problem when using: 3DEC, original DECICE algorithm, modified DECICE algorithm (FCP) and new DECICE algorithm (NEW).

Simulation times for 3DEC are comparable to those of the original DECICE algorithm for fewer elements but decrease in comparison as the number of elements increases. This behavior is in agreement with what is reported by Cundall (1988) when comparing the CP scheme to the direct-testing method.

For simulations conducted using the new contact detection scheme within DECICE, the speed-up over the original algorithm (and hence 3DEC) is dramatic. For a relatively small number of elements (100), the observed speed-up is 12, a full order of magnitude faster. As the number of elements increases, the measured speed-up becomes much more significant. For 500 elements, the new algorithm performs approximately 21 times faster than the old algorithm. This reduces the simulation time from nearly two days to just over two hours. In fact, in these trials, the largest simulation time observed using the new algorithm (approximately two hours for 500 elements) is only half of the smallest simulation time observed using the old algorithm (almost five hours for 100 elements).

Another important observation, however, is the rate at which the speed-up occurs. Using the old algorithm, the execution time, normalized by the time required for 100 elements, is plotted versus the number of elements (scaled by 100) in Figure 3.30. As the number of elements increases, the simulation time increases approximately by two (slope of 2). That is, for a problem involving n times as many elements, the execution time will increase by a factor of $2n$. Using the new algorithm, the rate of growth is decreased from $2n$ to n. This decrease in growth is attributed to implementing the FCP contact detection procedure, as is evident from the corresponding curve (for FCP) in Figure 3.30. For 500 elements, the simulation time is only approximately five times that of the simulation time for 100 elements, indicating a linear relationship. This is a significant difference when considering the fact that the initial simulation time

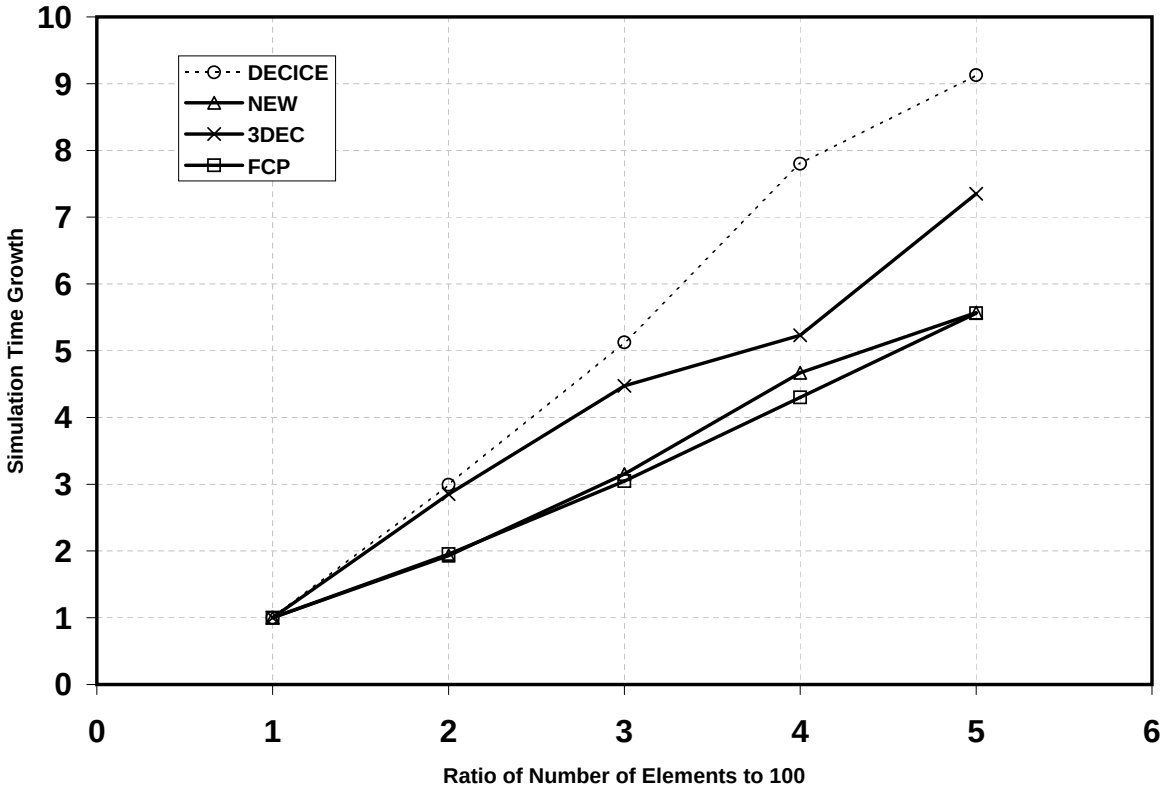

Figure 3.30: Observed speed-up in simulation time for simple box-filling problem when using: 3DEC, original DECICE algorithm, modified DECICE algorithm (FCP) and new DECICE algorithm (NEW).

for the old algorithm, $t_{\text{old}}(100) = 16973$ seconds, is more than an order of magnitude greater than the simulation time required using the new algorithm, $t_{\text{new}}(100) = 1318$ seconds.

3.4 Summary

DECICE is one of only two commercially available software which utilize polyhedral elements in discrete (or distinct) element modeling. The major obstacle limiting the growth of the tool has been the out-dated algorithms which were implemented when the code was created in the early 1980s.

The bulk of the computational effort within DEM is focused in the contact detection/resolution stage. The newly implemented contact detection algorithm within DECICE has led to a significant speed-up of the algorithm. Simulations conducted have shown that the running-time of DECICE has decreased by a factor of magnitude, up to 21 times faster than the original version. This speed-up is observed for approximately 500 elements. Simulation time required for 500 elements using the new algorithm is less than half of the simulation time required for 100 using the old algorithm.

Simulation time for the trials yield a direct linear relationship (slope= 1) between execution time and number of elements. Originally in DECICE, simulation times increased twice as fast (slope= 2). Further analysis should be conducted for an increasing number of elements to determine if this pattern continues. Nonetheless, the results indicate that the incorporation of the new contact detection scheme has successfully improved the performance and thus applicability of the DECICE code for larger problems.

Chapter 4

Parallel Improvement

Performance enhancements of the DECICE code via contact detection algorithm improvement were addressed in the previous chapter via a new multi-tier contact detection/resolution scheme utilizing the FCP algorithm of Nezami et al. (2004), axis-aligned bounding boxes, and an approximation of the time of collision. Simulations involving a relatively small number of polyhedral elements (500) exhibited a factor of magnitude decrease in the execution time of DECICE (up to 21 times faster than the original version).

Computer hardware and architecture have also evolved greatly since DECICE was originally formulated by Applied Mechanics Inc. in 1986. Multiprocessor and/or multi-core computers have been a driving force for the need of redevelopment and extension of algorithms to the high-performance computing (HPC) environment. The implementation of an efficient parallel algorithm for the DEM and in particular DECICE is discussed in this chapter. The target platform is a shared memory NUMA based SGI Origin 3000 system.

4.1 Background

OpenMP is a powerful set of compiler directives and routines for high-level languages like C++ and Fortran. It is used to construct a parallel algorithm within DECICE which may execute in a multiprocessor environment. To address the potential for parallel improvements within DECICE, some background on parallel computations is first discussed.

4.1.1 Parallel architecture

To understand the applicability of parallel algorithms it is necessary to first describe the differences in parallel computer architecture upon which multiprocessor computers are based. Although there are specific enhancements depending on the manufacturer, the two main classes of architectures are *shared* and *distributed* memory. Memory storage and communication between processors which is performed differently on each of these systems is detailed below.

The distributed memory architecture forms the basis of what is commonly referred to as *clusters*. In this set-up, each processor has its own local memory which is not directly available to other processors in the group. Communication between nodes (processors) is achieved via message-passing interfaces such as MPI or PVM. All communication is directed through a central hub, as depicted in Figure 4.1. Shared memory computers may be divided into two main types - *symmetric multiprocessor (SMP)* and *non-uniform memory access (NUMA)* systems. In both systems, each processor has access to all memory but not in the same manner. In a SMP system, all processors have identical access to a single shared memory (see Figure 4.2). The time required for two unique processors to read data from this shared memory is the same. Within NUMA systems, the shared memory is divided amongst processing

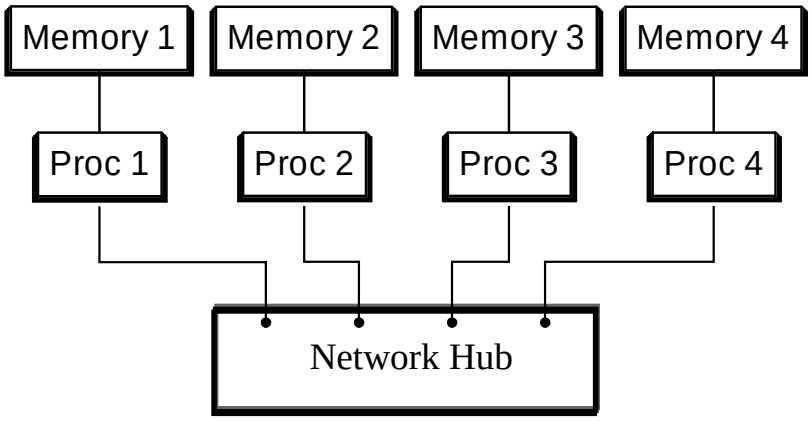

Figure 4.1: Schematic diagram of distributed memory multiprocessor computer.

units (see Figure 4.3). Each group of processors has access to its own local memory and other partitions of memory, but local memory access is faster. In this sense, the time required to read data from memory depends on the memory location relative to the processor attempting to read it, and thus is non-uniform.

4.1.2 Compiler directives

Compiler directives are targeted for each type of architecture. OpenMP is used on shared memory systems and MPI (message-passing interface) is typically used on distributed memory systems, although it can be used on a shared memory system. Algorithms using OpenMP typically use the FORK-JOIN model (see Figure 4.4) in which there is a single master thread (processor) which initiates variables and processes. Parallel calculations begin (fork) and end (join) with a set of directives,

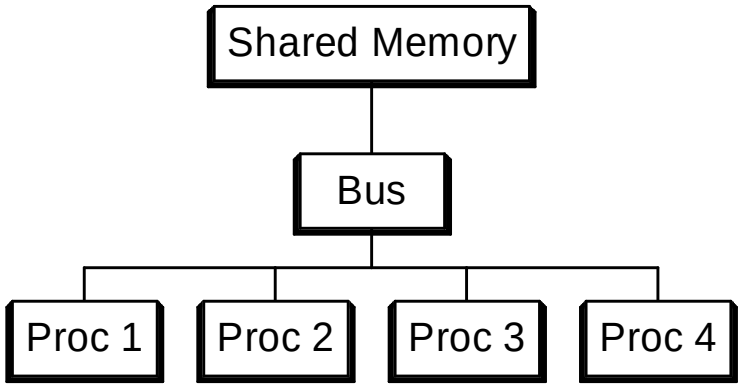

Figure 4.2: Schematic diagram of symmetric multiprocessor computer.

which divide the load among the processors. Multiple fork-join regions may exist. The main concern when using OpenMP is proper load balancing so that no processors remain idle during the parallel section. The main benefit of OpenMP is that it is often easier to implement in comparison to other parallel directives such as MPI but it is much harder to write scalable programs (i.e., programs in which the execution time scales with the number of processors). The disadvantage of using MPI is that memory has to be transferred between processors. When large data structures exist, the time required to pass information between processors (communication time) often supersedes the potential benefit of the parallel algorithm.

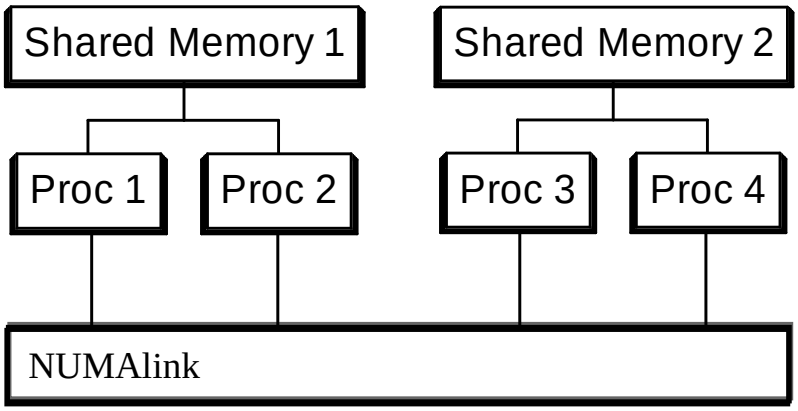

Figure 4.3: Schematic diagram of NUMA architecture computer.

4.1.3 Past contributions

Studies considering parallel discrete element simulations were conducted for two-dimensional problems by Jr. and Konduri (2001), Schafer et al. (2002), and Hustrulid (1995) and in three-dimensions by Henty (2000) and Zhao (1997).

Jr. and Konduri (2001) developed a parallel version of a discrete element technique used at NCSU and Los Alamos National Laboratory used for studying energetic materials and shock phenomena. The two-dimensional simulations use circular elements and employ a spatial decomposition algorithm in order to parallelize the code. A speed-up of about five was observed for simulations conducted on a distributed memory system (cluster) of eight processors with 100,000 elements. Schafer et al. (2002) also used two-dimensional circular discrete elements to test the effectiveness of using

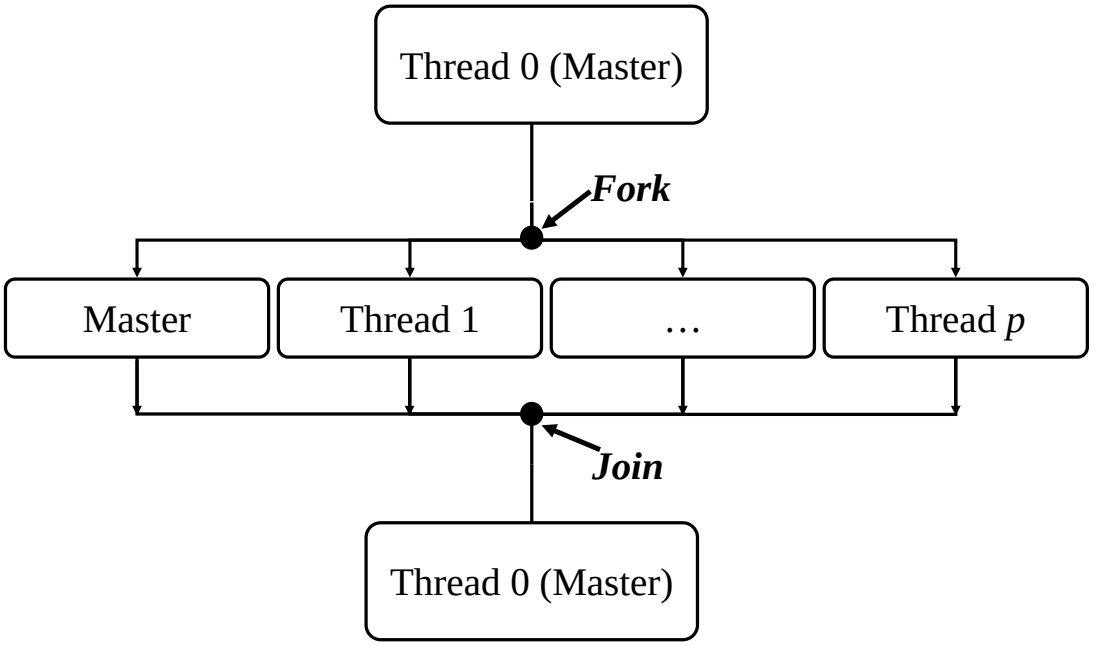

Figure 4.4: Schematic diagram of FORK-JOIN model.

Field Programmable Gate Arrays (FPGA) on a single CPU. These devices allow the user to form FPGA-based co-processors which may be used to simulate multiple processor parallel computers. A spatial decomposition algorithm was used to obtain a speed-up of approximately 30 using 1500-2500 elements with ideal speed-ups in the range 50-100. Hustrulid (1995) used circular discrete elements and a parallel algorithm based on spatial decomposition to obtain a speedup of nearly eight times on a 32-processor distributed memory computer. He noted that communication seemed to be the limiting factor in his study which would be further magnified by an extension to three dimensions.

Henty (2000) discusses the advantages/disadvantages of message passing versus shared memory parallelism in his discrete element simulations, since load balancing using the two sets of parallel directives is quite different. A hybrid model was also constructed

for use on an SMP cluster, but performed poorly in comparison to the MPI version. On a single shared memory computer, it was concluded that OpenMP will perform better than MPI in three dimensions.

Zhao (1997) (see also Hashash (2006)) used OpenMP to implement a parallel version of DBLOKS3D on the NCSA supercomputers. Their algorithm was based again on a spatial decomposition of the domain in which particles were grouped into boxes. Updating and purging of arrays was necessary to maintain compatibility between the boxes. The results indicated a maximum speed-up of nearly 3.7 on 32 processors of a NUMA-based system for 60,000 elements. Zhao (1997) claimed that standard domain decomposition techniques were not effective in the parallelization of the code and that better load balancing was required. The purging of arrays was the main drawback to the algorithm, since it had to be performed in serial.

4.2 Parallel Algorithm

OpenMP will be used to implement a parallel version of DECICE. Simulations are conducted on a 52-processor shared memory SGI Origin 3000 series computer, a powerful multi-processing system built upon the NUMA architecture, maintained by the Faculty of Mathematics at the University of Waterloo.

With the data arrays existing in DECICE, a complete domain decomposition and purging of arrays (as in Zhao (1997)) would require extensive code redevelopment and hence is not suitable. The algorithm developed in this thesis is a combination of the domain, object-oriented, and perfectly parallel approaches to high performance computing. The domain decomposition technique is used during the initial contact phase of the algorithm and an object-oriented/perfectly parallel decomposition is

used elsewhere. Dynamic binning of the domain is achieved using two methods: (i) a user specified arrangement of bins and; (ii) a parallel recursive coordinate bisection algorithm based upon the location of element centroids. The user-specified binning algorithm reads the required number of bins in each coordinate direction from the user. Allowable divisions entered by the user must be a power of two, i.e. 2^p where $p = 1, 2, 3, ...$ Binning in a single coordinate direction is accomplished by dividing the current span of that direction into equal parts. The total number of bins may be obtained by multiplication of the number of bins in each direction. For systems of particles which are densely packed, this algorithm should be able to achieve adequate load balancing, but when sparsely distributed assemblies of particles are modeled, a more efficient binning scheme must be used. Particular details of the second algorithm which use the location of the element centroids to partition the elements into bins will be discussed later.

4.2.1 Parallel algorithm during contact detection

The contact detection algorithm within DECICE consists of three stages:

1. sort the elements into boxes/bins;
2. check axis-aligned bounding boxes (AABBs) for proximity search;
3. apply modified FCP algorithm to resolve true contact.

A domain decomposition technique is applied to stages 1 and 2 to perform parallel calculations over the bins and check proximity using AABBs (see Figure 4.5). During the first stage, each thread processes a single bin at a time with additional bins being considered when a processor becomes available. Load balancing amongst processors will depend on the binning configuration. During the proximity search, using the

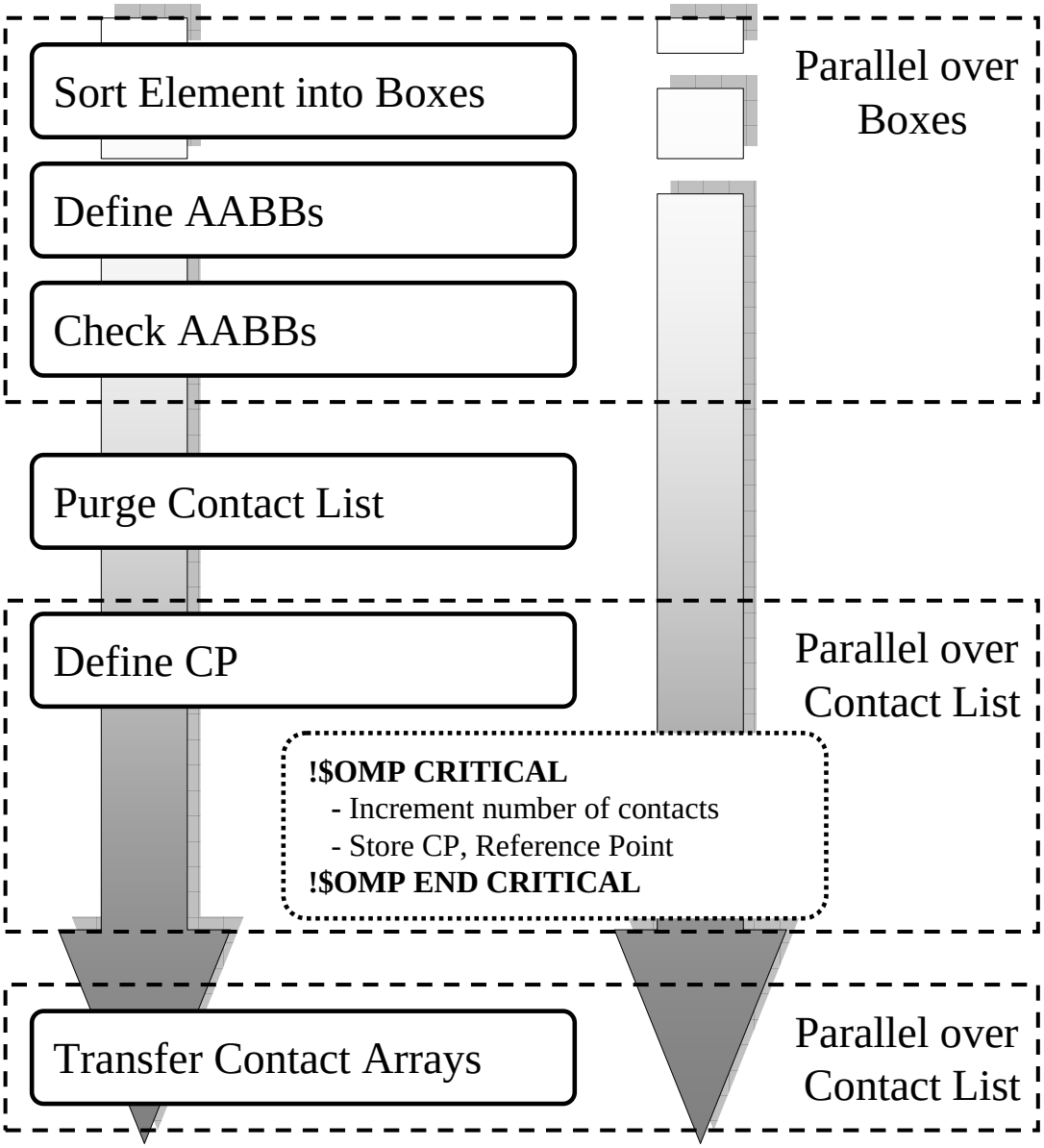

Figure 4.5: Parallel scheme applied during stages 1 and 2 of contact detection scheme

AABBs, potential contacts may be checked simultaneously by more than one processor.

The first two steps create a refined contact list which is then combined and traversed in parallel in stage 3. Instead of having local storage arrays on each processor, a global data structure is updated in a critical region when a true contact is identified. Only one processor at a time may enter the critical region. A flag is used within the critical region to ensure that a potential contact pair is only recorded once in the final contact list, removing the need to purge the contact list array after this stage is complete. This is not optimal but data structure purging, which was considered a main drawback of the algorithm of Zhao (1997), is the other alternative when implementing such a scheme.

Note that the critical region is only entered when stage 3 of the contact detection algorithm is reached. A smaller refined list exists at this point in comparison to the original list as a result of the multi-tier implementation of the contact detection scheme. Then the number of contacts is updated and the geometry of the contact (common plane normal and reference point) is stored within the critical region. The pointers to contact force addresses are updated in parallel using a previous copy of the global data structure in the final step.

4.2.2 Parallel algorithm during solution scheme

The solution scheme consists of three main stages. Rigid body motion and deformation are first calculated based upon the governing equation. The decoupled form of these equations makes the solution scheme ideal for parallel calculations. Stresses are computed in the next stage based upon constitutive relationships and data available from stage 1. Interaction forces are updated in the final stage using the standard

spring-dashpot model as discussed previously.

A flowchart depicting parallel version of the solution scheme is depicted in Figure 4.6. Stages 1-2 of the algorithm are parallelized over the number of elements. In stage 3, the obvious extension is to parallelize over the contact list which consists of pairs of elements. Parallel calculations over the contact list would generally result in a race condition when trying to update the applied force at the centroid of an element. For example, thread 0 (processing the contact of element 1 and 2) may be updating the force at the centroid of element 1, while, at the same time, thread 1 (processing the contact of element 1 and 3) is attempting to update it, which results in a race condition. To avoid this situation, parallel calculations in this stage are performed over the individual entries in the contact list. The result is that a single contact (eg., element 1 and 2) is processed twice - once to resolve the force for element 1 and once for element 2. This requires additional processing effort but removes the race condition.

The data structure implemented within the new contact detection scheme of DECICE allows for the separation of *resolving* and *updating* the forces. The calculated interaction forces for each contact are therefore *resolved* in parallel over the contact list, and then the global forces applied to the element centroid are *updated* in parallel over the elements which occur in the contact list. That is, in the latter step, each processor considers a single element at a time and traverses the contact list to determine net element centroid force.

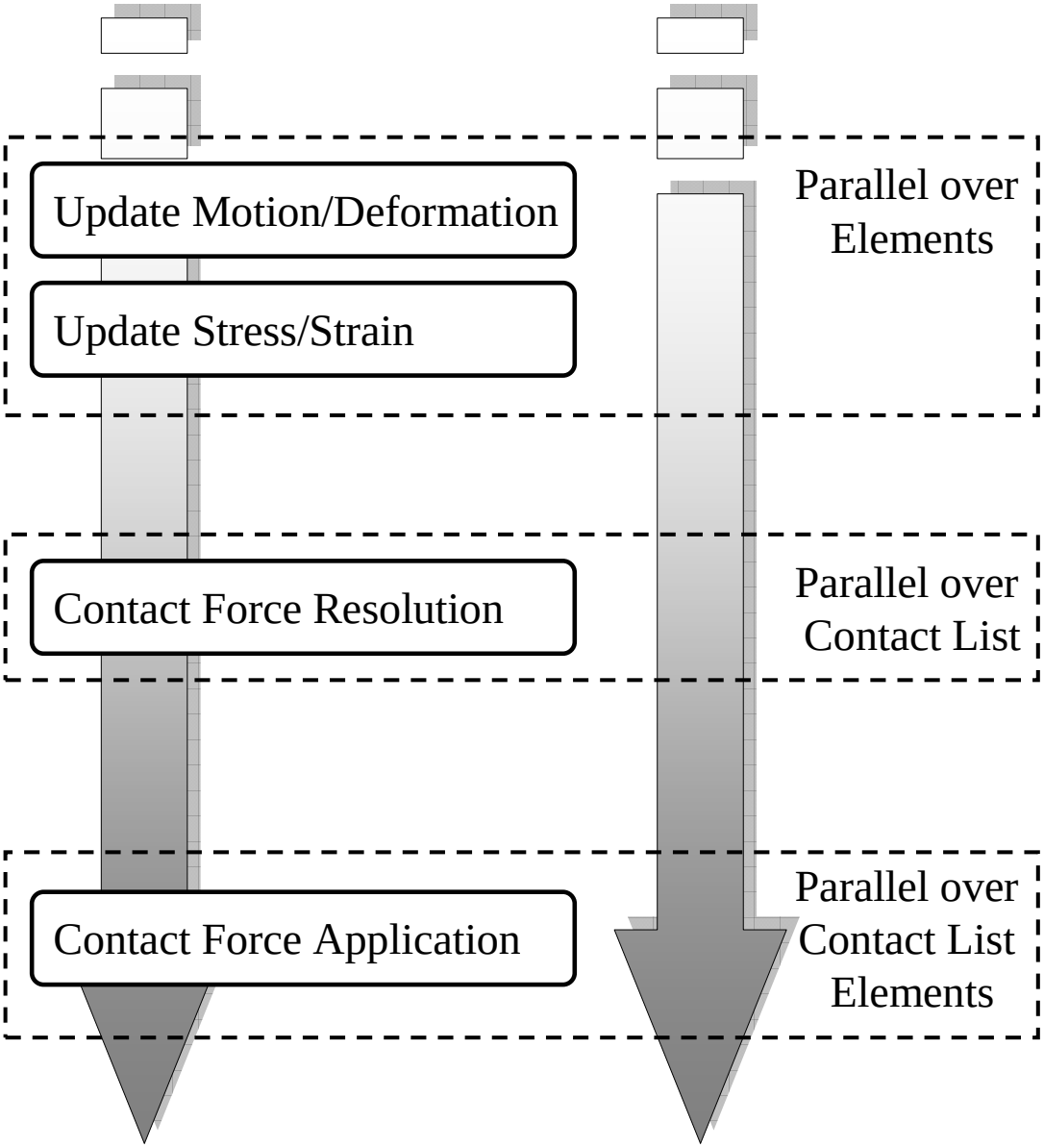

Figure 4.6: Parallel scheme applied during solution scheme

4.3 Results and Discussion

The result of implementing the parallel algorithm outlined in this chapter within DECICE is discussed in this section. A model consisting of a 25cm x 20cm box below a number of randomly generated cubic elements (8-nodes) uniformly distributed throughout the domain is used to test the parallel algorithm. The average dimensions of the randomly generated elements are 2cm by 2cm by 2cm. Timing results are recorded using in-code constructs for 30,000 time-steps. Execution time is measured from post-geometry construction to the end of the simulation. Calls to I/O routines are minimized by setting the output frequency large. The actual number of elements is five more if the box base and four sides are included, but for the purposes of this study the number of randomly generated elements is referenced. To obtain times which are independent of contact tolerances and time-steps, the complete contact detection algorithm is called at every time-step. Since this portion of the code typically dominates the bulk of the computational effort of discrete element method and the solution scheme is expected to be perform better (since it is nearly perfectly parallel), these results are expected to be representative of true execution times.

4.3.1 Speed-up results

The speed-up results for DECICE using a single bin during stage 1-2 of contact detection are shown in Figure 4.7 for 100, 500 and 2000 elements. The measured speed-up is 6.6 for 100 elements, 4.8 for 500 elements, and 2.2 for 2000 elements on 16 processors. When using only one bin, the first two steps in the parallel implementation of the contact detection algorithm (sorting and proximity search) are essentially negated, since it executes in parallel over the bins. The effect of the single bin, as expected, is magnified for a greater number of elements, since more time is spent performing the sorting and proximity search in serial. Note that a single bin is equivalent to having

no spatial or domain decomposition during the sorting/proximity search stages of

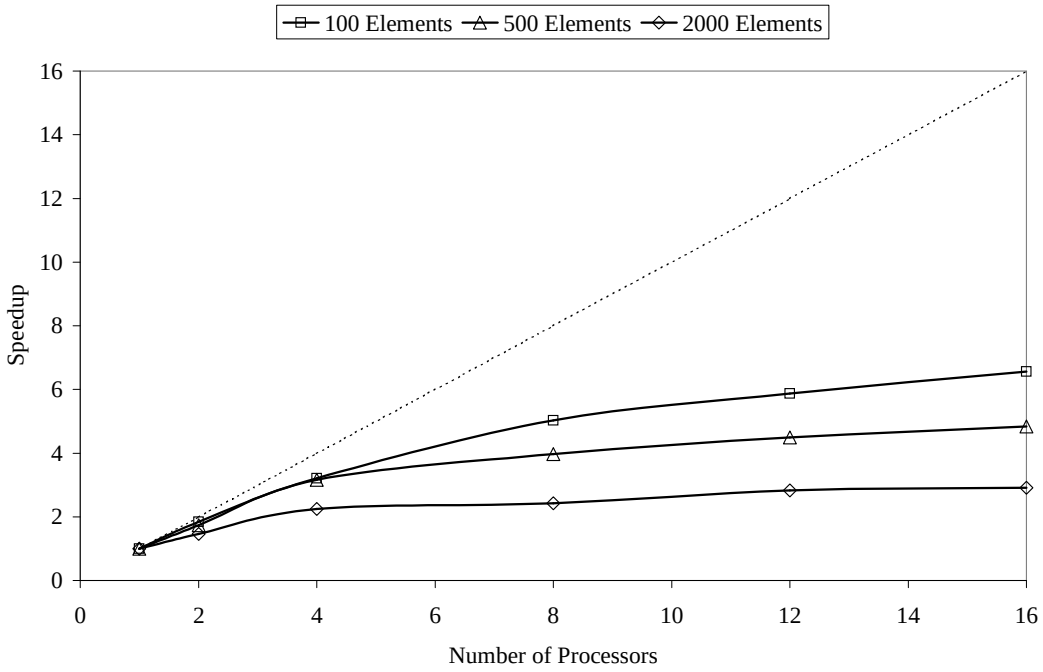

Figure 4.7: Speed-up results for 100, 500, and 2000 elements when using only a single bin (i.e., contact detection stage 1 and 2 are executed in serial).

contact detection, since these stages execute in parallel over the bins.

The effect of the number and direction of the spatial decomposition (i.e., bins) is investigated by varying the number of bins in the x- and y- directions from 1 to 2 and in the z-direction from 1 to 16 for the 2000 element case. The simulations conducted are arranged into groups according to the total number of bins and listed in Table 4.1.

The effect of the binning is first exhibited in Figure 4.8 by the super-linear performance (speed-up is greater than one) of the algorithm on two processors. Division of the space into bins distributes the number of elements between processors and hence the number of element-to-element proximity searches is reduced, leading to the

Simulation Group (# of Bins)	x-y-z Decomposition
1	1-1-1
2	2-1-1; 1-2-1; 1-1-2
4	2-2-1; 2-1-2; 1-2-2; 1-1-4
8	2-2-2; 1-2-4; 2-1-4; 1-1-8
16	2-2-4; 2-1-8; 1-2-8; 1-1-16

Table 4.1: Simulations are grouped in numbers according to the total number of bins utilized in sorting/proximity search sections of the contact detection algorithm.

increased performance. With perfect load balancing and ideal problem geometry, the number of proximity searches would reduce from nearly two million to nearly 500,000 - a factor of four. As the number of processors increases, the speed-up growth slows significantly, since the remaining processors are idle during this stage. A maximum speed-up of 5.7 is observed on 16 processors when using two bins in the vertical direction.

Figures 4.9-4.11, in which simulations use four or more bins, depict a similar super-linear performance of the algorithm on 2-4 processors. The maximum speed-up is 9.1 for four bins (1-1-4 case), 11.5 for eight bins (1-1-8 case), and 12.6 for 16 bins (2-1-8 case) on 16 processors. Since the elements are uniformly distributed in the region above the rectangular box and the vertical range of elements is largest, division of the domain in the vertical direction typically produces the best speed-up results. As the number of bins increases, however, the difference in the binning orientation becomes less pronounced. In the case of 16 bins, for instance, all sets of bin divisions yield a speed-up of 12.0 or greater (except the 2-2-4 division, which yields a speed-up of 11.1).

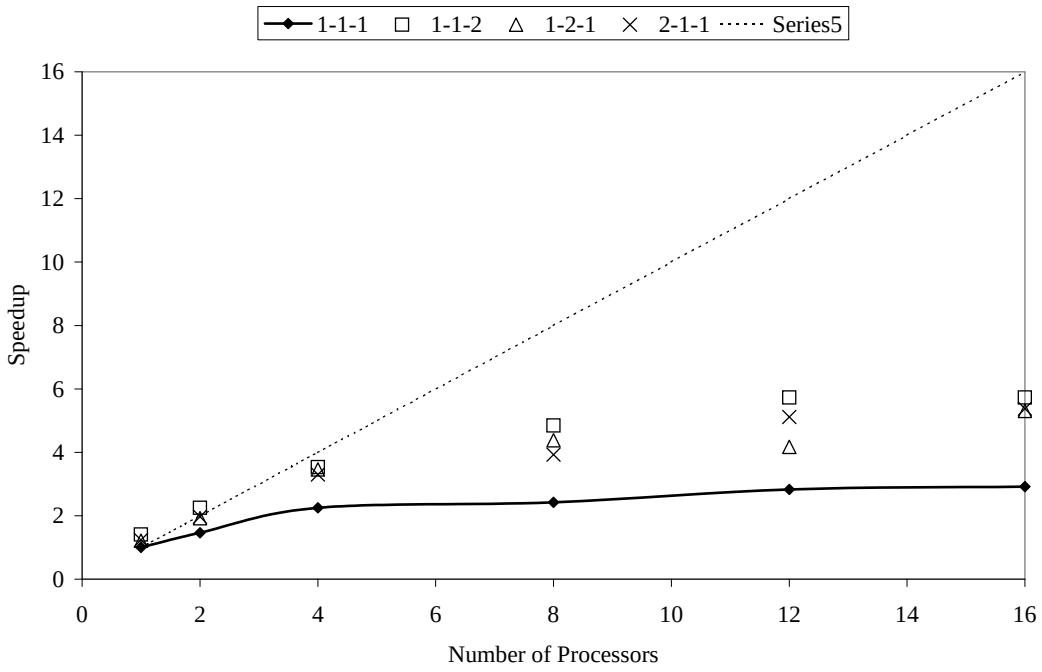

Figure 4.8: Speed-up results for 2000 elements using the two-bin grouping with different orientations. The speed-up with one bin and the 1-1 line is shown for comparison.

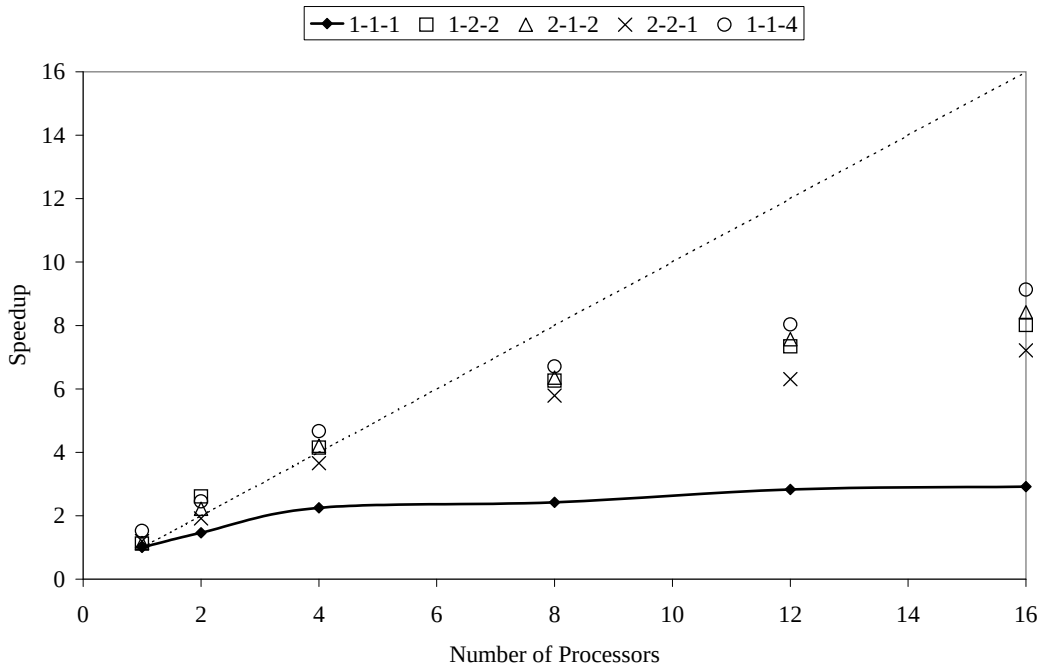

Figure 4.9: Speed-up results for 2000 elements using the four-bin grouping with different orientations. The speedup with one bin and the 1-1 line is shown for comparison.

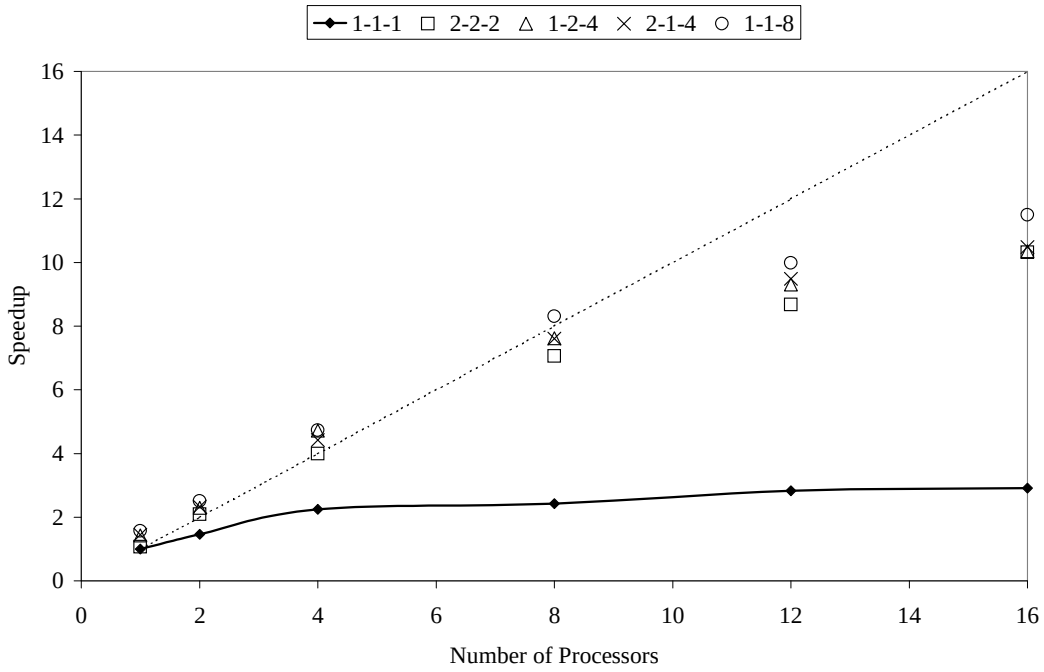

Figure 4.10: Speed-up results for 2000 elements using the eight-bin grouping with different orientations. The speed-up with one bin and the 1-1 line is shown for comparison.

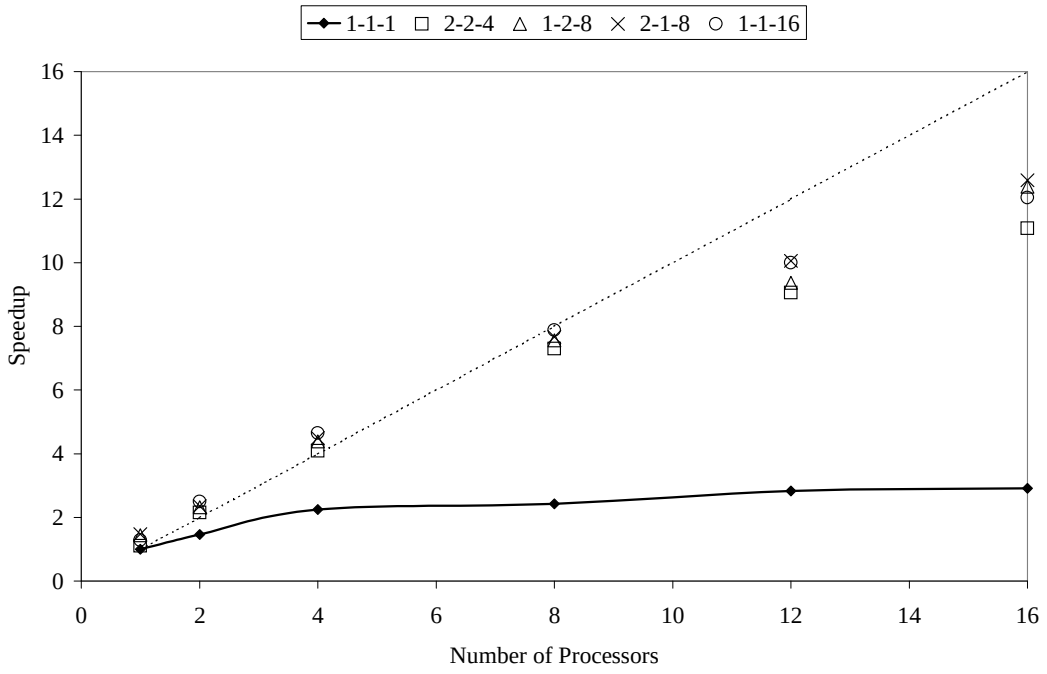

Figure 4.11: Speed-up results for 2000 elements using the 16-bin grouping with different orientations. The speed-up with one bin and the 1-1 line is shown for comparison.

4.3.2 Scalability

To investigate where the speed-up originates from and determine whether serial calculations account for the overall sub-linear growth, the execution time of individual parallel sections is measured for the simulation involving 2000 elements. Since domain decomposition in the z-direction yielded the maximum observed speed-up in general, the simulations are arranged so that the domain is divided into p-bins in the z-direction on p-processors. For example, on eight processors, the domain is divided into eight bins in the z-direction. For referencing purposes, the total time is recorded during the following parallel regions:

- Contact Stage 1-2: includes the domain decomposition and proximity refinement using AABB;
- Contact Stage 3: includes application of the modified FCP algorithm to the refined contact list and updating of old (previous time step) contact arrays;
- Force Resolution: includes the time required to resolve the contact geometry, compute incremental normal and shear components of the force, and update the element centroid based upon these interaction forces;
- Motion: includes the time exhausted during the calculation of rigid body motion and deformation; and
- Stress: includes the time exhausted during stress calculation.

The results which follow make reference to these individual sections.

The bulk of the computational effort, approximately 80-90 percent, is focused during the contact detection stage as shown in Figure 4.12. This figure shows a bar graph depicting the time spent in each of the parallel sections per 300 time-steps. Figures

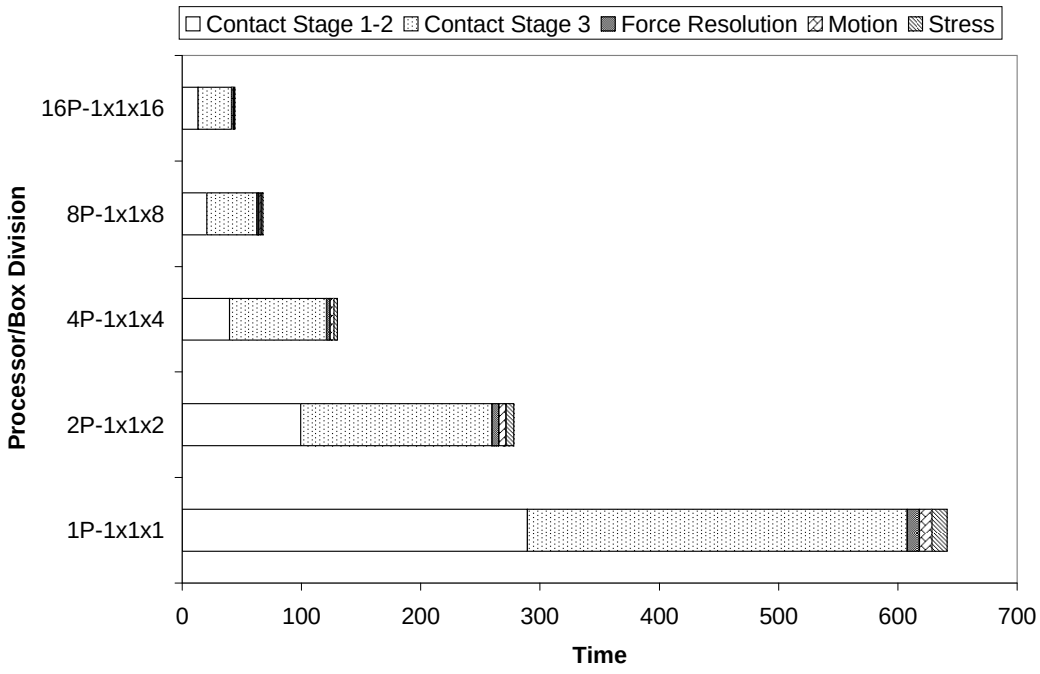

Figure 4.12: Total time during each parallel section for each simulation with binning 1-1-p on p-processors.

4.13-4.14 display the individual speed-up results of each of the parallel regions as the number of processors and spatial subdivisions is increased. A significant speed-up

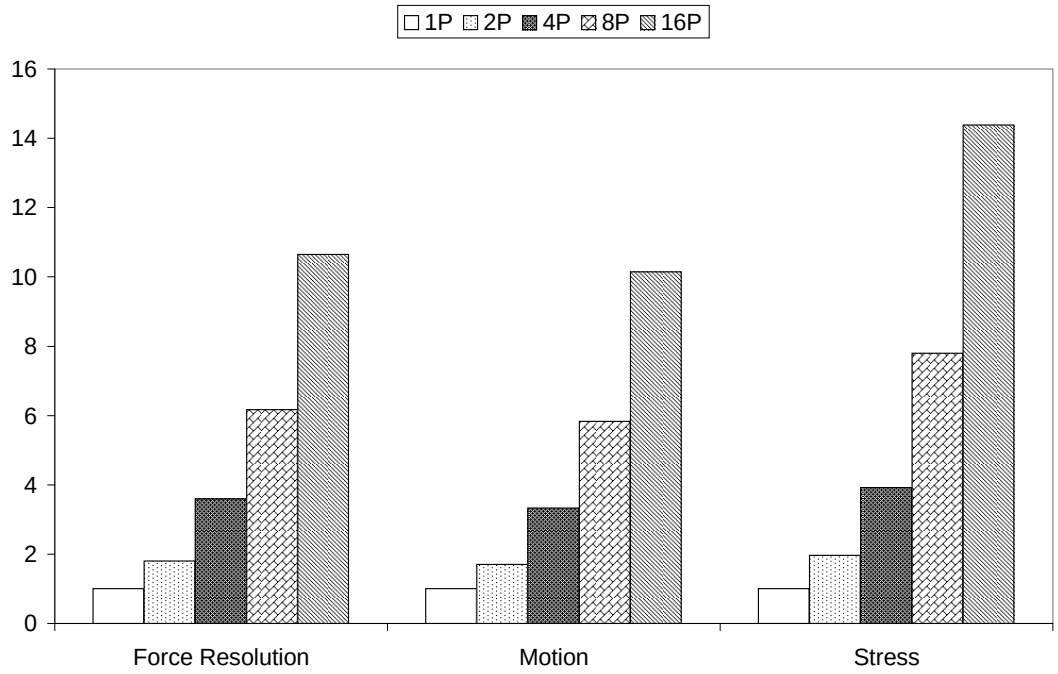

Figure 4.13: Speed-up by component of solution scheme.

is observed for the calculation of stresses, rigid body motion/deformation, and force resolution sections as the number of processors increases (Figure 4.13). The stress calculation speed-up is nearly ideal (14.4 on 16 processors) and the speed-up during the force resolution and motion stages are also significant (>10 on 16 processors).

This large gain in performance is expected for the stress and motion sections since they are parallelized over the number of elements. The force resolution and update stage also performs quite well when the resolution stage is performed in parallel over the contact list followed by the updating of the contact forces in parallel over the number of elements (eliminating the race condition).

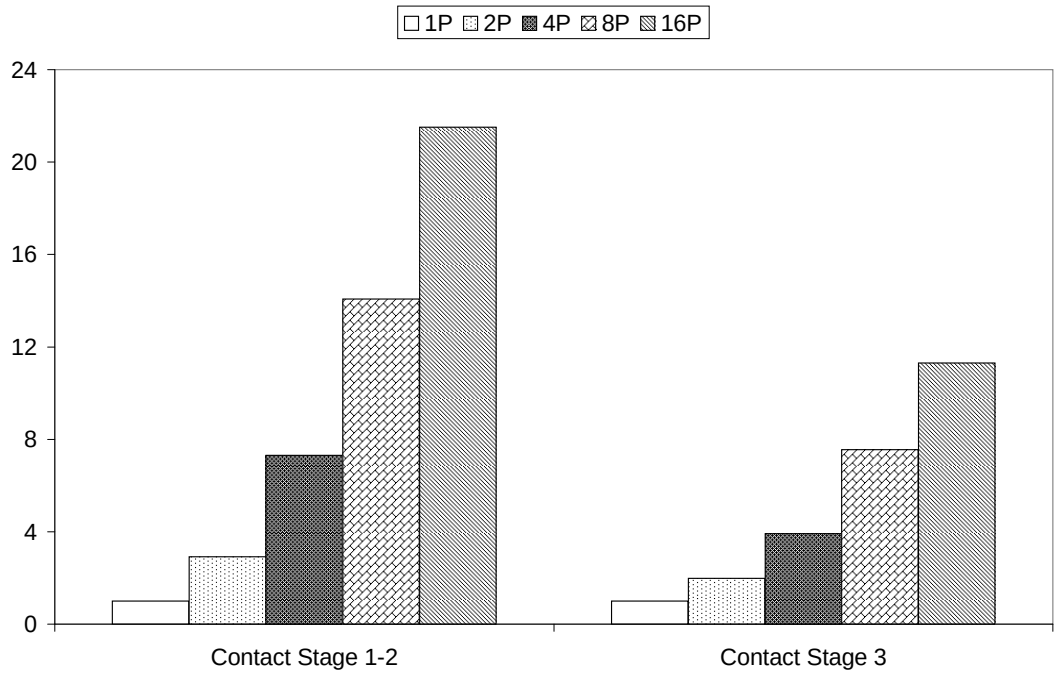

Figure 4.14: Speed-up by section of contact detection algorithm.

The stress and motion calculations do not result in ideal speed-up as a result of the storage arrangement associated with the NUMA architecture. Most physical quantities within DECICE are housed in large global storage arrays. The time required to access a particular instance of data depends on the location of that entry with respect to the processor requesting it. If the data is not local to the requesting processor, the local memory of a different partition must be accessed through the NUMAlink bus, resulting in slightly less than ideal speed-up results.

The speedup during Contact Stage 1-2 is super-linear, as alluded to earlier when including the effect of the binning. When the simulation is conducted on 16 bins for all processors, the results show (see Figure 4.15) that the binning accounts for approximately half of the measured speed-up and the parallel implementation the other half.

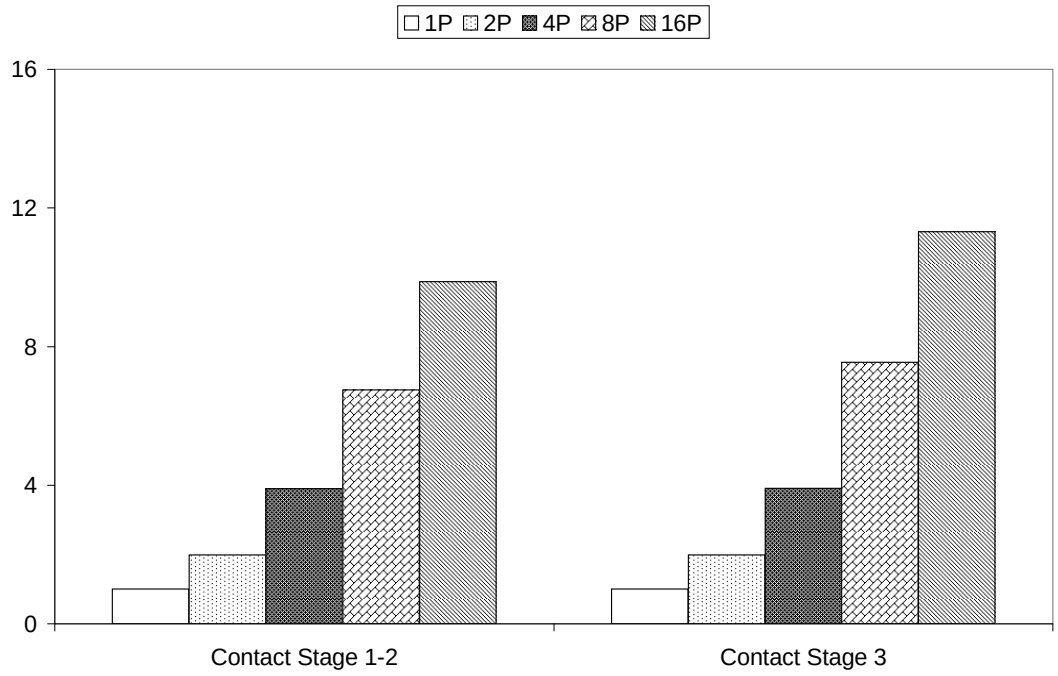

Figure 4.15: Speed-up by section of contact detection algorithm using 16 bins on all processors.

The parallel implementation of the modified FCP algorithm during Contact Stage 3 also performs well, as it is essentially ideal on two and four processors and reaches a value of nearly 12 on 16 processors. The effect of the critical section directive during this stage is therefore minimal when using 2000 elements due to the multi-tier implementation of the contact detection scheme. Using the user-specified binning and proximity search (with AABBs), the list of potential contacts is significantly reduced before entering employing the FCP algorithm. As a result, the competition between processors during the critical section of the FCP algorithm is minimized.

4.4 Load Balancing - Dynamic Binning

The orientation and number of bins used during the sorting and proximity search sections of the contact detection algorithm is important in the efficiency of the parallel algorithm. Proper division of the domain into bins is necessary to maintain load balancing amongst the individual threads. In the current simulations, the domain was divided into uniform bins depending on the grid specified by the user, and hence improper load balancing can occur for problems involving a non-uniform distribution of elements.

A procedure for dynamic binning of the domain is implemented in parallel, based upon the recursive coordinate bisection (RCB) algorithm using element centroids. The user specifies the number of bins for the simulation but the orientation of the bins is determined in parallel dynamically during the execution of the DEM. The procedure for dividing a single bin into two based upon centroid location is as follows:

1. From element centroids, select the coordinate direction which spans the largest distance - this will be the direction of the division.

2. Using this coordinate direction, find the median location (the coordinate which divides the bin so that half of the values are below and half the values are above the plane with normal direction determined in step 1);

3. The current bin is divided into two bins using the median value. These bins may be further divided by repeating steps 1-3.

In this way, load balancing across the threads is achieved by keeping the number of elements in each bin as close as possible (duplicate elements lying on the boundary may still result in non-equal numbers of elements in each bin). The above procedure can only be applied when the number of bins is a power of two, since the median is utilized. This may be modified to split a single bin into more than two bins if required but not implemented in this study. Using this algorithm, non-uniform and multi-directional bins are created to ensure load balancing across the threads.

Simulations are conducted for two configurations: the configuration discussed in previous section, and a slightly modified problem in which a single additional element is positioned above the randomly generated elements. If the distance from the lower containment box to the highest random element is X, then the distance to this new element is 2X. Thus, dividing the spatial domain equally into two bins without regard for element locations would leave a single element in the top bin and the remaining 2000 elements in the lower bin. The speed-up results for Contact Stage 1-2 using two, four, eight, and 16 bins are shown in Figures 4.16-4.17 for when employing the equal and dynamic binning approaches, respectively. Other stages are not included in the presented results, since they are all parallel over loops/lists which are independent of the bin-size and orientation. In the first set of simulations (Figure 4.16), the distribution of elements is uniform so the equal binning strategy performs better.

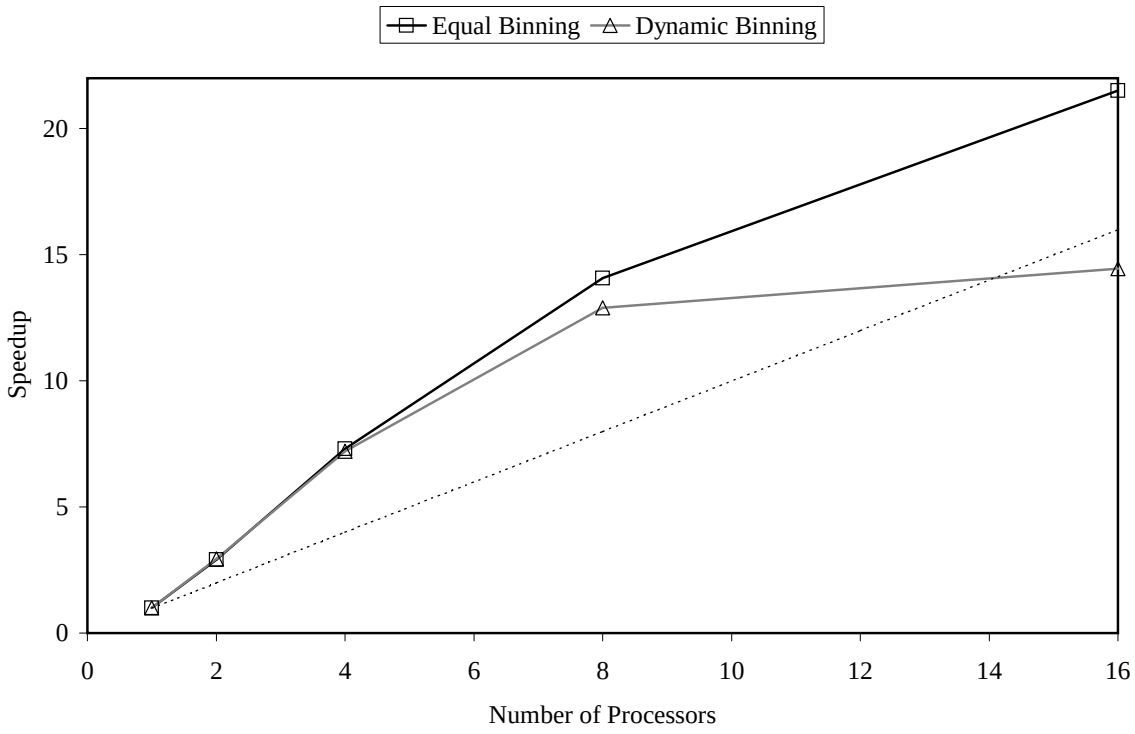

Figure 4.16: Speed-up results during Contact Stages 1-2 for problem configuration with 2000 elements using equal and dynamic binning.

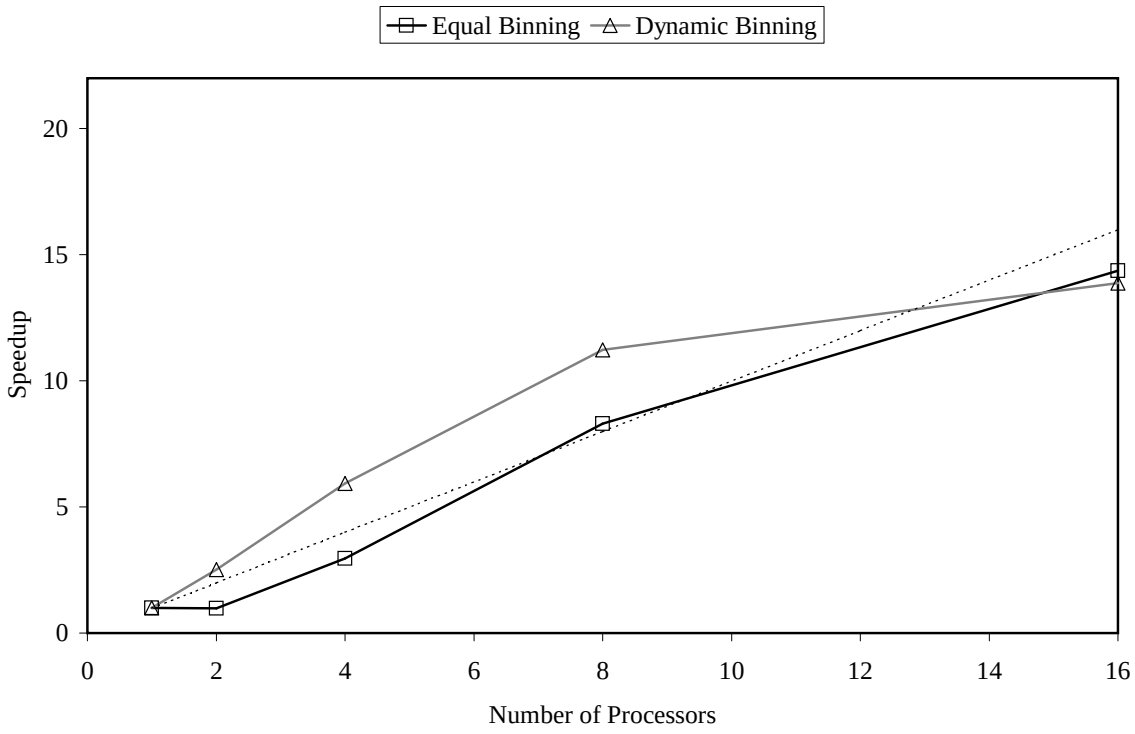

Figure 4.17: Speed-up results during Contact Stages 1-2 for problem configuration with 2000 + 1 elements using equal and dynamic binning.

This is due to the extra computational effort required to define the binning configuration using the recursive coordinate bisection algorithm as the number of processors increases; the work is minimal in the equal binning case. For the second set of simulations, the dynamic binning approach in general yields better results. The equal binning algorithm executes at approximately the same speed on two processors as on a single processor as indicated by the constant speed-up observation in Figure 4.17. This was expected, since the lower 2000 elements are being processed using only a single processor.

The number of processors working on the lower 2000 elements lags behind the dynamic binning approach by a factor of two due to the geometric configuration. For instance, when eight processors are used, only four of them are actually working and four remain idle in the upper half of the domain, leading to a speed-up comparable to the dynamic binning approach on only four processors. Load balancing can therefore become a major issue using the equal binning approach when simulations involve clusters of dense particles. In this simulation, as the number of processors increases to 16, the extra effort required to define the 16 bins outweighs the improvement it offers over the equal binning algorithm, but this is partly due to selected problem geometry.

4.5 Summary

Computational resources and execution times often limit the size of simulations which can be conducted using discrete element method. The goal of this chapter was to present an algorithm which extends the capabilities of DECICE to a multiprocessor system. The target platform was an SGI Origin 3000 series computer located at the University of Waterloo.

Simulations conducted indicate that a speed-up of approximately 12 can be expected on 16 processors with proper domain decomposition. Load balancing is achieved via a parallel dynamic binning scheme derived from the recursive coordinate bisection algorithm. This binning scheme yields super-linear performance overall in comparison to execution times where no binning is used for a low number of processors. Even with the effect of binning removed, an overall speed-up of 10 is still achieved. Results also indicate that serial portions of the DECICE code account for an additional 2-15% of total simulation time (not including the serial portions which exist in the parallel implementation of contact detection algorithm or the I/O routines). Future improvements of the DECICE code should focus on improving these regions as well as the storage structure to allow for an investigation of distributed memory multi-processor systems.

PART II. EXPERIMENTAL AND NUMERICAL CONTRIBUTIONS TO ICE-STRUCTURE INTERACTION

Chapter 5

Problem Set-up and Relevant Literature

5.1 Introduction

This chapter marks the transition from discrete element considerations in Part I of the thesis to the application problem. Comfort et al. (1999) state that numerical analysis is the next step in understanding the behavior of the Kulluk drillship in various ice conditions. The Kulluk was originally designed in the 1970s and has proven so effective that it was recommissioned in 2006 to drill three more wells in the Beaufort Sea.

Due to the success of the design, there have been several experimental attempts at modeling the structure. The large amounts of full-scale data from onboard measurements have further motivated these studies. This chapter presents a description of the mechanical properties of the full-scale ship and ice conditions. A discussion of the expected failure modes and associated forces on platforms with a similar shape is presented along with a review of empirical and experimental observations.

Figure 5.1: Artist conception of the Kulluk drillship as seen in Bonnemaire et al. (2007).

Three model scale experiments conducted in the past three decades (Nixon and Ettema, 1987; Wessels and Iyer, 1985; Comfort et al., 1982) are discussed as well the key results from a full-scale data source (Wright, 1999). These four sources of Kulluk data will serve as the necessary base from which to compare the results from a 1:40 scale model test conducted at the NRC Institute for Ocean Technology and the numerical predictions of DECICE.

5.2 Problem Description

An artists' conception of the Kulluk drillship from Bonnemaire et al. (2007)is shown in Figure 5.1. It has a deck diameter of 81 meters and a waterline diameter of 70 meters. Other key mechanical properties are summarized in Table 5.1. The drillship was moored via an axisymmetric system of up to twelve 3.5 inch cables. A typical

Property	**Value**
Overall beam (m)	81
Waterline beam (m)	67.9
Beam at bottom (m)	62
Depth (m)	18.4
Draft (m)	11.5
Slope at waterline (degrees)	31.5
Displacement (kg)	27999000
Vertical center of gravity (m)	13.2
Vertical moment mass (kg·m)	14.4092×10^9

Table 5.1: Mechanical properties of full-scale Kulluk drillship.

configuration of the mooring lines is shown in Figure 5.2. The water depth at the seven drilling locations which were recorded was 25-50 meters and properties of a typical mooring configuration are given in Table 5.2. Ice conditions in the area included ice ridges, large floes, pack ice, and unbroken level ice. Due to icebreaker support, unbroken level ice was rarely encountered, but all instances of such events were recorded.

This research presents the results of a 1:40 model scale experiment of the Kulluk conducted at the NRC in Chapter 6. The precise details of the model and test set-up will be addressed at that point. Chapter 7 presents the numerical setup of the problem using DECICE when the Kulluk drillship is moored and the incorporation of a numerical spread mooring algorithm.

5.3 Ice-structure Interaction

The goals associated with modeling ice-structure interaction are mainly associated with improving structural design by means of predicting ice loads. A wide range of purpose-specific structures are currently operating in harsh conditions. Various types of structures are identified in this section.

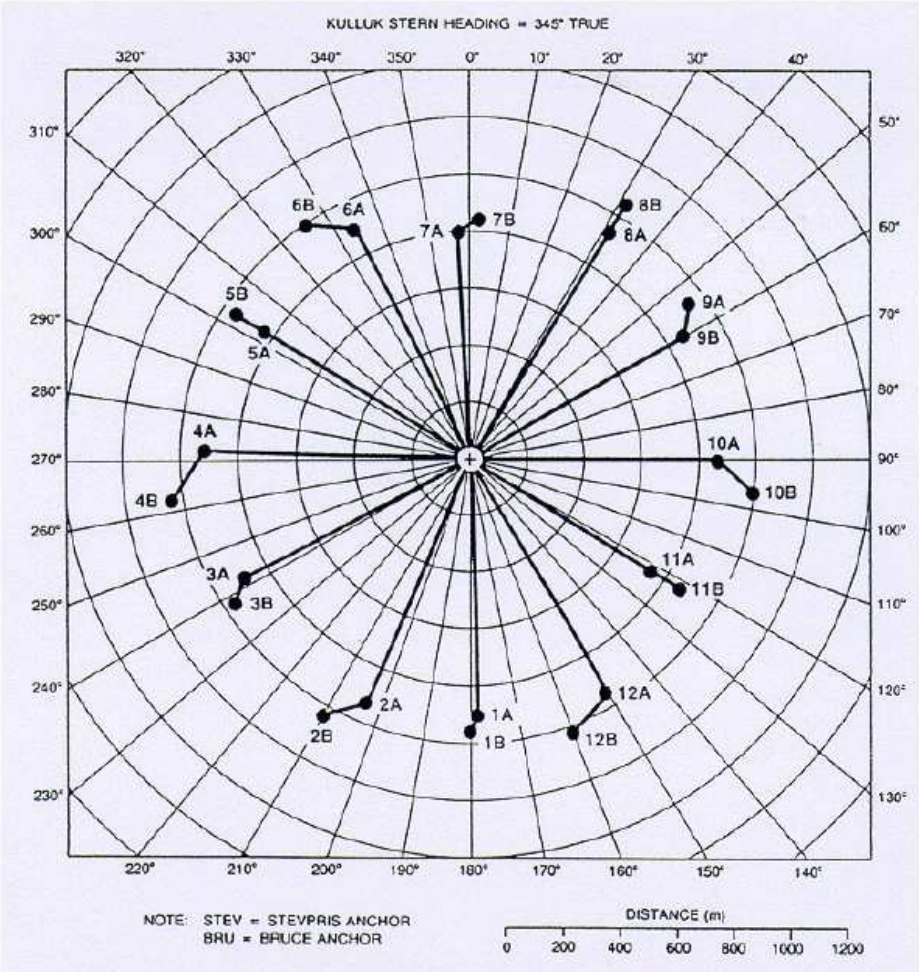

Figure 5.2: Typical configuration of the mooring system from Wright (1999).

Property	Value
Water depth (m)	32.0
Number of lines	9
Line diameter (in)	3.5
Line type	wire rope
Breaking strength (tonnes)	520

Line Number	Length (m)	Orientation (degrees)	Pretension (tonnes)
1	-	-	-
2	639	164	195
3	772	196	200
4	-	-	-
5	732	255	210
6	530	285	60
7	666	316	220
8	-	-	-
9	621	14	210
10	601	45	180
11	723	76	70
12	584	106	70

Table 5.2: Mechanical properties of typical mooring system.

Figure 5.3: Picture of an artificial island with a sandbag protected shoreline (from Timco and Johnston (2002)).

5.3.1 Types of offshore structures

Artificial islands, bottom-mounted structures, and floating structures are the three main classes of offshore structures. Each of these has advantages and disadvantages associated with its implementation, maintenance and operation.

Artificial islands exist in areas where shallow coastal areas (less than 10 meters) favor their construction (see Figure 5.3). It is difficult to construct these facilities further from shore, since a lot of maintenance is required to ensure that the island does not erode or break apart. They are, however, extremely resistant to ice forces.

Bottom-mounted structures are also quite resistant to ice loads, since they are fixed to the floor of the ocean (see Figure 5.4). They exist in many forms from conical to

Figure 5.4: Aerial photograph of Hibernia GBS off the Grand Banks of Newfoundland, a bottom mounted structure (from Hibernia (2009)).

cylindrical and may be constructed in deeper water (10-100 meters) than artificial islands. The type of structure used depends on the type and amount of ice anticipated at the drilling site.

For deeper waters (up to 2000 meters), floating structures are essentially the only economically viable option. These structures are susceptible to excessive ice forces and may only operate seasonally in harsh environments. In addition, the movement of the ice sheet may create instantaneous conditions where the structure must cease its drilling until a safe connection can be maintained. Drill ships, barges, semi-submersibles, floating caissons, and ice-mounted platforms are all examples of floating structures. Mooring these structures to the ocean floor via cables may also be possible in certain conditions to improve stability.

Forces on floating structures are dependent on both the particular design of the structure and the ice conditions encountered. The Kulluk drillship is a floating structure

dominated by an upward-sloping conical design at the point of impact. The benefit of the conical (sloped walls) design over the cylindrical (vertical walls) design is the resultant magnitude of the ice forces. Most of the modeling to date focuses on a downward-sloping design, but trends in failure modes are expected to be similar for an upward-sloping structure. The next sections present the results for downward-sloping structures, such as bridge piers, but the analysis can be extended somewhat to upward-sloping structures. It is also important to note that although the extensions can prove valuable in comprehending the ice interaction with these structures, the Kulluk platform is not completely an inverted cone. It is largest at its top and narrows towards the center to form the conical shape, but it flares out near the bottom of the structure to prevent ice pieces from moving beneath the structure (so that they do not interact with the mooring lines).

5.3.2 Modes of failure

Since bending failure dominates the ice-structure interaction for sloping structures, the type of conical ship is sometimes classified as either upward-breaking or downward-breaking (with respect the direction of ice failure). An upward-breaking design is a downward-sloping ship (or bridge pier) and vise-versa. This direction of breaking terminology is adopted for the remainder of the analysis when referencing the type of ship.

For vertical structures, ice fails in crushing, whereas for sloping structures, ice fails in bending. The type of failure and resulting ice load are also dependent on the size of the structure, since ice tends to build up around wider structures. Croasdale and Metge (1991) compare failure modes for narrow versus wide and vertical versus conical structures (downward-sloping). The study concluded that bending failure associated with sloping conical structures produces smaller forces on the structure than does

crushing failure. Due to the slope of the structure, ride-up may occur which then leads to adfreeze conditions that are generally non-existent for vertical structures. Special coatings may be adhered to the structure to prevent the bonding of the ice to the slope. As structures become wider, the advantages of these conical structures become less pronounced due to ride-up of large deposits of ice which carry significant loads (via its weight). Ice ride-up may even increase to the point where it contacts the deck of the drilling platform. An downward-breaking design as is used for the Kulluk drillship would eliminate these increased ride-up forces but are more susceptible to the formation of a rubble pile in front of the structure as pieces are pushed down and around the inverted cone.

5.3.3 Past analytical and empirical studies of inclined structures

The prediction of ice forces on inclined structures has been either empirically or analytically considered by Danys and Bercha (1975), Semeniuk (1975), Edwards and Croasdale (1976a), Ralston (1977), Croasdale (1980), Croasdale et al. (1994), Frederking et al. (1985), Nevel (1992), and Lau et al. (1999). The analytical methods are mostly based on assuming a beam or plate on an elastic base is subject to a vertical load at one of its ends. The vertical load causing bending failure is computed, which yields a corresponding peak horizontal load based on the geometric relationship together with ride-up and frictional forces for upward-breaking structures. Reviews and comparisons of physical data with analytical methods were presented by Sodhi (1987), Macellus et al. (1988), Cammaert and Muggeridge (1988), Sanderson (1988), Wessels and Kato (1989).

Ralston (1977) used a plastic limit analysis to predict the peak horizontal load on an

upward-breaking cone as

$$F_H = A_4 \left(A_1 \sigma_f h^2 + A_2 \rho_w g h D^2 + A_3 \rho_w g h (D^2 - D_T^2) \right) \tag{5.1}$$

where σ_f is the flexural strength, h is the ice thickness, $\rho_w g$ is the specific weight of the sea water, D, D_T are the diameter of the cone at ice impact and top, respectively. The constants A_1-A_4 are constants which depend on either the cone angle α or the parameter $\rho_w g D^2/\sigma_f h$, as discussed in Ralston (1977). For completeness of this discussion, these constants may be calculated as:

$$\begin{aligned}
A_1 &= \frac{1 + 2.711 x \ln(x)}{3(x-1)} && (5.2)\\
A_2 &= 0.075(x^2 + x - 2) && (5.3)\\
A_3 &= \frac{0.9}{4\cos\alpha}\left(1 + \frac{\mu}{\tan\alpha}\mathrm{Ell}_2(\sin\alpha)\right) - \mu\frac{0.9}{4\tan\alpha} f(\alpha,\mu) g(\alpha,\mu) && (5.4)\\
A_4 &= \frac{\tan\alpha}{1 - \mu g(\alpha,\mu)} && (5.5)\\
f(\alpha,\mu) &= \sin\alpha + \mu\cos\alpha \mathrm{Ell}_1(\sin\alpha) && (5.6)\\
g(\alpha,\mu) &= \left(\frac{1}{2} + \frac{\alpha}{\sin 2\alpha}\right) / \left(\frac{\pi\sin\alpha}{4} + \frac{\mu\alpha}{\tan\alpha}\right) && (5.7)
\end{aligned}$$

where $\mathrm{Ell}_{1,2}$ are complete elliptic integrals of the first and second kind and x is the solution of

$$x - \ln(x) + 0.0830(2x+1)(x-1)^2 \left(\frac{\rho_w g D^2}{\sigma_f h}\right) = 1.369. \tag{5.8}$$

From right to left, the terms in equation (5.1) represent the required breaking force, buoyant force, and clearing force for an upward-breaking conical structure. It was noted, however, that for a downward-breaking conical structure, the same analysis is valid when replacing ρ_w in the above formulae with $\rho_w/9$ to account for the difference in forces to submerge the ice into the water instead of lifting it out of the water. This provides a simple means by which to estimate the peak horizontal load analytically for a inverted cone, not the Kulluk design. The Kulluk design is a 31.5° downward-breaking conical structure at the point of ice impact, but its slope changes significantly

(eventually to 90° and then to −45° at skirt level) as the depth of the structure is traversed.

5.3.4 Past experimental studies of inclined structures

Experimental findings of failure processes and ice load events have been presented by Haynes et al. (1983), Wessels (1984), Kato (1986), Hirayama and Obara (1986), Clough and Vinson (1986), Maattanen (1986), Lau et al. (1988), and Lau and Williams (1991). As the ice sheet moves towards the structure, localized crushing occurs at the interface of the structure. This creates an interaction force normal to the structure face as well as a frictional component, since the ice is pushed upwards (or downwards) along the structure. The result is a complex three-dimensional stress state induced in the ice as it continues to advance around the structure. These internal ice stresses grow until failure occurs in the ice sheet in any combination of the following failure modes: bending, crushing, shear (compression), buckling or splitting. For upward-breaking structures, observations show that the bending mode of failure dominates the interaction under the following conditions: low inclination angle (10-60°), low ice-cone friction coefficient, small ice thickness, and low ice drift speed.

Flexural stresses govern the failure of sheets when it fails via bending. The two main types of bending cracks observed are radial and circumferential (see Figure 5.5). If the cone diameter is small in comparison to the ice thickness, radial cracks are observed at 60° intervals around the front of the cone. As the diameter of the cone increases, circumferential cracks dominate the failure mechanism with radial cracks appearing later. For both small and large diameters cones, the peak horizontal load develops during the circumferential cracking.

At increased speeds, inclination angle, ice thickness and roughness the failure mode

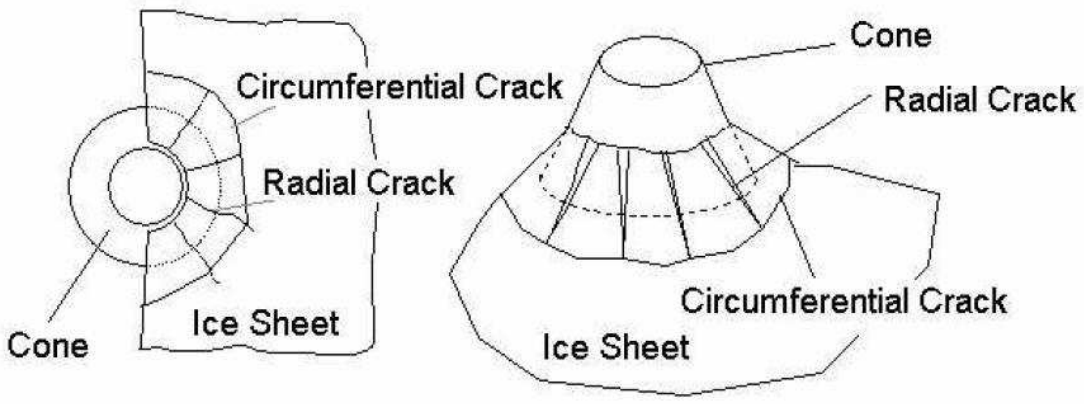

Figure 5.5: Formation of radial and circumferential cracks when ice fails via bending against an upward breaking structure (from Yan et al. (2003)).

may change abruptly to shear failure or crushing (Wessels, 1984). Haynes et al. (1983) showed that the velocity at which the transition from one failure mode to the other occurs increases with increasing inclination angle. For thin ice, circumferential cracks are observed at distances slightly greater than the characteristic length and for thick ice sheets, shear failure dominates (Maattanen, 1986). As the inclination angle grows to 75° and above, the ice sheet fails in crushing (Michel, 1978).

For upward-breaking structures, the broken ice pieces either get pushed up along the face of the structure (wide structures), referred to as "ride-up" or clear around the structure (narrow). When the ice rides up, it may roll back onto the pushing sheets and further complicate the interaction process through the development of a rubble pile at the front of the structure (see Figure 5.6). For downward-breaking cones, the gravitational effect is replaced by the buoyant force which acts to push the broken ice pieces up against the structure. As the ice is pushed downward and around the structure, the broken pieces may also roll back around and form a rubble pile front of the structure (with an appropriate hull shape). They may also get pushed

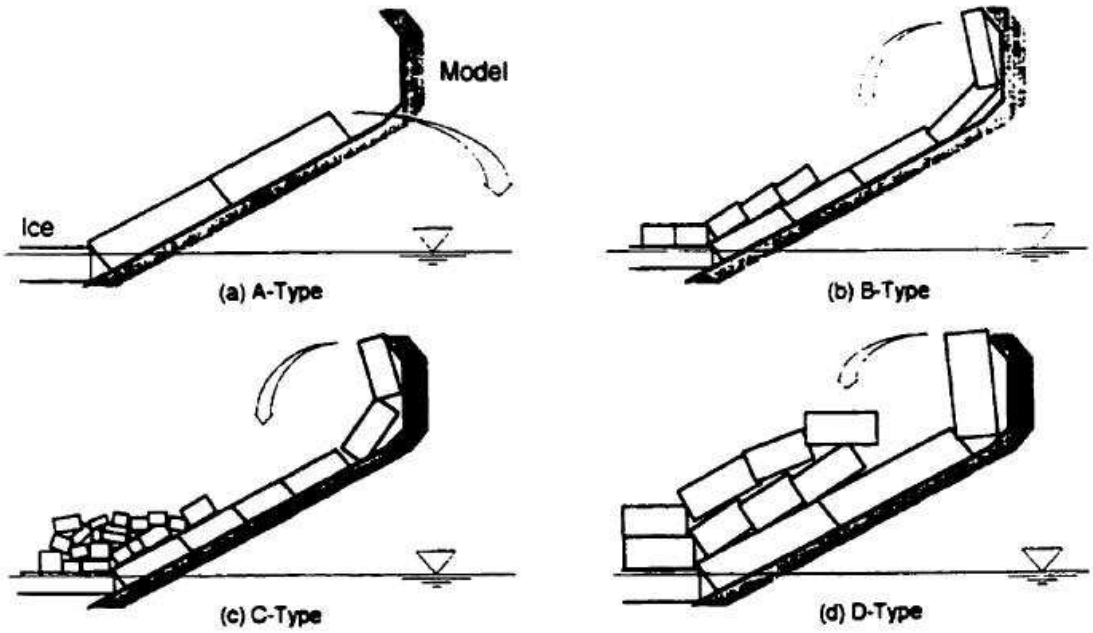

Figure 5.6: Formation of a rubble pile in front of the structure as the ice sheet advances (from Izumiyama et al. (1994)).

to the bottom of the structure where the pieces may interact with crucial equipment or mooring lines.

5.4 Ice Forces on Downward-breaking Conical Structures - Experimental Models

Previous experiments involving the dynamic moored response of a downward-breaking conical structure similar to that of the Kulluk in unbroken ice have been conducted at:

1. the Iowa Institute for Hydraulic Research , IIHR, (University of Iowa) by Nixon and Ettema (1987)

2. the Hamburg Model Ship Basin (HSVA, located in Germany) by Wessels and Iyer (1985)

3. the laboratory (in Calgary) of Arctec Canada Limited (ACL) by Comfort et al. (1982).

The IIHR conducted a series of tests on floating moored structures during this period on various other ice formations as well (rubble ice - Ettema and Matsuishi (1985b) Nixon and Ettema (1988); ice floes - Ettema and Matsuishi (1985a)) but the unbroken ice sheet experiment is of interest here. There experiment consisted of 42 tests involving a 1:45 scale model of the Kulluk shown in Figure 5.7 and urea-doped ice sheets with varying thickness (10-40mm) and flexural strengths (25-50kpa). Both the "fixed" and moored (via a four-point, spring-based mooring system) model were towed through the ice sheet at velocities in the range 0.02-0.20m/s. The word fixed is emphasized, since it was not able to undergo displacements as a result of the ice

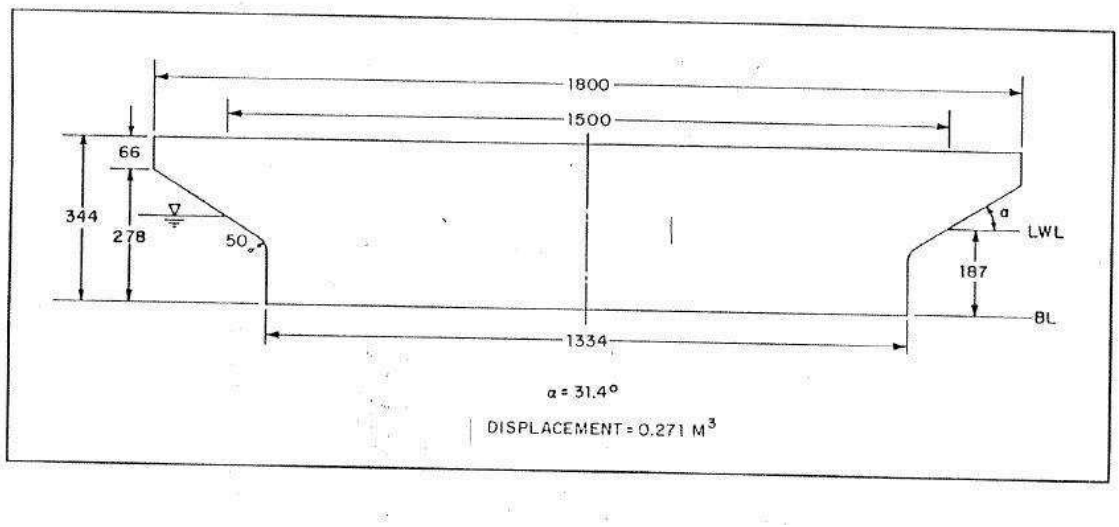

Figure 5.7: Model of Kulluk ship used in IIHR experiments (from Nixon and Ettema (1987))

sheet forces but was towed through the ice tank. Important characteristics of this experiment are:

1. the mean loads were reported along with peak loads given by the mean load plus two standard deviations;

2. the model platform did not contain the hull "skirt", as it was referred to, at its base to prevent the ice from riding under the structure (see Figure 5.8).

The report documented the effect of mooring stiffness, ice thickness, ice drift velocity and ice strength on the displacement and forces incurred by the platform. For both fixed and moored platforms, the mean horizontal force (and mooring force in the latter case) increased, in general, with increasing velocity and thickness. There were instances reported where an intermediate velocity would yield the maximum force. During all these tests, a significant amount of ice actually rode down and underneath the structure, which was uncharacteristic of the real operation observations but consistent with the effect of not having the hull skirt. As expected, and outlined in the

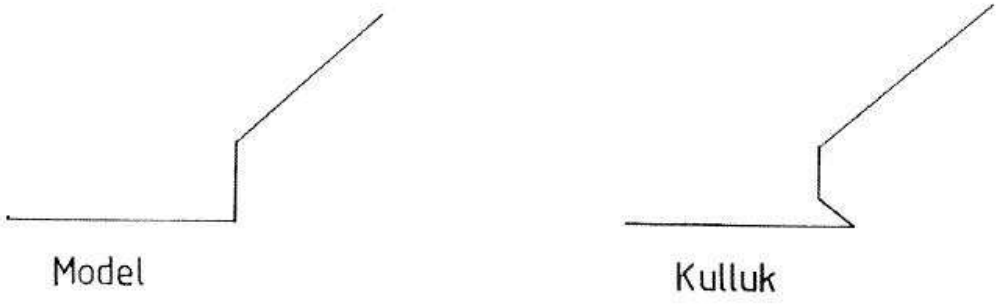

Figure 5.8: The IIHR model ship (left) and the "skirt" at the bottom of the Kulluk drillship (from Nixon and Ettema (1987))

previous section for wide structures, bending failure dominated the simulations with circumferential cracks appearing as the ice sheet impacted the hull, followed by radial cracks. The broken pieces were either cleared around the side of the structure, rode down and beneath it, or rotated back and onto the advancing sheet, which led to the formation of a rubble pile or ridge. The motion of the moored platform was described as "regular but stochastic"; it would be pushed back and then surge forward regularly, but with smaller displacement effects superimposed.

The HSVA tests were summarized by Wessels (1984). A series of 152 tests were conducted to investigate the behavior of fixed and floating cones in level ice, ice ridges, and pack ice. Parameters investigated were cone angle and waterline diameter, ice thickness, velocity, and the ice-structure friction coefficient. Although most of the tests considered a fixed upward breaking cone, several experiments were included to address the effect of inverting and mooring the cone. Wessels (1984) concluded that inverting the conical structure in level ice resulted in a 50% decrease in the peak horizontal load and mooring the structure reduced it further by another 50%. The

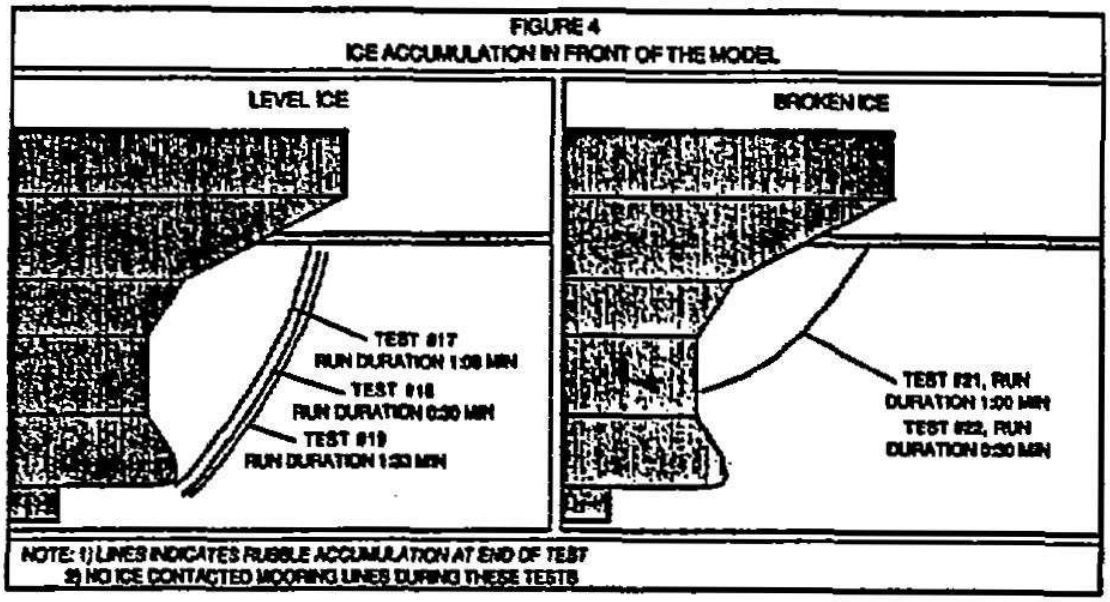

Figure 5.9: Side profile of Kulluk model used the Arctec Canada tests (from Abdelnour et al. (1987)).

peak horizontal load increased with increasing velocity and ice thickness.

The Arctec Canada tests performed by Comfort et al. (1982), described in a subsequent paper by Abdelnour et al. (1987), used a 1:30 scale model of the Kulluk and investigated level broken and unbroken ice sheets (see Figure 5.9) with thickness 0.5-1.5m (full-scale values, for actual thickness divide by 30), velocity 0.025-1.00m/s, and flexural strengths 310-840kPa. Both the fixed and moored condition was considered again, but in this case the platform was moored to the basin floor via a set of 12, axially distributed spread mooring lines comparable to the true system (see Figure 5.10). The failure of the ice was described as follows:

> "In sheet ice, the clearance behavior around the model appeared to be generally similar for all ice thicknesses and speeds of interaction tested. Ice contacting the forward side of the Kulluk failed in bending in a cusp

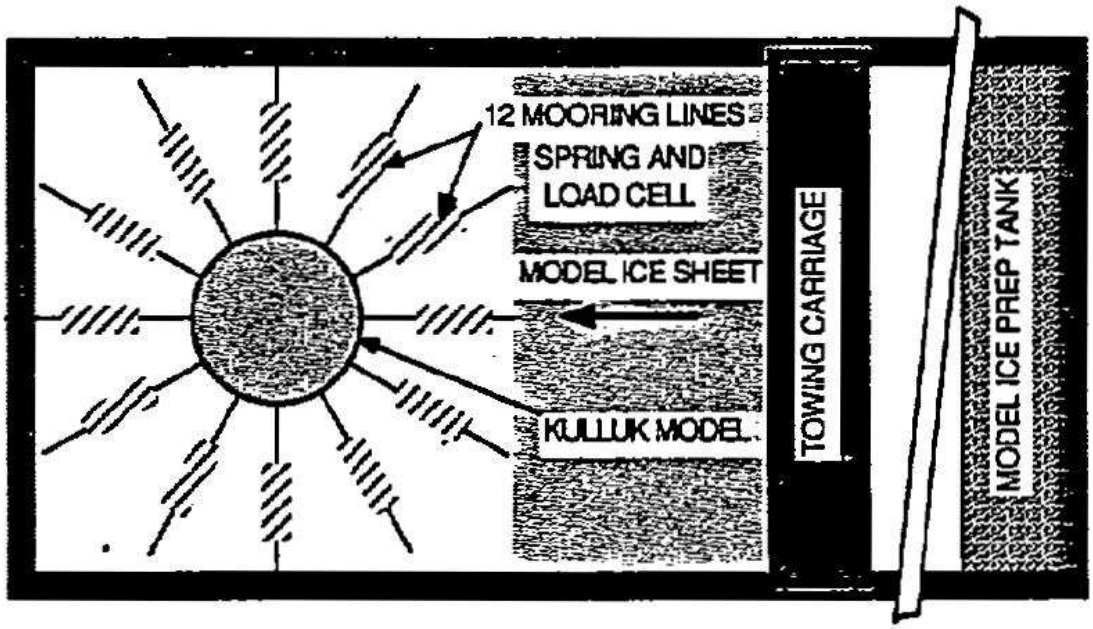

Figure 5.10: Tank set-up and mooring configuration used in the Arctec Canada tests (from Abdelnour et al. (1987)).

> pattern around the model after sufficient crushing had occurred at the edge to produce bending failure. Ice pieces were then deflected downward along the face of the model. After reaching the first knuckle (for thin ice), the ice pieces were deflected outwards from the model and a rubble accumulation started to build as buoyancy forces tended to move the ice pieces back to the ice surface. For thicker ice, the incoming ice failed in larger piece sizes which appeared able to downride to a greater extent before lodging on one of the knuckles thereby creating instability and commencing the growth of a rubble pile in front of the model." (Abdelnour et al., 1987)

This was reported as similar to what was observed of the full-scale problem in the Beaufort sea. However, the amount of rubble ice or ice build-up in front of the platform appeared to be greater in the experimental tests than observed in the field.

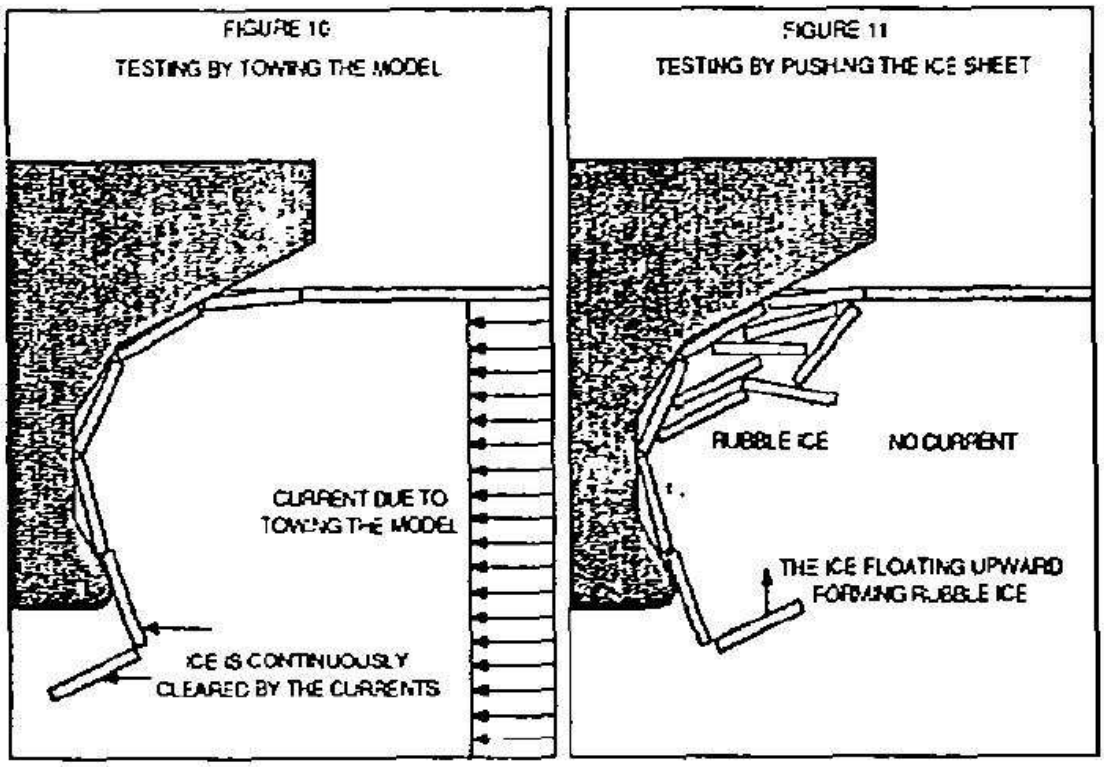

Figure 5.11: Tests by Arctec Canada were conducted by towing the model (left) and pushing the ice sheet (right) (from Abdelnour et al. (1987)).

The mean and peak horizontal forces increased with increasing ice thickness and drift velocity and loads were larger in all when the structure was fixed (20-100% greater in comparison to the moored platform). These loads were also higher than the HSVA tests; this was attributed to the lower density of the model ice which was used in the Arctec experiments. Ice density is an important factor, since buoyancy forces acting on the ice sheet as it impacts and forms a rubble pile in front of the structure, account for a significant portion of the loads. Of the two sets of tests that were completed by 1) towing the structure and by 2) pushing the ice sheet (see Figure 5.11), pushing the sheet yielded results which were more consistent with what was observed in the field. Towing the model simulated large currents which are not typical of conditions

in the Beaufort Sea.

5.5 Ice Forces on Downward-breaking Conical Structures - Full-scale Results

Full-scale results are reported in a series of PERD reports by B. Wright & Associates Ltd (Wright et al., 1998; Wright, 1999, 2000). The main purpose of the reports is to extract information about the peak loads on the structure from the data which was recorded while the drillship was in operation from the mid 1970s to early 1990s. Most of the data is extracted from a six year period, beginning in 1983, when the Kulluk entered the Beaufort sea and drilled twelve wells (seven different locations) in waters ranging in depth from 25m to 50m. The data was originally recorded as a system to support real-time decision-making on ice-breaker support and drilling response to advancing ice formations. During the six year period, the Kulluk only had 44.7 down days and seven emergency "move-off" locations in a total of 585 operating days (92% efficiency).

A second use for the real-time data has evolved over the past decade, since it is the only moored vessel to be "stationkept" and monitored in almost a full range of ice conditions. The sophisticated real-time monitoring system has thus provided a unique database of information (including data about ice conditions, mooring loads, vessel response, and ice management). The Kulluk was designed to endure loads up to 750 tonnes, displacements of 1.5-3.0 meters, and peak mooring line tensions of 260 tonnes in drilling mode, and 1000 tonnes, 3.0-6.0 meters, 390 tonnes in survival mode. When load and displacements fell into the first regime, drilling ceased but the platform remained moored. For larger forces, an emergency disconnect would be

initiated. The operation alert status is shown in Figure 5.12. Wright et al. (1998);

KULLUK ENVIRONMENTAL ALERT STATUS

COLOUR CODE	MEANING	HAZARD TIME (HT) MINUS SECURE TIME (ST)	DRILLING RESPONSE	MARINE RESPONSE
Green	Normal operation	HT-ST is more than 12 hours	Normal operations	Normal watch
Blue	Early alert	HT-ST is less than 12 hours	Normal operations	Alert watch & ice management
Yellow	Early warning	HT-ST is less than 6 hours	Restrict operations to available lead time	Begin preparations for hazard and ice management
Red	Drilling must stop, vessel may move off	HT-ST is zero	Secure well as appropriate	Final preparations for hazard and ice management
Black	ICE: vessel must move off WEATHER/WAVE: vessel must stream off on moorings	HT for disconnect is less than 2 hours	Disconnect	ICE: Move Kulluk off site WEATHER/WAVE: Stream off on moorings

Figure 5.12: Operation alert status for real-time decision-making onboard the Kulluk drillship (from Wright (1999)).

Wright (1999, 2000) recognize that the load data presented is not a completely accurate depiction of the events but was mainly put forth to show general trends in the data. Although an abundant amount of data was recorded, much of it was estimated by visual inspection, and precise measurements could not be made after the fact. The reports contain information about:

- the number, length, and orientation of mooring lines deployed as well as the pretension and operating tension in each line (see typical recording from onboard monitoring system in Figure 5.13);
- ice concentrations (for pack ice), ice thickness, ridge concentrations and heights, floe sizes, and ice-drift speed and direction;
- global loads on the mooring systems; individual tensions in mooring lines and

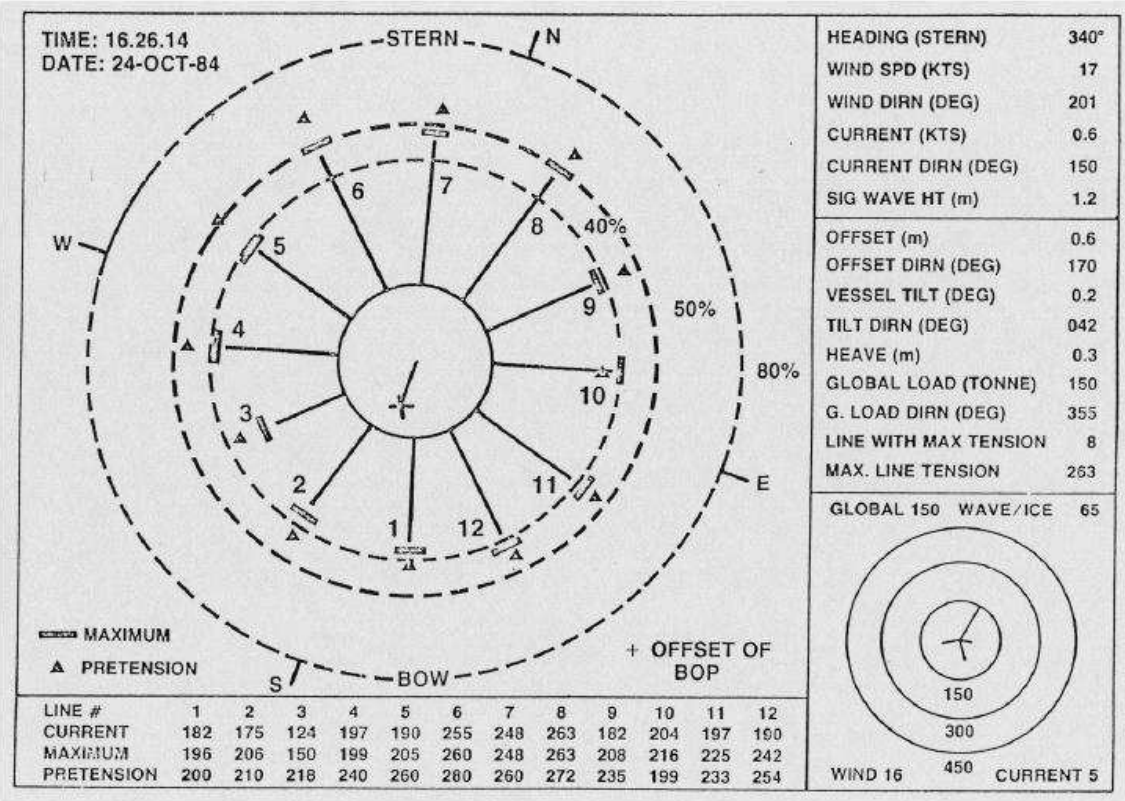

Figure 5.13: Screenshot of the monitoring system onboard the Kulluk drillship (from Wright (1999))

.

displacements; the global mooring load was estimated by vector addition of individual line tensions.

Table 5.3 describes the means by which information was reported onboard the vessel. Most of the details about the size and type of ice formation were made via visual estimates. Other parameters were estimated or inferred. For flexural strength, the

Property	**Estimation Procedure**
Total ice concentration	Visual estimate
Ice concentration by type	Visual estimate
Ice thickness by type	Visual estimate
Typical floe size	Visual estimate
Larger floe size	Visual estimate
Ridging concentration	Visual estimate
Typical ridge sail height	Visual estimate
Typical ridge keel depth	Based on keel/sail ratio of 4.5
Larger ridge sail height	Visual estimate
Larger ridge keel depth	Based on keel/sail ratio of 4.5
Related comments	Any related points
Ice drift speed	Sequential radar fixes
Ice drift direction	Sequential radar fixes
"state" of the cover	Close, open, pressured ice
Flexural strength	Inferred from other parameters

Table 5.3: Method of estimating ice information onboard the Kulluk drillship (from (Wright, 1999)).

ice temperature was estimated from the air temperature. If the air temperature was below -2° Celsius, then the flexural strength was estimated using the following procedure:

1. Calculate salinity from $S = 4.6 + 91.6h$ (Kovacs, 1997);

2. Calculate brine volume from $v = S(0.532 - 49.2/T)$ (Kovacs, 1997);

3. Calculate flexural strength from $\sigma_f = 1.76\exp(-5.88\sqrt{(}v))$ (Timco and O'Brien, 1994);

Using these observations, Wright et al. present results for ice conditions ranging from level ice to pack ice to ice ridges. The Kulluk typically operated with full icebreaker support, so level ice interaction was not common, but several instances were recorded and presented in the reports.

Following from Keinonen et al. (1996), the force data (F_h) was normalized to a flexural strength of 500kPa (to reduce any variation coming from the flexural strength) and a temperature of -10° Celsius (to reduce any variation coming from ice friction), using the following scaling factors:

$$F_h^* = (0.63 + 0.00074\sigma_f)F_h \tag{5.9}$$

$$F_h^{**} = (1 - 0.0083(T + 30))F_h^*. \tag{5.10}$$

The result of this normalization on the load data, F_h^{**} is shown in Figure 5.14 along with the upper bound line $y = 204x + 37$ which was estimated based upon a statistical analysis of the data (drawing a best-fit line through the mean-plus-two standard deviations of the bins in a histogram plot). These results were digitized using GoldenSoftwares' Grapher software (www.goldensoftware.com). When normalizing the thickness to one meter, no apparent trend could be observed in increasing drift velocity. The series of reports also contained a comparison of the loading data with the three model scale experimental tests discussed in the previous section. The level of agreement between the three experiments and the full-scale data is listed as "not bad" with a particular explanation of the non-conformity of data in each test (see Figure 5.15). The HSVA results are said to be in good agreement but the IIHR and Arctec tests peak load measurements over-estimate the actual observed data (by a factor of 2 in the latter case). The higher flexural strength of the model ice in the IIHR experiments and the high ice friction coefficient in the Arctec experiments were the suggested sources of the anomalies.

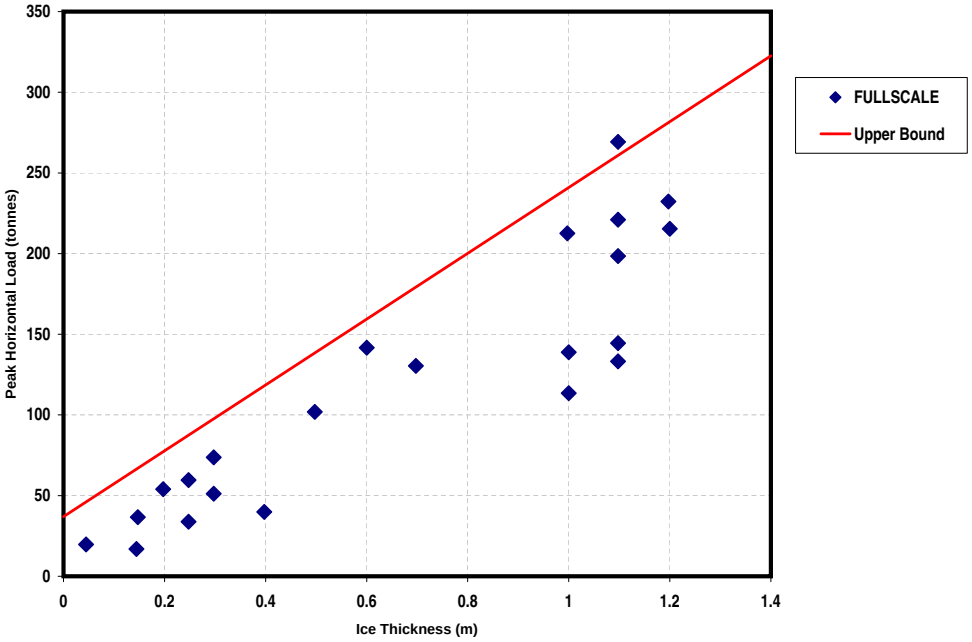

Figure 5.14: Normalized horizontal loads in level unbroken ice versus thickness.

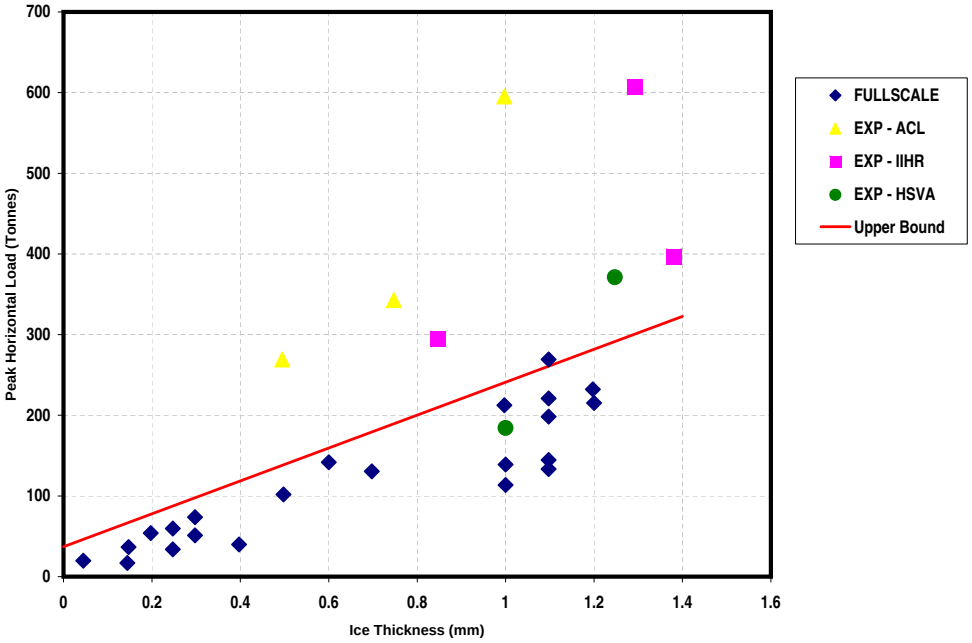

Figure 5.15: Normalized horizontal loads in level unbroken ice versus thickness plotted with experimental tests results of Nixon and Ettema (1987), Wessels and Iyer (1985), Comfort et al. (1982). .

5.6 Ice Forces on Downward-breaking Conical Structures - Numerical Modeling

In 1998, Wright et al. listed analytical/numerical tools which exhibited particular promise in predicting ice loads on moored structures. They include:

1. SHIPSIM (Sandwell)- a computer program for computing ice forces on structures in various ice and mooring conditions. This program has not been tested extensively although it has been applied successfully to various problems involving moored structures;

2. AKAC (Canmar 1996 Joint Industry Project) - analytical method based upon previous experimental and full-scale tests which provides only a rough estimate of anticipated loads. It also does not directly consider mooring forces or the displacement response of the moored structure.

3. DiscIt (Norwegian Institute of Technology) - discrete element code for simulating the behavior of a moored structure using circular discs.

4. IceSim (CHC/NRC) - discrete element code using disks or spheres capable of simulating tens of thousands of elements. This code has been used successfully to simulate models of ice-structure interaction and river ice jams.

Although no particular tool has emerged as a clear favorite in the past decade, the author is aware of ongoing work (especially with IceSim at the NRC). Without a major review of the DEM and its applications, the report also insightfully suggested that the developing discrete element method did offer "a method for fairly thorough analytic assessments of moored vessel stationkeeping in moving pack ice conditions in the near future" (Wright, 1999).

The goal of the current numerical simulations is to provide some estimate of horizontal ice loads on these conical structures so that expensive time-consuming experimental tests can be ceased. Numerical predictions are usually based on mathematical, empirical, and constitutive approximations and thus correct force predictions must be widely verified before they are accepted as accurate. Derradji-Aouat (1994) used a finite element program to investigate the effects of ice thickness, size and strength on ice loads for a rigid conical pier (upward-breaking structure). Barker et al. (2000b) used the numerical method of Sayed et al. (2000) to study ice forces around the "Kulluk" design in two-dimensions (plan view). The method uses an implicit integration of the governing equations for a particle-in-cell method with a visco-plastic constitutive model. For specific details of the method, refer to Sayed et al. (2000) or Barker et al. (2000a). The simulations show good comparison with the experimental observations of Wright (1999), but the true nature of the problem was lost in simplification to two-dimensions, since the physical interaction of the ice sheet and the sloping structure was not modeled.

5.7 Summary

This chapter formally presented the problem to be investigated for the remainder of this thesis. A discussion of ice-structure interaction, several experiments, and a full-scale data set form the basis by which to analyze and compare the results.

Chapter 6

Experimental Investigation

6.1 Introduction

Experimental simulations of a 1:40 scale model of the Kulluk drillship were conducted at the NRC-IOT in August-September of 2005. This work was completed by the technical staff of the NRC-IOT under the supervision of Dr. Michael Lau. The role of this author in the physical experiments was to analyze the results and provide complimentary predictive numerical simulations in the next chapter. Cole (2005) summarized the experimental setup and procedure which were conducted in multiple ice formations including a level unbroken ice sheet, a level pre-sawn ice sheet, and pack ice. For completeness, a description of the physical experiments is provided in this chapter.

6.2 Experiment Set-up

6.2.1 Facility

The test apparatus located at the NRC facilities in St. John's, Newfoundland, is a 76m-long by 12m-wide by 3m-deep ice tank, one of the largest ice tanks in the world. A series of views of the tank as well as a schematic are given in Figures 6.1 and 6.2, respectively. At one end of the tank is a 15m trimming dock separated from the

Figure 6.1: Ice tank at the NRC Institute for Ocean Technology in St. John's, Newfoundland (from National Research Canada of Canada (2009)).

remainder of the tank by a retractable thermal barrier, while at the other end is a melt pit where leftover ice is discarded and permitted to melt. The refrigeration is a computerized ammonia-based, two-stage mechanical compression technique which allows for temperatures from -30° to 15° Celsius and growth at a rate of three millimeters per hour.

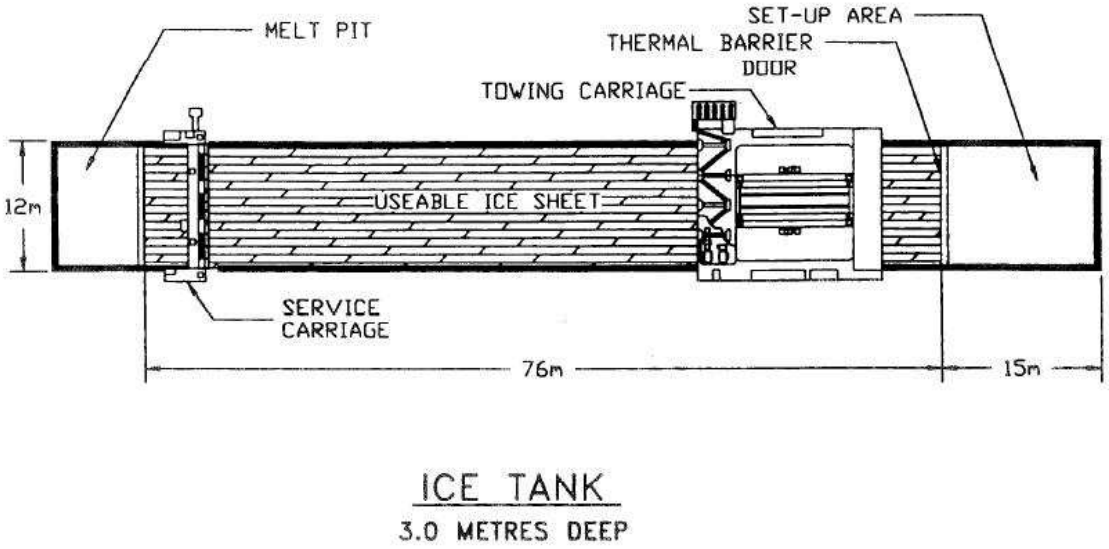

Figure 6.2: Plan view of the NRC-IOT ice tank.

There are two main carriages which may traverse over the ice tank for testing and service purposes, as seen in Figure 6.3. The larger steel carriage which is 15m long, 14.2m wide, and 3.96m high and weighs approximately 80,000 kilograms, is typically used to propel (tow) models through the tank. It sits on steel and sprocket wheels which are attached to a track on the sides of the tank that allow for speeds from 0.002-4.0 meters per second. The service carriage is much smaller and may only obtain speeds up to 0.5 meters per second. It is composed of three individual platforms which may be lowered to the ice surface to test current ice conditions and properties.

6.2.2 Kulluk model

A model with length scale ratio 1:40 was constructed at the NRC-IOT to conduct the experimental trials. The relation of model and full-scale parameters of the Kulluk structure are given in Table 6.1. The final Kulluk model constructed is shown in

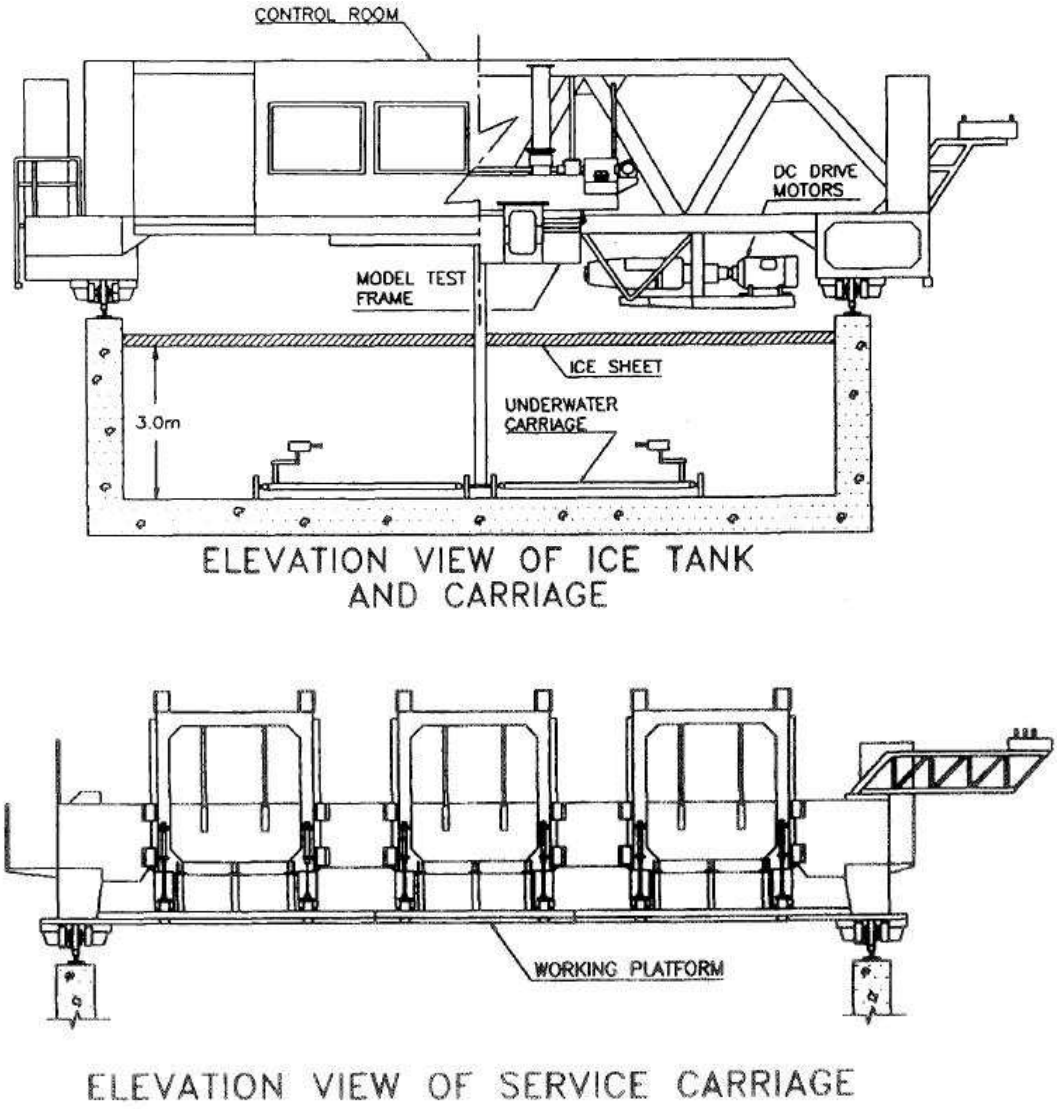

Figure 6.3: Schematic view of tank carriages.

Parameter	full-scale	Model Scale
Overall Beam (m)	81	2.025
Waterline Beam (m)	67.9	1.698
Beam at hull bottom (m)	62	1.552
Depth (m)	18.4	0.460
Draft (m)	11.5	0.288

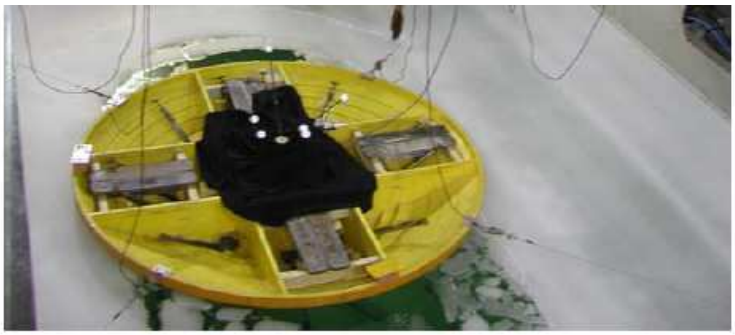

Figure 6.4: Picture of final 1:40 model of the Kulluk platform (from Cole (2005)).

mooring system. The four poles, forming a rigid square frame, were connected to the model by load cells, making 45° angles with the horizontal and vertical directions and a wire cable. The cable passed through a pulley at the bottom of the mooring pole, then through another pulley at the top of each pole, and was finally attached to a spring with a manufacturer-specified spring constant. Three different springs with constants of 0.612 kN/m, 1.191 kN/m, and 2.451 kN/m were used to simulate the behavior of the twelve-line mooring system that was used in the Beaufort Sea. The springs, load cells, and data acquisition system were all carefully calibrated before each experiment by the staff at the NRC-IOT.

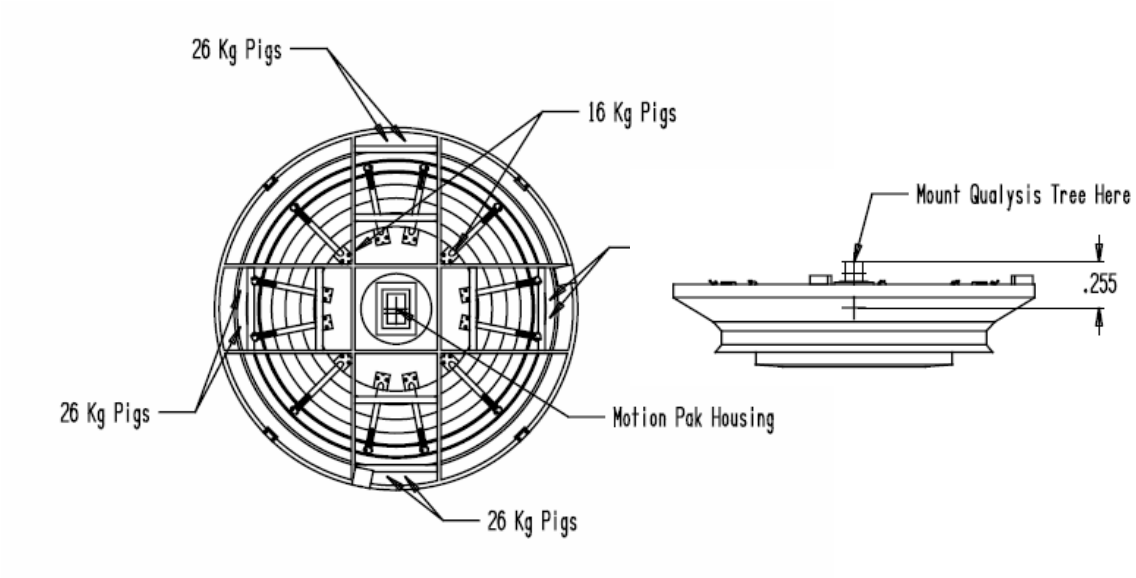

Figure 6.5: Final 1:40 model of the Kulluk platform (from design documents in Cole (2005)).

6.2.3 Model scaling

To correctly model ice conditions, maintaining a correct scale between model and full-scale parameters is important. These "laws of similitude" have been the focus of much attention in the past (Nogid, 1959; White and Vance, 1967; Michel, 1970, 1978; Schwarz, 1977; Atkins, 1975; Atkins and Caddell, 1974; Vance, 1975). Timco (1984) presented the laws for models which fall into two categories: (i) in which gravity and inertial forces are dominant; (ii) in which ice-crushing is dominant. The first category is applicable to problems involving icebreakers, ice ride-up, and any other problems where the main mode of failure is flexure or bending. The correct scaling of this problem is characterized in terms of the Froude number (Fr), Reynolds number (Re), Cauchy number (Ca), and Ice number (I_c). The Froude number relates the gravitational and inertial forces, the Reynolds number relates the viscous and inertial forces, the Cauchy number relates the elastic and inertial forces, and the Ice number

relates the cracking and inertial forces (Atkins and Caddell, 1974) of the model and full-scale experiments. For complete similitude all of these numbers must be the same at the full- and model scales. In practice however, this may only be accomplished if the Froude and Reynolds numbers are equal - i.e., the ratio of full-to-model-scale fluid viscosities is $\alpha^{\frac{3}{2}}$, where α is the length scale. This is not typical of fluids which are used for the experiments but does not usually pose a problem unless the tests involve high speeds and/or high scaling α (Timco, 1984). Most model ice is, therefore, fit to scale using the Froude and Cauchy numbers while ignoring the Reynolds number. Based upon these parameters, the correct scaling for this problem is shown in Table 6.2 for $\alpha = 40$.

Parameter	Full-to-Model-Scale Ratio
Length (L)	α
Time (t)	$\sqrt{\alpha}$
Velocity (v)	$\sqrt{\alpha}$
Acceleration (a)	1.0
Mass (m)	α^3
Force (F)	α^3
Density (ρ)	1.0
Ice Strength (σ)	α
Ice Thickness (h)	α
Ice Elastic Modulus (E)	α
Poisson Ratio (ν)	1.0
Friction (f)	1.0

Table 6.2: Correct scaling of full-to-model-scale experiments from Timco (1984).

6.2.4 Model ice

The Froude and Cauchy consistent model ice used at the NRC-IOT is a water-based mixture formed with a chemical additive EGADS (Ethylene Glycol - Aliphatic Detergent - Sugar). Typical additive percentages are 0.39%, 0.036%, and 0.04%, respectively. When the ice is grown, up to a thickness of 150mm, the chemical compound

is trapped in brine pockets which allow for model-scale strengths in the range 10-120kPa. The density of the water-EGADS mixture is lowered to that of seawater by injecting bubbles during the freezing process.

6.2.5 Experiment testing sequence and tank set-up

This experiment involved three ice formations: level ice, pre-sawn ice, and pack ice. The focus of this research is on level ice but the testing sequence for all types and the location of each of the experiments is shown in Figure 6.6. A total of five tests are conducted for a single sheet of ice. The level ice tests are performed between the 15m and 30m marks, followed by the pre-sawn tests between the 35m to 50m marks. With reference to Figure 6.6, the main towing carriage propels the model through level ice sheet (Test 1), followed by the pre-sawn test (Test 2) at the 35m mark on the same side of the tank. It then returns back to the 15m mark to perform the level ice test (Test 3) and then another pre-sawn test (Test 4). A pack ice test is later conducted (Test 5) at the location where Test 3 was previously completed.

6.3 Measurement of Ice Properties

Ice properties are recorded on a predetermined timeline during the experiments. The following ice properties are measured:

- ice thickness;
- compressive strength;
- flexural strength;
- elastic modulus;
- ice density;

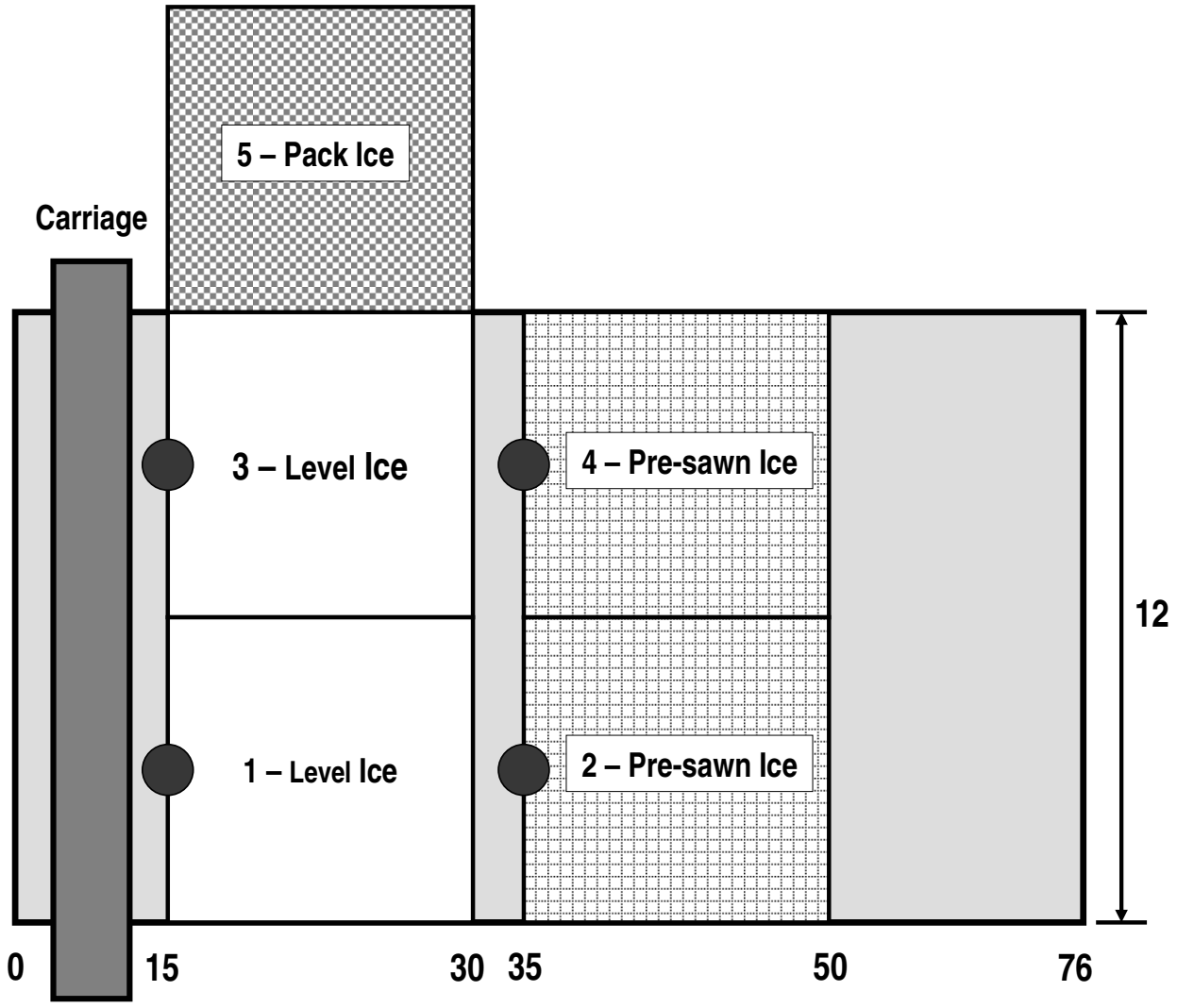

Figure 6.6: Ice tank configuration for physical experiments (measurements in meters).

- ice friction.

6.3.1 Measurement time-line

A typical experiment on a single ice sheet is conducted as follows. Before the level ice experiment, the elastic modulus and flexural strength at the North and South sides of the tank, and the ice thickness at the 20m, 40m, and 60m marks are recorded. At 15m and 30m an additional flexural strength test is performed to account for the dynamic effect. If the flexural strength measured at these locations is within the target values, the test proceeds after the density of the ice is recorded. Once the test is complete, the ice thickness in the channel created by the model is measured at two-meter intervals. Before the test on the pre-sawn ice is done, the density and flexural strength at the 35m and 50m marks are recorded. Ice thickness is again measured in the resulting channel after the test. Pack-ice tests are completed once the target concentration of ice is constructed. The ice friction is typically measured at the end of the day.

6.3.2 Flexural strength test

The flexural strength is measured using a cantilever beam test at the previously mentioned locations. At each location, five beams with thickness-to-width-to-length ratio of 1:2:5 are cut into the ice with one side still attached. Four of five beams are broken downward and one is broken upward using a hand-held spring gauge, allowing for the flexural strength to be calculated from cantilever beam theory as:

$$\sigma_f = \frac{6PL}{WH_f^2} \tag{6.1}$$

where σ_f is the flexural strength, P is the force required to break the beam, L is the length of the beam, W is the width of the beam, and H_f is the thickness of the beam.

The flexural strength reported is the mean of the four downward-breaking values. The ratio of downward-to-upward-breaking flexural strength is approximately 1.5, which is in agreement with other reports (Gow, 1977; Wessels, 1984). The flexural strength of the sea ice is typically dependent on both the salinity and temperature profile, but for the purposes of these experiments and the numerical simulations, it is assumed constant across the ice sheet.

6.3.3 Compressive (shear) strength test

The compressive strength of ice is measured by punching a circular puck with radius 17.5mm in a 200mm by 300mm sample of the ice. The shear strength σ_s is then calculated as

$$\sigma_s = \frac{P}{0.11h} \tag{6.2}$$

where P is the force require to punch the puck through the sample and h is the sample thickness. The compressive strength of naturally occurring ice is typically three times larger than the flexural strength (Wessels, 1984).

6.3.4 Ice density test

A sample of the ice is placed in a beaker filled with the EGADS solution. The full beaker weight is recorded. The floating sample pushed to submerge it and the weight is recorded again. The difference in the two weights (multiplied by gravitational constant) gives the force required to submerge the ice, and the density is then calculated from

$$\rho_i = \rho_w - \frac{P}{V} \tag{6.3}$$

where $\rho_i(\rho_w)$ is the density of ice (EGADS mixture), P is the submerging force, and V is the volume of the ice sample.

6.3.5 Ice-structure friction

The ice-structure friction coefficient is measured by holding a sample of ice and a load cell against the model and then moving the model. The results are interpreted by an apparatus called a "Friction Jig".

6.3.6 Test matrix

A total of 140 experiments were conducted in level unbroken ice to address the effects of ice thickness, ice flexural strength, platform velocity, and mooring stiffness. Table 6.3 presents the target values of each parameter and their corresponding full-scale value. The ice thickness and flexural strength are target values that are not exactly

Parameter	Target Value	Full-scale Value
Ice thickness h (mm)	10, 20, 30, 40	400, 800, 1200, 1600
Ice flexural strength σ_f (kPa)	12, 20	500, 800
Model velocity v (m/s)	0.005, 0.01, 0.025 0.05, 0.1, 0.2, 0.3	0.031, 0.063, 0.16, 0.32, 0.63, 1.26, 1.90
Mooring stiffness K (kN/m)	0.612, 1.191, 2.451	980, 1906, 3922

Table 6.3: Parameters investigated during model scale experiments of the Kulluk drillship at the NRC-IOT.

achieved. The experiment only proceeds if measurements on the ice yield values within 20% of these target values. Since the Kulluk model is towed via a set of four mooring poles in this experiment, it is prescribed an exact velocity and the mooring stiffness is determined by the spring constant.

6.4 Results and Discussion

The 140 experiments in level unbroken ice were conducted over a period of three months in 2005. Peak loads were determined by vectorially adding the measured loads

on the four mooring cables (via a load cell attached to the spring); displacements or offsets from the center of the four poles were also recorded. Note that the original data files were not supplied by the NRC at the time of this research; the data points were extracted from Cole (2005) (which was supplied by the NRC) using a third party software.

6.4.1 Peak horizontal offset

Effect of ice thickness

The peak horizontal offset versus the ice thickness is presented in Figure 6.7-6.9 for each mooring stiffness (0.612-2.451kN/m). Each figure contains two graphs which represent the response when the ice flexural strength is 500kPa (top) and 800kPa (bottom). The peak horizontal offset is plotted in these graphs versus the true (not target) ice thickness for each velocity investigated. The velocities are labeled V1-V7 in increasing order to reduce the clutter in the figures. Actual velocities may be obtained from Table 6.3.

The general trend observed from these figures is that the peak offset increases with increasing ice thickness. The only exception is in Figure 6.8 (top), where $K = 1.191$ and $\sigma_f = 500$kPa. The peak offsets for all velocities at the target thickness of 1.6 meters are all remarkably similar, leading to the conclusion that an error was made in the preparation of this figure by Cole (2005). For $K = 0.612$kN/m and $v \geq 0.16$m/s, the maximum offset is negative for all ice thicknesses. At the lower speeds $v < 0.063$m/s, the effect of the thickness on the sign of the offset is less pronounced. This could be an effect of the model ice behaving as a ductile instead of a brittle material. Theoretical considerations suggest that there should be a velocity at which this transition occurs. This point will be made clearer with the discussion of peak loads which will follow.

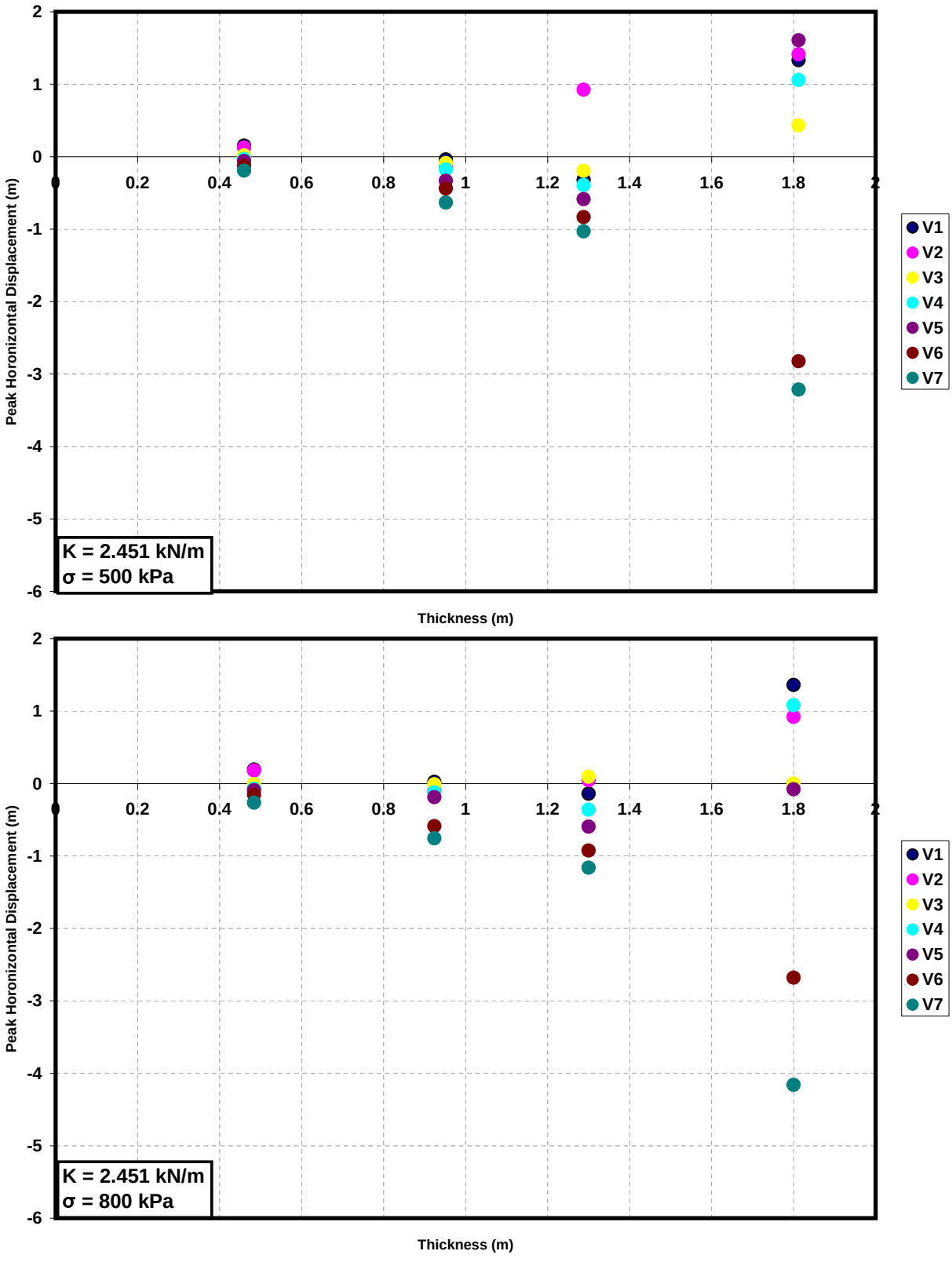

Figure 6.7: Peak horizontal offset versus ice thickness for seven investigated velocities and mooring stiffness $K = 2.451$kN/m. Top: 500kPa. Bottom: 800kPa.

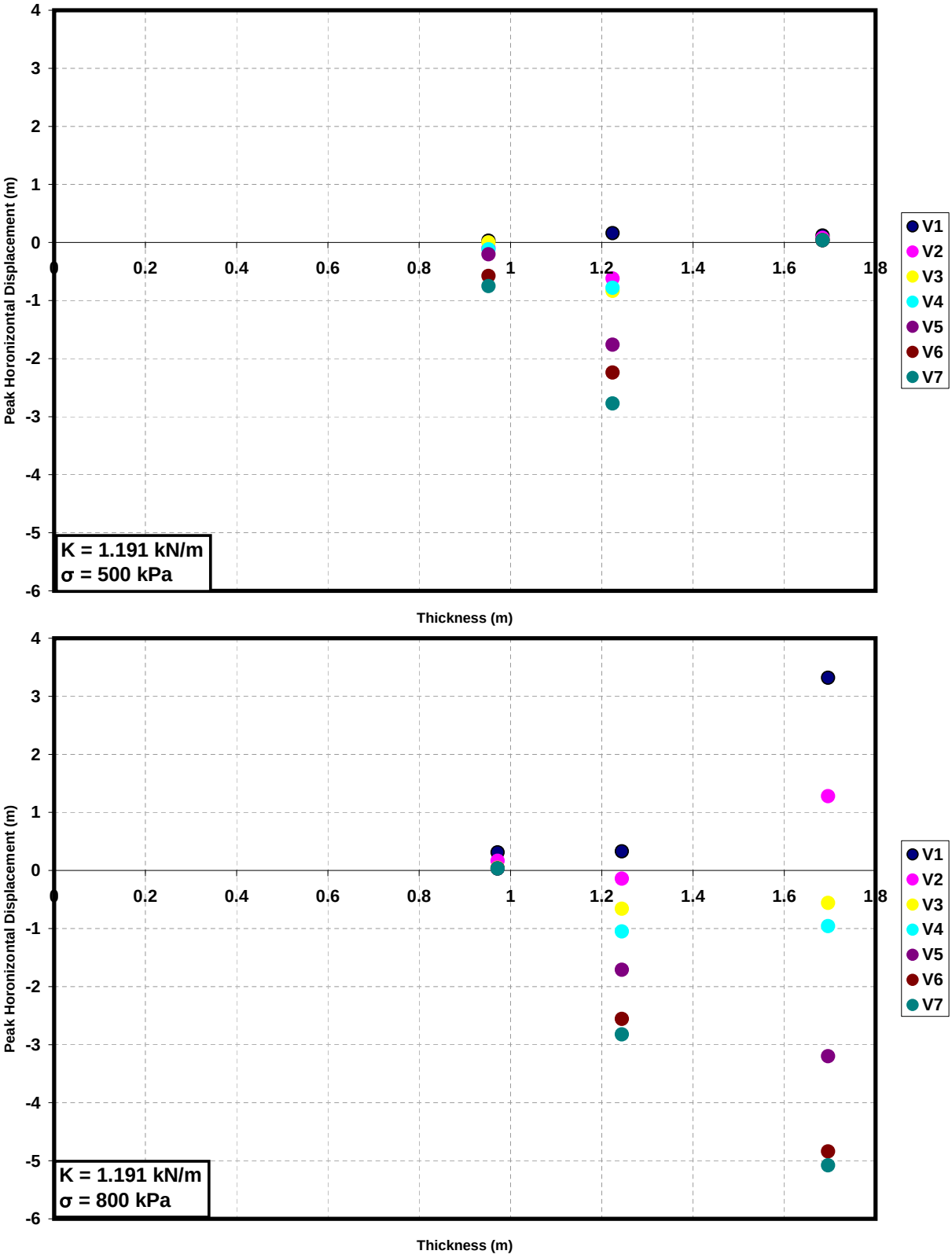

Figure 6.8: Peak horizontal offset versus ice thickness for seven investigated velocities and mooring stiffness $K = 1.191$kN/m. Top: 500kPa. Bottom: 800kPa.

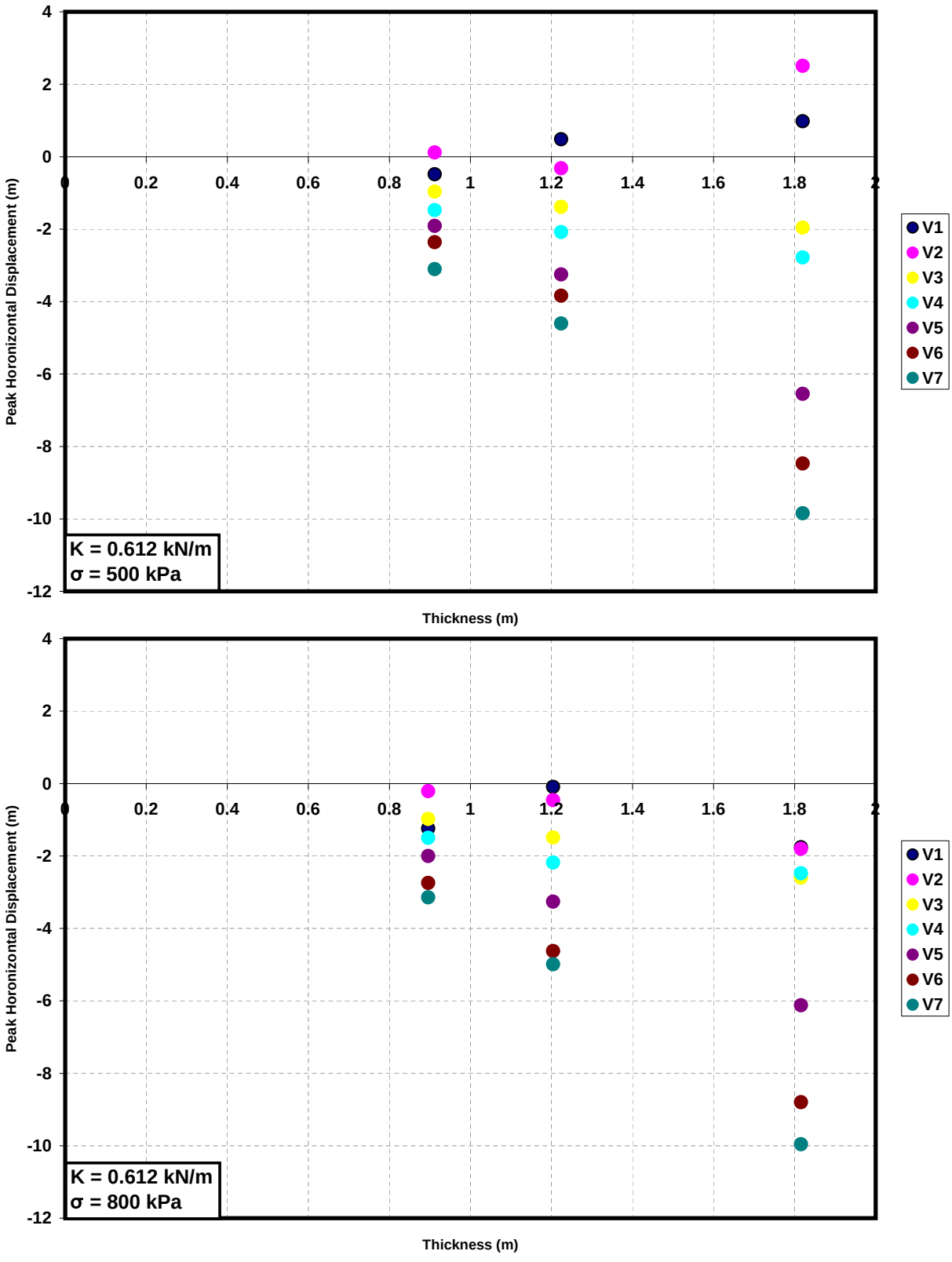

Figure 6.9: Peak horizontal offset versus ice thickness for seven investigated velocities and mooring stiffness $K = 0.612$kN/m. Top: 500kPa. Bottom: 800kPa.

At $K = 1.191$kN/m, the same pattern is observed, but values of the peak offset do become positive for an ice thickness of 1.6m. At $K = 2.451$kN/m, a similar pattern is observed for $h \leq 1.2$m, but the transition from negative to positive maximum offsets at $h = 1.6$m occurs at $v = 0.63$m/s as opposed to the lower velocity of $v = 0.063$m/s. Again, this could be explained by the transition of the underlying material behavior or by the transition of the mode of failure from bending to shear. A transition to shear failure would cause an immediate increase in the peak loads and hence have a direct result on the offsets as the mooring system works to restore the drillship to its equilibrium position. The larger loads would cause the model to displace further in the x-direction and generate larger than expected mooring forces, causing the ship to surge forward into the approaching ice sheet. The velocity at which the bending to shear failure transition occurs for brittle ice typically decreases for increasing ice thickness. This, combined with the transition from ductile to brittle behavior, may explain the lack in conformity in the sign of the peak offset.

Effect of mooring stiffness

Mooring stiffness also has a direct impact on the magnitude of the peak offsets. For the stiffest system ($K = 2.451$kN/m), Figure 6.7, the data has a peak-to-peak amplitude of about 5m. This increases to 8.5m when the stiffness is decreased to $K = 1.191$kN/m and to 12m when $K = 0.612$kN/m. As the velocity and ice thickness increase, the stiffness of the mooring system becomes more important in reducing the peak offsets experienced, since the loads are also expected to increase with increasing velocity and thickness. As expected, the stiffer system restricts the movement of the platform, which in turn adds to its stability. Since previous studies have indicated that a moored structure has lower loads than a fixed structure, the effects of this increased stability or limited movement on the resultant loads still needs to be investigated.

Increasing of the mooring stiffness, for example, could further limit the offset to the point that the mooring system could simulate the behavior of a fixed structure, causing increased loads. The mooring system should be stiff enough to limit the peak offset expected but not so stiff as to cause the generation of increased loads.

Effect of ice velocity

Figures 6.10-6.13 display the peak offsets versus velocities for each thickness. Horizontal lines at ± 3 are also included for comparison purposes. From this series of

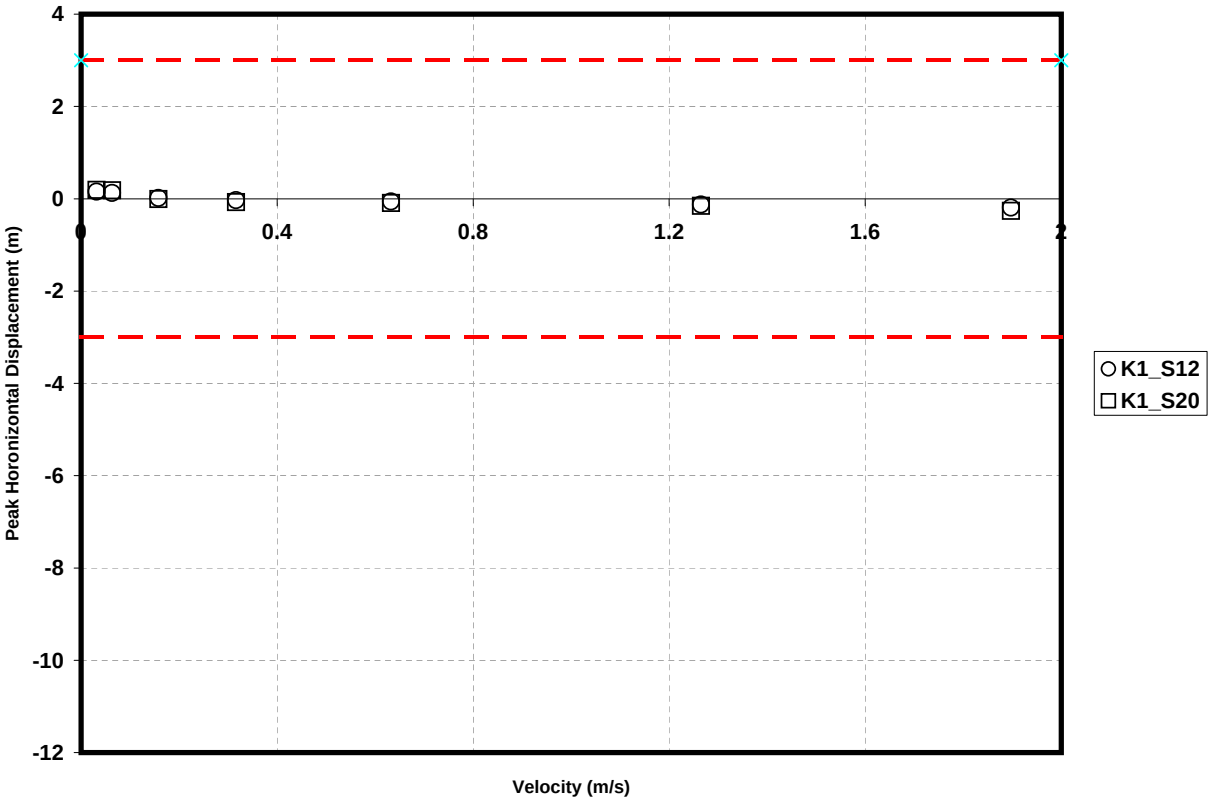

Figure 6.10: Peak horizontal offset versus ice velocity for $h = 0.4$m.

figures, it is evident that the peak offset increases for increasing velocity and this effect is more pronounced as the mooring stiffness decreases (see Figure 6.11, compare K3 vs K1). The peak offset appears to have a non-linear (perhaps quadratic) dependence

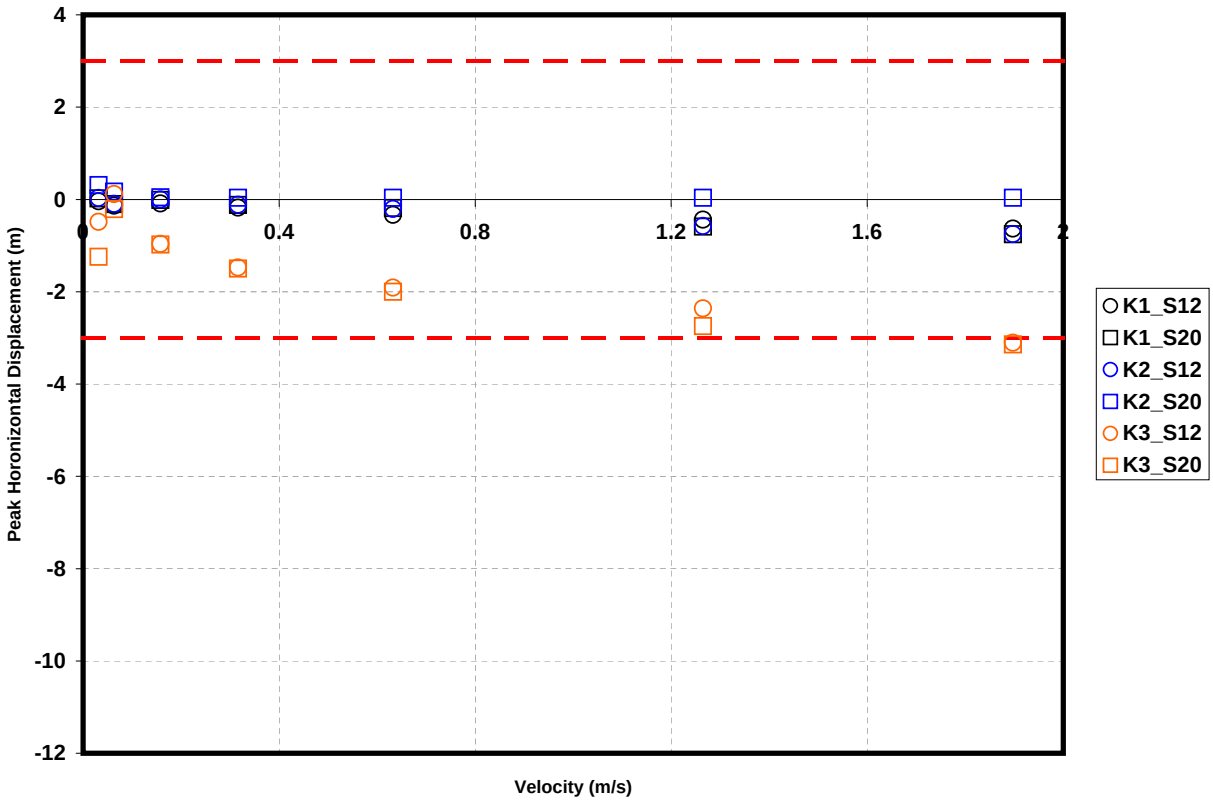

Figure 6.11: Peak horizontal offset versus ice velocity for $h = 0.8$m.

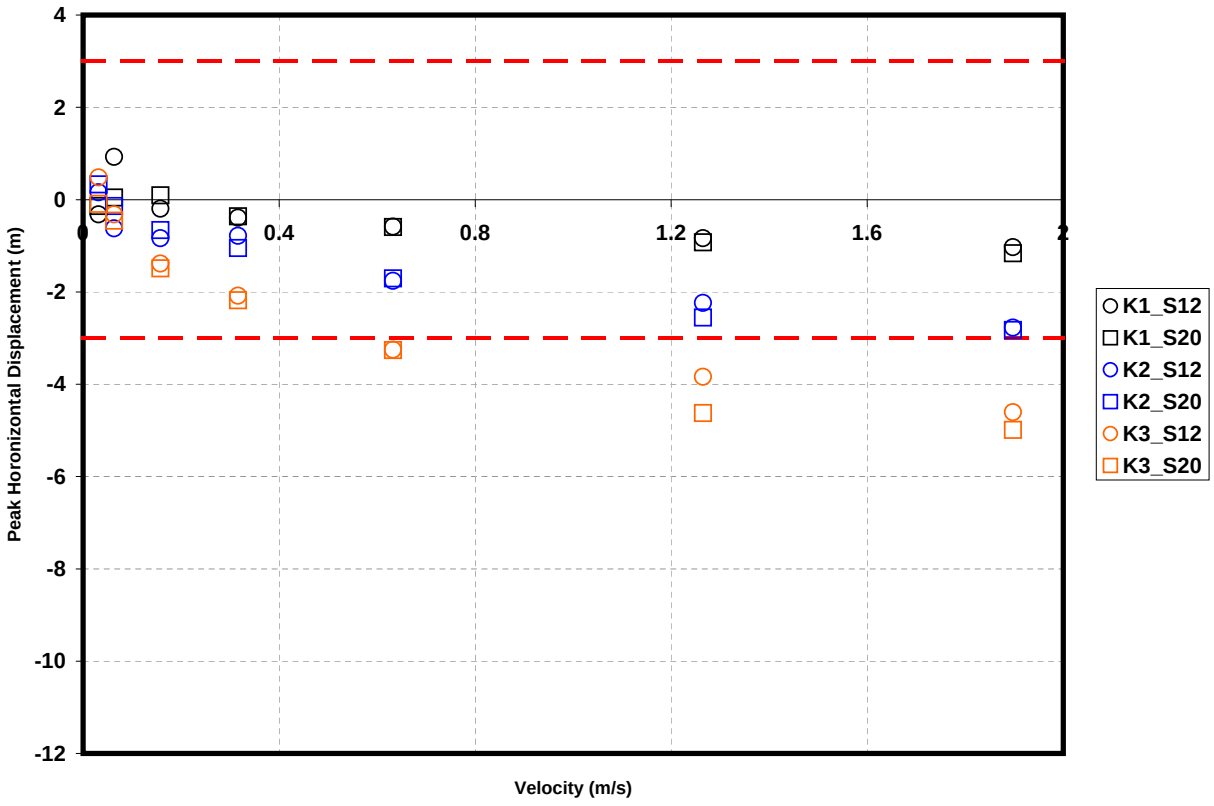

Figure 6.12: Peak horizontal offset versus ice velocity for $h = 1.2$m.

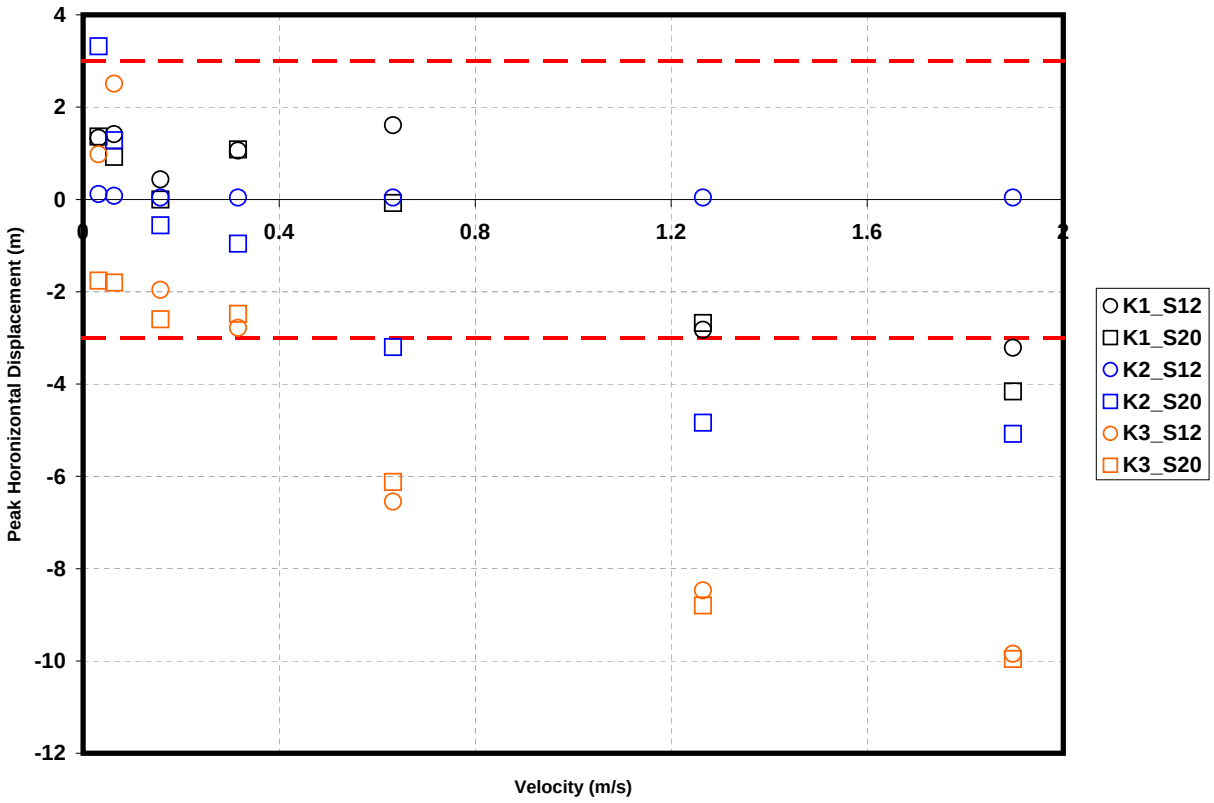

Figure 6.13: Peak horizontal offset versus ice velocity for $h = 1.6$m.

at low velocities but becomes almost linear as the velocity increases. This dependence is unclear at the smallest ice thickness, since only the stiffest springs were utilized, but is amplified as the thickness increases. Typical ice velocities in the Beaufort Sea and off the east coast of Canada are $0.15 - 0.25$m/s, which indicates that use of mooring systems comparable that used in the experiments would minimize any need for emergency disconnects as a result of platform movement (emergency disconnect is issued typically when offset exceeds 5% of water depth, or up to three meters, hence the accompanying horizontal lines at $\pm$3m in the graphs). As the velocity increases, the stiffest system maintains adequate stability; peak offset only exceeds 3m at $v = 1.90$m/s for $h = 1.6$m. Peak offsets of the least stiff system increase quickly, with both thickness and velocity yielding a moored platform that would require an emergency disconnect for almost all ice thicknesses above 1.0m and velocities greater than 0.6m/s. The intermediate stiffness is consistent and produces results that are between these two bounding cases.

Effect of flexural strength

Figures 6.10-6.13 (top and bottom) indicate that there appears to be very little effect of the flexural strength on the peak offset for increasing velocity. The results for the different flexural strengths seem nearly to overlay one another in most cases.

Summary

The peak offsets seem to be influenced by the thickness, velocity, and mooring stiffness. To visualize this dependency, the offset is plotted versus the velocity and thickness on a three-dimensional axis for each stiffness and interpolated to create surface plots. The results of the analysis are given in Figures 6.14 and 6.15 for each flexural strength. In both cases, the surface shading is lightest when the system is stiffest ($K = 2.451$), which corresponds to the smallest offsets. The shading becomes slightly

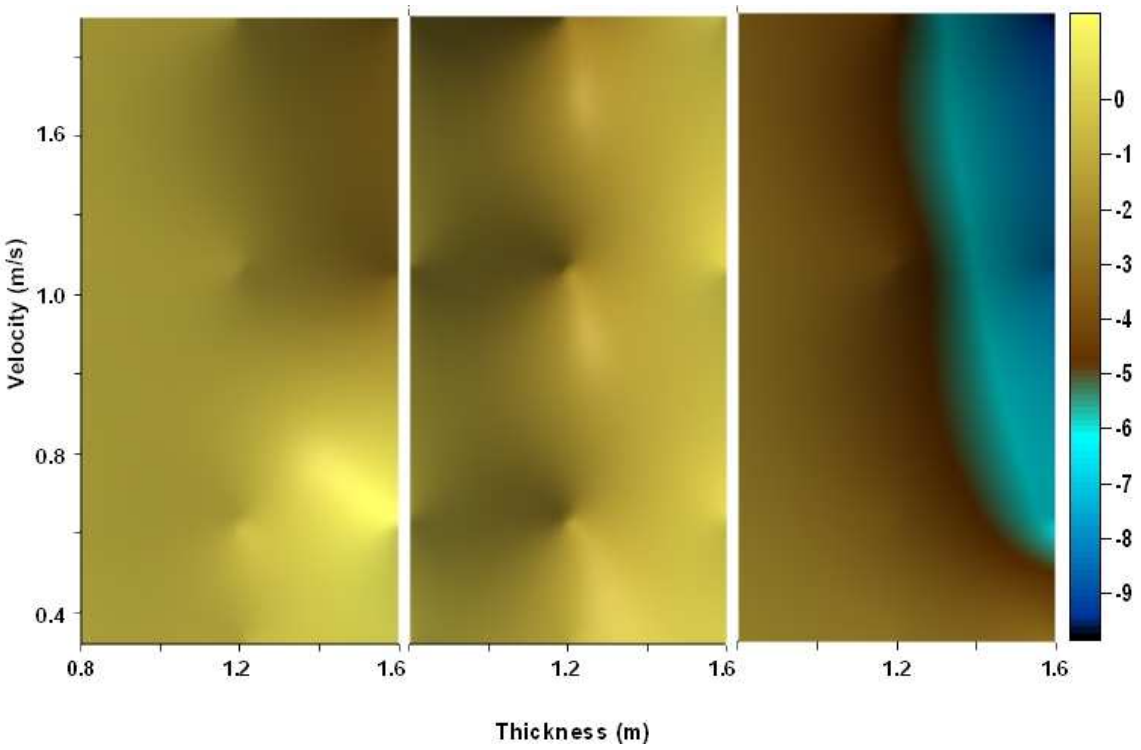

(a) $K = 2.451$ (b) $K = 1.191$ (c) $K = 0.0612$

Figure 6.14: Interpolated surface plot of peak offsets versus ice thickness and velocity for $\sigma_f = 500$kPa.

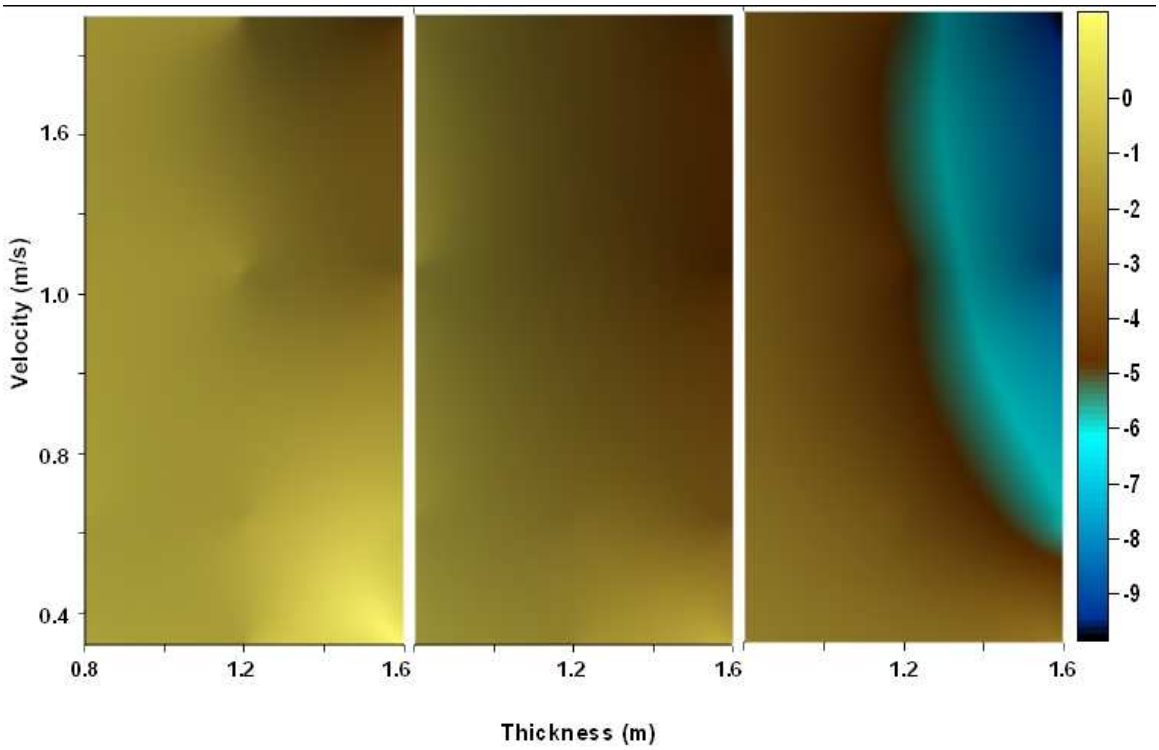

(a) $K = 2.451$ (b) $K = 1.191$ (c) $K = 0.0612$

Figure 6.15: Interpolated surface plot of peak offsets versus ice thickness and velocity for $\sigma_f = 800$kPa.

darker for the intermediate stiffness but the effect of the increasing ice thickness and velocity on the offset is clear in Figures 6.14(c) and 6.15(c). The offsets increase significantly in these graphs, as indicated by the tendency towards the blue shading corresponding to an offset of about 6m-9m. There is a clear transition point in these surface plots, which may be viewed as phase planes, depicted when a combination of velocity and ice thickness yield larger offsets. The blue region in both figures also appears to be parabolic in nature, suggesting a quadratic dependency on both the velocity and thickness.

6.4.2 Peak horizontal loads

Effect of ice thickness

The peak horizontal load versus the ice thickness is presented in Figure 6.16-6.18 for each mooring stiffness (0.612-2.451kN/m). The arrangement of figures is the same as it is for the peak horizontal offsets. In almost all cases, the peak force is monotonically increasing with ice thickness. As the thickness increases, the minimum-to-maximum range of observed data increases significantly, especially for the case of $h = 1.6$m, where the range of data is nearly 3500 tonnes. Neglecting the effect of velocity, a power law best-fit through the data results in power laws ranging from $h^{1.83}$ to $h^{2.43}$ for each of the graphs presented. Therefore, on average, the peak loads appear to increase with the square of the ice thickness. The larger power of 2.43 is a result of the increased sparsity in the data at $h = 1.6$.

Effect of mooring stiffness

For ice thickness below $h = 1.2$m, there is no significant impact of the mooring stiffness on the peak load data; the results are quite similar, although the peak offsets were up to 3m different. The resulting forces are on the order of 500-1000 tonnes for $h = 1.2m$

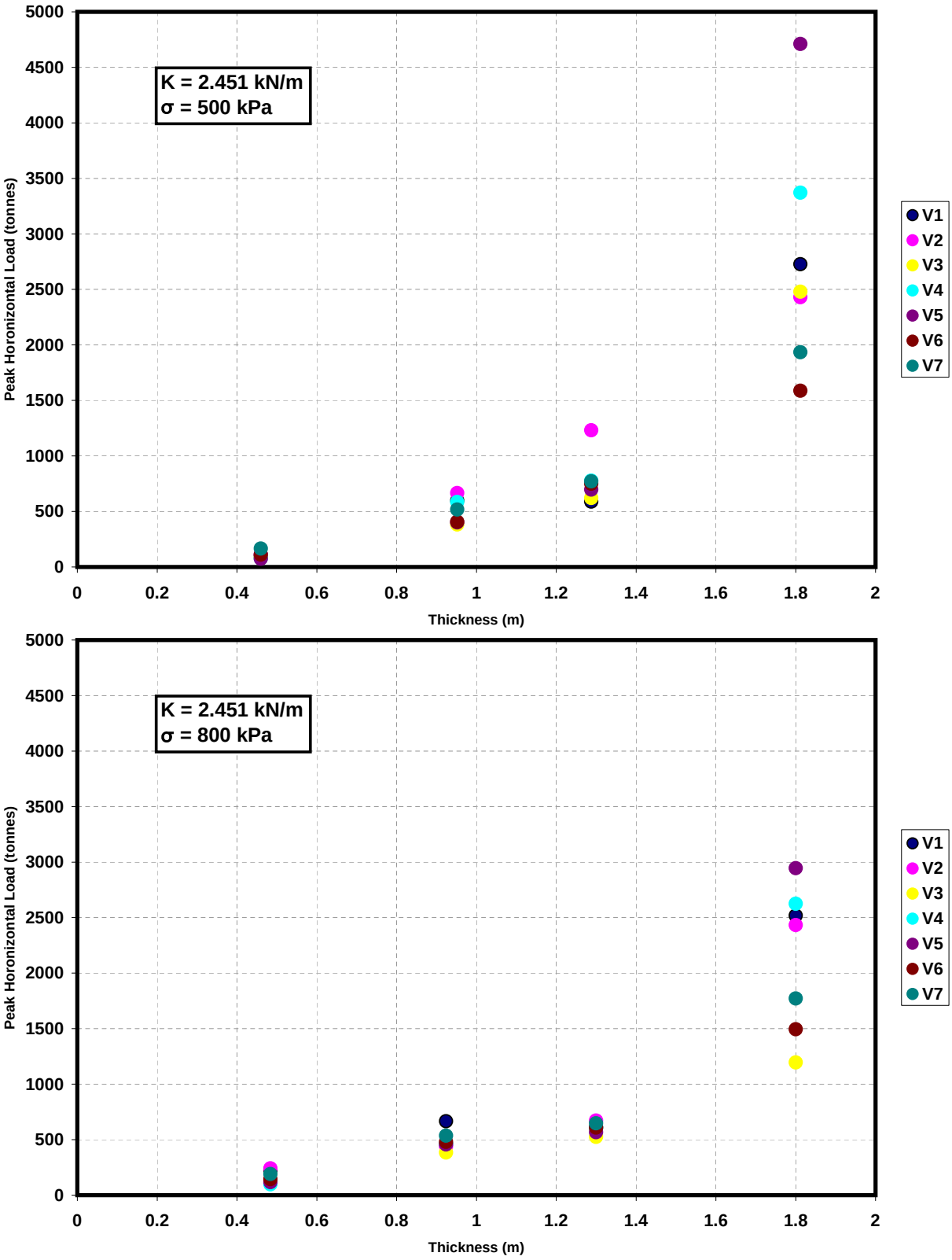

Figure 6.16: Peak horizontal load versus ice thickness for seven investigated velocities and mooring stiffness $K = 2.451$kN/m. Top: σ_f =500kPa. Bottom: σ_f =800kPa.

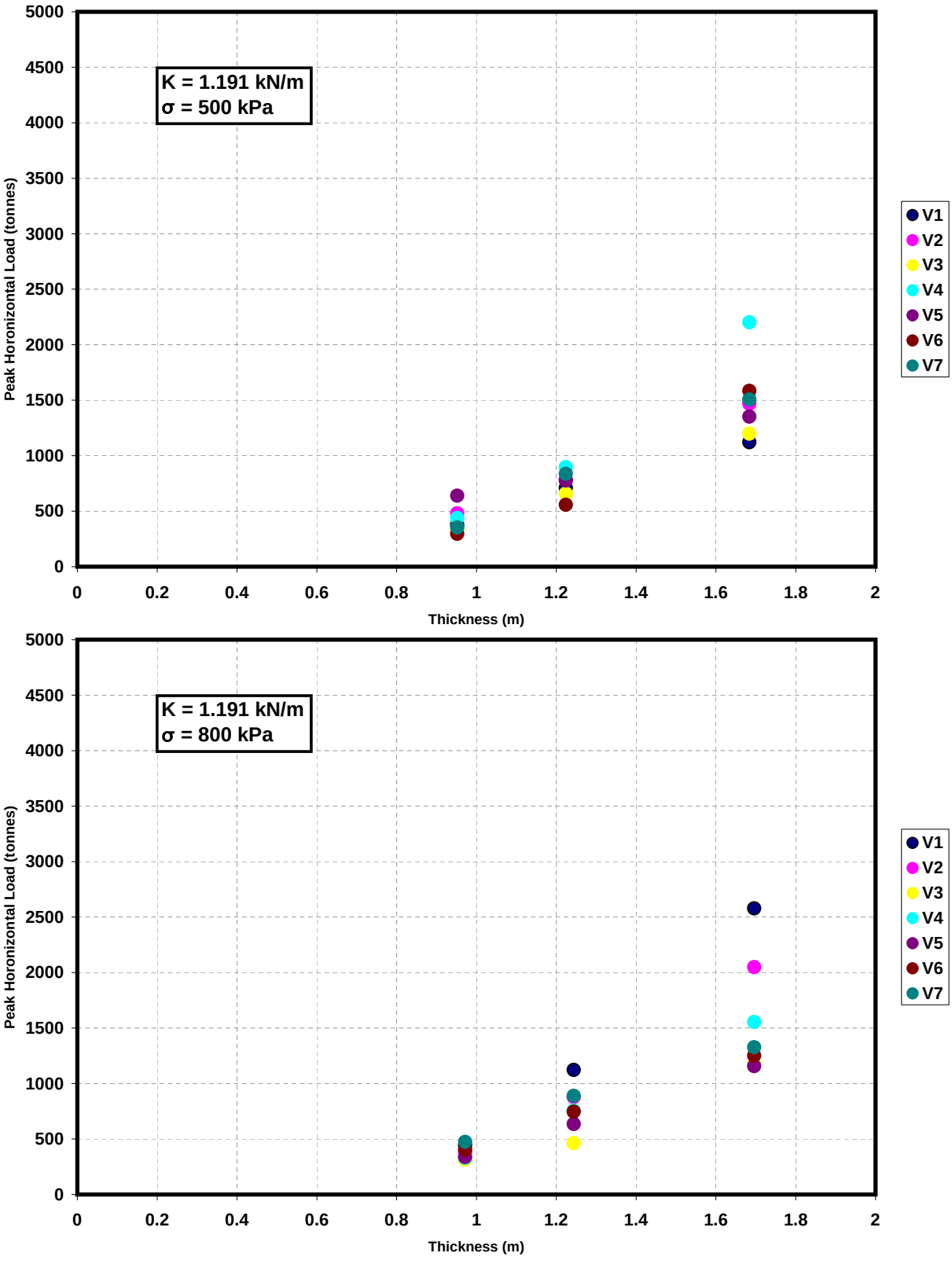

Figure 6.17: Peak horizontal load versus ice thickness for seven investigated velocities and mooring stiffness $K = 1.191$kN/m. Top: σ_f =500kPa. Bottom: σ_f =800kPa.

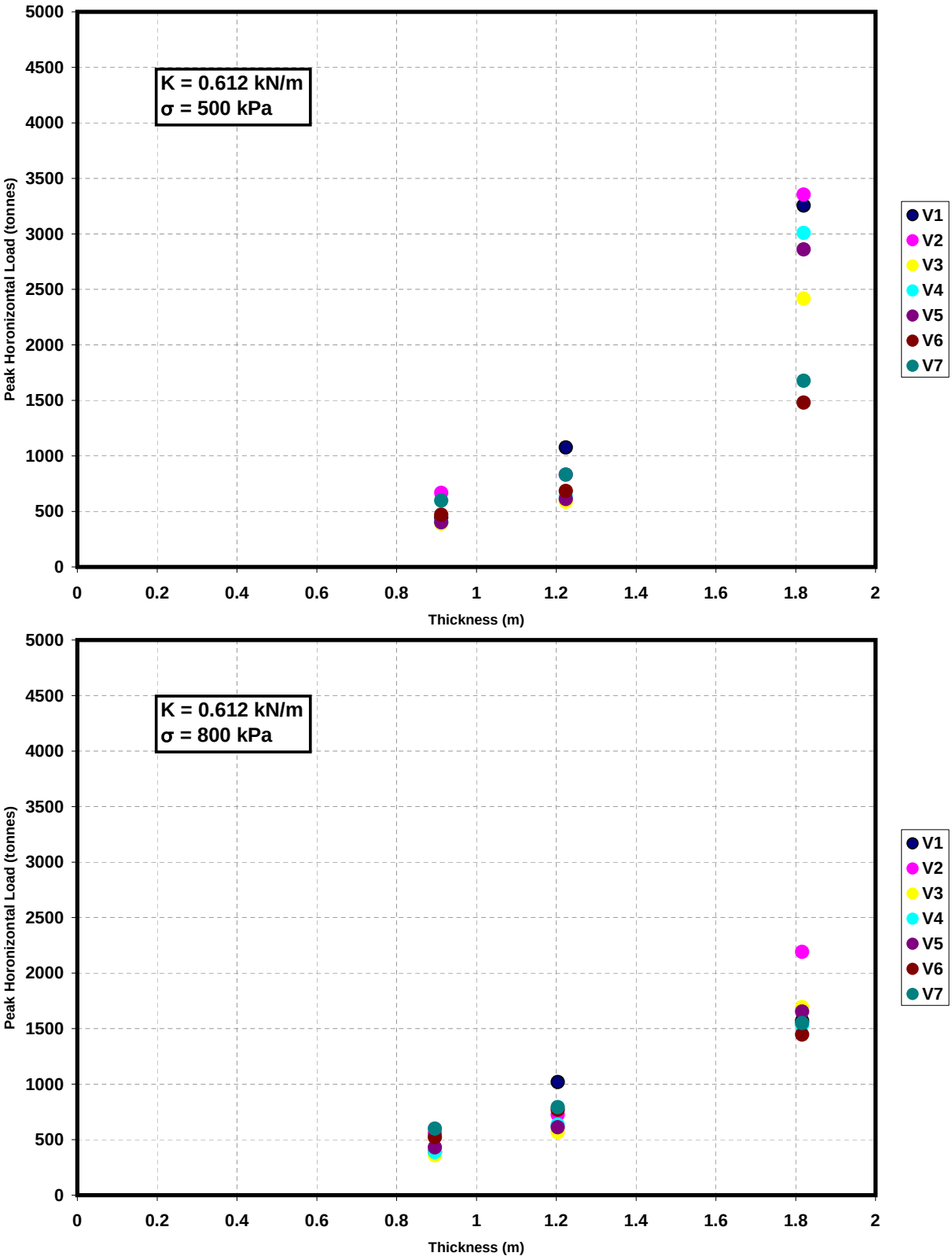

Figure 6.18: Peak horizontal load versus ice thickness for seven investigated velocities and mooring stiffness $K = 0.612$kN/m. Top: σ_f =500kPa. Bottom: σ_f =800kPa.

in for $K = 2.451$kN/m. As the stiffness decreases, the platform displacement increases but the peak loads are in the same range. At an increased ice thickness of $h = 1.6$m, the horizontal force is maximum for the stiffest system and reduces significantly for the other levels of stiffness, indicating that the effect of the stiffness on the peak load increases for increasing stiffness. This may be explained by a possible change in failure mode (from bending to shear) as the thickness increases (resulting in increased forces).

Effect of ice velocity

The peak load data is plotted versus model velocity in Figures 6.19-6.22. There

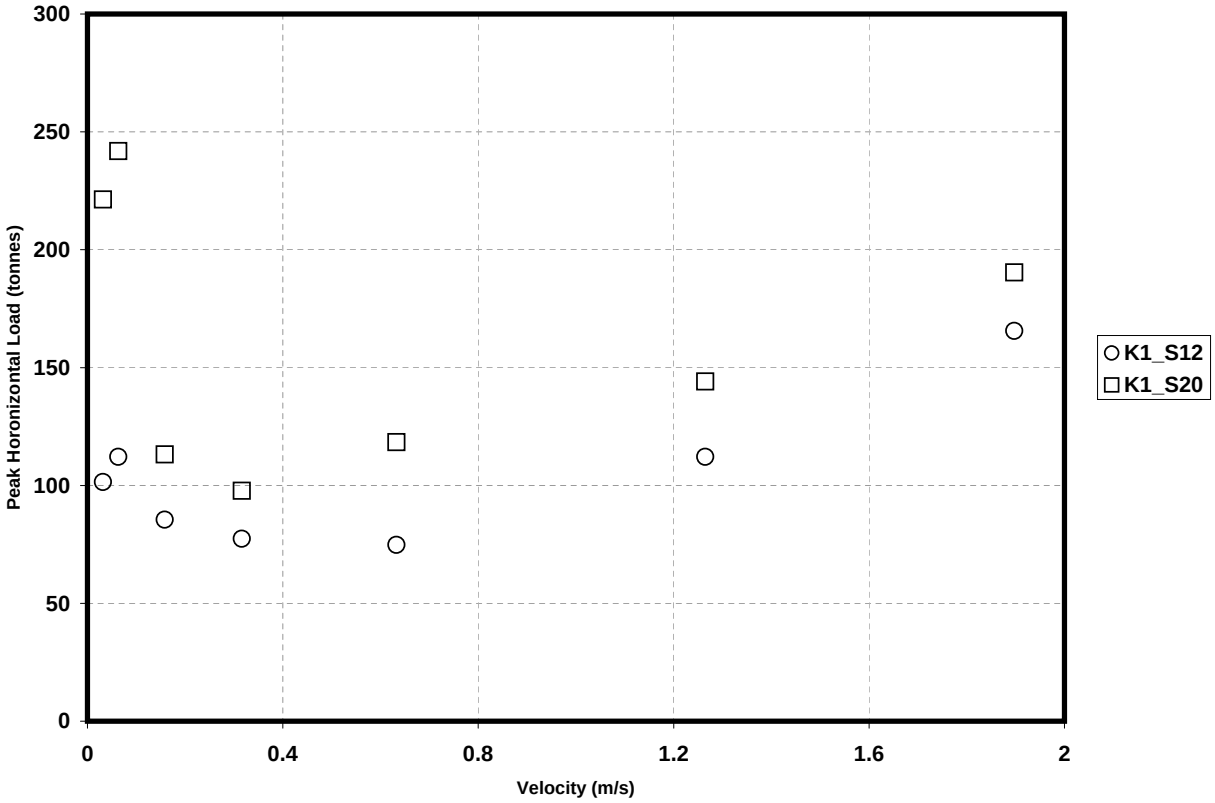

Figure 6.19: Peak horizontal load versus ice velocity for $h = 0.4$m.

appear to be two different behaviors in these graphs separated by a distinct transition

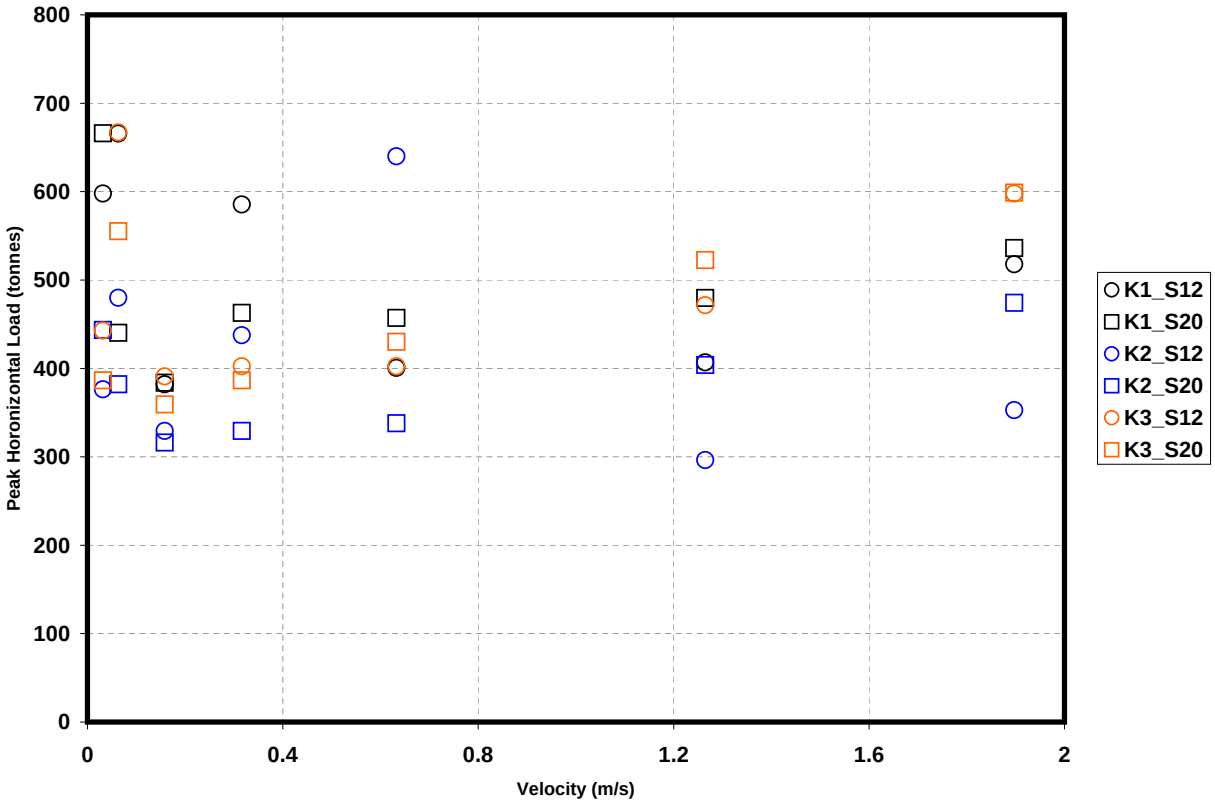

Figure 6.20: Peak horizontal load versus ice velocity for $h = 0.8$m.

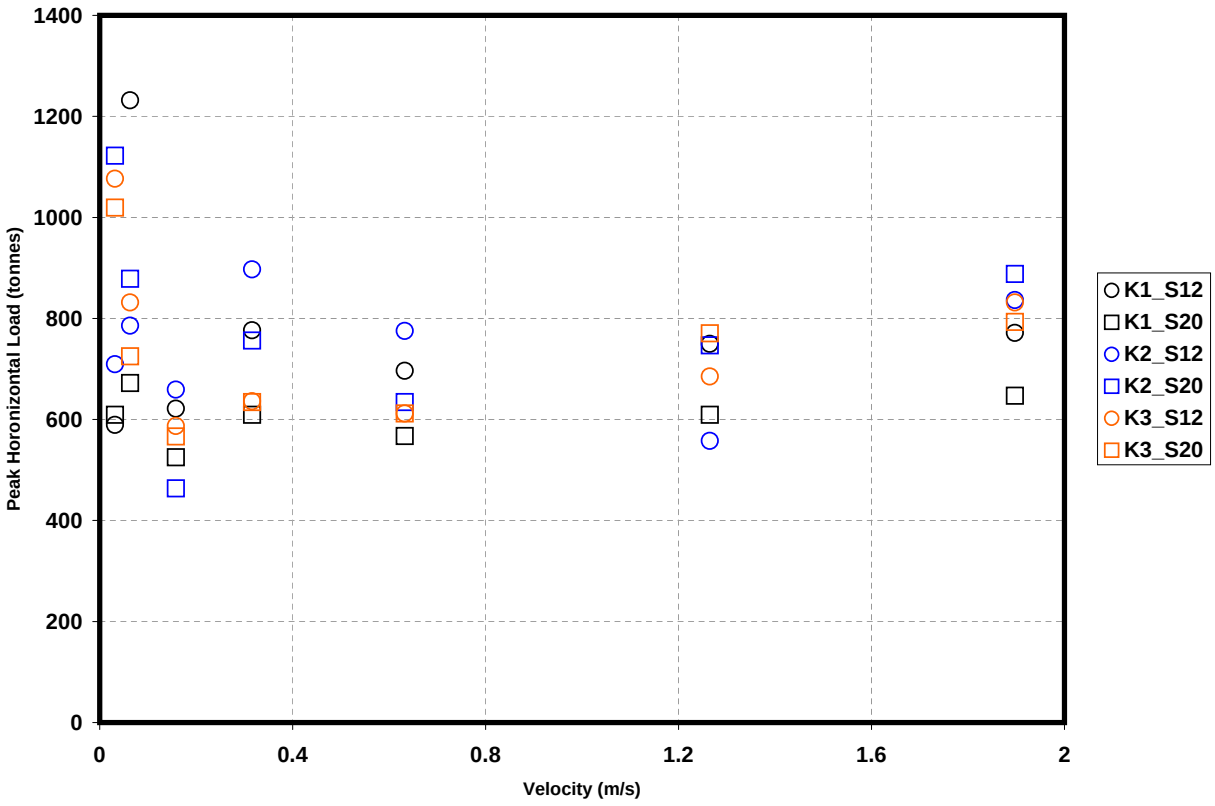

Figure 6.21: Peak horizontal load versus ice velocity for $h = 1.2$m.

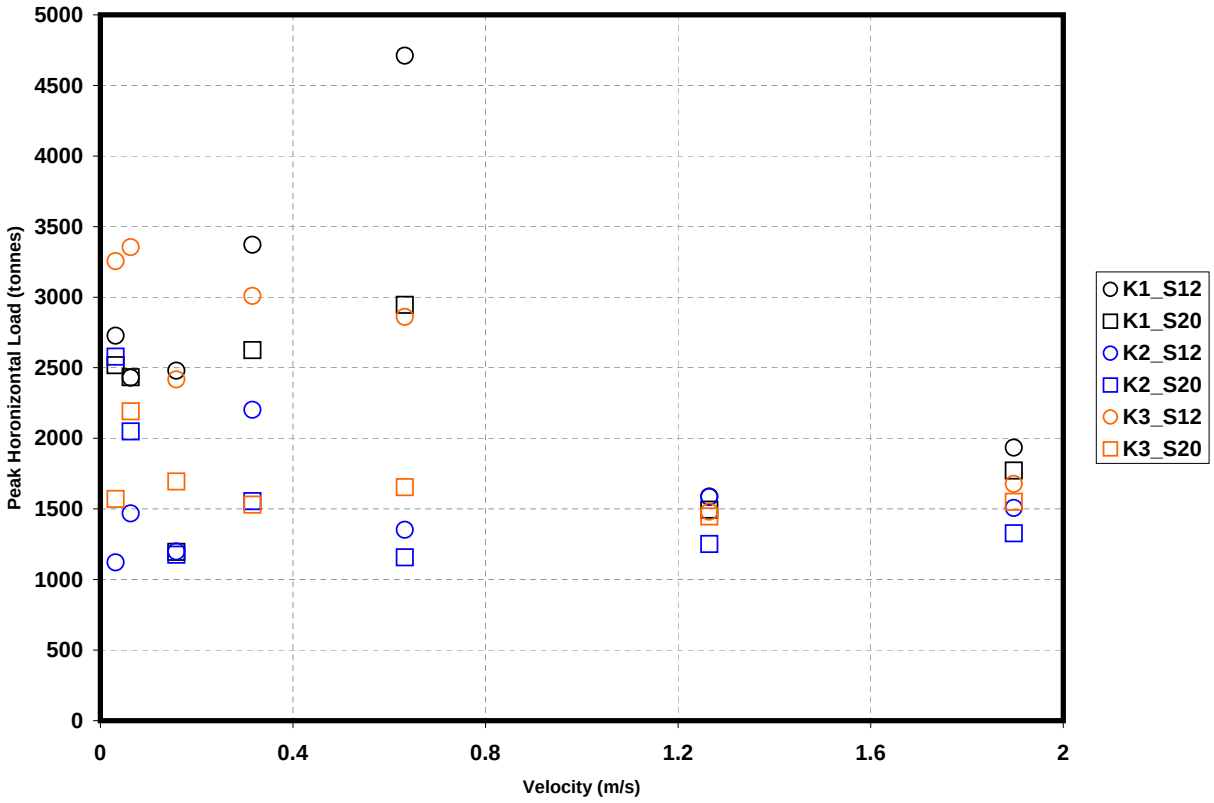

Figure 6.22: Peak horizontal load versus ice velocity for $h = 1.6$m.

velocity in each case. This difference is most clearly exhibited in Figure 6.19. For $v < 0.31$m/s, the peak load data is decreasing at a non-linear rate, and for $v \geq 0.31$m/s the dependency on the velocity appears to be linear. This is explained by the transition from ductile to brittle behavior of the ice as the velocity (and strain rate) increases. Nadreau and Michel (1984) observed that ice behaves as a linear elastic ductile material for small strain rates, but as the strain rate increases (above $10^{-3}\ s^{-1}$), the failure is observed as brittle. Empirical relationships relating the strain rate to velocity v and structure diameter D of the form

$$\dot{\epsilon} = \frac{v}{nD} \tag{6.4}$$

have been presented by Toussaint (1977) ($n = 4$), Ralston (1978) ($n = 2$), and Palmer et al. (1983) ($n = 1$). Given a diameter of $D = 70$m at ice impact, the resulting strain rates are in the range

- $0.56 \times 10^{-3} - 2.26 \times 10^{-3}$ for $v < 0.31$m/s; and
- $1.13 \times 10^{-3} - 4.52 \times 10^{-3}$m/s for $v \geq 0.31$m/s.

The lower bounds on each of these ranges result from equation (6.4) with $n = 4$. These lower bounds classify the ice behavior as ductile for $v < 0.31$m/s and brittle for $v \geq 0.31$m/s according to Nadreau and Michel (1984), and therefore explain the transition observed in the data in Figures 6.19. This transition is less pronounced in Figures 6.20-6.22 due to the scatter in the data but is still present. The velocity at which transition occurs also increases as the ice thickness increases. Extrapolating from where the linear behavior appears to meet the non-linear behavior, transition appears to occur at approximately $v = 0.31$m/s for $h = 0.4$m, $v = 0.4$m/s for $h = 0.8$m, $v = 0.5$m/s for $h = 1.2$m and $v = 0.6$m/s for $h = 1.6$m.

Due to this difference in constitutive behavior, there are two regimes in which the

velocity has an effect on peak loads. In the brittle regime which is of key interest in this thesis, the peak loads increase slightly with velocity. When the ice behaves as a ductile material, the behavior is also dependent on the thickness - at low thickness, the load decreases with increasing velocity, but as the thickness of the ice increases to $h = 1.6$m, the results are much more sporadic and not much of a pattern is observable. Surprisingly, the maximum force does not occur at maximum velocity. As a result of these regimes, the peak force in most cases occurs at $v = 0.03 - 0.06$m/s in the ductile regime.

Effect of flexural strength

As was the case for the peak offsets, the flexural strength does not have a significant effect on the peak ice loads, especially at higher velocities when the ice behaves as a brittle material.

Summary

The peak horizontal loads are influenced predominantly by the thickness and velocity but also slightly by mooring stiffness. To visualize this dependency, the offset is plotted versus the velocity and thickness on a three-dimensional axis for each stiffness and interpolated to create surface plots. The results of the analysis are given in Figures 6.23 and 6.24 for each flexural strength. In all cases, the maximum loads occur at the smallest velocity and highest thickness as indicated by the light blue to brown shading, with the absolute maximum occurring for the stiffest mooring configuration ($K = 2.451$kN/m). Based upon these results, the intermediate stiffness, $K = 1.191$kN/m, yields the lowest overall loads. Figure 6.23(b) contains only a small area of brown shading (corresponding to approximately 2400 tonnes) and Figure 6.24(b) contains the least area of light blue shading (corresponding to approximately 1600 tonnes). Combining this observation with the peak offset results, it is

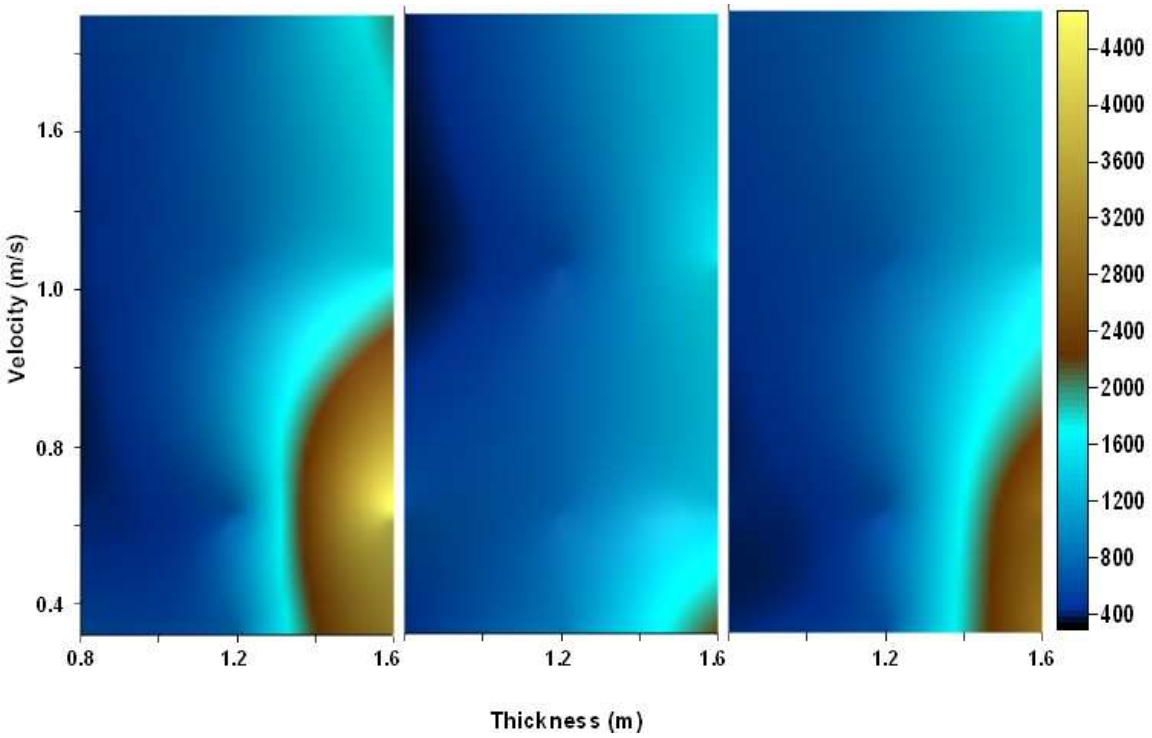

(a) $K = 2.451$ (b) $K = 1.191$ (c) $K = 0.0612$

Figure 6.23: Interpolated surface plot of peak load versus ice thickness and velocity for $\sigma_f = 500$kPa.

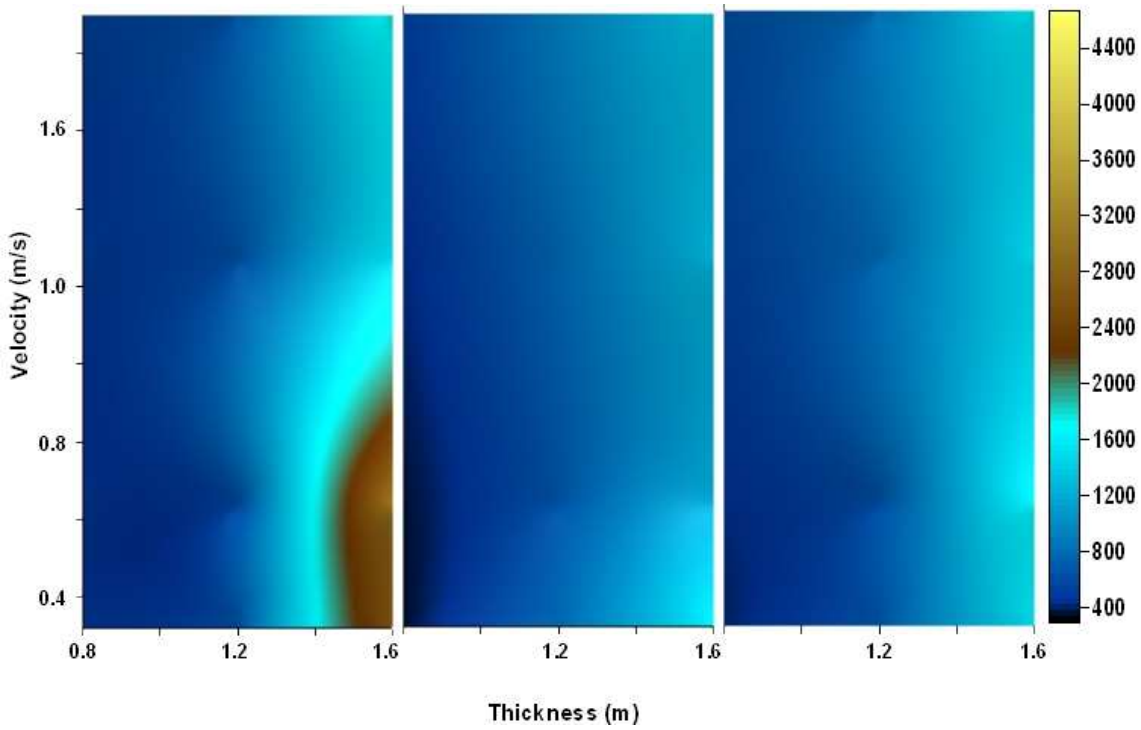

(a) $K = 2.451$ (b) $K = 1.191$ (c) $K = 0.0612$

Figure 6.24: Interpolated surface plot of peak load versus ice thickness and velocity for $\sigma_f = 800$kPa.

evident that there is an optimal value for the mooring stiffness which could minimize the expected peak loads by allowing the platform a slightly larger displacement (in comparison to the stiffest system available).

6.4.3 Comparison with previous results

The current peak load data, scaled according to equations (5.9)-(5.10), is plotted along with the full-scale results of Wright et al. (1998) and the three previous experiments (Nixon and Ettema, 1987; Wessels and Iyer, 1985; Comfort et al., 1982) in Figure 6.25. The data points are in good agreement with the full-scale results for the smallest thickness, $h = 0.4$m. Then, for increasing thickness, although the data points are consistent with the previous experimental studies for $h \leq 1.4$m, they are over-predicting the peak force (in comparison to the full-scale results) by 200-300%. The peak force increases much faster in the current experiments than was observed in the full-scale data measurements but was consistent with analytical formulae (Edwards and Croasdale, 1976b; Ralston, 1977; Nevel, 1992) and empirical observations (Afanas'ev et al., 1973; Edwards and Croasdale, 1976a; Pearce and Strickland, 1979; Brooks, 1981; Hirayama and Obara, 1986; Kato, 1986) for forces on inclined structures which display a power of two dependency on the ice thickness. In the three other experiments, the overestimate of peak loads was attributed to the model ice material properties or the high friction coefficients or flexural strengths of the ice. Neither of these is the case in this experiment, yet the peak load results are much higher. Another observation in the previous tests was that a larger rubble pile formed in front of the structure than was observed in the field. This would explain the larger ice loads, since the build-up of ice in front of the structure would cause increased clearing loads.

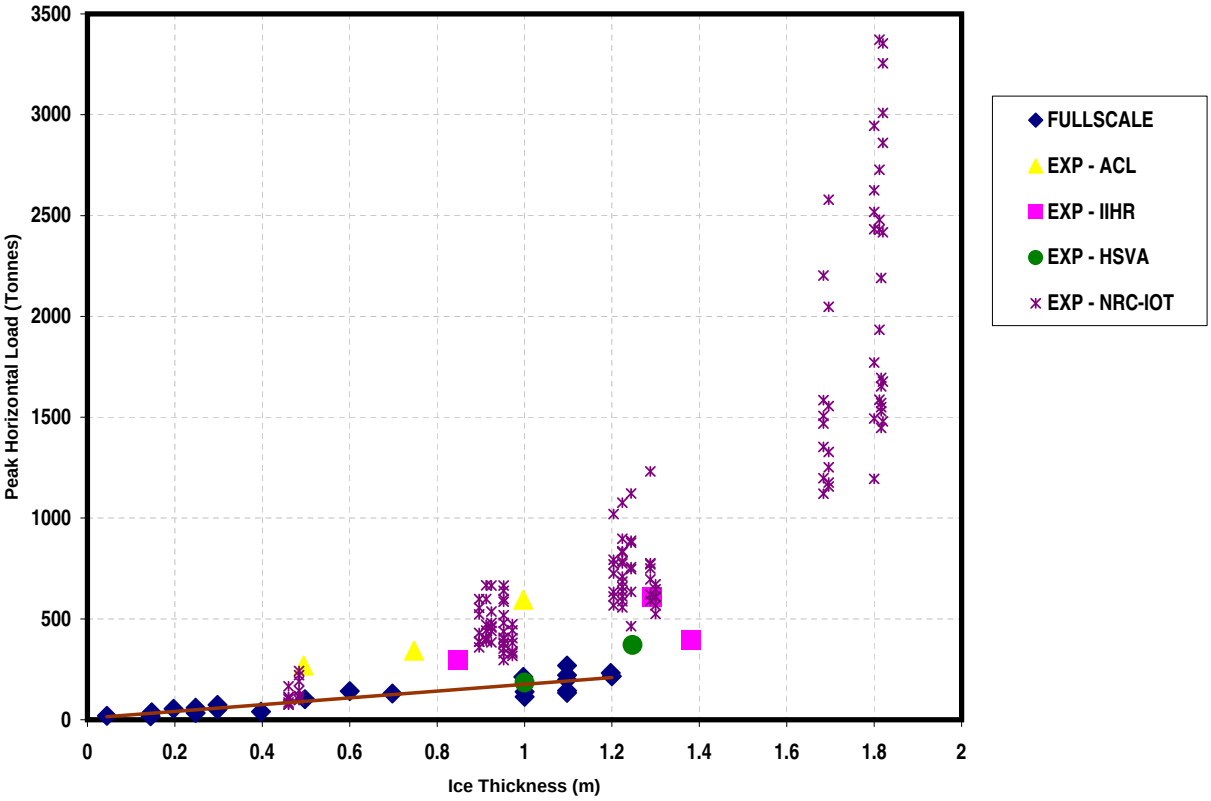

Figure 6.25: The current experiment peak load data plotted with the full-scale data of Wright et al. (1998) and the three previous experimental studies.

6.5 Summary

This chapter presented the results of 140 experiments conducted in level ice using a 1:40 scale Kulluk model. The tests were performed in the ice tank at the NRC-IOT in St. John's, Newfoundland. The results indicate that peak offsets may be limited by increasing the mooring stiffness but this causes a subsequent increase in the peak mooring force. Both ductile and brittle behavior of the ice was observed in the experiments as the velocity was varied. The peak observed loads are larger than those observed in the field but agree with the three previous experiments involving an inverted conical structure and also with the power of two dependency laws put forth in previous analytical and empirical studies.

Chapter 7

Computational Study

7.1 Introduction

The purpose of this chapter is to simulate the response of a full-scale Kulluk drilling barge in level unbroken ice using DECICE. This includes an investigation of the ice loads and description of the subsequent ice-structure interaction. The key parameters of the investigation which are derived from the experimental tests conducted at the NRC-IOT are given in Table 7.1. In the main series of simulations, the effect of a moving ice sheet on a moored drilling structure is addressed. Select trials will also be conducted to compare the response of the moored structure with a fixed structure. Unless otherwise noted, the numerical problem set-up for the moored response will be identical to that of the fixed structure.

Parameter	Experiments	Numerical Model
Ice thickness h (m)	0.4-1.6	0.4-1.6
Ice velocity v (m/s)	0.03-1.9	0.25-1.0
Flexural strength σ_f (kPa)	500, 800	500,800

Table 7.1: Range of parameters to be investigated numerically.

7.2 Numerical Set-up

The ice cone interaction model was constructed in DECICE and solved using the explicit solution scheme described in Chapter 2, with the default time-step. According to field and experimental investigations, it is possible that the crushing mode of failure may occur at the leading edge of the ice sheet. Correct modeling of this mechanism is currently beyond the scope of the numerical capabilities of the DECICE code, both for physical modeling and computational reasons.

Due to the axi-symmetric nature of the problem (and to save computational effort), only half of the problem is modeled numerically using DECICE. The basic problem geometry, at time $t = 0$s, is shown in Figure 7.1. The key components are: (1) the rigid structure; (2) the level ice sheet; (3) the push block; and (4) the symmetry plane. Each of the key components is discussed in the following subsections.

7.2.1 Modeling the structure

The physical dimensions of the numerical Kulluk drillship were modeled as closely as possible to the true full-scale ship. Figure 7.2 shows the dimensions and measurements used in the current experiments, and the geometrical properties are summarized in Table 7.2 The ship is modeled as a 24-sided (12-sided due to the symmetry plane) conical structure with a 81m deck diameter and 67.8m waterline diameter. The slope at waterline is 31.5° and decreases the diameter of the platform to a minimum of 56.5 meters before flaring out at the bottom of the structure. Since the curvature of the hull has to be approximated with polygons, the slope of the model changes from 31.5° at waterline to 60° and then 90° from top to bottom. The hull "skirt" is located 9.8 meters below the waterline and slopes away from the structure at approximately a 45° angle. The total height of the platform is 18.4 meters and the vertical center of

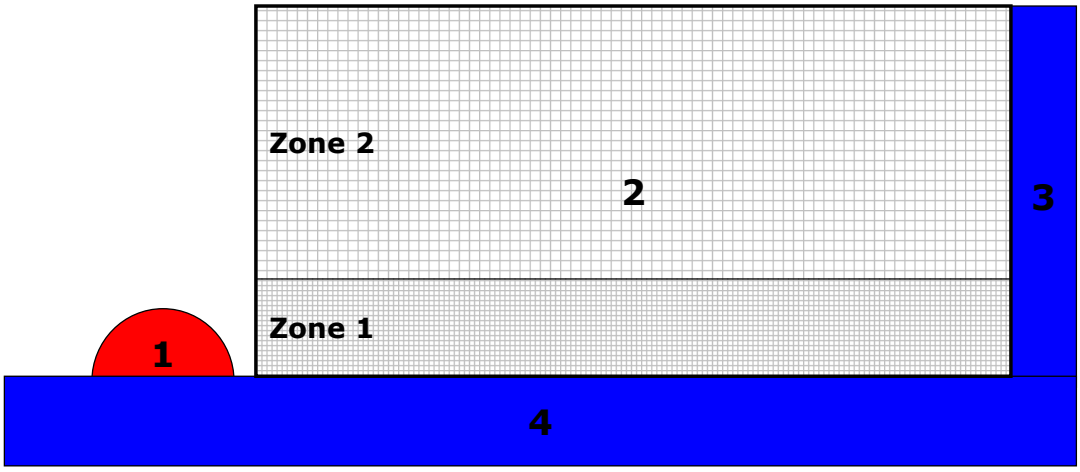

(a) schematic view

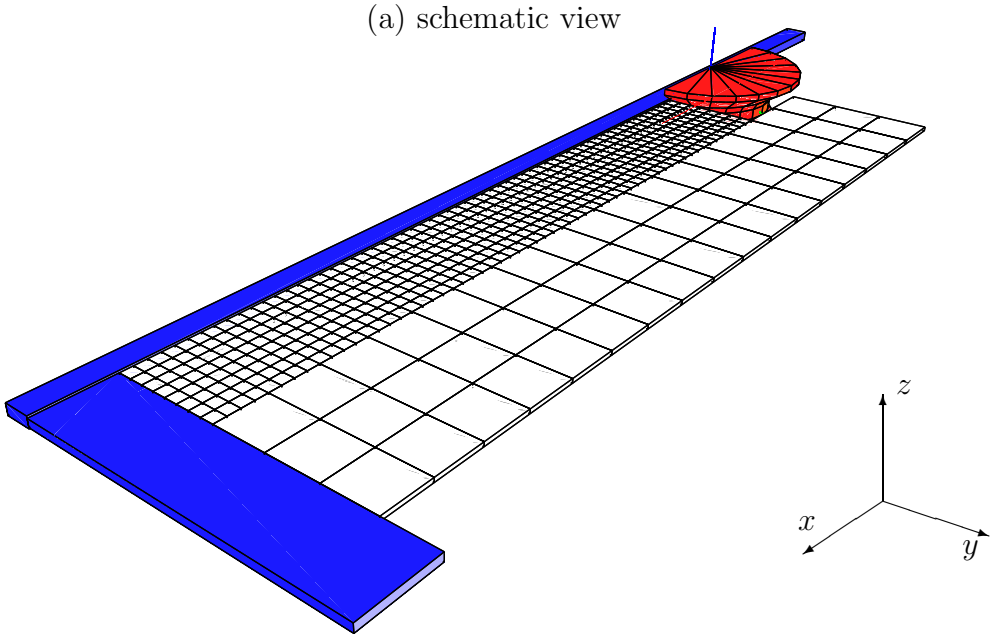

(b) numerical model constructed and positive coordinate system

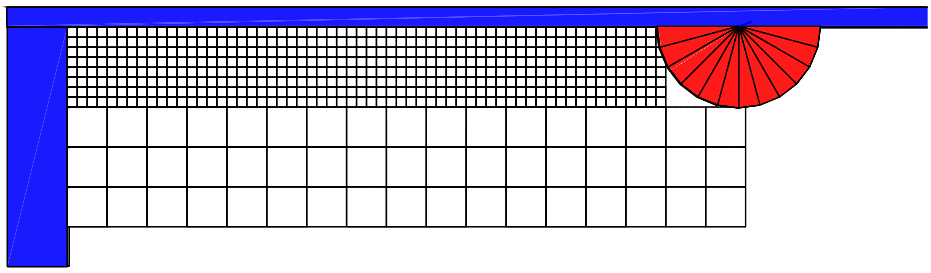

(c) plan view of numerical model

Figure 7.1: Typical problem geometry used in the numerical simulations.

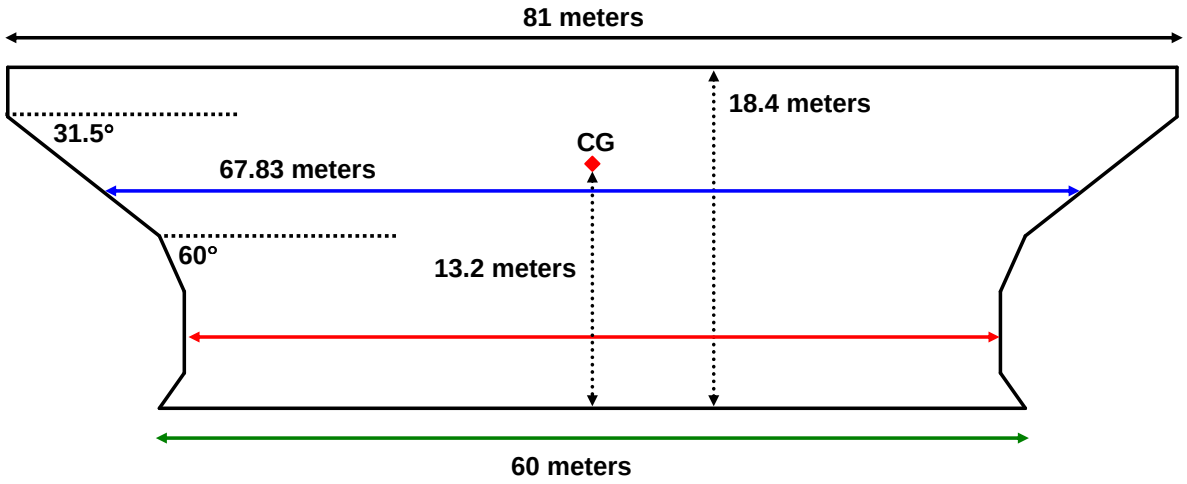

(a) Side profile

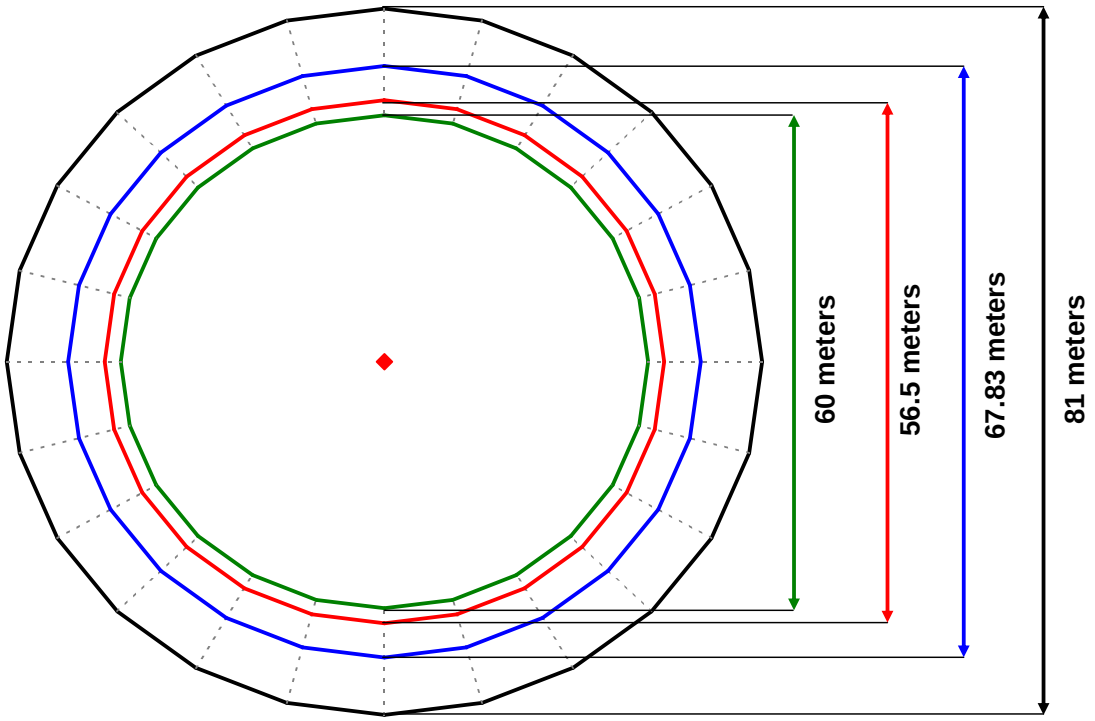

(b) Plan view

Figure 7.2: Dimensions of the numerical model representing the Kulluk drillship.

Property	Value
Overall beam (m)	81.00
Waterline beam (m)	67.83
Beam at bottom (m)	60
Depth (m)	18.4
Draft (m)	11.7
Slope at waterline (degrees)	31.5
Displacement (kg)	27999000
Vertical center of gravity (m)	13.2
Vertical moment mass (kg·m)	14.4092×10^9

Table 7.2: Geometrical and mechanical parameters of the ice sheet.

gravity is located 13.2 meters from the base of the structure.

The Kulluk is modeled as a rigid element (i.e., no deformation permitted). In most of the simulations the platform is moored, but as noted there are cases in which it is fixed. In these cases larger horizontal loads are expected due to the non-compliance of the ship.

7.2.2 Modeling the ice

Ice behaves as a linear elastic ductile material for small strain rates, but as the strain rate increases ($> 10^{-3}\ s^{-1}$) the failure is observed as brittle (Nadreau and Michel, 1984). Several empirical relationships of the form

$$\dot{\epsilon} = \frac{v_i}{nD} \tag{7.1}$$

have been presented to relate strain-rates to the ice-indentation velocity, v_i, and structure diameter, D ($n = 4$, Toussaint (1977); $n = 2$, Ralston (1978); $n = 1$, Palmer et al. (1983)). The measured velocity of ice floes in the Beaufort Sea, where the Kulluk drillship operated was 0.18-0.35m/s (Bercha, 1985) and the waterline diameter of the ship is approximately 70 meters (Barker et al., 2000b). Resultant strain rates

based on equation 7.1 are in the range $0.5 - 5 \times 10^{-3}\ s^{-1}$. The velocity and diameter in the numerical simulations yield strain rates in the range $0.9 - 15 \times 10^{-3}$. Ice is therefore modeled as an isotropic elastic brittle material in the numerical simulations, following from the above analysis of Nadreau and Michel (1984).

The discrete element division of the 300m by 100m ice plate is composed of two zones of plate-bending elements. The first zone, discretized with 5×5m elements, is the section of the ice sheet representing the channel that a moving structure would pass through. During the simulations almost all of the failure occurs in this zone. The second zone is discretized with elements which are scaled by four in length and width but have the same ice thickness. Increasing the width of this zone did not have a significant impact on the simulations, since failure typically occurred in the first zone, which was welded to the symmetry block.

Earlier studies using DECICE have shown that the peak forces and fracture patterns are relatively independent of the mesh, provided that the mesh is initially well-conceived, based upon previous experience with the problem under investigation (Intera Technologies Inc., 1984). Observations on sloping conical structures indicate that the ice sheet fractures into pieces with a diameter of 10-20 times the ice thickness. Sheet ice with a larger thickness generally fractures into smaller pieces (i.e., smaller than 10 times the thickness). The ice thickness in this investigation is 0.4-1.6m which suggests that the thinnest ice will fracture into pieces with a diameter of 4.0m and thicker ice will fracture into pieces of 16.0m (or less, since thicker ice fractures into smaller pieces). The current discretizetion of 5m-long and 5m-wide ice pieces permits fracturing of the ice into pieces of approximately a 2.5m diameter (of the circumscribed circle/sphere), which is well below the observed fracture piece size.

Plate-bending elements are used to model the ice as implemented by Mustoe et al. (1987) within DECICE using the rigid spring element approximation. Each bending element is composed of four discrete deformable elements joined together with a series

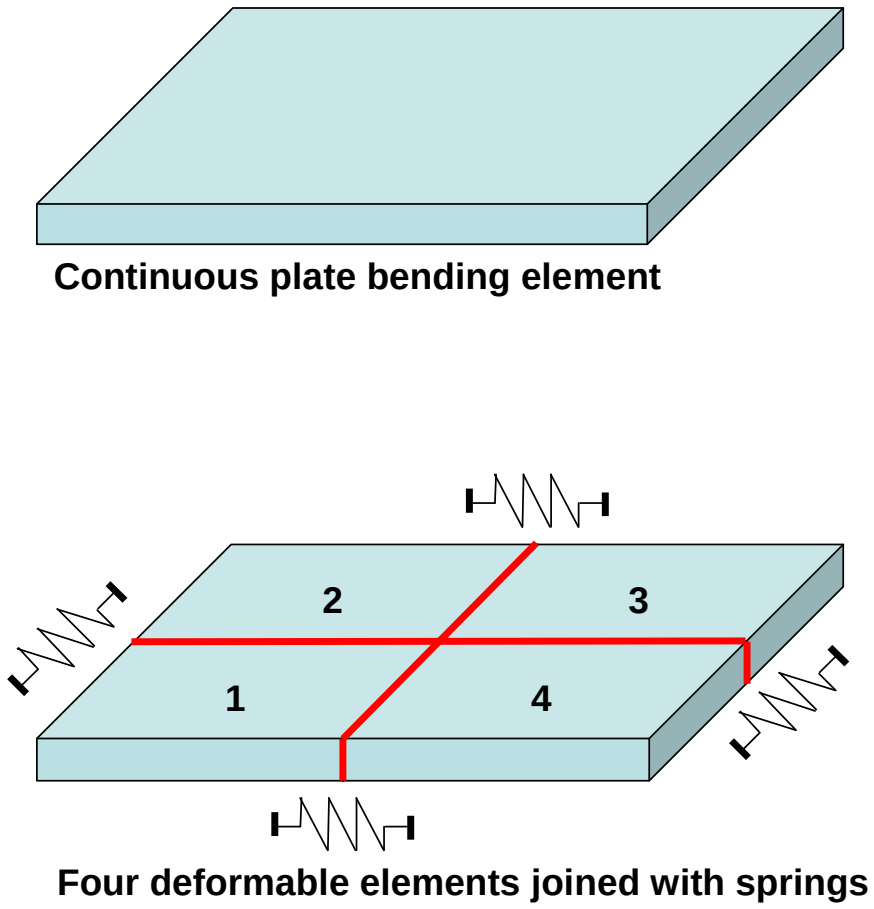

Figure 7.3: Plate element consisting of four elements locked together along common mesh faces with stiffness calculated by equating the curvature to the curvature of a Euler beam subject to bending.

mass approach (Kawai et al., 1978), which requires replacing the mass and stiffness coefficients with effective mass and stiffness terms based upon the geometry, material

properties, and bending moments of the plate element as

$$k = \frac{2EI}{l_{\text{avg}} h^2} \tag{7.2}$$

where E is the elastic modulus, I is the second moment of area, l_{avg} is the average length of the elements, and h is the plate thickness. For more information, or a convergence analysis, see Mustoe et al. (1987); Mustoe (1992). It should be noted that when these plate-bending elements are locked together, the program generated stiffness coefficients automatically replace the user specified stiffness coefficients along the inter-element mesh lines. Specifying an inter-element stiffness of the ice-sheet is therefore redundant until the plate fails, but for practical purposes it is set to the same value as the ice-structure stiffness coefficient.

The failure model is Mohr-Coulomb with tension cut-off. Compressive (shear), tensile, and flexural failure can occur, but the anticipated dominant mode of failure for the problem under consideration is flexural. The plate-bending elements are permitted to fracture both through their centroid (as previously described for each mode of failure) and along inter-element mesh lines. Since fracturing along meshlines specifies the orientation of the fracture plane, this type of failure typically occurs later than failure within an element. Upon fracture, numerical stability is maintained by preserving kinetic energy and releasing strain energy into the cracked elements over the time-steps following failure. In addition to exceeding the failure criteria, an element is only permitted to crack if it is adjacent to a free edge (or previously cracked element) and if neither of its neighbors is further from the failure criteria than is the element under consideration. This requirement ensures that fractures propagate through the ice sheet in a direction which originates at the point of contact of with the structure.

7.2.3 Symmetry and Push Block

Two other rigid elements are required. The first acts as a symmetry plane, and the second is a rigid block which pushes the ice-sheet at the desired velocity. The symmetry plane is completed fixed with a friction coefficient of 0.0 so that it does not slow the movement of the oncoming ice sheet. The symmetry plane extends approximately 2.2 meters below the water line. Clearing is expected to proceed in the direction away from this symmetry block, but ice pieces may move under it when large rubble piles form. A similar symmetry block was also used by Lau (2001). The push block also has a null friction coefficient and movement is constrained in all but the x-direction.

7.2.4 Damping

Since the solution procedure is based upon a super-position of the dominant modes of vibration, the choice of damping coefficients can have a large effect on the behavior of the ice-structure interaction. There are three main modes of vibration in a system involving multiple interacting bodes which lead to the three types of damping: rigid body motion, deformation, and inter-element vibration. DECICE allows for three types of damping to reduce the oscillations: mass damping, internal damping, and stiffness damping.

Mass damping and internal damping are used to damp the rigid body motion and internal deformation of elements. Since the equations of motion and deformation for elements within DECICE are decoupled, this means that the damping terms apply to a separate set of equations during the solution scheme, one for rigid body motion and one for deformation. Mass damping acts as a drag force in a simulation in which the damped elements are in motion, and internal damping reduces the non-physical

oscillation of deformable elements as forces are applied at their boundaries.

Stiffness damping is more of a non-physical quantity which is implemented to damp the inter-element springs representing contact points. This type of damping can lead to non-physical adhesion forces and the presence of unreal inter-element forces during the contact phase of two elements. For that reason, it is better to avoid the use of this type of damping in numerical simulations.

The choice of damping coefficients depends on the material and geometric properties of the constructed system. Care should be taken in the choice of these parameters because the under-damped, critically damped, and over-damped response may induce different system behaviors. For example, if the rigid body motion is critically damped, the problem reduces quickly to its equilibrium when static problems are solved, but in the dynamic problem it results in a non-physical behavior (the drag force eliminates the movement of the damped elements). Over-damping the rigid body vibrational mode of the system will also result in varied results since the system is typically controlled by rigid body motion. The user manual suggests using a fraction of the lowest dominant rigid body vibration frequency. The internal deformation modes of vibration usually occur at much higher frequencies than do rigid body modes. Since these are secondary oscillations, they should be critically damped.

To determine the dominant modes of vibration, the easiest strategy is to first run the problem without any damping. Then, utilize the kinetic or strain energies or the stress/strain in order to estimate the fundamental frequencies of rigid body and internal deformation. The procedure of Lau (2001) and Intera Technologies Inc. (1986) suggests determining dominant modes from the kinetic and strain energies after a vertical impulse is applied to the floating, undamped ice sheet. To determine

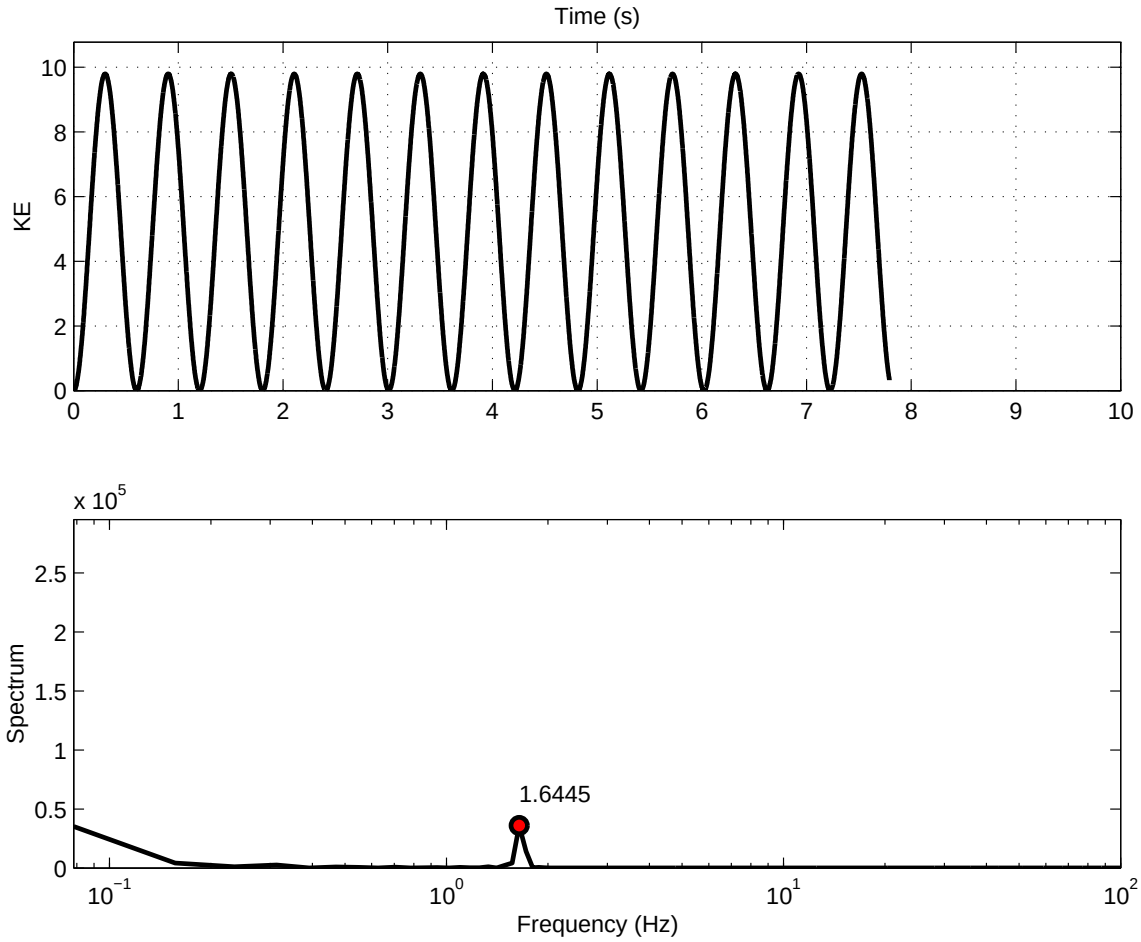

Figure 7.4: Plot of kinetic energy versus time in 0.4m thick sheet ice (top) and power spectral density of the kinetic displaying the dominant modes of vibration (bottom). The labeled frequency represents the dominant rigid body mode.

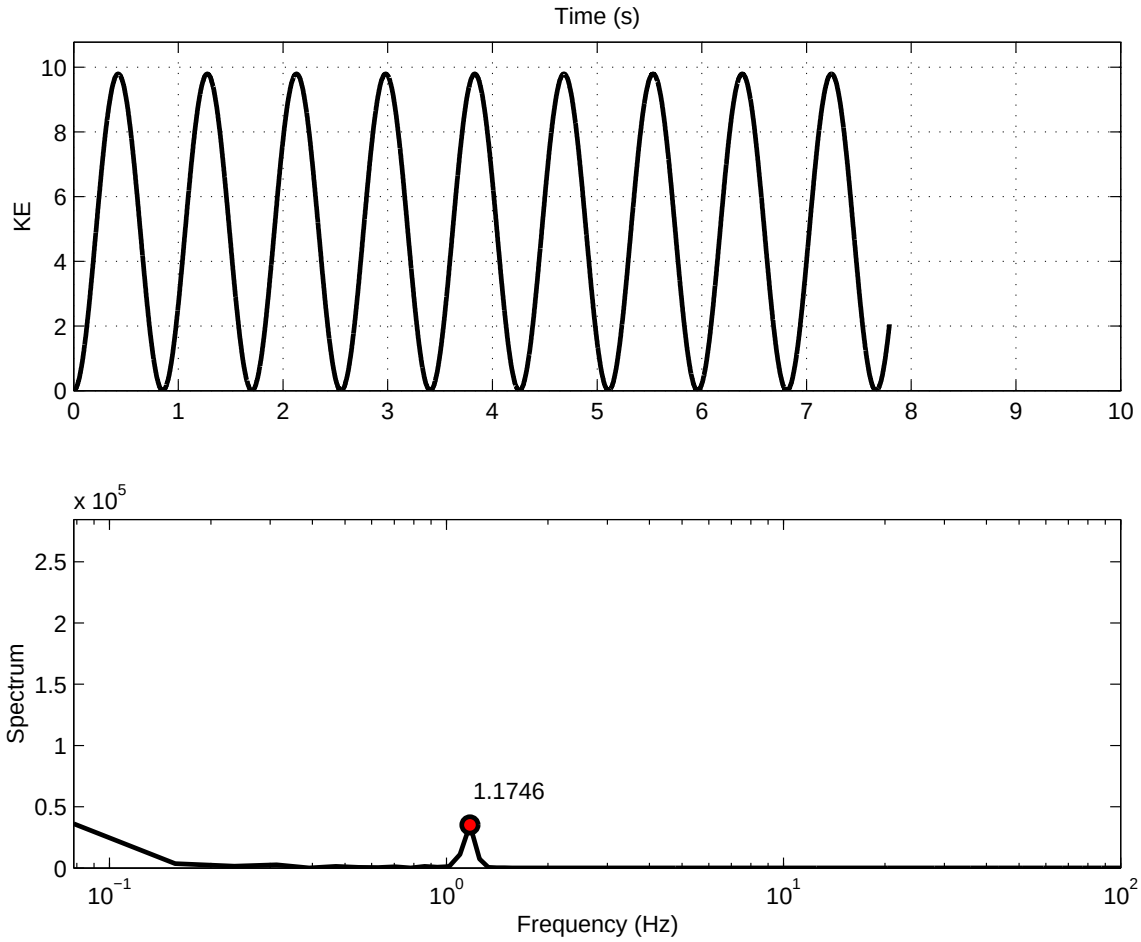

Figure 7.5: Plot of kinetic energy versus time in 0.8m thick sheet ice (top) and power spectral density of the kinetic displaying the dominant modes of vibration (bottom). The labeled frequency represents the dominant rigid body mode.

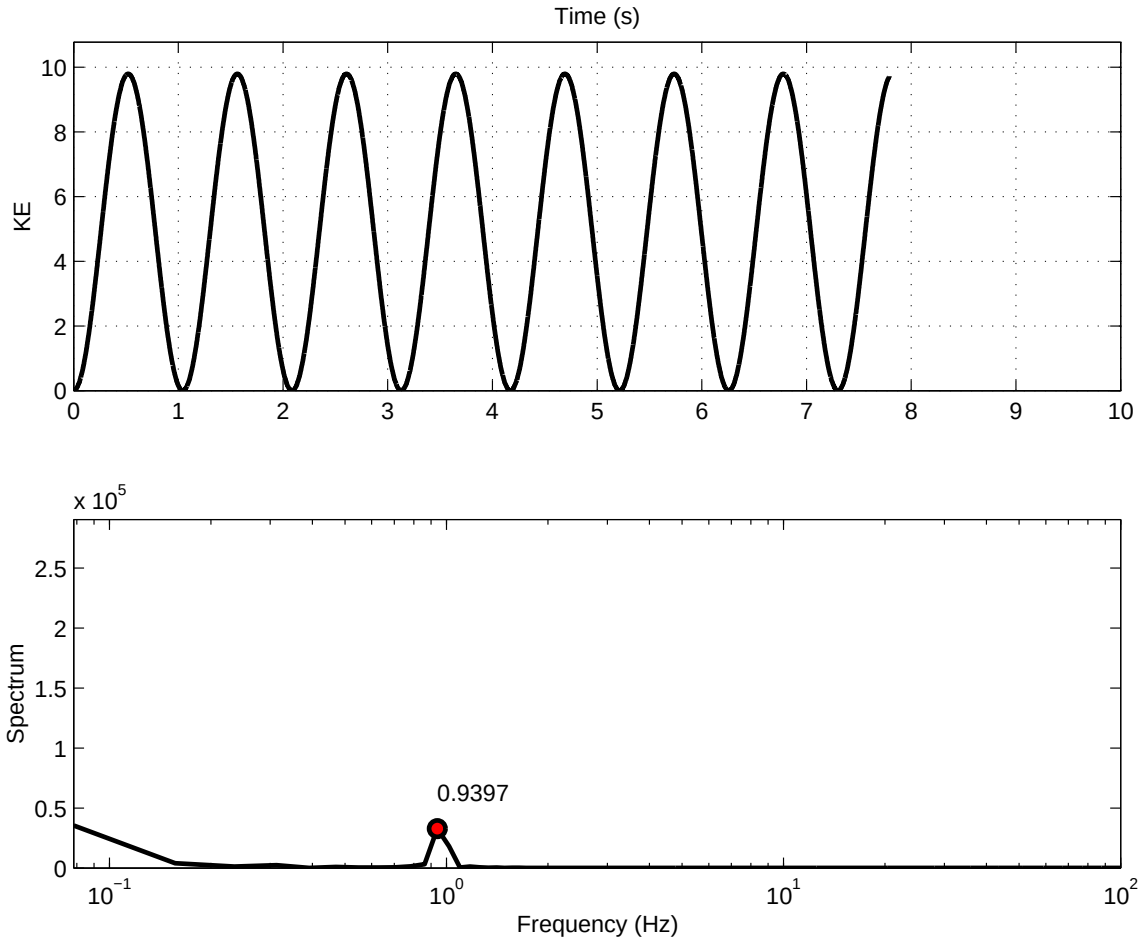

Figure 7.6: Plot of kinetic energy versus time in 1.2m thick sheet ice (top) and power spectral density of the kinetic displaying the dominant modes of vibration (bottom). The labeled frequency represents the dominant rigid body mode.

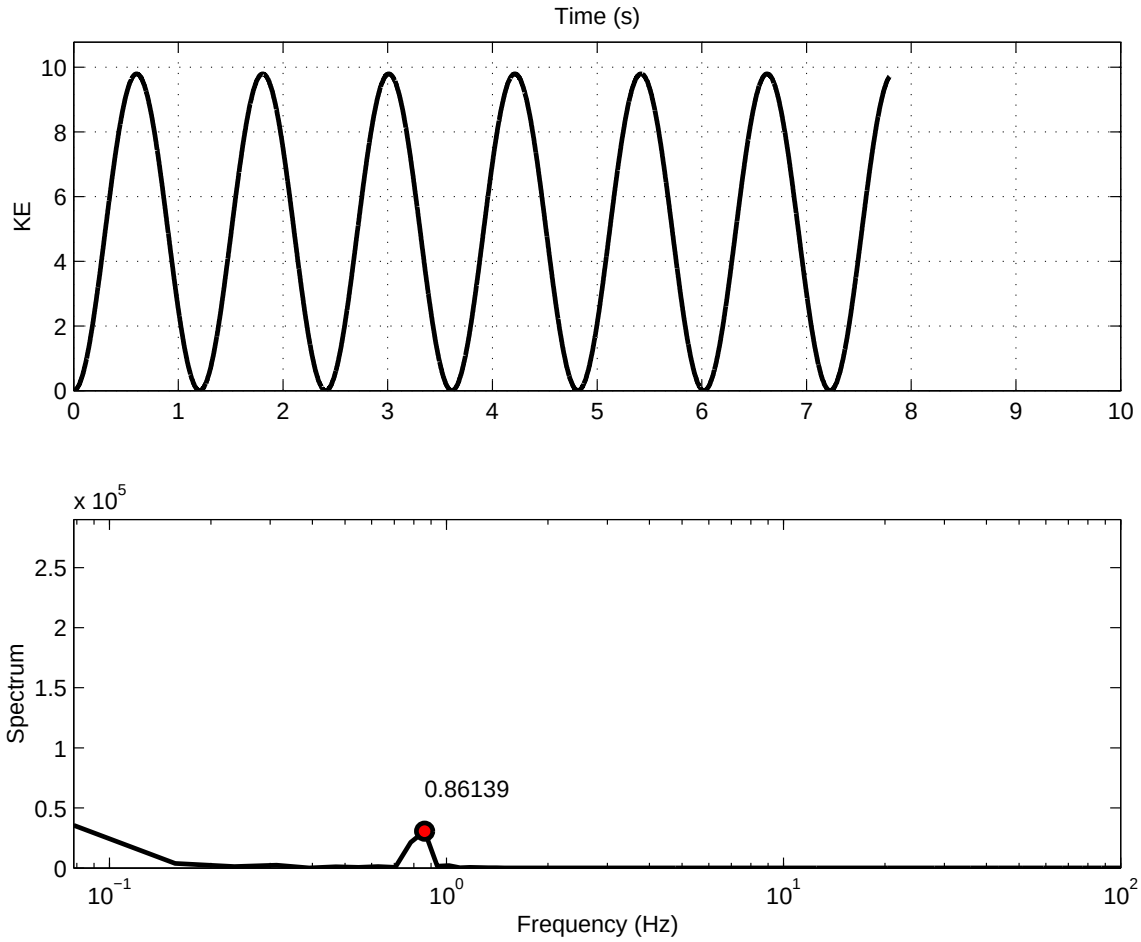

Figure 7.7: Plot of kinetic energy versus time in 1.6m thick sheet ice (top) and power spectral density of the kinetic displaying the dominant modes of vibration (bottom). The labeled frequency represents the dominant rigid body mode.

Ice thickness (m)	0.4	0.8	1.2	1.6
Mass Damping Frequency (Hz)	1.6445	1.1746	0.9397	0.8614
Internal Damping Frequency (Hz)	92.87	64.74	52.00	44.01

Table 7.3: Critical frequencies which are used to damp the dominant rigid body and deformation modes of vibration.

the dominant frequencies, or spectral decomposition, of the curves, a Fast Fourier Transform (FFT) is applied to the responses and the spectra of dominant frequencies are plotted. Figures 7.4-7.7 show the kinetic energy with corresponding spectral analysis for ice sheets with thickness h =0.4-1.6m. There is only one dominant mode of vibration associated with each of these curves, which represents the frequency of the rigid body mode. The dominant frequency is 1.6445Hz at $h = 0.4$m and reduces to 0.86139 as the ice thickness increases to $h = 1.6$m.

The deformation mode is typically at a higher frequency and would appear as a secondary wave form causing minor oscillations about this observed pattern in the strain or strain energy. To determine the critical frequency, the strain rate of the elements in the first zone is investigated. Figures 7.8-7.11 display the strain rate and corresponding spectral decomposition for element No. 4 (closest ice element to the structure face) for the duration of the above simulations. The dominant deformation frequency for ice thickness $h = 0.4$, 0.8, 1.2 and 1.6 meters is 92.87, 64.74, 52.00, and 44.01Hz, respectively. Table 7.3 summarizes the critical values for rigid body and internal damping which are deduced from this analysis and input into DECICE for each simulation. Throughout the numerical simulations, 100% critical internal damping is used, since the oscillations are secondary, and 5% critical mass damping (since it acts as a drag force), as was the practice in Lau (2001).

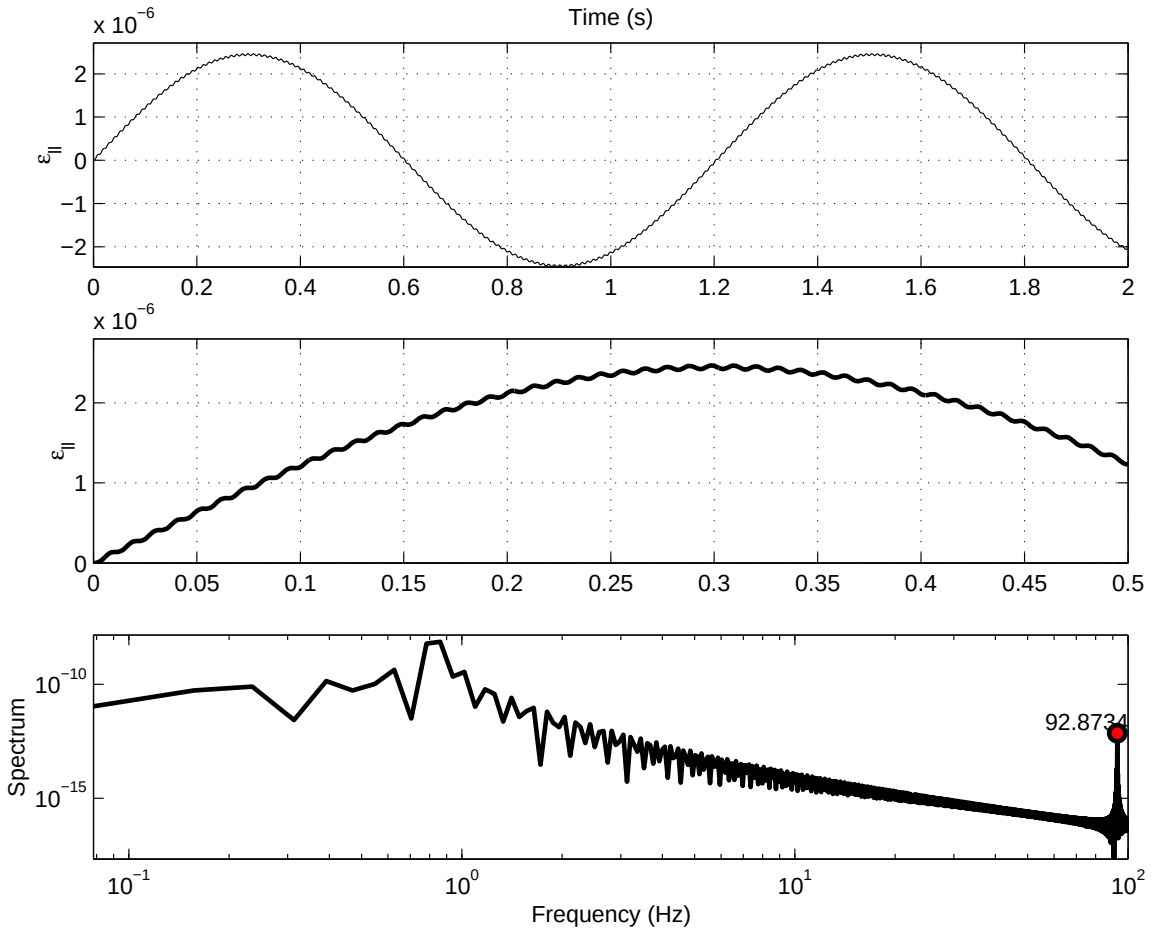

Figure 7.8: Plot of bending strain rate versus time in 0.4m thick sheet ice for the duration of the simulation (top), for the first 0.5 seconds (middle), and the power spectral density of ll-strain rate displaying the dominant modes of vibration (bottom). The labeled frequency represents the internal deformation mode.

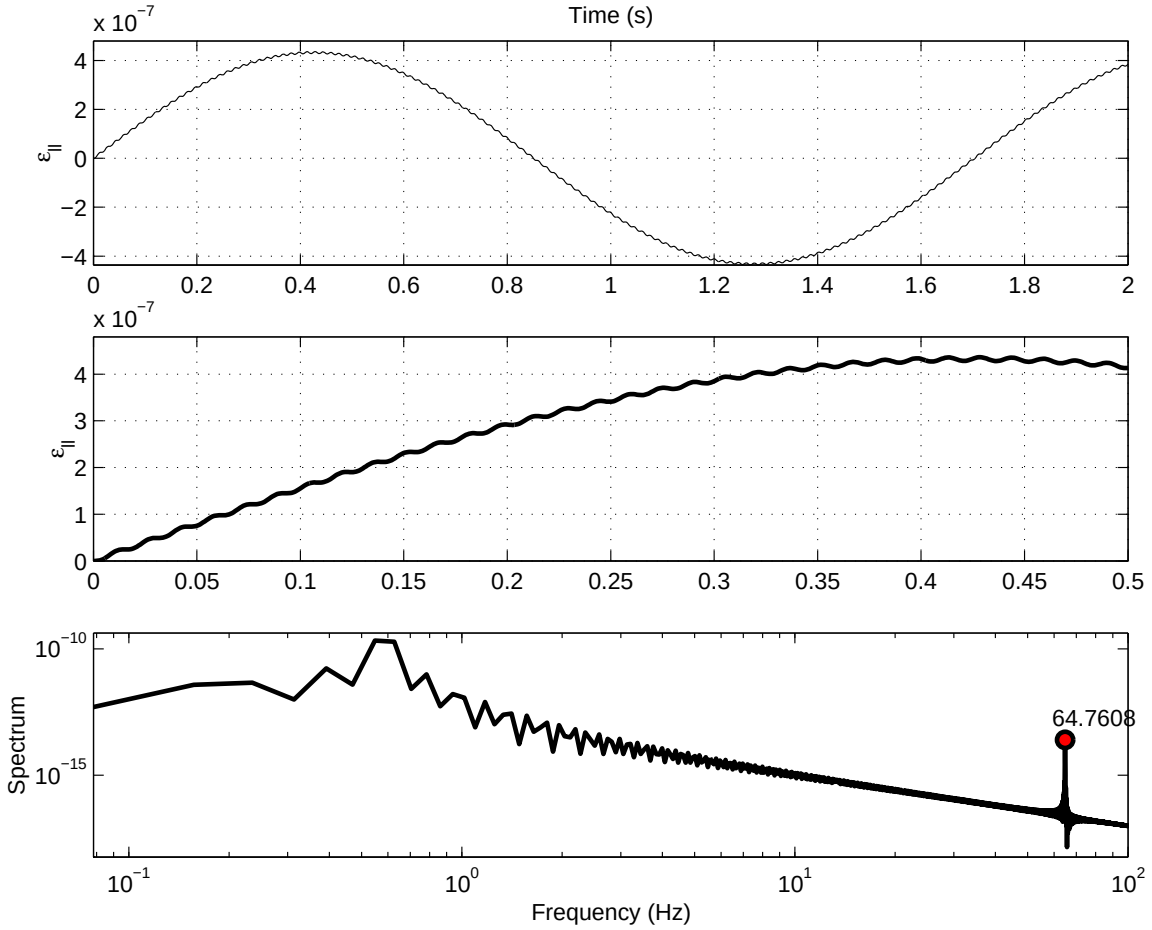

Figure 7.9: Plot of bending strain rate versus time in 0.8m thick sheet ice for the duration of the simulation (top), for the first 0.5 seconds (middle), and the power spectral density of ll-strain rate displaying the dominant modes of vibration (bottom). The labeled frequency represents the internal deformation mode.

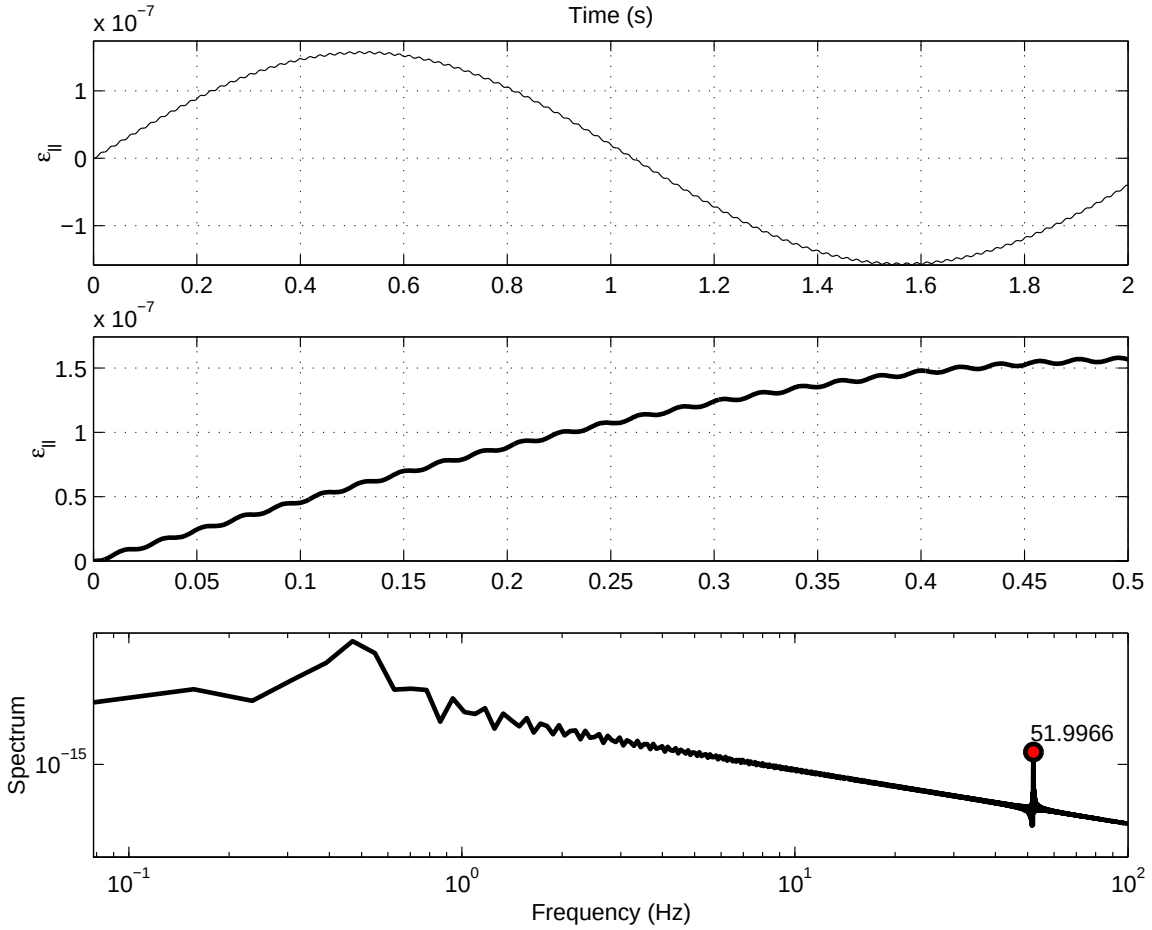

Figure 7.10: Plot of bending strain rate versus time in 1.2m thick sheet ice for the duration of the simulation (top), for the first 0.5 seconds (middle), and the power spectral density of ll-strain rate displaying the dominant modes of vibration (bottom). The labeled frequency represents the internal deformation mode.

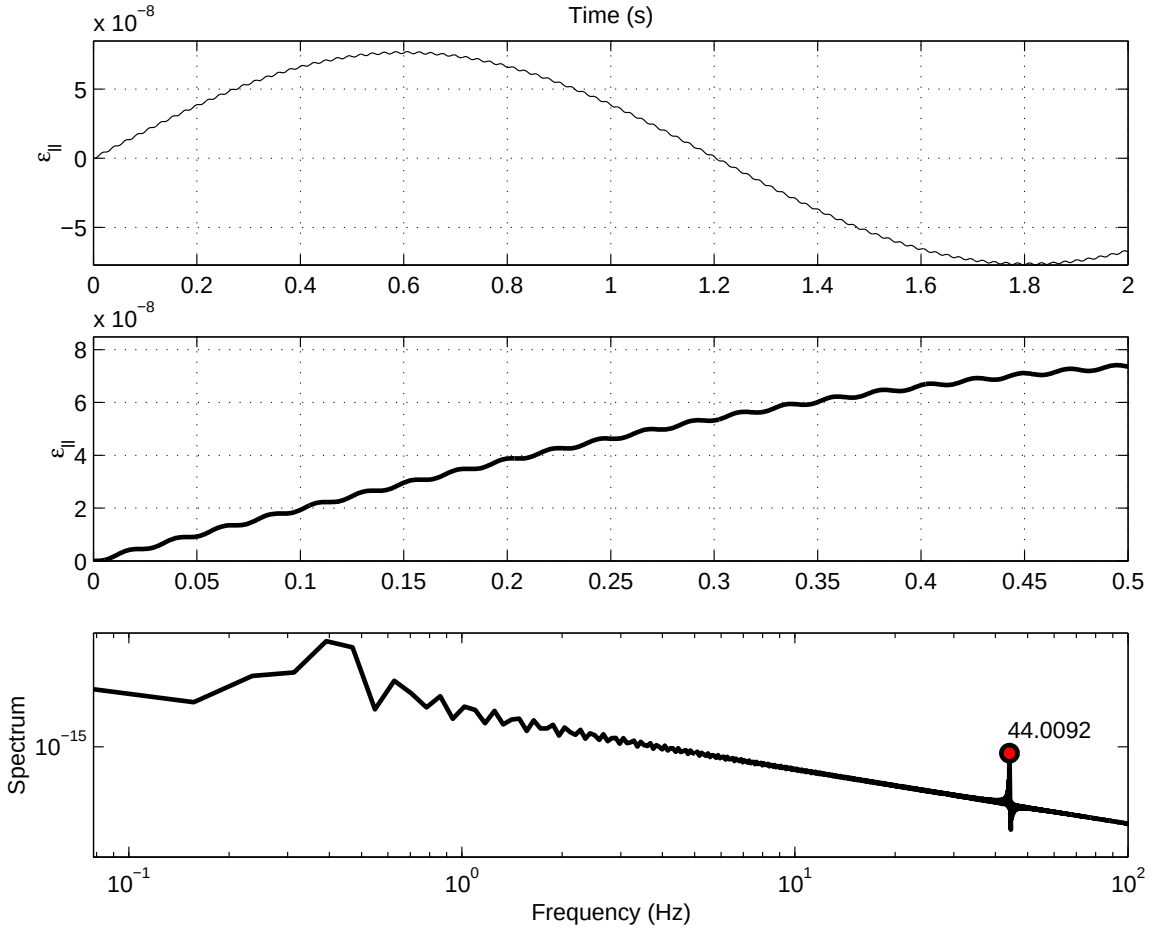

Figure 7.11: Plot of bending strain rate versus time in 1.6m thick sheet ice for the duration of the simulation (top), for the first 0.5 seconds (middle), and the power spectral density of ll-strain rate displaying the dominant modes of vibration (bottom). The labeled frequency represents the internal deformation mode.

Ice thickness (m)	0.4	0.8	1.2	1.6
Solution Scheme	3D Explicit Time Stepping			
Constitutive Model	Elastic-Brittle; Mohr-Coulomb failure criteria			
Element Type	Cone: Fixed Rigid Element Ice: 3D plate bending Elements			
Mass Damping Frequency (Hz)	1.6445	1.1746	0.9397	0.86139
Mass Damping Fraction (%)	5			
Internal Damping Frequency (Hz)	92.87	67.74	52.00	44.01
Internal Damping Fraction (%)	100			
Bending stiffness (N/m) (generated)	1.67×10^6	3.33×10^6	5.00×10^6	6.67×10^6
Ice-structure inter-element stiffness (N/m)	1.67×10^6	3.33×10^6	5.00×10^6	6.67×10^6
No. of Time-steps	1,000,000-3,000,000			
Initial Time-step (s)	0.655E−3	0.655E−3	0.655E−3	0.655E−3
Time-steps between crack	10			
Min. element volume (m^3)	5	10	15	20
Output Interval(s)	History: 0.05; Geometry 2.0			

Table 7.4: Numerical parameters used in the DECICE simulations of a rigid conical drillship.

7.2.5 Investigation parameters

Computer simulations involve both numerical and geometrical/mechanical parameters. The numerical parameters utilized in these experiments are given in Table 7.4.

The solution procedure and damping inputs in this table have been discussed in the previous paragraphs. The program generated bending stiffness which replaces the input stiffness when elements are locked together are displayed in Table 7.4 along with the ice-structure normal interaction stiffness. The initial time-step and number of time-steps is also presented but do not represent an accurate estimate of the final time, since the time-step automatically decreases by up to 85% when elements fracture.

Ice Thickness (m)	0.40			0.80			1.20			1.60		
Drift Speed (m/s)	0.25	0.50	1.00	0.25	0.50	1.00	0.25	0.50	1.00	0.25	0.50	1.00
Ice Sheet Length (m)	300											
Ice Sheet Width (m)	100											
Zone 1 Width (m)	40											
Compressive strength (kPa)	1500											
Flexural strength (kPa)	500 (800)											
Tensile Strength (kPa)	500											
Elastic Modulus (MPa)	1.0											
Poisson Ratio	0.3											
Ice-cone friction	0.15											
Density (ice) (kg/m^3)	900											
Density (sea water) (kg/m^3)	1000											
Friction Angle ($^\circ$)	30											

Table 7.5: Geometrical and mechanical parameters of the ice sheet.

The ice sheet properties are given in Table 7.5. The velocity, thickness, and flexural strength have been discussed. The compressive strength is set as three times the flexural strength in the simulations as observed in the field (see Wessels (1984)) and the ratio of ice to sea water thickness is 0.9 (ρ_w=1000 kg/m^3, ρ_i=900 kg/m^3). Increasing the width of the channel from 100 to 200m did not have a significant influence on the measured loads, since the ice sheet is welded along the symmetry plane but did add to the total number of elements. Therefore, a channel width of 100m was selected for the simulations.

7.3 Implementation of Mooring

Simulations involving fixed or rigid structures can often lead to significant differences in measured results for ice-related problems. Additional forces imposed by a mooring system must therefore be computed for the proper simulation of moored offshore structures. In the experimental investigation conducted parallel to this study at the NRC-IOT, significant differences were observed depending on the mooring stiffness of a four-point mooring system. Booton (1987) developed the numerical `NMOOR3` software to model the restoring forces and moments of a spread mooring system, depicted in Figure 7.12. The modeled system, which may include up to 20 individual mooring lines of varying sizes and materials, may be used to predict resultant loads/moments on a structure when the mooring lines are subjected to surge, sway, heave, roll, pitch and yaw motions. In 2005, Lau and Stanley (2005) used the work of Booton (1987) to develop `SPREAD_MOORING`, an algorithm for mooring load analysis. The study documents the details of the theory behind the original `NMOOR3` software, provides verification of its use in moored structure problems, and presents a user manual to assist in its use. Their procedure for calculating the resultant mooring loads on a structure is integrated into DECICE.

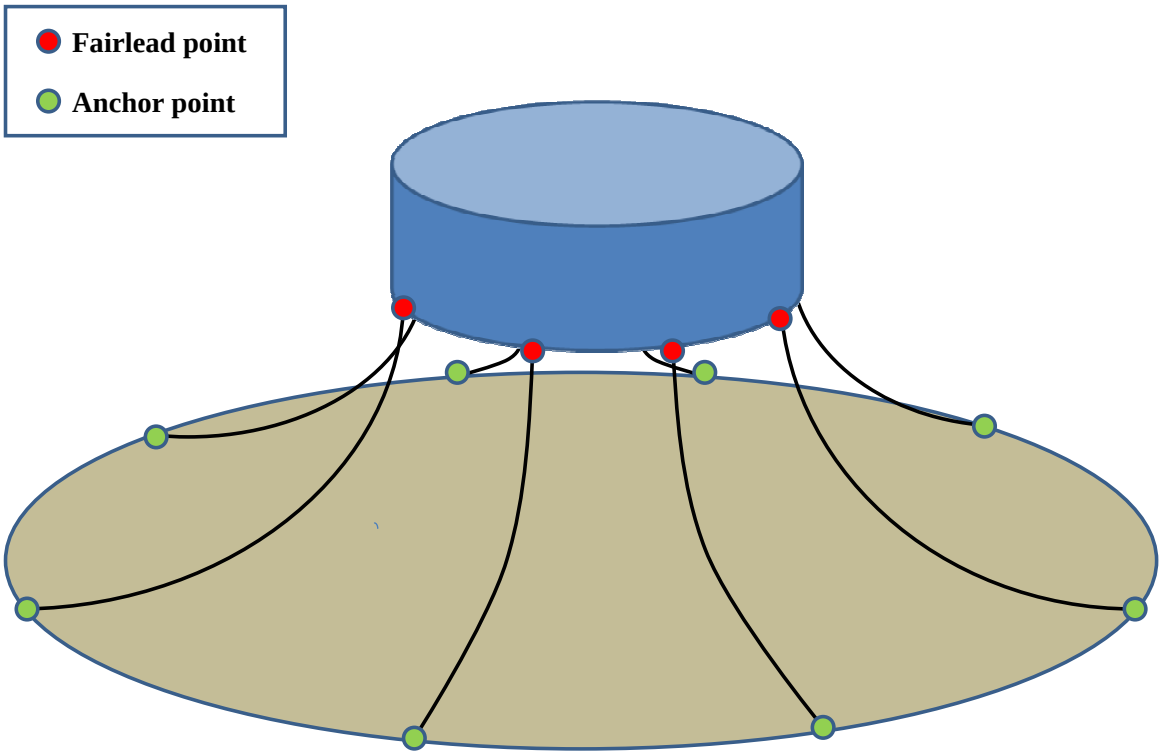

Figure 7.12: Schematic view of a spread mooring system

A summary of the mooring load calculations are presented in the next section followed by details of the implementation into the DECICE program.

7.3.1 Mooring calculations within the SPREAD_MOORING algorithm

The SPREAD_MOORING algorithm employs an iterative procedure to calculate restoring forces over a range of displacements. Input data to describe each of the possible 20 moorings lines, which may be composed of up to three segments of different size (cross-sectional area) and material, are required. Material properties, position and orientation of the mooring line must also be input to describe a single mooring line. The shape of the mooring line is calculated using a hyperbolic function following from catenary theory (which deals with the shape of a flexible cable suspended between fixed points under gravitational pull).

The displacement at the end of the cable, due to a tension applied at that end, may be calculated using the mooring line equation of Orgill and Wilson (1986). Under the assumption that a single line consists of a long upper section, a heavy middle section, and an end section connected to an anchor (see Figure 7.13), there are three resultant shapes of the mooring line depending on how much of the line lies on the ocean floor:

(i) the middle and bottom section are resting on the ocean floor (see Figure 7.14a);

(ii) the bottom section and part of the middle section are resting on the ocean floor (see Figure 7.14b);

(iii) part of the bottom section lies on the ocean floor (see Figure 7.14c).

In each of these three cases, the remainder of the mooring line extends from the ocean floor to the mooring location (fairlead point). For each mooring line, the equations from Orgill and Wilson (1986) are used to calculate the tension. A force-displacement table is then generated for the vertical and horizontal tension in the line as the mooring (fairlead) position varies. Once this table is available for each mooring line, the tension resulting from each of the displacements is determined by table look-up and interpolation. The total restoring force and moments are then calculated by superposition of the results for each of the individual mooring lines.

Limitations of this implementation for the calculation of mooring loads are: (i) the line stretch is approximated; (ii) the lines are assumed in slack mode; and (iii) the friction between the ocean floor and the resting line is neglected. Further, only small translations and rotations can be considered using this algorithm. For a more detailed description of the algorithm and discussion of its verification, the reader is referred to Lau and Stanley (2005).

To integrate this mooring system into DECICE code, several sections were modified. First, new keyword flags were created to read material and input properties of the mooring system such as position, orientation, number of mooring lines and type/size of each segment. Additional common variables, arrays and reformatting were also required to obtain results which could be utilized within the DECICE algorithm. The result is an updated version of DECICE which has mooring system capabilities integrated through the tested `SPREAD_MOORING` algorithm.

The `SPREAD_MOORING` algorithm within DECICE proceeds in the following manner as seen in Figure 7.15. When the program begins, mooring line properties and line configuration are read from the user input file. For each mooring line, the tension is

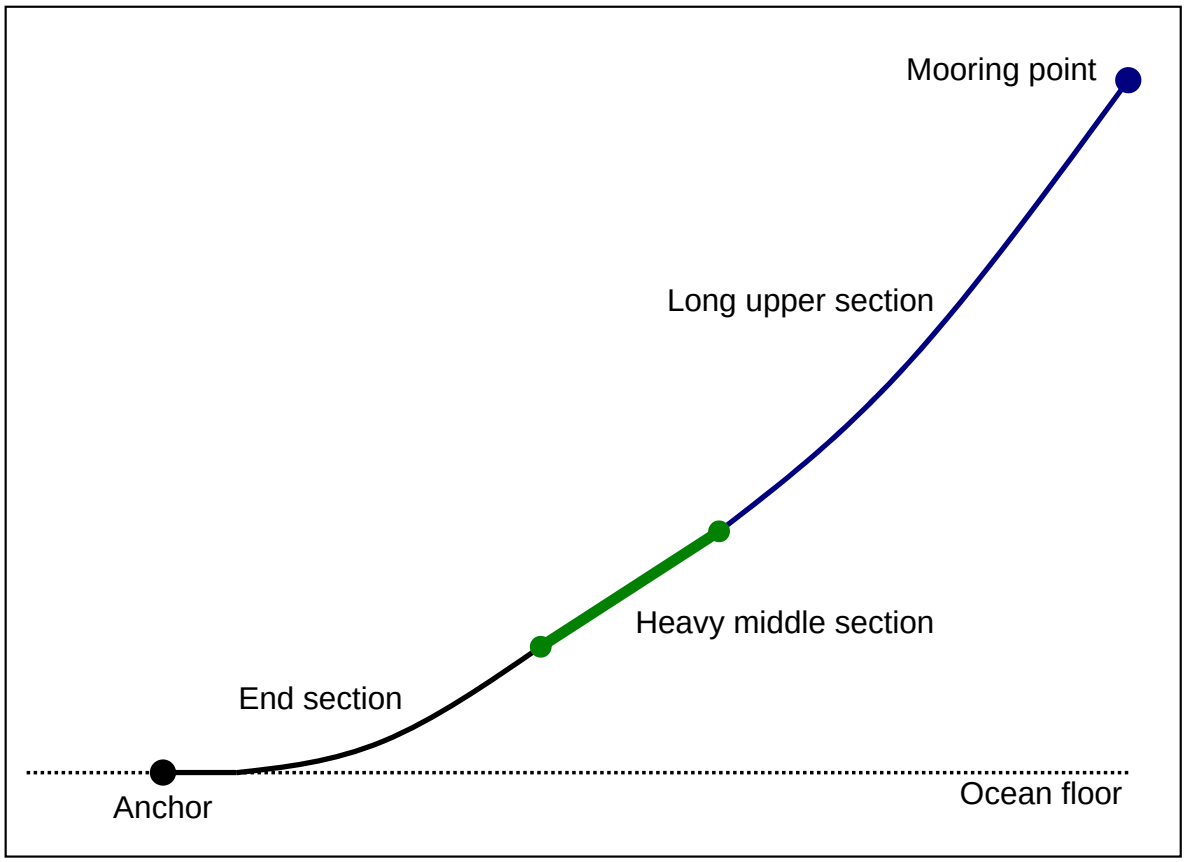

Figure 7.13: A mooring line consisting of three segments considered by Orgill and Wilson (1986).

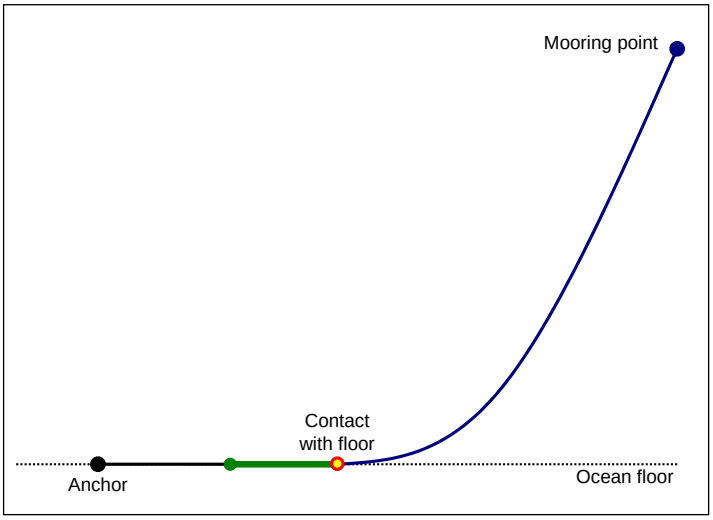

(a) bottom and middle section rest on ocean floor

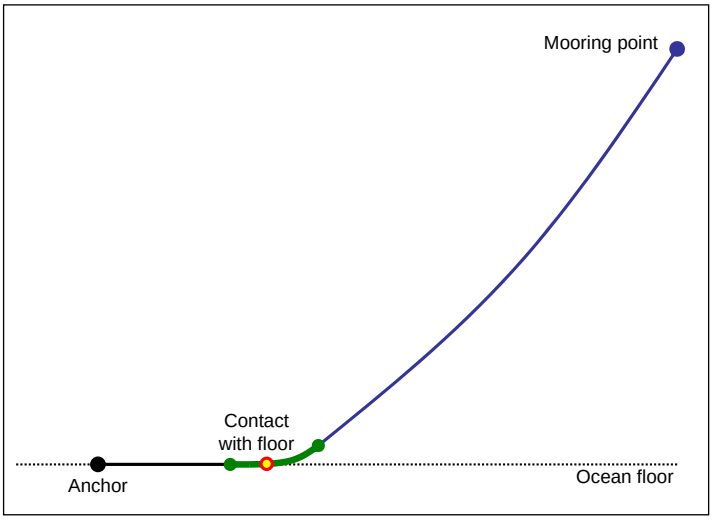

(b) middle bottom and part of middle section rest on ocean floor

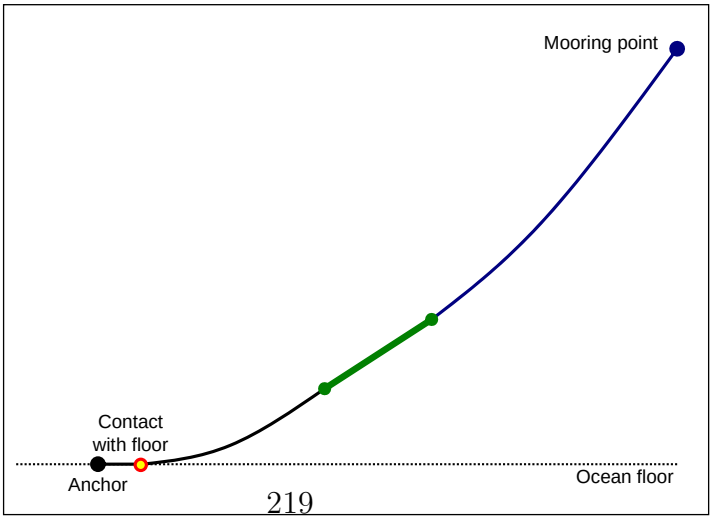

(c) part of bottom section rests on ocean floor.

Figure 7.14: Geometry of the three configurations for the three-segment mooring line.

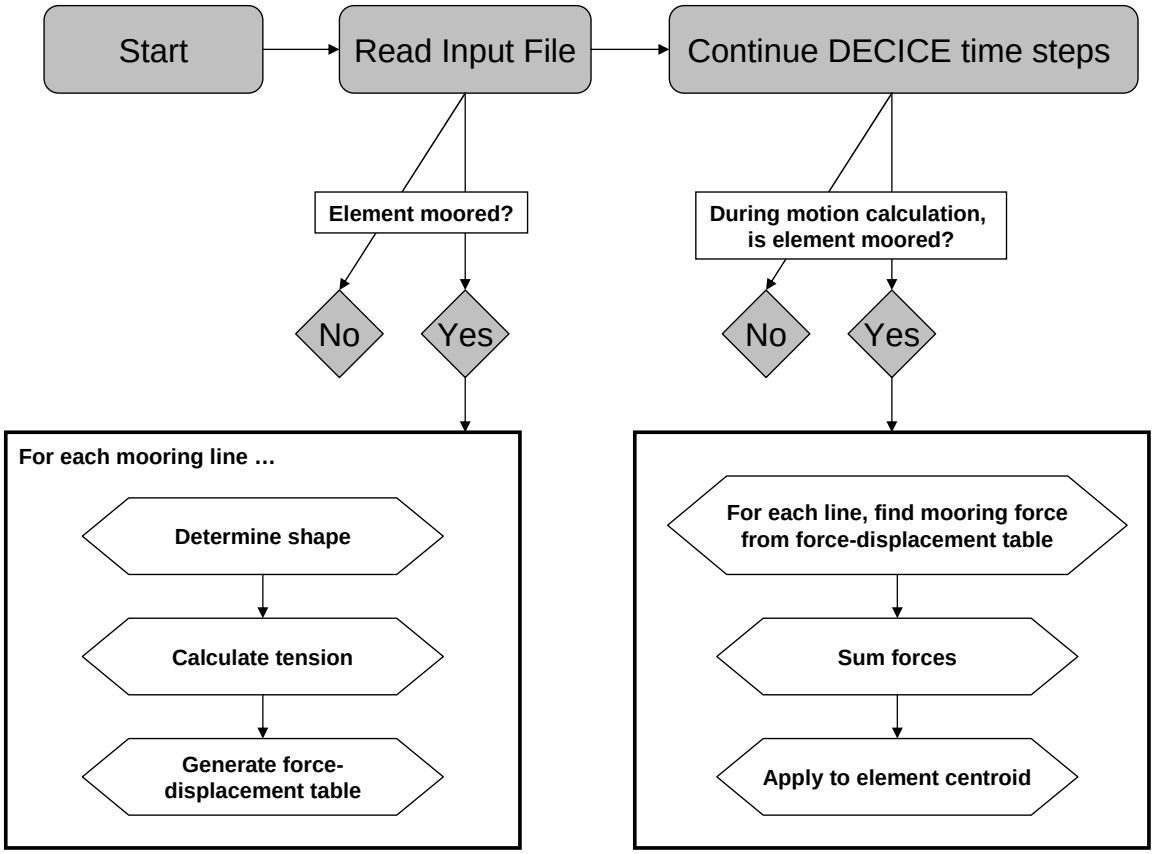

Figure 7.15: Flow chart of mooring algorithm incorporated into DECICE.

calculated and then a force-displacement table is generated. Note this step is only done once at the beginning of the simulation. At each time step thereafter, the application and calculation of the mooring load occurs during the solution stage. At time t_j, the displacement of each element is calculated. If the element is moored via the set of mooring lines, the mooring algorithm is called to compute the restoring force based upon this displacement. The displacement is used to look up and interpolate the associated mooring force for each line. The forces resulting from each line are added (vectorially) and the resultant force is applied to the moored element at its centroid.

Property	Value
Water depth (m)	35.0
Number of lines	6
Line diameter (in)	3.5
Line type	wire rope

Line Number	Length (m)	Orientation (degrees)	Pretension (tonnes)
1	600	15	200
2	600	15	200
3	600	15	200
4	600	15	200
5	600	15	200
6	600	15	200

Table 7.6: Mechanical properties of mooring system used in numerical simulations.

7.3.2 Numerical mooring system parameters

Properties of a typical mooring system configuration used in the Beaufort Sea were presented in Chapter 5. The input for the DECICE simulations are derived from these and recorded in Table 7.6. Six radially symmetric 600m wire rope mooring lines are implemented in the numerical setup to restrict the movement of the 12-sided half conical structure. In relation to the positive x-axis, they are located at 15° and every 30° increment thereafter up to 165°. They are attached to the structure at the edge of the hull skirt and the water depth is assumed to be 35 meters. DECICE requires the user to input the weight per unit length and elastic modulus multiplied by the cross sectional area, which for a wire rope, is 283N/m and 6.7E8N (determined from supplementary information in the appendices of Lau and Stanley (2005)). The effect of the water depth on the mooring system and resultant loads/offsets is also investigated through a secondary set of simulations involving a water depth of $D_w =$ 55m.

7.4 Results and Discussion

The effect of key parameters (thickness, velocity, flexural strength) on the peak horizontal offset and force are addressed in this section through three sets of simulations which utilize the following parameters:

(i) $\sigma_f = 500$kPa, $D_w = 35$m.

(ii) $\sigma_f = 800$kPa, $D_w = 35$m.

(iii) $\sigma_f = 500$kPa, $D_w = 55$m.

The first set of experiments involves ice with a flexural strength of $\sigma_f = 500$kPa in a water depth of $D_w = 35$m. The entire range of ice thicknesses and velocities are presented as well as a review of the effect of each of the parameters on the peak forces and offsets. A secondary set of experiments is then conducted in which the flexural strength is increased to $\sigma_f = 800$kPa, $D_w = 35$m, and finally a third set in which $\sigma_f = 500$kPa, $D_w = 55$m. The full time-history results are included for the first set of simulations to display typical patterns but are excluded for the other results to avoid unnecessary repetition, except in specific circumstances where a particular observation should be highlighted. The complete results are first presented for the peak platform offsets and then the peak forces are addressed. Comparisons are made with past results and the results of Chapter 6, where applicable. Due to the symmetry of the problem, force measurements are scaled by two in the numerical simulations.

7.4.1 Peak horizontal offsets - $\sigma_f = 500$kPa - $D_w = 35$m

The time histories of the horizontal offset of the moored structure are presented in Figure 7.16 for $h = 0.4$-1.6m. The three velocities of interest (0.25, 0.50, 1.0m/s) are plotted on a single axis for each thickness. Each figure also is plotted on the same

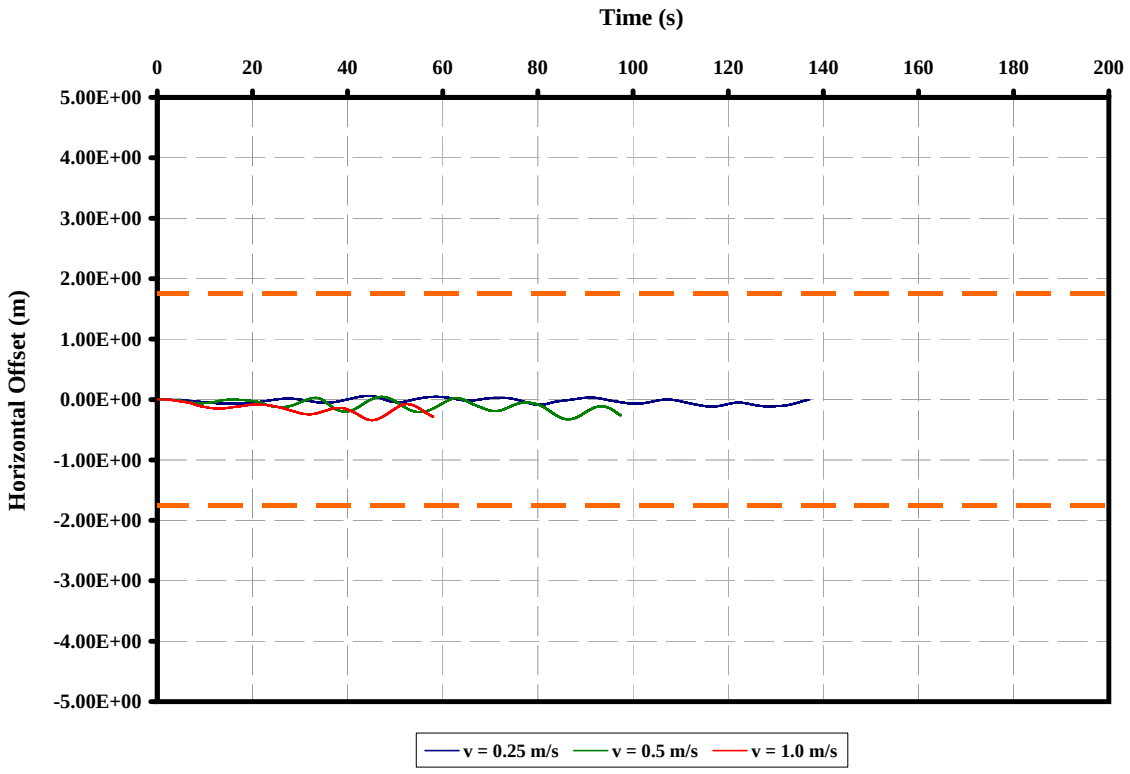

(a) $h = 0.4$m

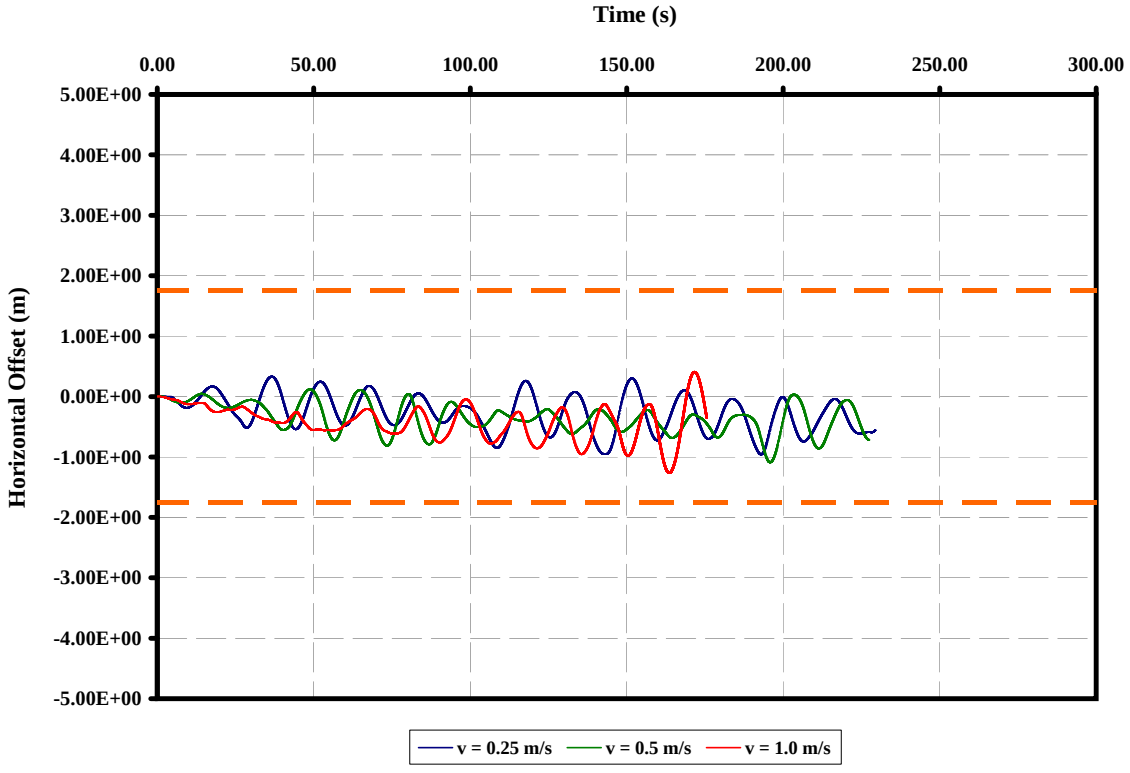

(b) $h = 0.8$m

Figure 7.16: Time history of horizontal displacement of structure for $h = 0.4$-1.6m with $\sigma_f = 500$kPa, $D_w = 35$m.

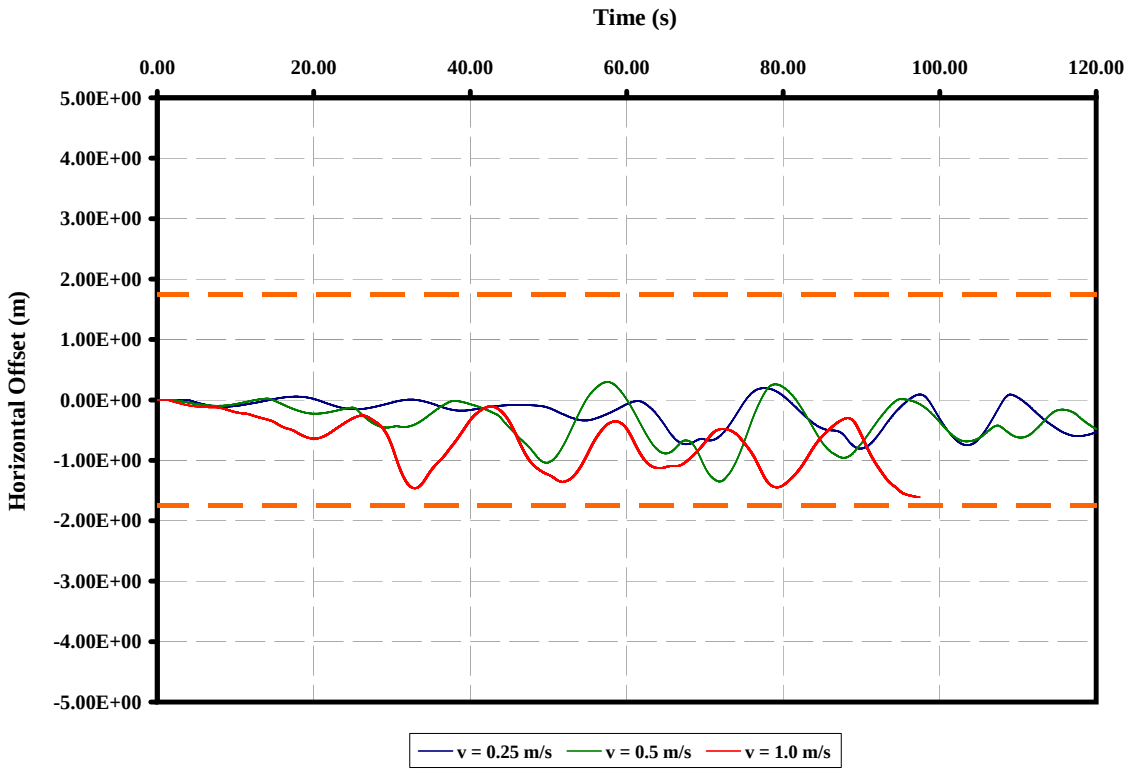

(c) $h = 1.2$m

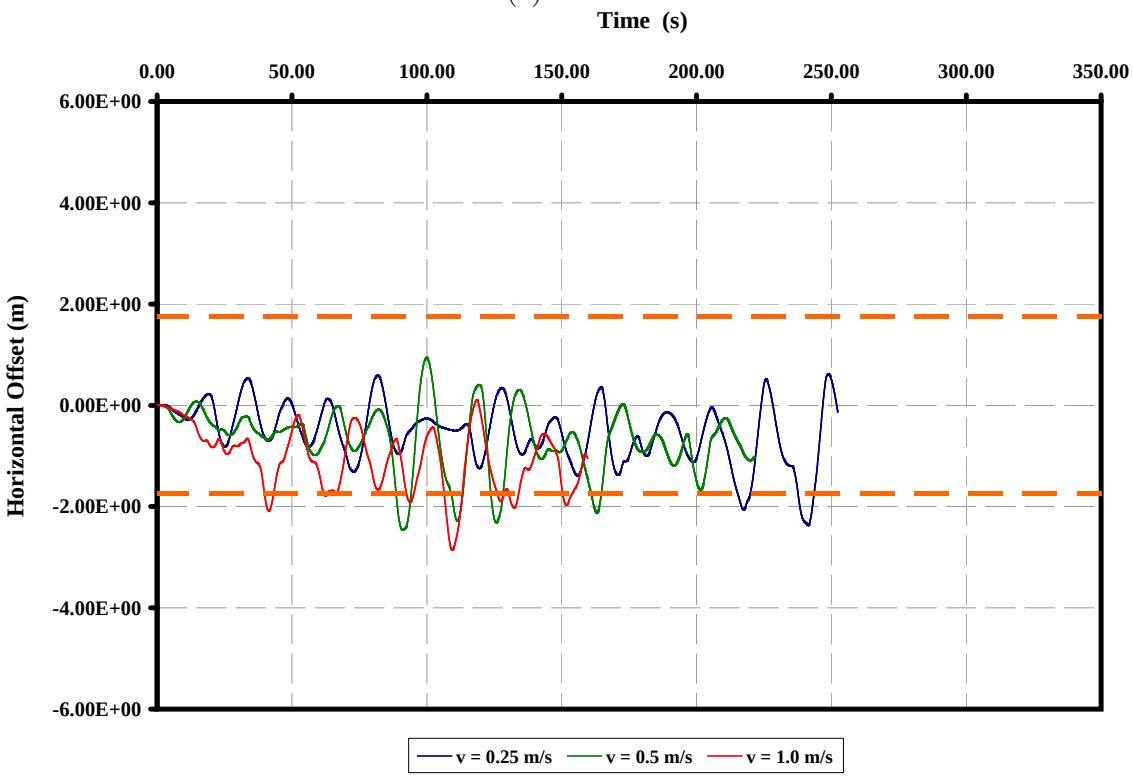

(d) $h = 1.6$m

Figure 7.16 (continued)

y-scale to highlight the effect of both the thickness and velocity. Each curve in these graphs exhibits are clear periodic nature. The wave forms are analyzed using a Fast Fourier transform to determine the dominant frequency in comparison to the natural excitation frequency of the moored platform. The natural frequency of the platform is determined to be $f_p = 0.0626$ by applying an initial horizontal impulse to the platform in the absence of the ice sheet in a separate simulation. The ratio of dominant frequency in each of the horizontal offset time histories to natural platform oscillation frequency is presented in Figure 7.17. At $h = 0.4$m, the approaching ice

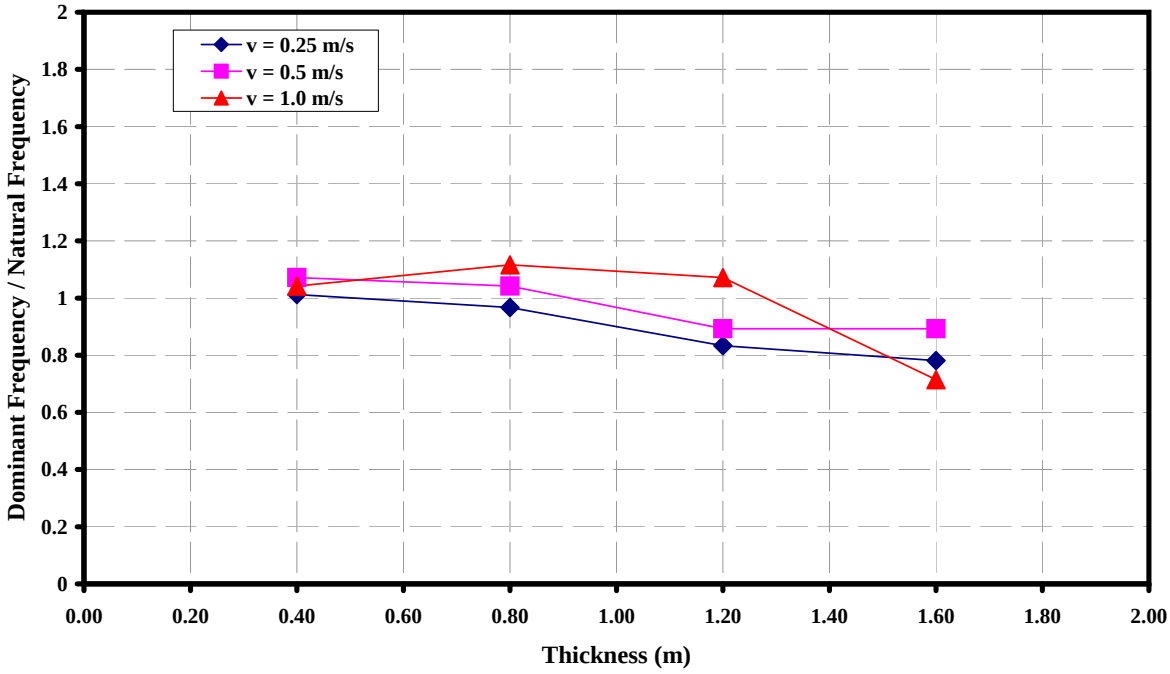

Figure 7.17: Dominant frequency in horizontal offset time histories scaled with the natural excitation frequency of $f_p = 0.0626$Hz versus ice thickness.

sheet causes very little change to the natural excitation frequency for all velocities. As the thicker ice gets pushed against the platform, the dominant frequency gets further away from the natural excitation frequency of the platform. At lower thickness, the platform motion is controlled by the stiffness of the mooring system, since the ice is

not thick enough to influence the platform motion. At higher ice thickness, however, the motion of the platform is increasingly controlled by the forces generated to break and clear the ice, as indicated in Figure 7.17. When the vibrations are controlled by the forcing frequency, and this frequency approaches the natural vibration frequency, resonance may occur which typically results in higher amplitude oscillations.

Effect of ice thickness

Since the platform may oscillate in the positive and negative x-directions, there is a maximum and minimum offset which is observed (minimum being the largest negative value). The mean offset of the platform is negative in all cases as a result of ice movement but the peak values are not. Figure 7.18 displays the peak horizontal offsets in the negative and positive directions versus the ice thickness. As expected, the absolute maxima occur in the negative direction. Also plotted on these graphs is the threshold value which corresponds to the offset at which an emergency platform disconnect must be called. These threshold offset values are calculated as 5% of the water depth (1.75m) as outlined in Wright et al. (1998). For $h \leq 1.2$m, the peak offset does not exceed this threshold value but for $h = 1.6$m, all three negative extremes fall outside the dotted lines. The peak offset appears to be linearly dependent on the ice thickness, h, in the numerical simulations as opposed to the h^2 dependency observed in the experiments conducted at the NRC-IOT. The offset is, however, extremely dependent on the mooring system, which was quite different at the NRC-IOT. In the numerical spread mooring system, the shape and water depth at fairlead position are important, but there are also basic assumptions, as outlined in Section 7.3.1, which could account for the difference. The results are presented along with the experimental results of the NRC-IOT for velocities near the range 0.25-1.0m/s in Figure 7.19. For the smallest ice thickness, the offsets are small and similar in both the numerical and experimental simulations. The numerical results for the $h > 0.4$m

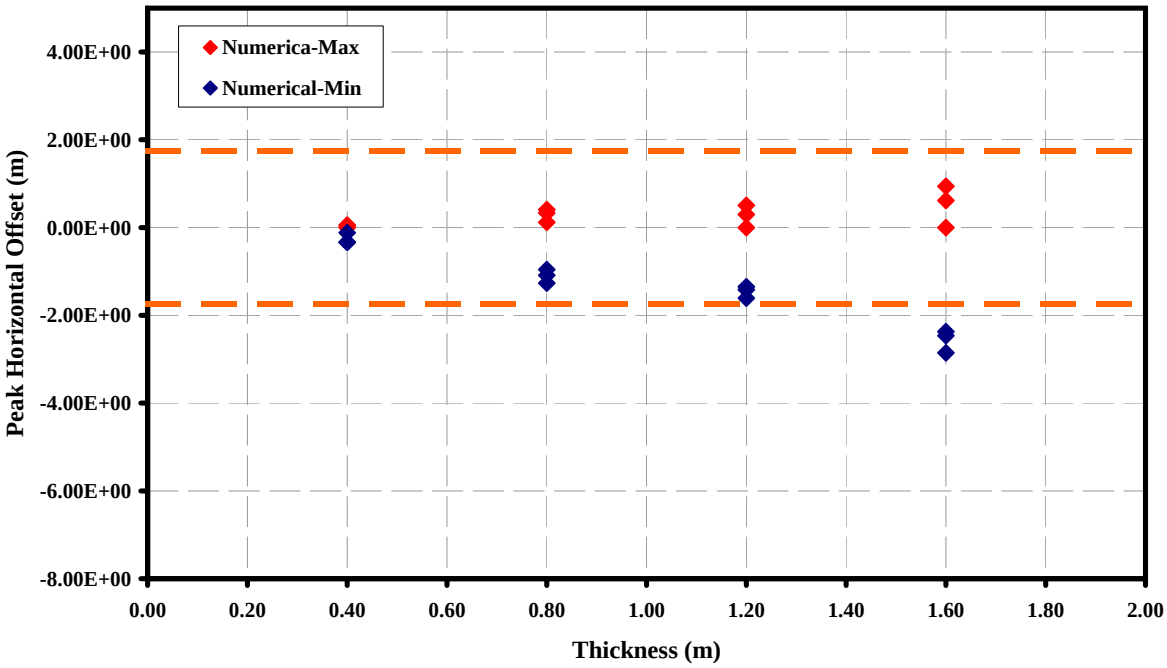

Figure 7.18: Maximum and minimum horizontal offsets versus the ice thickness with threshold value for platform disconnect for $\sigma_f = 500$kPa, $D_w = 35$m.

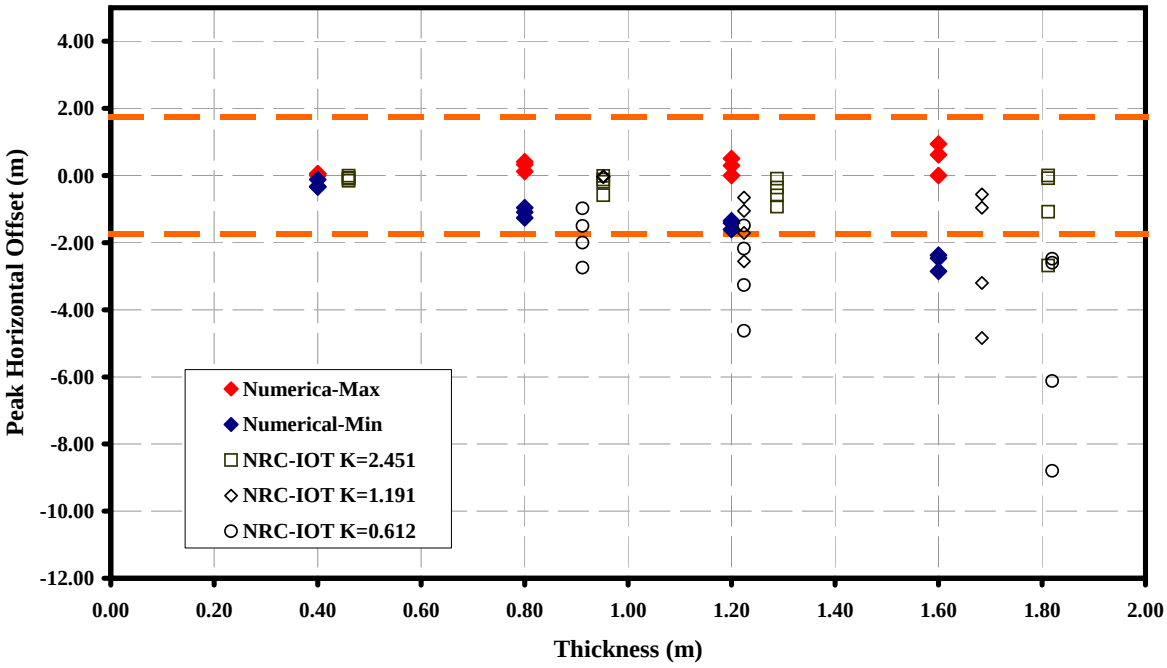

Figure 7.19: Absolute maximum offsets observed in the numerical simulations compared with the experiments conducted at NRC-IOT.

however do not appear to follow the trend of the physical experiments for a single value of the mooring stiffness (spring constant) K. Considering that the experimental and numerical mooring systems are different, however, a pattern is observed in comparing the numerical and experimental results: at $h = 0.8$m, the numerical results compare well with experimental results of the least stiff system - $K = 0.612$kN/m; then, at $h = 1.2$m, the numerical results are comparable to the experiments with the intermediate stiffness - $K = 1.191$kN/m; finally, at $h = 1.6$m, the numerical results are in agreement with the results of the stiffest system - $K = 2.451$kN/m. The modified graph, seen in Figure 7.20, exhibits good agreement between the numerical

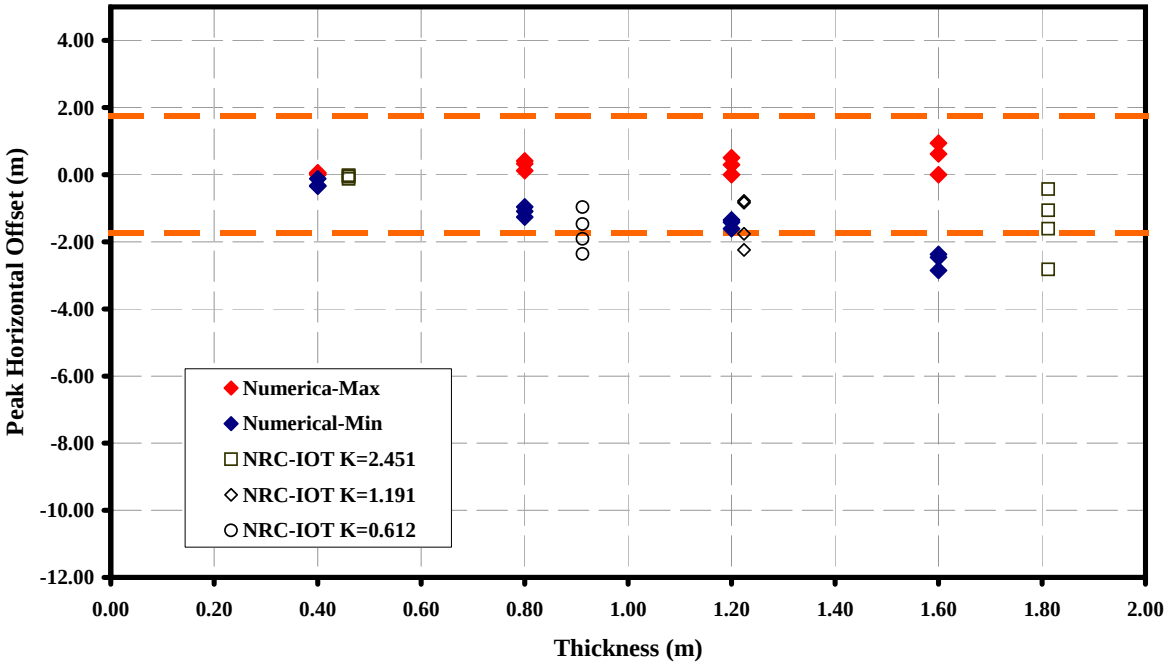

Figure 7.20: Maximum offsets observed in the numerical simulations compared with the experiments conducted at NRC-IOT for select spring stiffness and thickness.

results for the peak offset and the experimental results for select values of the spring stiffness at each ice thickness. This suggests that as the ice thickness (and subsequent ice load) increases, the spread mooring system implemented in the numerical scheme

inherently becomes stiffer as a result of the force-displacement relationship in the mooring equations of Orgill and Wilson (1986). This is not possible in the NRC-IOT experiments, since springs are used with a fixed stiffness. The force and offset in the experiments are therefore proportional to one another, since Hooke's law governs the load-displacement relationship.

Effect of velocity

The peak offsets versus ice velocity are shown in Figure 7.21. The velocity has little effect on the peak values observed. The ice thickness appears to be a more dominant factor, as is evident by the increasing offset of the nearly horizontal offset versus velocity lines.

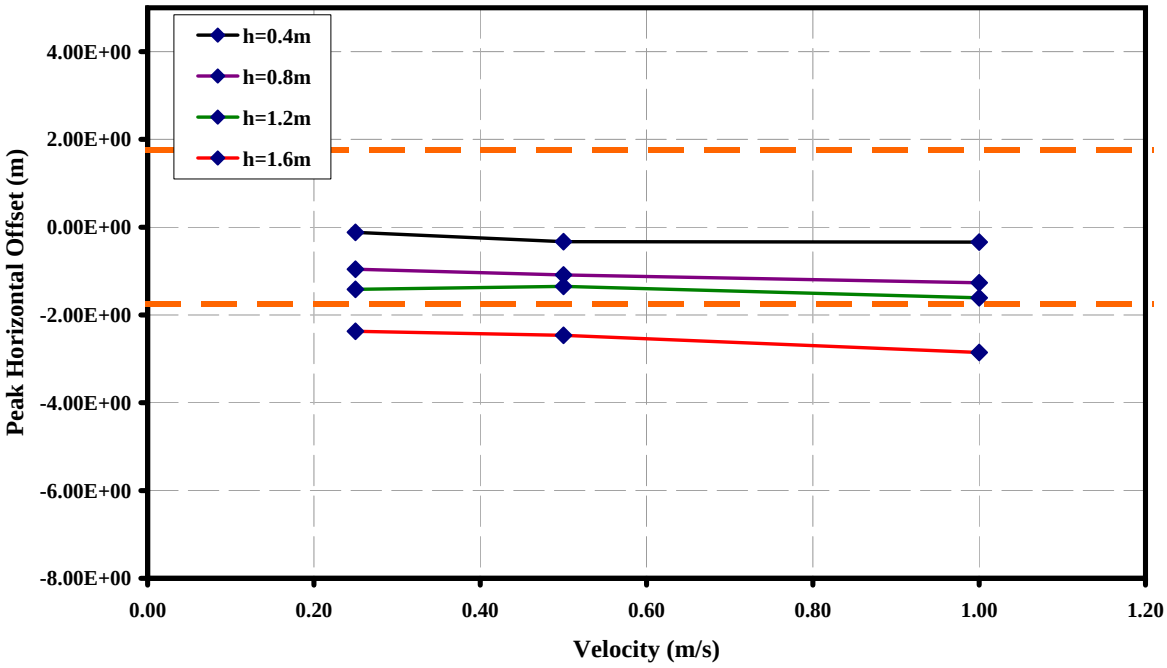

Figure 7.21: Maximum horizontal offsets versus velocity for each ice thickness with threshold value for platform disconnect for $\sigma_f = 500$kPa, $D_w = 35$m.

7.4.2 Peak horizontal offsets - $\sigma_f = 800$kPa - $D_w = 35$m

The dominant frequencies scaled with the natural excitation frequency of the platform, as discussed in the previous section, are presented in Figure 7.22. The variation

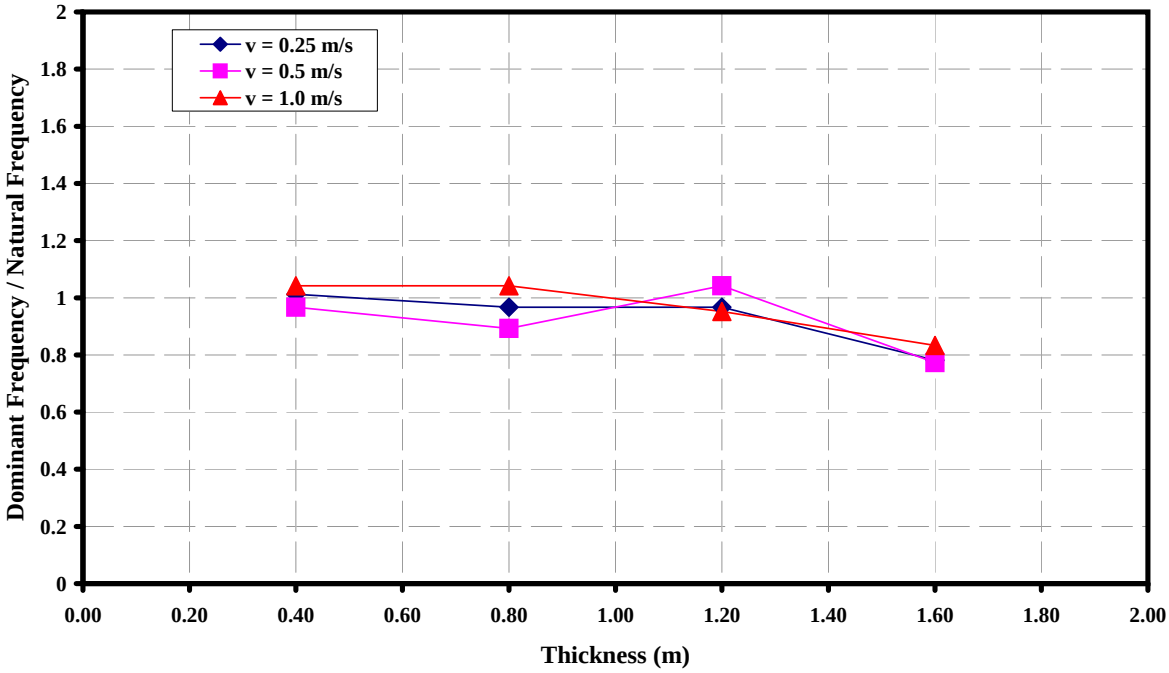

Figure 7.22: Dominant frequency in horizontal offset time histories scaled with the natural excitation frequency of $f_p = 0.626$Hz versus ice thickness.

of the dominant frequencies away from the natural excitation frequency is again increasing with increasing ice thickness, as was observed for $\sigma_f = 500$kPa.

Effect of ice thickness and increased flexural strength

The mean offset of the platform is negative in all cases as a result of ice movement. Figure 7.23 displays the peak horizontal offsets in the negative and positive directions versus the ice thickness. The absolute maxima occur in the negative direction. The offset again appears to increase linearly with ice thickness, h, but at a

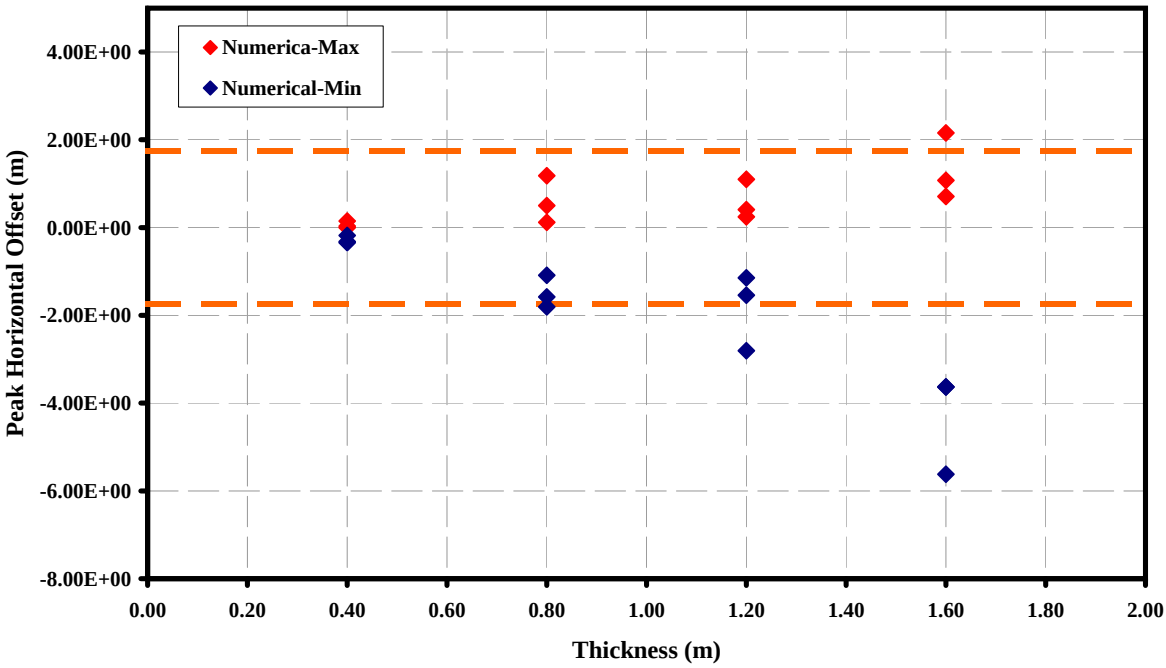

Figure 7.23: Maximum and minimum horizontal offsets versus the ice thickness with threshold value for platform disconnect for $\sigma_f = 800$kPa, $D_w = 35$m.

larger slope. The maximum value obtained for two largest ice thickness, $h = 1.2$m and $h = 1.6$m, are much larger than the corresponding values at the lower flexural strength ($\sigma_f = 500$kPa).

The experimental simulations displayed very little effect of the ice flexural strength on the horizontal offsets. The numerical simulations also show minimal effect for $h \leq 0.8$m, but as the ice thickness increases, the effect of the flexural strength on the peak offset is amplified and significant, as seen in Figure 7.24. The magnitude

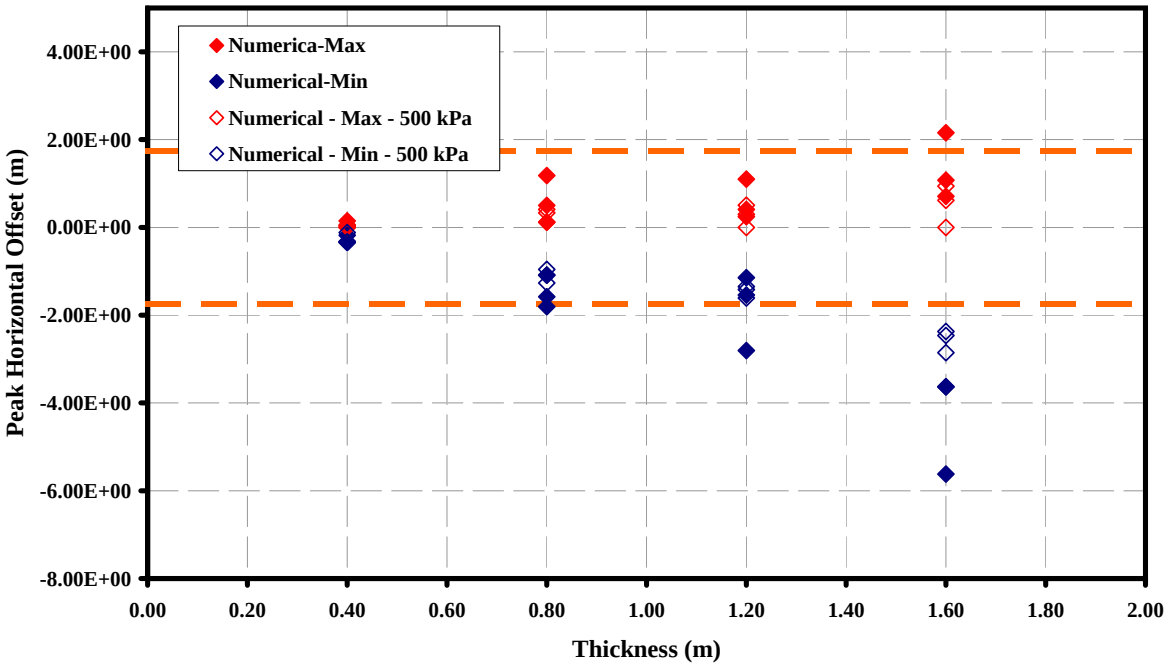

Figure 7.24: Maximum and minimum horizontal offsets versus the ice thickness with threshold value for platform disconnect for $\sigma_f = 500$ and 800kPa.

increases by up to a factor of 2 for the largest ice thickness investigated ($h = 1.6$m). However, only a single point at $h = 1.2$m and $h = 1.6$ actually deviate by a large percentage from the results for σ_f=500kPa. These correspond to simulations $h = 1.2$m, $v = 1.0$m/s and $h = 1.6$m, $v = 0.25$m/s. If these two points were not present in

the data, the conclusions about the flexural strength outlined herein would change. Figure 7.25 displays the time history of the peak offset for each velocity at $h = 1.6$m.

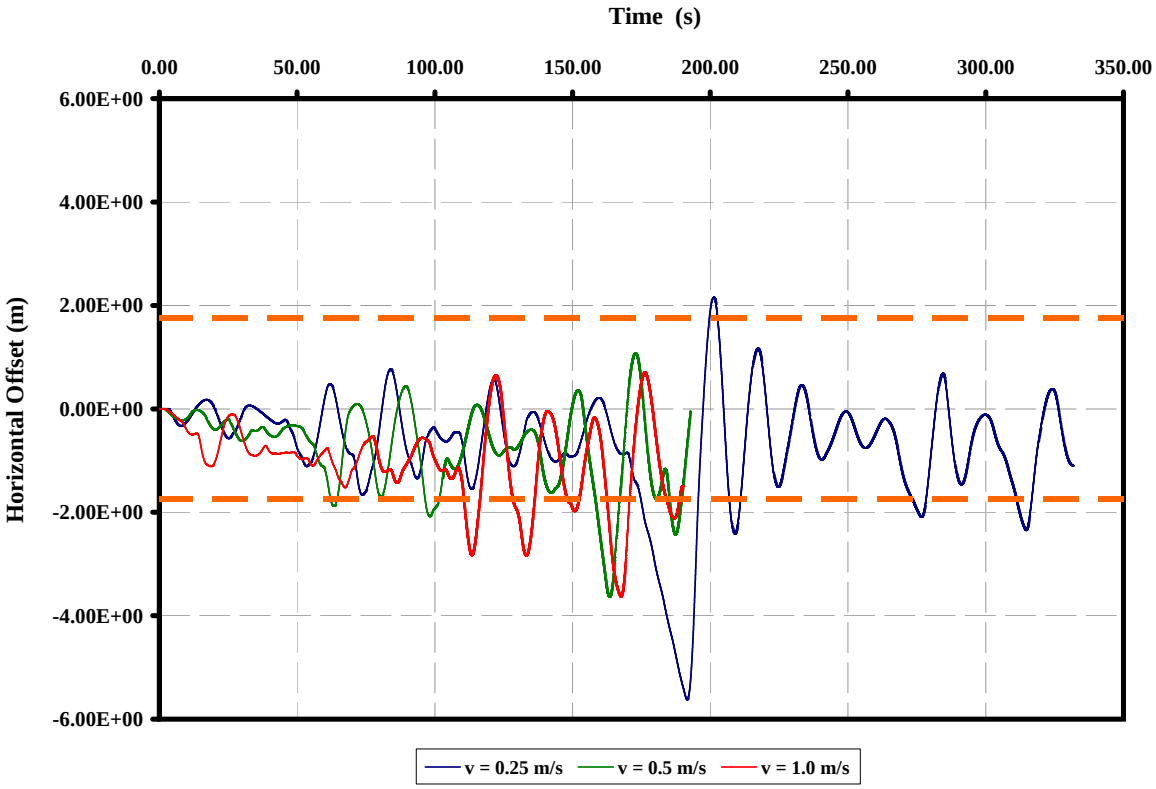

Figure 7.25: Time history of horizontal displacement of structure for $h = 1.6$m with $\sigma_f = 800$kPa, $D_w = 35$m.

The peak reported value of the offset for $v = 0.25$m/s is only observed at one instance in the curve, near time $t = 190$s, and for the remainder of the simulation is consistent with the offset of the other two velocities. This irregular pattern corresponds to a period of shear failure of the ice sheet (as opposed to bending failure, which typically dominates the simulations), resulting in increased loads and displacements. This period of shear failure will be highlighted in the discussion of failure modes (Section 7.5).

Although the peak offset results at $\sigma_f = 800$kPa are larger than their corresponding values at $\sigma_f = 500$kPa, they are still within the range observed in the experimental investigations, as seen in Figure 7.26. At $h = 0.8$m, the experiments with

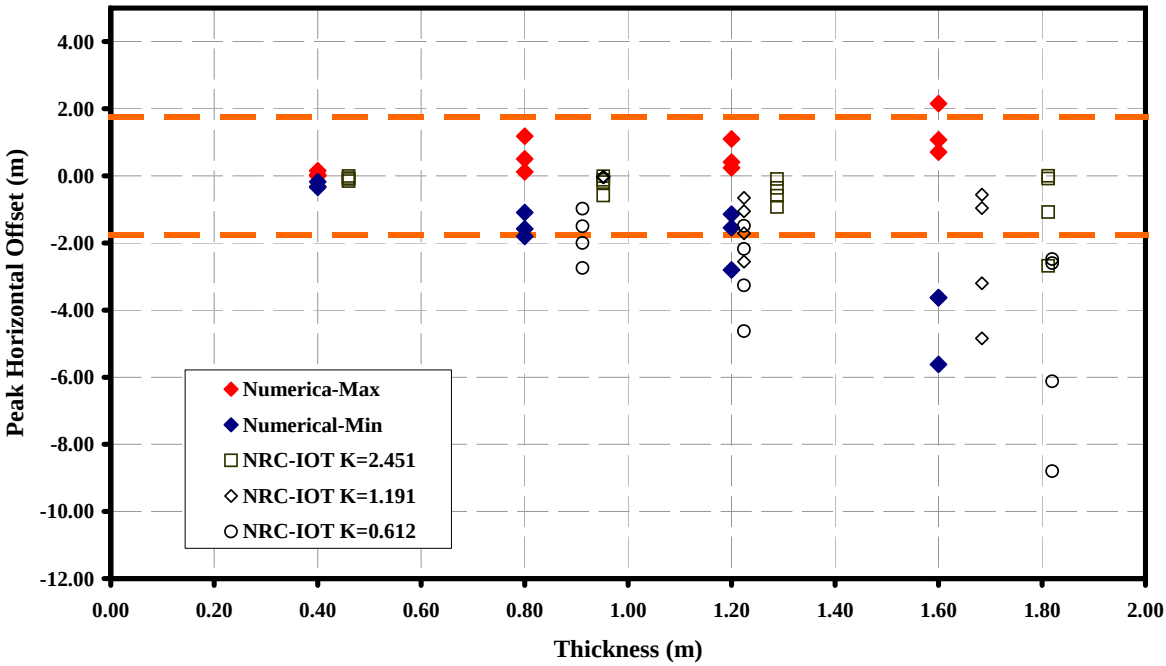

Figure 7.26: Absolute maximum offsets observed in the numerical simulations compared with the experiments conducted at NRC-IOT.

$K = 0.612$kN/m, and at $h = 1.2$m, the experiments with $K = 1.191$kN/m are the best match. For $h = 1.6$m, the results are closest to (but about 15% greater than) the results from the intermediate spring stiffness $K = 1.191$kN/m.

Effect of velocity

The peak offsets versus ice velocity are shown in Figure 7.27. The velocity appears to be a secondary and less pronounced effect on the peak offsets than the ice thickness. The two points which are not consistent with the pattern are those noted in the previous section. Further investigation will show that these irregularities correspond

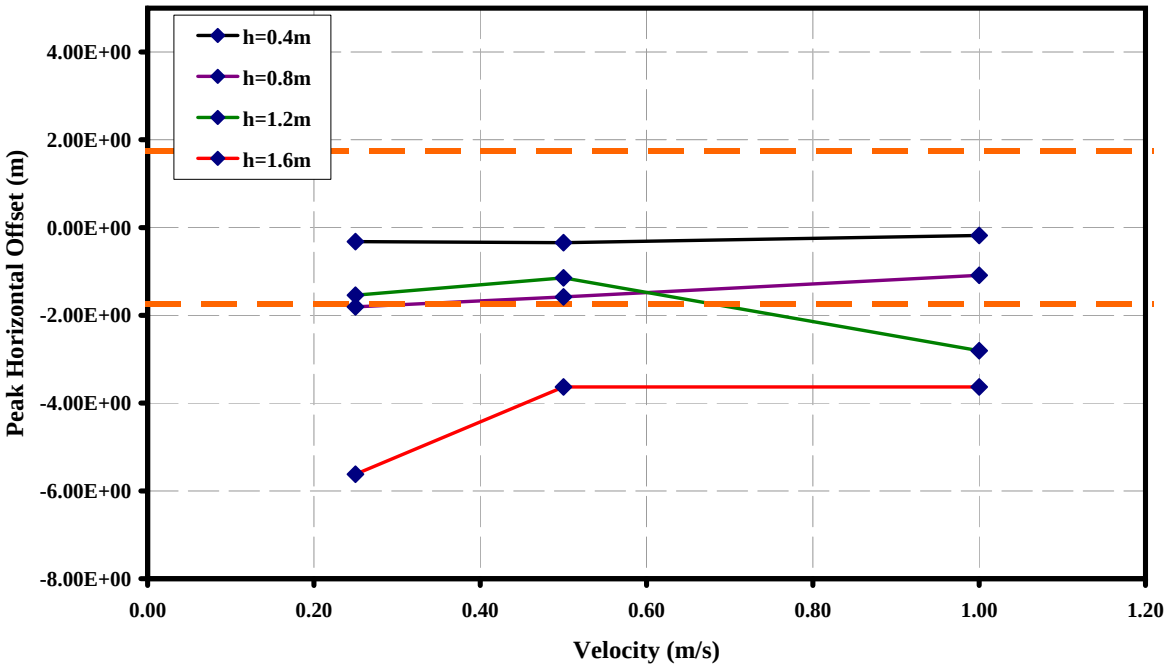

Figure 7.27: Maximum and minimum horizontal offsets versus velocity for each thickness with threshold value for platform disconnect for $\sigma_f = 800$kPa, $D_w = 35$m.

to the occurrence of shear (or compressive) failure of the ice sheet. This will be noted again when discussing the peak forces and shown graphically in the snapshots of the simulation. The occurrence of shear failure here agrees with field and experimental observations that there is a point (dependent on ice thickness, velocity, and strength) at which the mode of failure switches from bending to shear. Although individual instances of shear failure may have occurred in other simulations, these simulations mark the first occurrence of shear dominated failure (and hence the larger offsets).

7.4.3 Peak horizontal offsets - $\sigma_f = 500$kPa - $D_w = 55$m

This set of simulations is used to determine the effect of the water depth in the simulations on the peak offsets.

The dominant frequencies scaled with the natural excitation frequency of the platform (in this case $f_p = 0.0572$) are presented in Figure 7.28. The results are consistent with the conclusions at $\sigma_f = 500$kPa, $D_w = 35$m, except at $h = 1.6$m, $v = 0.5$m/s where the dominant frequency is very close to the natural excitation frequency. In the previous two subsections, the forcing to natural frequency ratio was furthest from 1.0 at $h = 1.6$m. The result of this difference on the peak offset will be addressed in the following discussion.

Effect of ice thickness and increased water depth

The mean offset of the platform is negative in all cases as a result of ice movement. Figure 7.29 displays the peak horizontal offsets in the negative and positive directions versus the ice thickness. The absolute maxima occur in the negative direction. Note that the threshold value for offset in these figures has increased to 5% of 55m or 2.75m. The mooring offsets have increased significantly in comparison to a water depth of

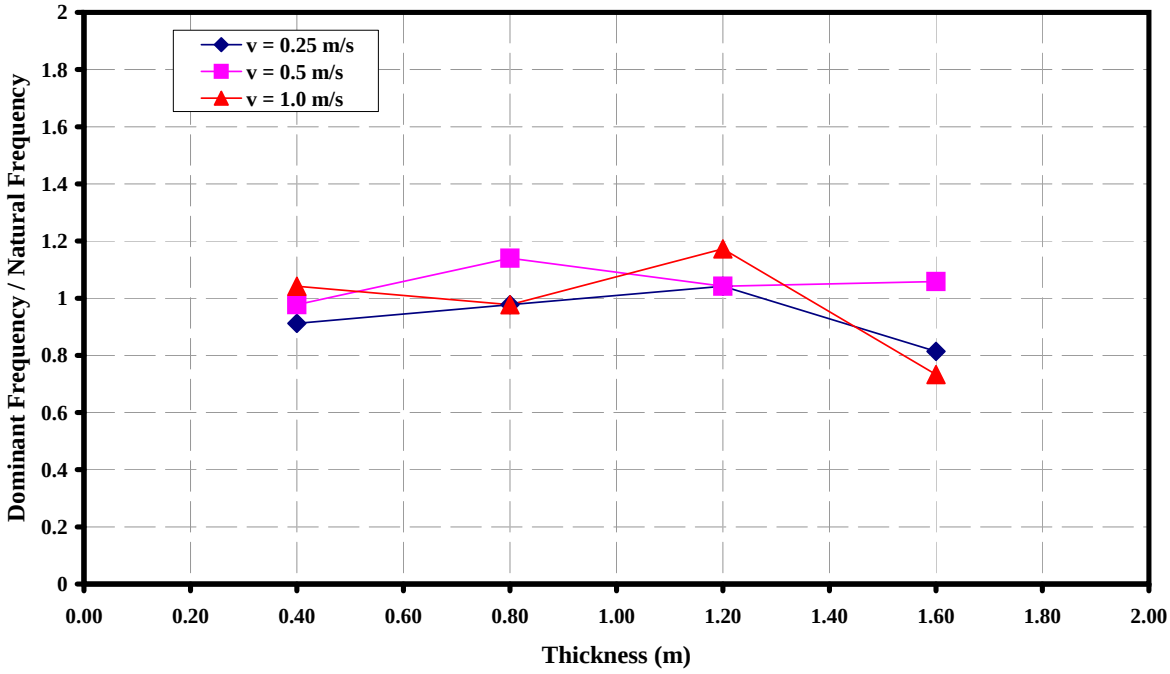

Figure 7.28: Dominant frequency in horizontal offset time histories scaled with the natural excitation frequency of $f_p = 0.0572$Hz versus ice thickness.

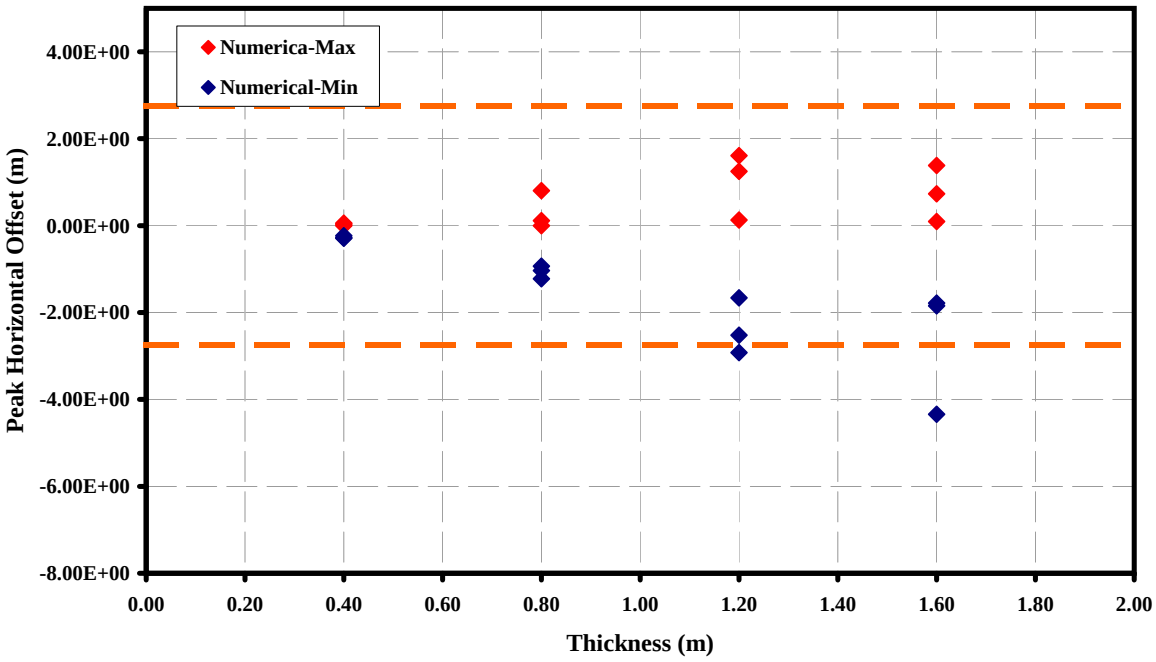

Figure 7.29: Maximum and minimum horizontal offsets versus the ice thickness with threshold value for platform disconnect for $\sigma_f = 500$kPa, $D_w = 55$m.

35m as seen in Figure 7.30. Qualitatively, however, the offsets are quite similar in

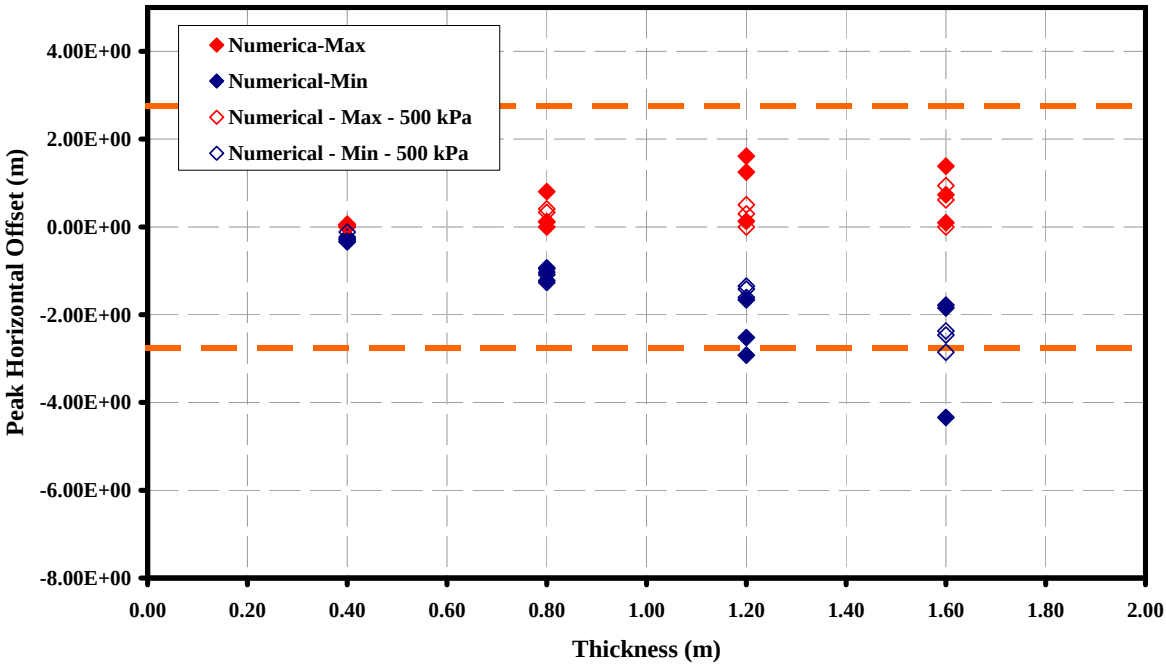

Figure 7.30: Maximum and minimum horizontal offsets versus the ice thickness with threshold value for platform disconnect for $D_w = 35$ and 55m.

comparison to the threshold value. The measured offset appears to increase linearly with the ice thickness in the increased water depth to a maximum that exceeds the threshold value at $h = 1.6$m, but most of the measured offsets are below this critical value. These are identical conclusions to those discussed at $\sigma_f = 500$kPa in 35m of water. The magnitude of the peak offsets and the threshold values have been scaled accordingly but the observations with respect to one another remain the same. Note that the peak value at $h = 1.6$m corresponds to $v = 0.5$m/s, the data point at which the forcing and natural frequencies coincided.

The results again fall within the range of experimental values, as seen in Figure 7.31. At $h = 0.8$m and $h = 1.2$m, the experiments with $K = 0.612$kN/m are the

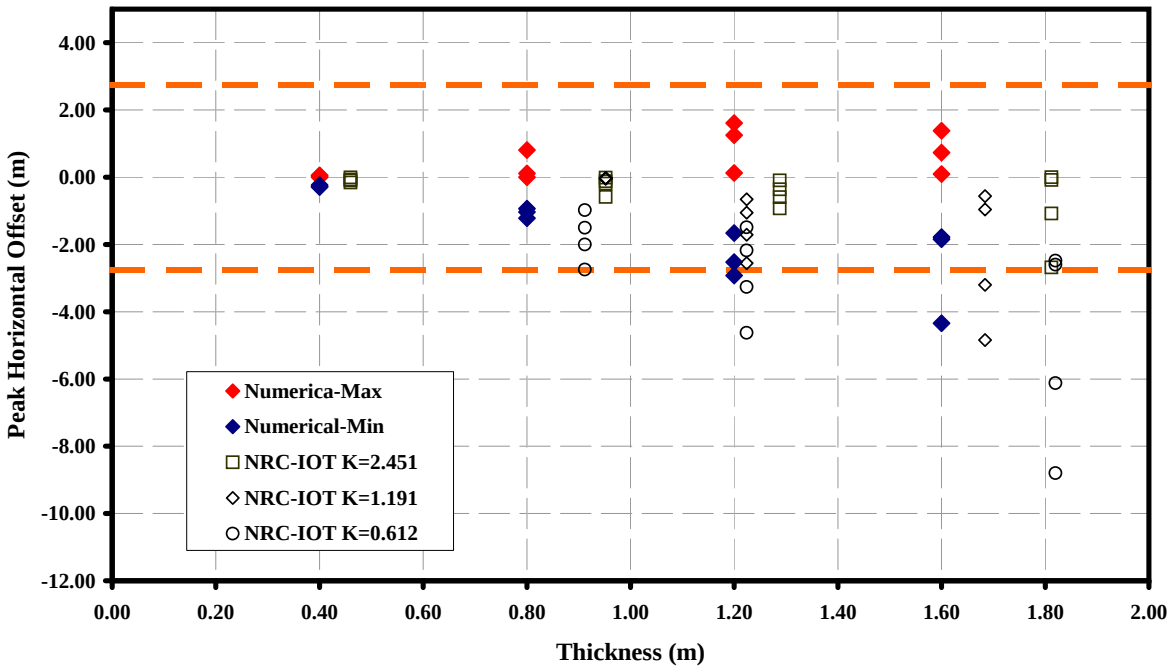

Figure 7.31: Absolute maximum offsets observed in the numerical simulations compared with the experiments conducted at NRC-IOT.

best match. For $h = 1.6$m, the results are closest to the results from the intermediate spring stiffness $K = 1.191$kN/m. In all three sets of simulations, the agreement of the numerical data with the stiffness-specific experimental data varied. In the first set of experiments, the numerical data at increasing thickness corresponded to the experimental results at increasing spring stiffness. Then, at $\sigma_f = 800$kPa, the numerical results changed to agree with the intermediate spring stiffness results (possibly due to the effect of a failure mode change), and now, the results differ again as noted above. This point exhibits the importance in correct physical modeling of the mooring system. A different mooring system may cause significant differences in the results that were recorded during the NRC-IOT experiments.

Effect of velocity

The velocity also appears to have a minimum effect in this set of simulations, except when $h = 1.6$m (see Figure 7.32). At $h = 1.6$m, $v = 0.5$m/s, the peak offset increases significantly. Peak offsets and loads were also noted at intermediate velocities in previous studies (Nixon and Ettema, 1987). The power spectra analysis presented in the first part of this section showed us that at this velocity and thickness, the forcing frequency is very close to the natural excitation frequency of the platform. When this occurs, larger offsets/loads are observed as a result of the frequency resonance. This resonance effect is not restricted to the largest ice thickness, $h = 1.6$m, but the ice thickness/velocity/strength must yield forces which are significant enough to govern the periodic motion of the platform. Hence, resonance at lower ice thickness where lower global loads are observed is unlikely.

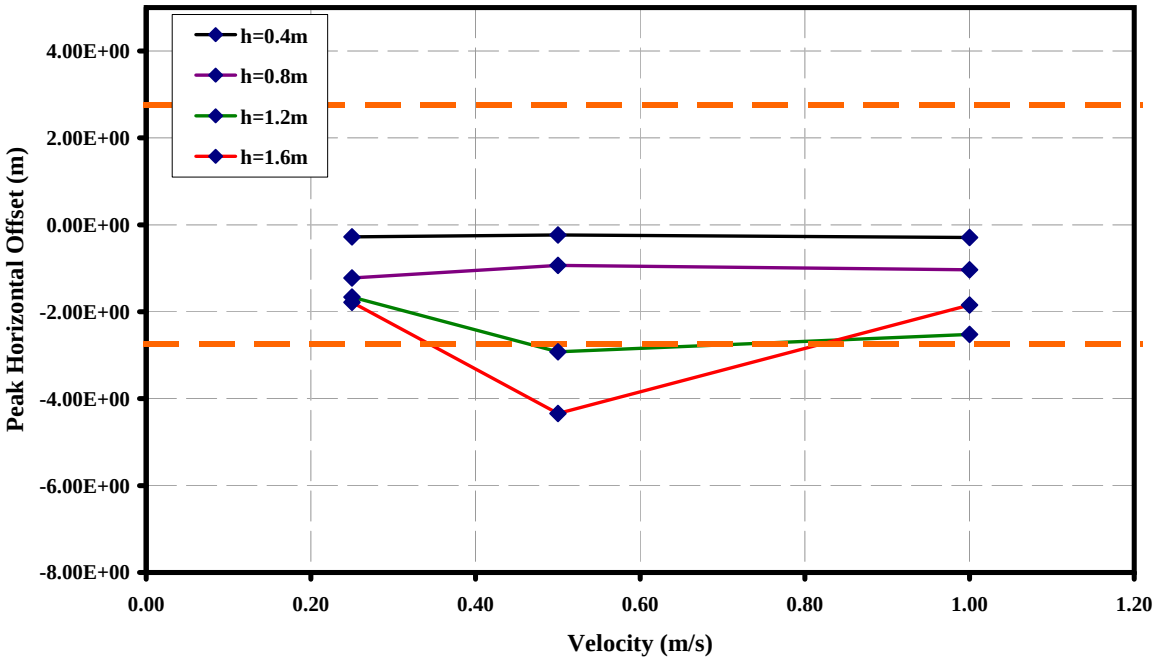

Figure 7.32: Maximum horizontal offsets versus velocity for each thickness with threshold value for platform disconnect for $\sigma_f = 500$kPa, $D_w = 55$m.

7.4.4 Peak horizontal loads - $\sigma_f = 500$kPa - $D_w = 35$m

The time histories of the applied and mooring force are presented in Figure 7.33-7.36 for $h = 0.4$-1.6m. The three velocities of interest (0.25, 0.50, 1.0m/s) are plotted in subfigures (a)-(c). The applied force is the force applied to the centroid of the rigid element representing the platform and the mooring force is the restoring force computed by the spread mooring algorithm using the system configuration and platform displacement. The difference in these two forces (not shown in the figures) represents the mass-acceleration of the tethered platform. As seen in these figures, the mooring force traces the upper boundary of the applied force. The absolute magnitude of the applied force (peak value in $-x$-direction) is generally larger, but it is the mooring force which is important in this investigation, since this is the force which has been recorded in the other experimental investigations and the full-scale data set. The difference in the two types of forces should be noted, however, since when the structure is fixed (instead of moored), the only force available is the applied force. The trace of the upper boundary of the applied force in this case would result in a line at zero. Thus, comparing it to the mooring forces which are reported in other experimental and field tests is somewhat inadequate, since the two forces are not equivalent. The applied force is calculated from hundreds of individual vertex-to-face or edge-to-edge contacts of the ice sheet with the platform, whereas the mooring force is dependent on the movement of the platform (which occurs as a result of the applied force). Hence, results which are presented later to exhibit the effect of fixing the platform as opposed to mooring it are only relevant in the context of the current investigation and not to be compared with past mooring force data.

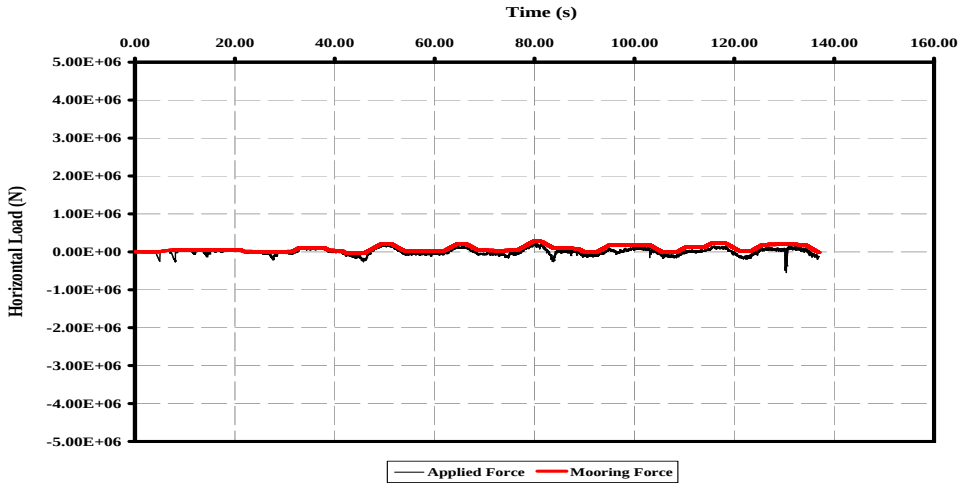

(a) $v = 0.25$m/s

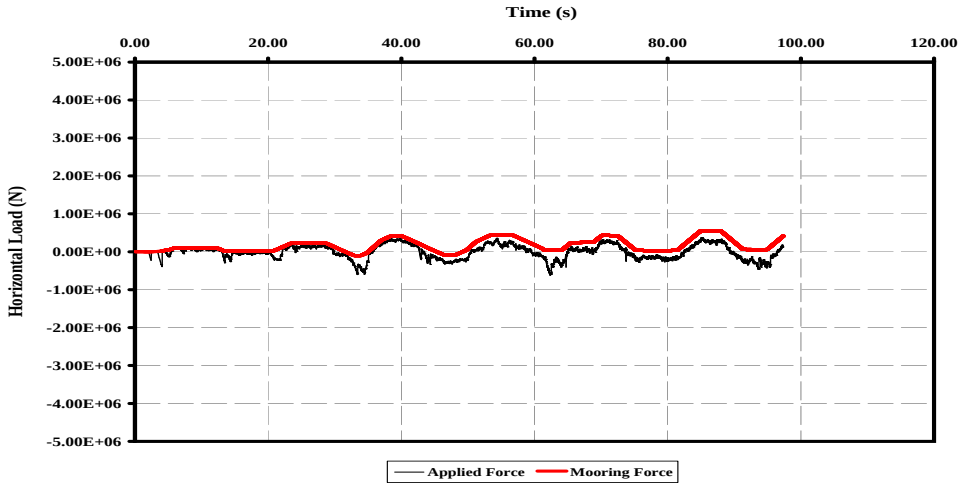

(b) $v = 0.5$m/s

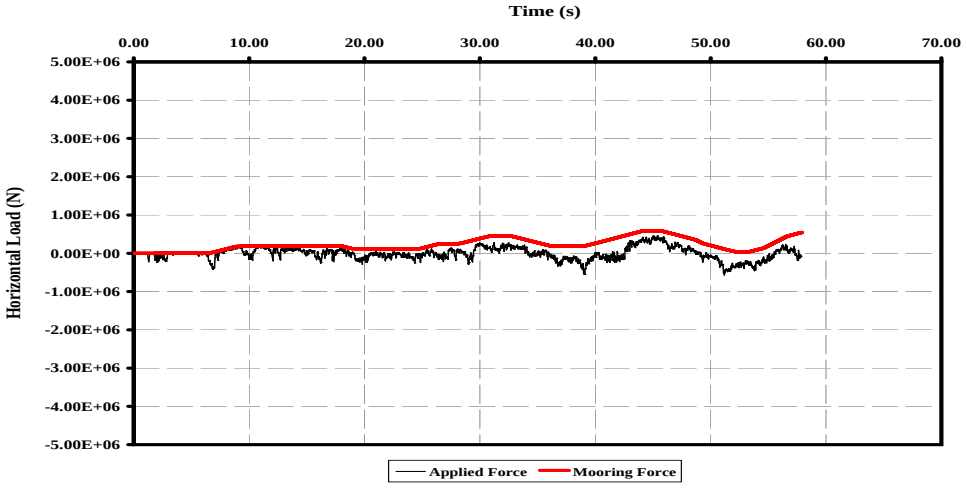

(c) $v = 1.0$m/s

Figure 7.33: Time history of applied and mooring horizontal forces for $\sigma_f = 500$kPa, $D_w = 35$m, $h = 0.4$m.

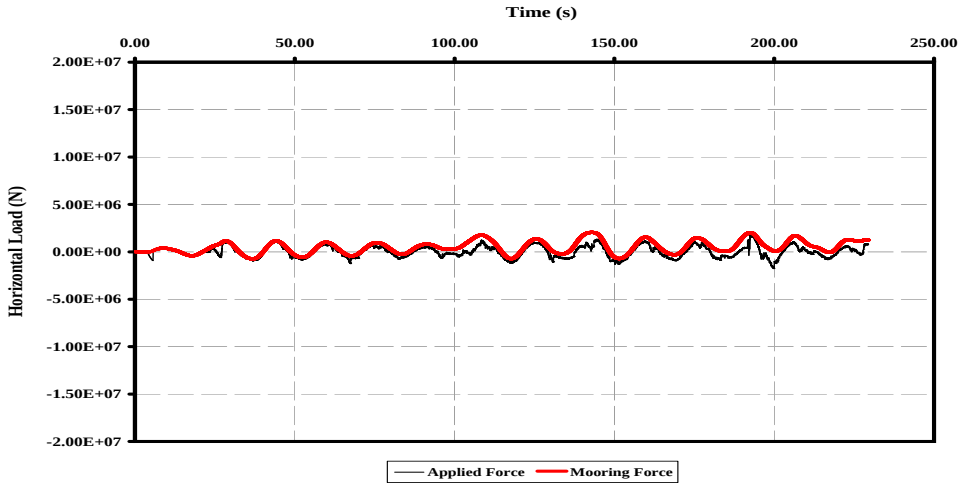

(a) $v = 0.25$m/s

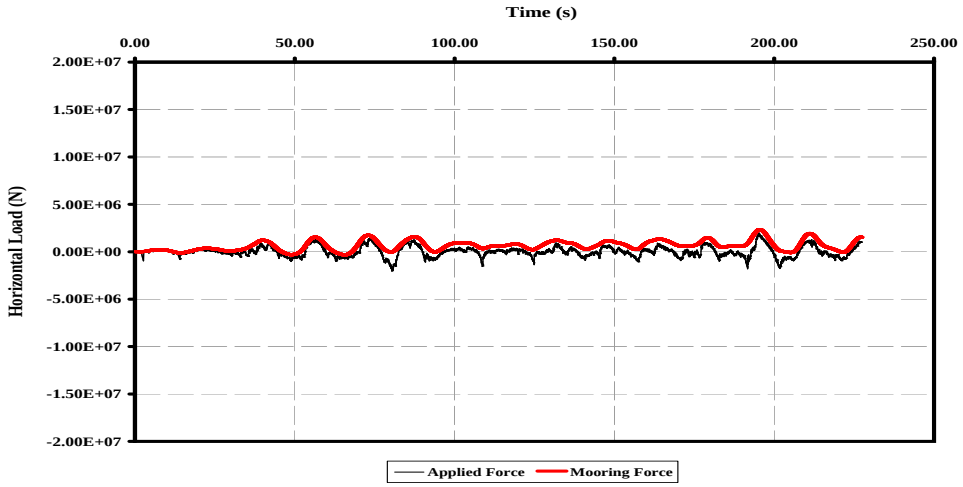

(b) $v = 0.5$m/s

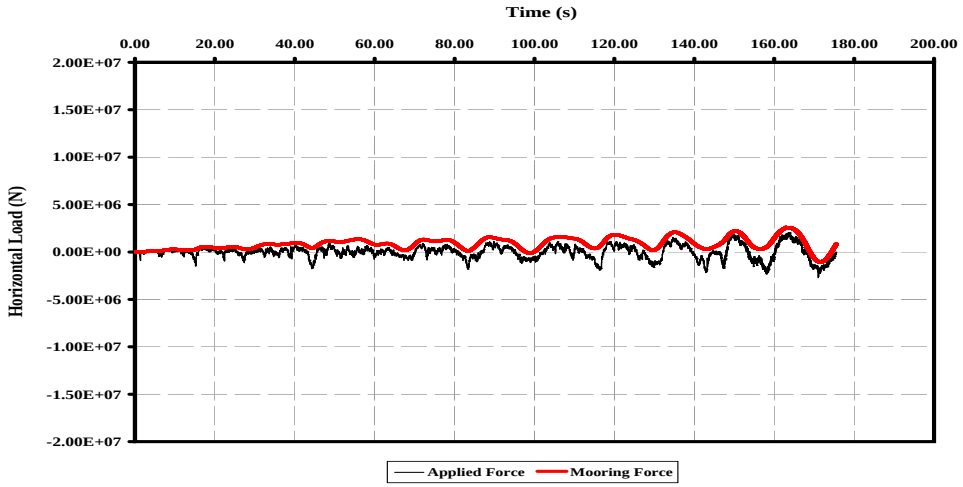

(c) $v = 1.0$m/s

Figure 7.34: Time history of applied and mooring horizontal forces for $\sigma_f = 500$kPa, $D_w = 35$m, $h = 0.8$m.

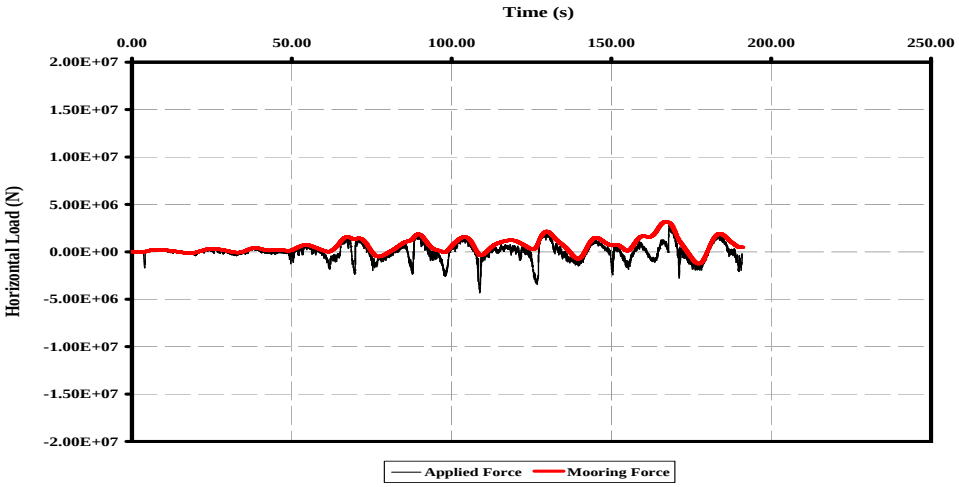

(a) $v = 0.25$m/s

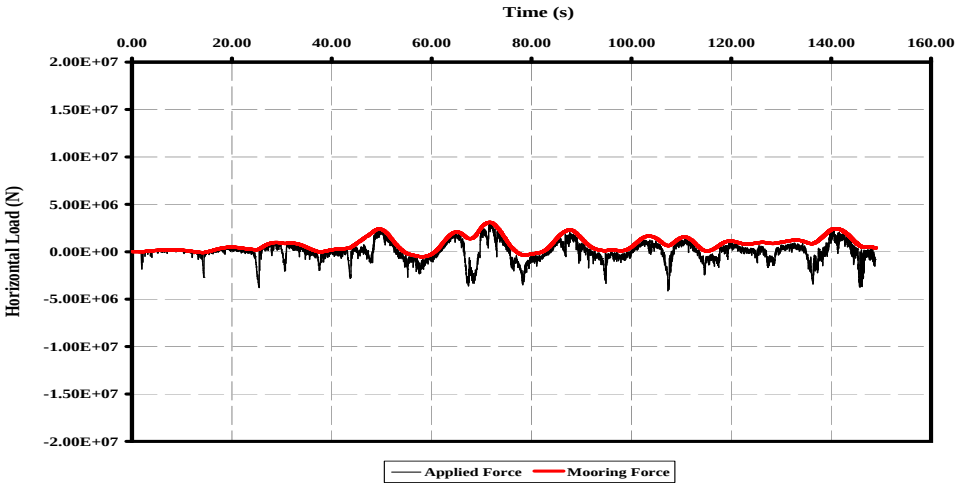

(b) $v = 0.5$m/s

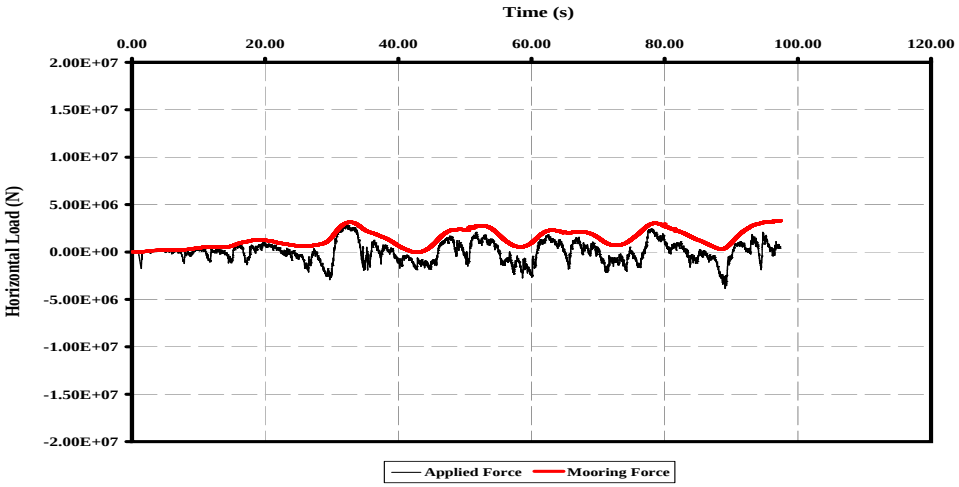

(c) $v = 1.0$m/s

Figure 7.35: Time history of applied and mooring horizontal forces for $\sigma_f = 500$kPa, $D_w = 35$m, $h = 1.2$m.

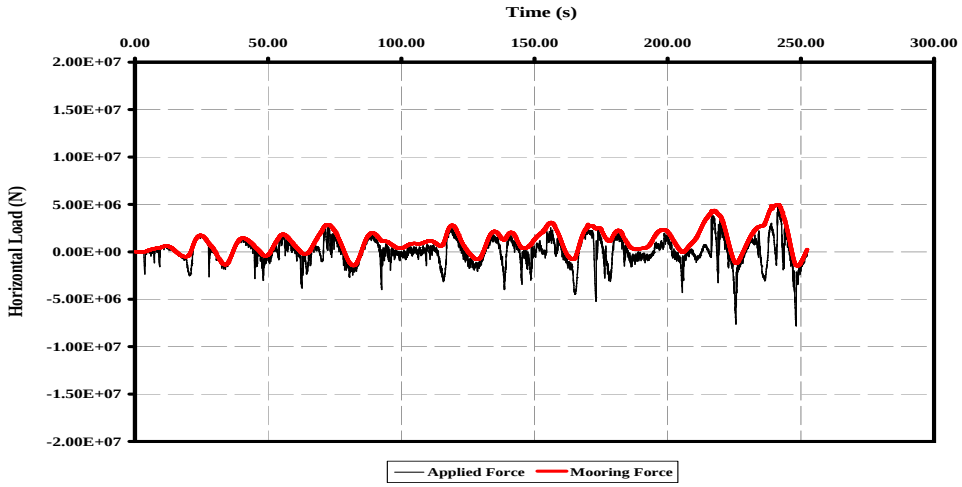

(a) $v = 0.25$m/s

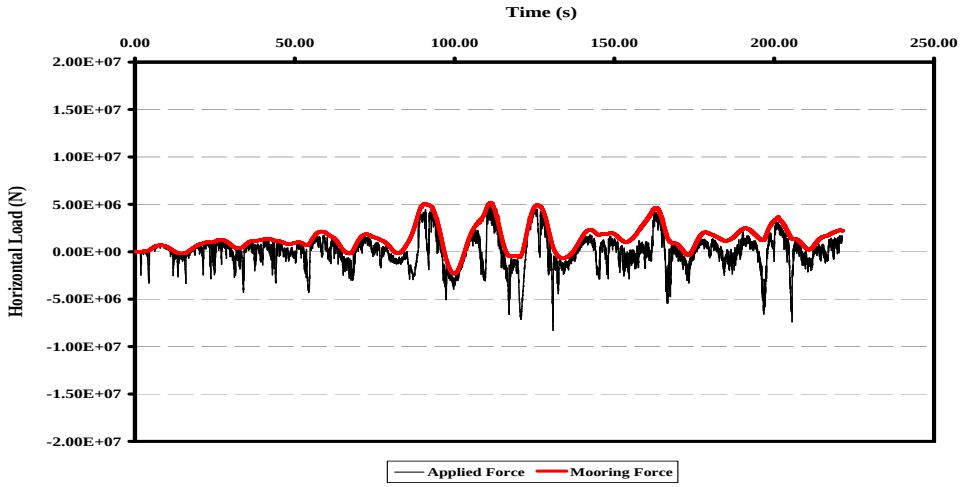

(b) $v = 0.5$m/s

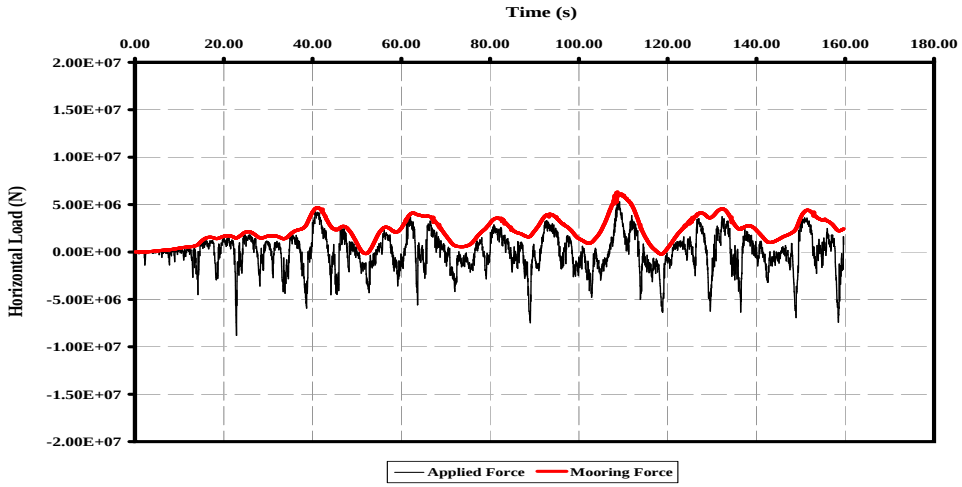

(c) $v = 1.0$m/s

Figure 7.36: Time history of applied and mooring horizontal forces for $\sigma_f = 500$kPa, $D_w = 35$m, $h = 1.6$m.

Effect of ice thickness

The peak values of the applied and mooring force are presented in Figure 7.37 for $\sigma_f = 500$kPa, $D_w = 35$m. Clearly, both the applied and mooring forces increase with ice thickness in the range $h = 0.4 - 1.6$m but a best-fit power law is included on each graph to evaluate the relationship. The applied force fit displays a power relationship of nearly h^2, which was also observed in the NRC-IOT experiments. The best fit of the peak mooring load is similar but the power is decreased slightly. As the ice thickness increases, both the applied and mooring force approach the design threshold force of 1000 tonnes. The applied force exceeds this threshold value for all velocities at $h = 1.6$m, but the mooring force only exceeds it at the highest velocity. The "Kulluk" drillship was designed to withstand an impact of level ice up to 1.2m thick. These numerical results confirm that this design goal is achieved for $\sigma_f = 500$kPa in a water depth of $D_w = 35$m.

These data points for the mooring force are plotted with the previous experiments and full-scale data set in Figure 7.38. The current numerical results for $h \leq 1.2$m fall within the range predicted by the past experiments (IIHR, Arctec, HSVA) for the peak mooring load. There was no previous experimental data for ice thicknesses above 1.4m, but the numerical results do appear to follow the trend in the data.

In comparison to the full-scale data set, the results overestimate the peak observed force by up to 200%, an observation that is in agreement with all other experimental studies. Wright et al. (1998) proposed that the data existing in their studies was not meant as a fully accurate description of the problem but was intended only to show trends in the recorded data. There are many potential sources of error in their data, as was pointed out by the authors, which include human error in recording visual estimates of the approaching ice formations, applicability of empirical formulae used

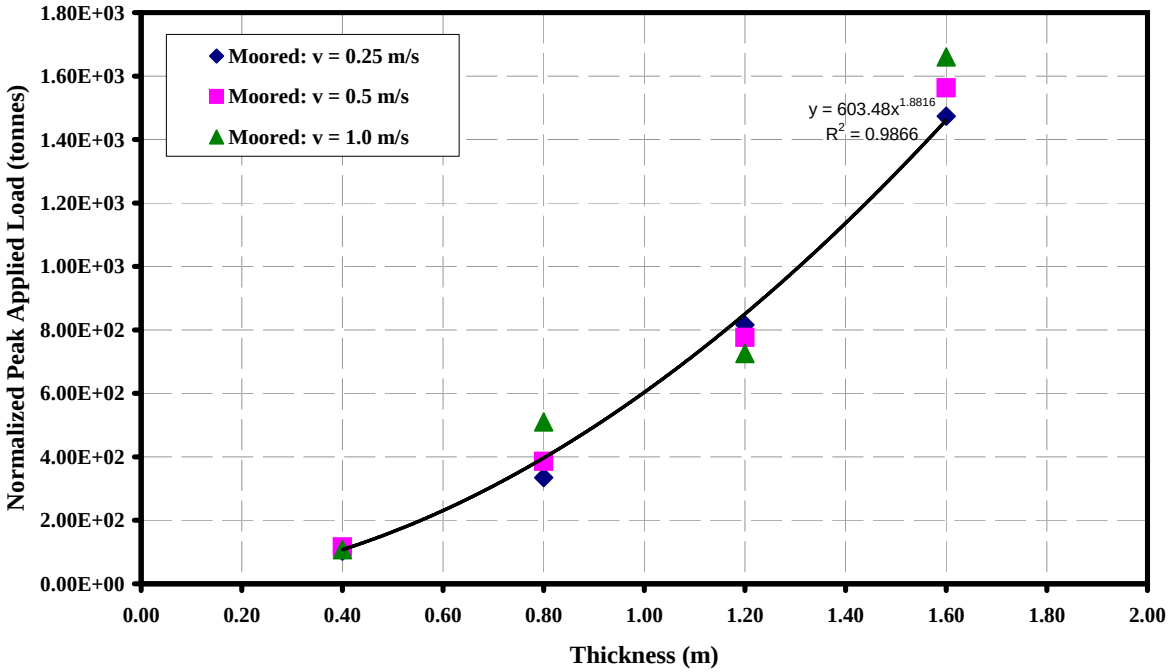

(a) applied force

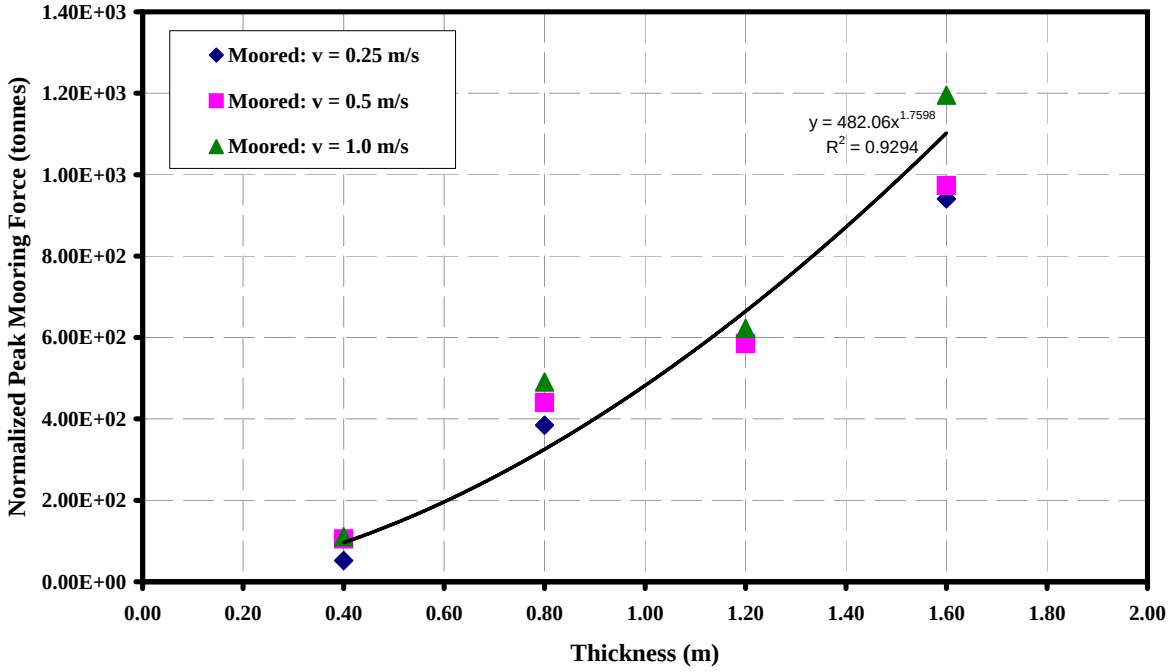

(b) mooring force

Figure 7.37: Numerical prediction of peak horizontal applied and mooring forces versus ice thickness for $\sigma_f = 500$kPa, $D_w = 35$m.

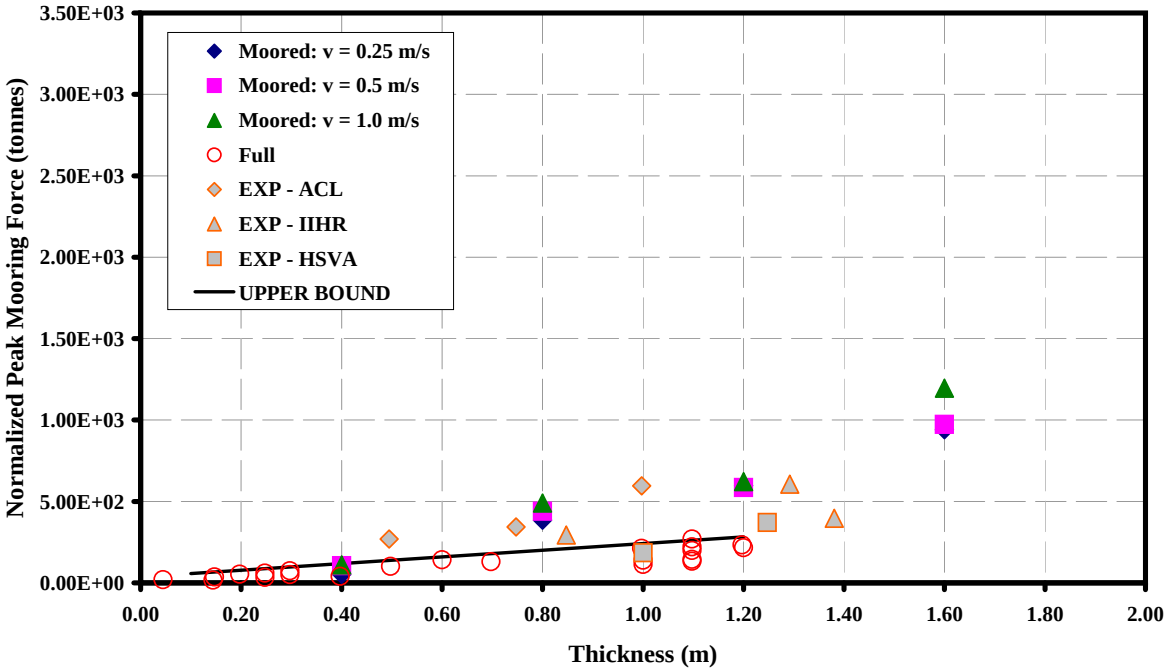

Figure 7.38: Numerical prediction of peak horizontal mooring forces versus ice thickness for $\sigma_f = 500$kPa, $D_w = 35$m together with the IIHR, HSVA, Arctec, and full-scale observations.

to estimate ice properties, and so on. To further highlight the possibility that the full-scale data set may be slightly underestimated, consider the analytical approaches of Croasdale (1980) and Ralston (1977) for ice interaction with a sloping conical structure. Croasdale (1980) presented a two-dimensional analysis of the ice interaction which consisted of a breaking force term and an ice ride-up force term. Ralston (1977) used a three-dimensional plastic limit analysis to present a model which includes terms for estimating the breaking force, ride-up force, and clearing force. More importantly, it was suggested that the forces on an inverted or downward-breaking cone could be estimated by reducing the density by a factor of nine to account for the ice-weight-to-buoyant-force ratio in the different configurations. The result of modifying these formulae is shown in Figure 7.39. The analytical prediction curves

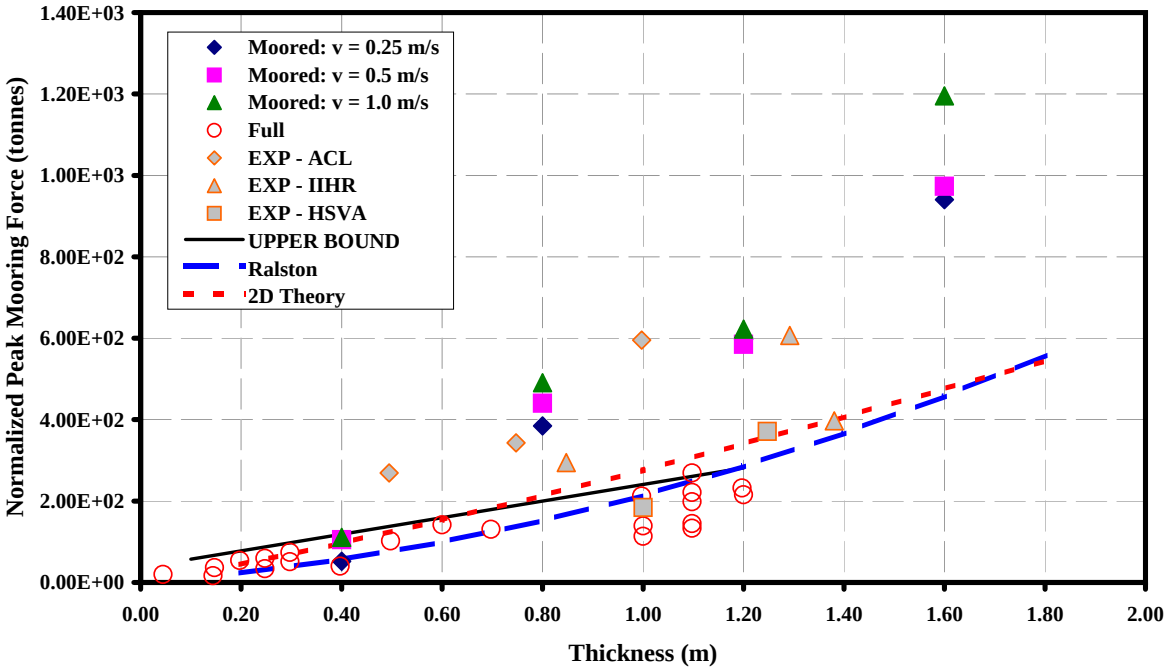

Figure 7.39: Numerical prediction of peak horizontal mooring forces versus ice thickness for σ_f = 500kPa, D_w = 35m together with the analytical methods of Ralston (1977), Croasdale (1980) and the IIHR, HSVA, Arctec, and full-scale observations.

are plotted as dashed lines together with the existing experimental and full-scale data values. For lower ice thickness, the analytical predictions underestimate the full-scale peak force data by approximately 50%, but as the ice thickness increases, the predictions are in better agreement. However, these predictions are for a sloping conical structure, which is quite different than the Kulluk design. At sea level, the Kulluk drillship is of the sloping conical form, so it is reasonable to assume that, if the ice breaks near the waterline, the force required to break the ice would be similar. Also, as the ice pieces move down along the structure, the buoyancy force may also be similar. The clearing force, however, which is not accounted for in Croasdale's approach, may be quite different for the case of the Kulluk design. Although the Kulluk shape begins as a sloping conical structure at the waterline, it changes slope direction completely from top to bottom of the hull. The ice pieces which move down along the approaching face of the structure are not moving at a constant slope, which is the assumption with the analytical formula of Ralston (1977). Instead, the ice pieces proceed along a curved face which at points correspond to a vertical wall and then are redirected again by the extruding hull skirt. Hence, if the ice pieces proceed down the face of the structure, it is natural to assume that the resulting clearing forces would be higher than those of a completely sloping conical structure. The amount of increase should be investigated in an alternate study since it is not the main purpose of the existing research. The clearing forces are increased by a factor of 10 in Ralston's model and plotted in Figure 7.40 for comparison. The analytical curve representing the upper bound shown in this figure is consistent with current numerical predictions, past experimental observations, and full-scale data at lower values of the thickness. The main purpose here is to highlight that the values of the peak load in the full-scale data set in comparison to existing analytical formulae are low (not to suggest that 10 is a correct scaling factor for the clearing force). The values in comparison to: (1) the existing analytical techniques on a simplified model of the structures' shape; (2) the

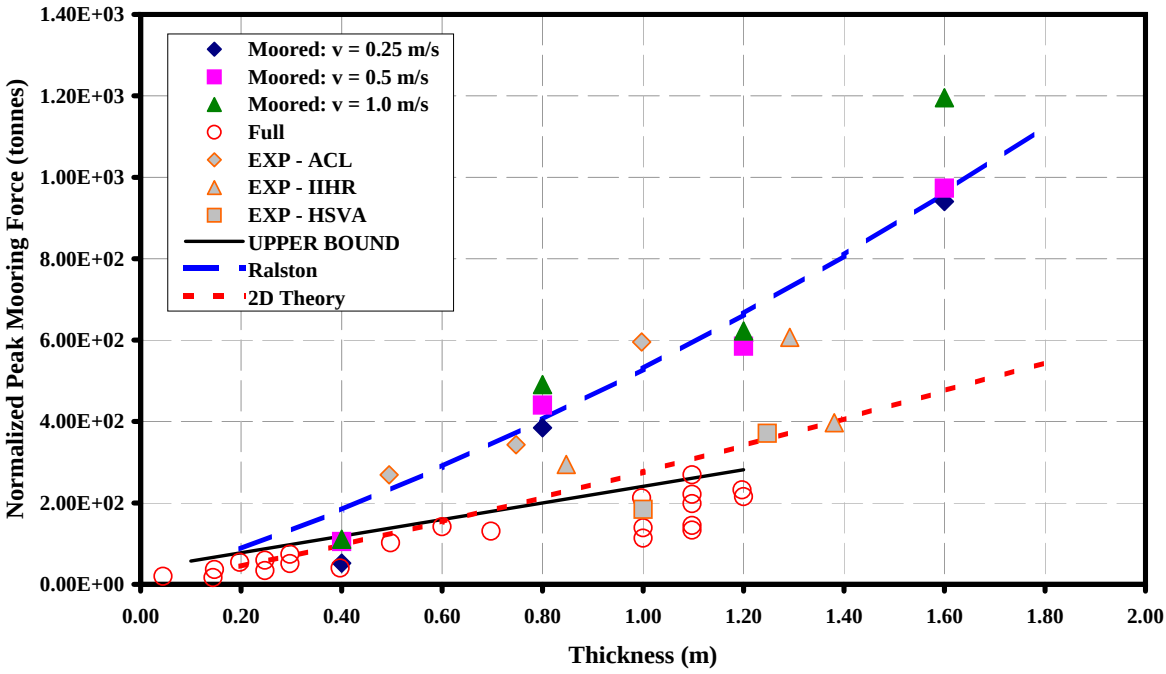

Figure 7.40: Numerical prediction of peak horizontal mooring forces versus ice thickness for σ_f = 500kPa, D_w = 35m together with the analytical method of Ralston (1977) (clearing force scaled by 10) and the IIHR, HSVA, Arctec, and full-scale observations.

existing experimental data; (3) the current experimental and numerical data, could then infer that it may be plausible that the full-scale data estimates may be too low. This is one possible explanation. A second is highlighted below.

Figure 7.41 presents the results of the NRC-IOT experiments (for select velocities in the range of the existing numerical simulations) together with the existing numerical, past experimental/full-scale data, and analytical prediction of Ralston (with factor of 10 included for the clearing force). The numerical data points lie within the range of

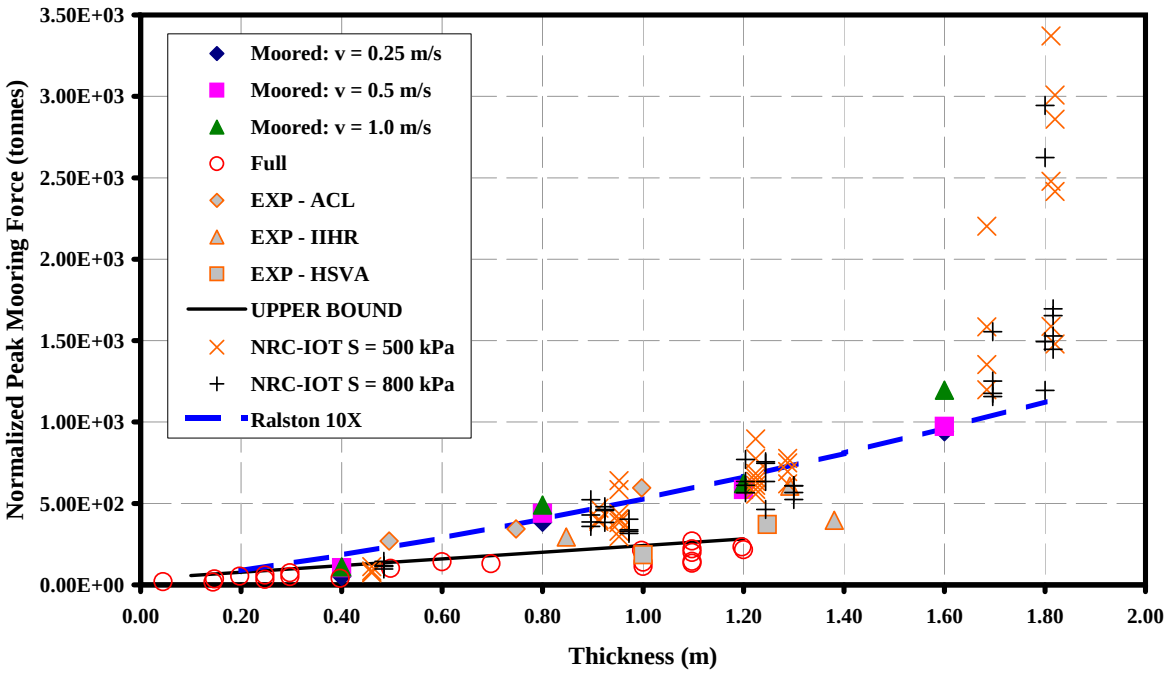

Figure 7.41: Numerical prediction of peak horizontal mooring forces versus ice thickness for $\sigma_f = 500$kPa, $D_w = 35$m together with the analytical method of Ralston (1977) (clearing force scaled by 10) and the NRC-IOT, IIHR, HSVA, Arctec, and full-scale observations.

observed experimental values for $h \leq 1.2$m. The experimental results are also consistent with the modified analytical method in this range. At $h = 1.6$m, the maximum magnitude of the numerical results only reaches the minimum of the NRC-IOT data.

One experimental result does not even make it into the upper bound of this graph. There are no other sources which present data at this ice thickness (possibly because the Kulluk was only designed to withstand a 1.2m ice sheet impact). This leads to the second possible explanation for the increase of ice loads observed in the experimental and numerical results. The three experimental studies conducted to date (Arctec, IIHR, HSVA) have all encountered the formation of a rubble-pile at the face of the Kulluk model. The rubble-pile was consistent with the full-scale observations but the pile formed in the experimental tests appeared to be much larger. A larger rubble pile in front of the advancing structure would undoubtedly result in higher ice forces and would be amplified as the ice thickness increases. The rubble pile formation was also observed in the numerical simulations (see Figure 7.42 for snapshot of numerical results). The numerical and experimental schemes may be incorrectly or unable to

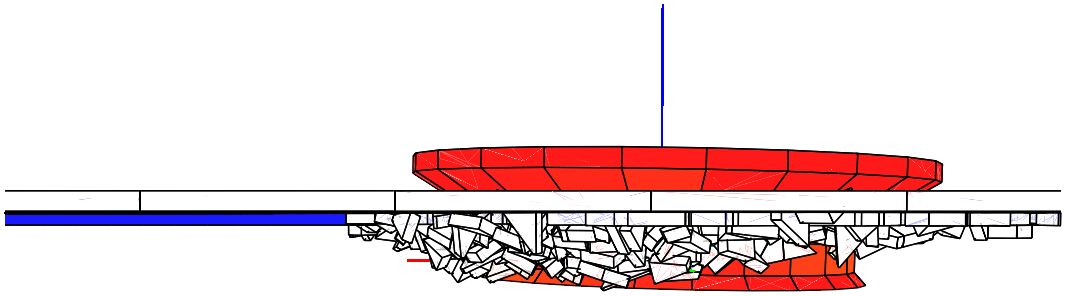

Figure 7.42: Snapshot of typical simulation in which a large rubble-pile formed in front of the platform.

capture certain aspects of the full-scale mechanics (such as the size of the rubble pile) which could lead to an overestimate of the peak forces. For instance, the numerical simulations are in absence of an ocean current and waves which could assist in the clearing of the ice pieces around the structure. Or, the NRC-IOT experiments utilize a four-point mooring system which may result in abnormally high load data (as appear to be the case for the peak offsets). At this point, any suggestion in uncertainty

of the full-scale data and/or the experimental/numerical data is just conjecture. Improved numerical modeling and experimental techniques as well as better real-time data acquisition systems may provide clarification in the future.

Effect of velocity

The peak applied and mooring force versus velocity are shown in Figure 7.43. At a given ice thickness, the overall trend in the data indicates a small increase in peak load as the velocity increases. The effect is clearly secondary to the thickness, which causes much larger increases in the peak load. This is in agreement with the trends observed in the previous studies and in the NRC-IOT experiments.

7.4.5 Peak horizontal loads - $\sigma_f = 800$kPa - $D_w = 35$m

The effect of increasing the flexural strength from $\sigma_f = 500$kPa to 800kPa is addressed in this section.

Effect of ice thickness and increased flexural strength

The peak values of the applied and mooring forces are presented in Figure 7.44 for $\sigma_f = 800$kPa, $D_w = 35$m. Again, both the applied and mooring forces increase with ice thickness in the range $h = 0.4 - 1.6$m with best-fit power laws of order near h^2. The increase in flexural strength has increased the largest value of the force significantly, but the maximum value at $h = 1.2$m is still beneath the 1000 tonne threshold. All values of the peak load at $h = 1.6$m exceed the threshold.

Figure 7.45 presents the results together with the previous observations and the numerical results at $\sigma_f = 500$kPa. Although most data points fall within the range of the previous data, an increase is observed in comparison to the same simulations

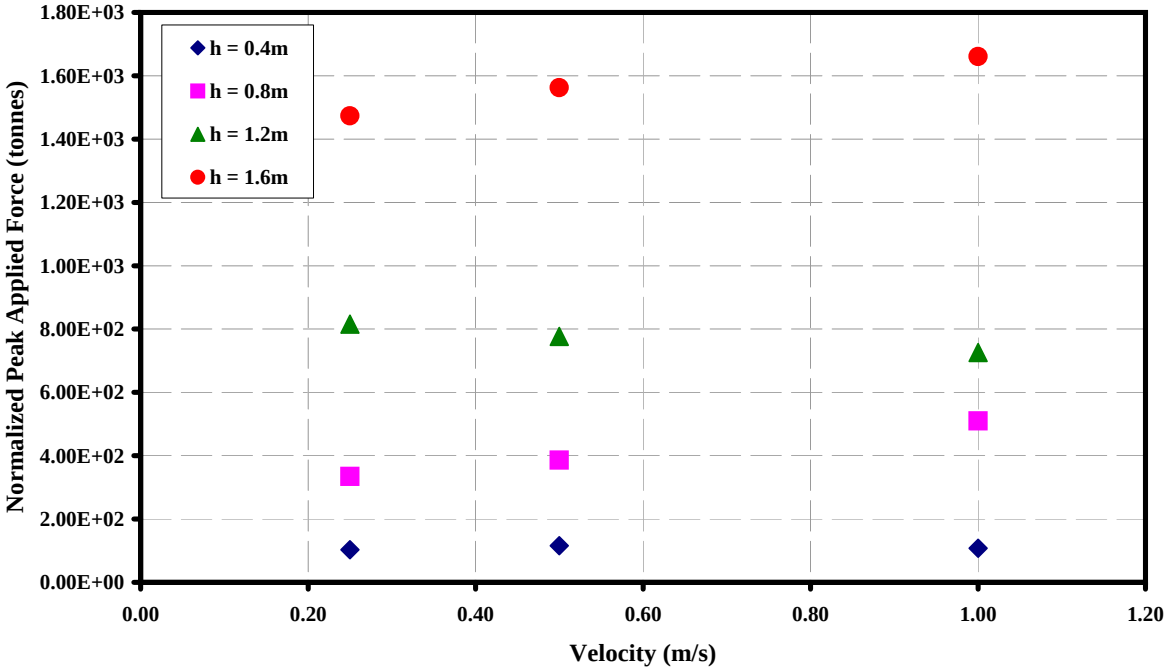

(a) applied force

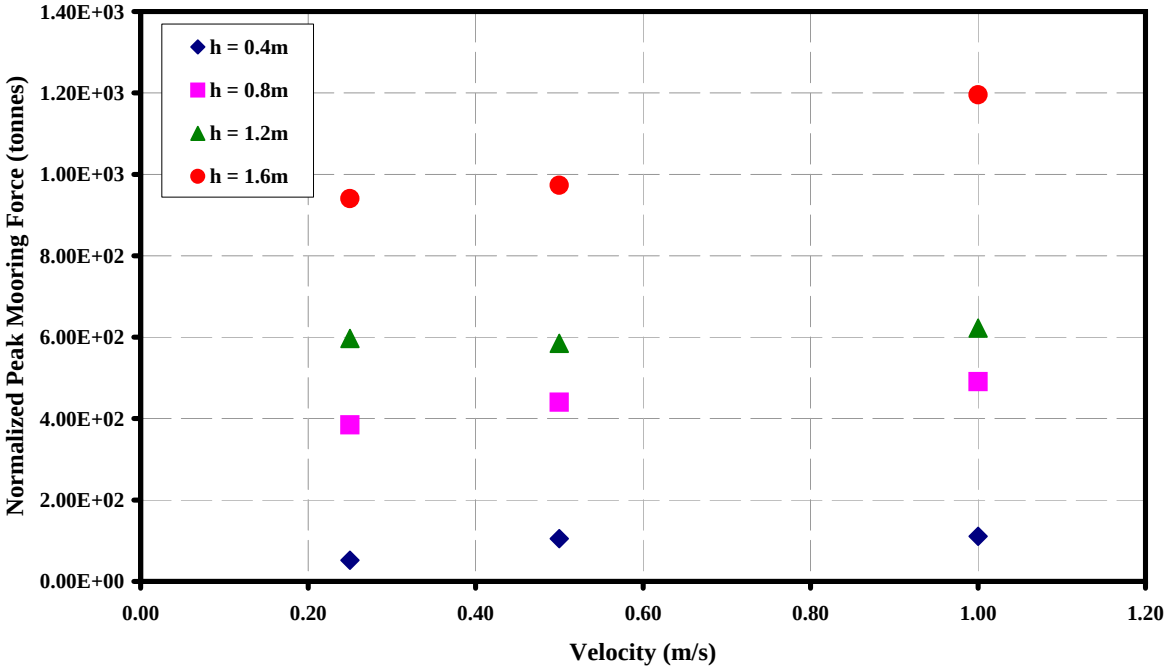

(b) mooring force

Figure 7.43: Numerical prediction of peak horizontal applied and mooring forces versus velocity for $\sigma_f = 500$kPa, $D_w = 35$m

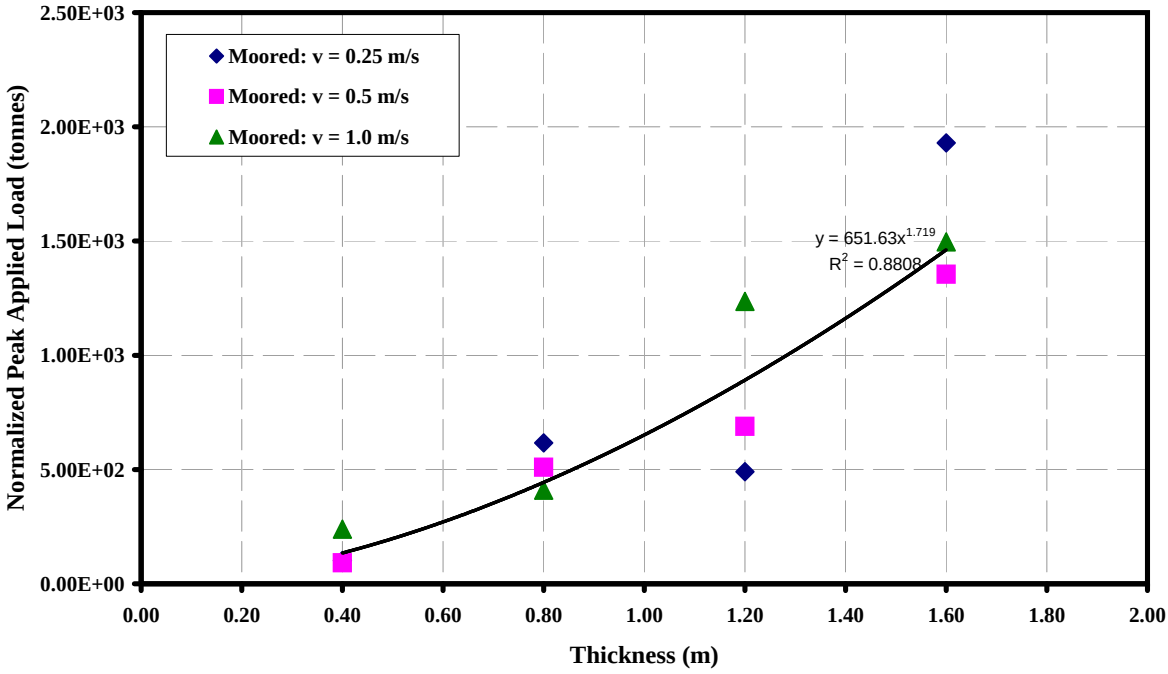

(a) applied force

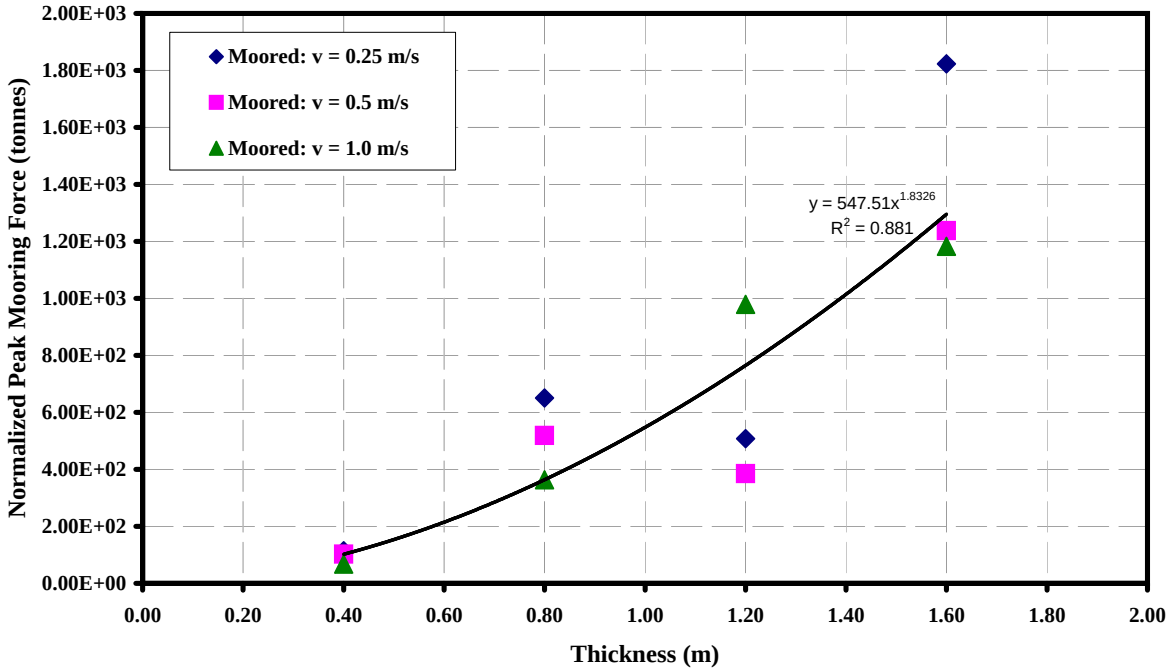

(b) mooring force

Figure 7.44: Numerical prediction of peak horizontal applied and mooring forces versus ice thickness for $\sigma_f = 800$kPa, D_u259 35m.

with $\sigma_f = 500$kPa. The two data points ($h = 1.2$m, $v = 1.0$m/s) and ($h = 1.6$m,

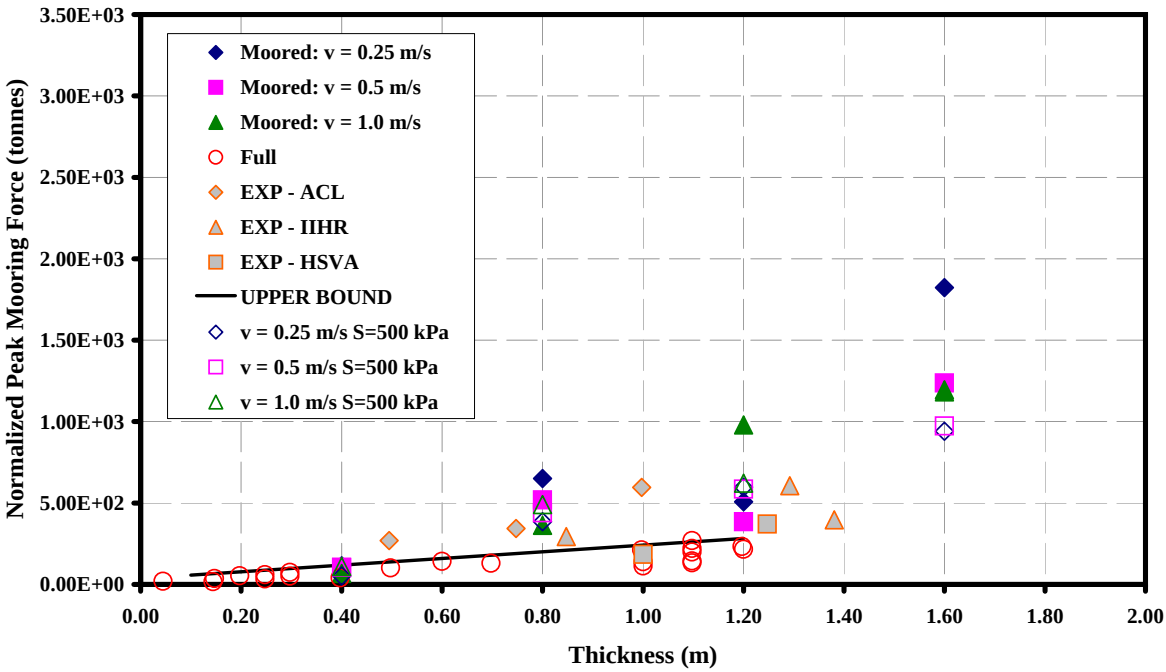

Figure 7.45: Numerical prediction of peak horizontal mooring forces versus ice thickness for $\sigma_f = 500$kPa and $\sigma_f = 800$kPa at $D_w = 35$m together with the IIHR, HSVA, Arctec, and full-scale observations.

$v = 0.25$m/s) display the largest deviation from the pattern. These are the same two points which were alluded to earlier during the discussion of the peak offsets at this flexural strength. The mooring forces for $h = 1.6$m, $v = 0.25 - 1.0$m/s are shown in Figure 7.46 for inspection. It should be noted that the magnitude of the mooring force at $v = 0.25$m/s is consistent with the magnitude of the force at the two larger velocities, except near time $t \approx 190$s. The curve exhibits a much larger peak at this location, which results from a period of time dominated by shear failure. This results in a value for the peak load that is higher than would be expected from the observed trend.

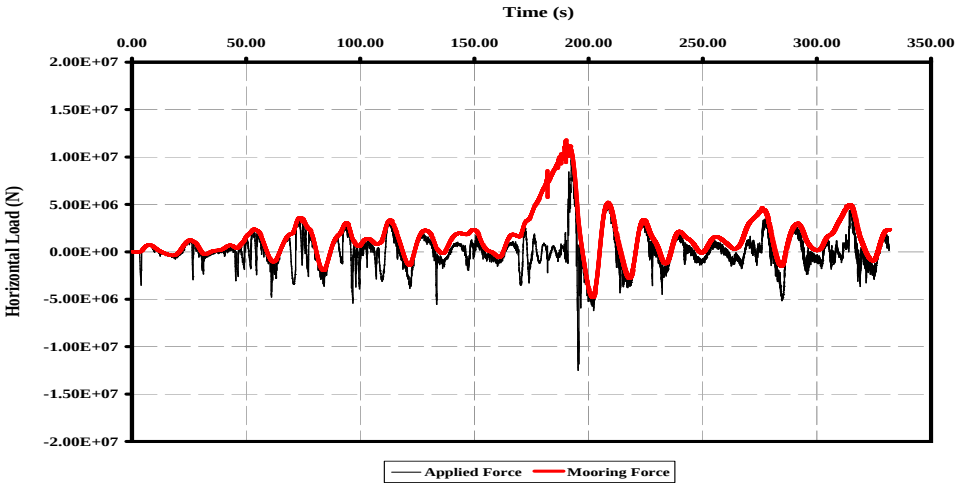

(a) $v = 0.25$m/s

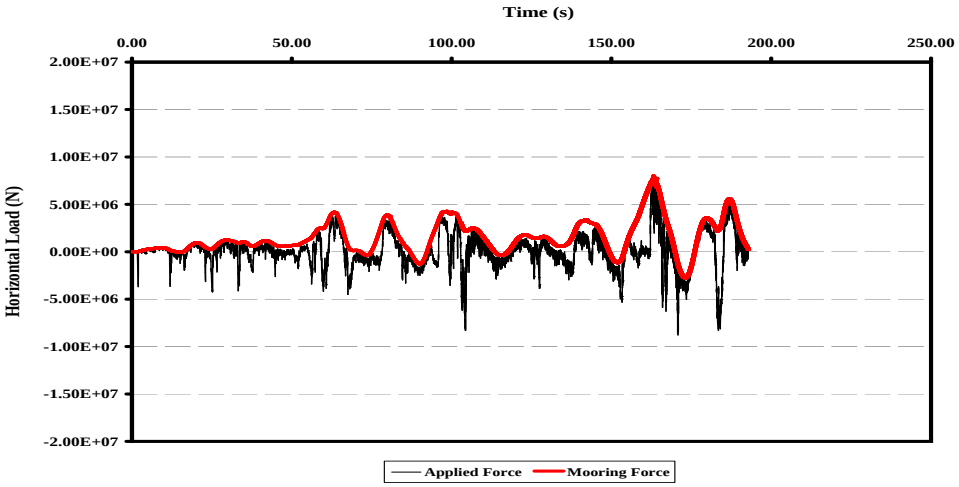

(b) $v = 0.5$m/s

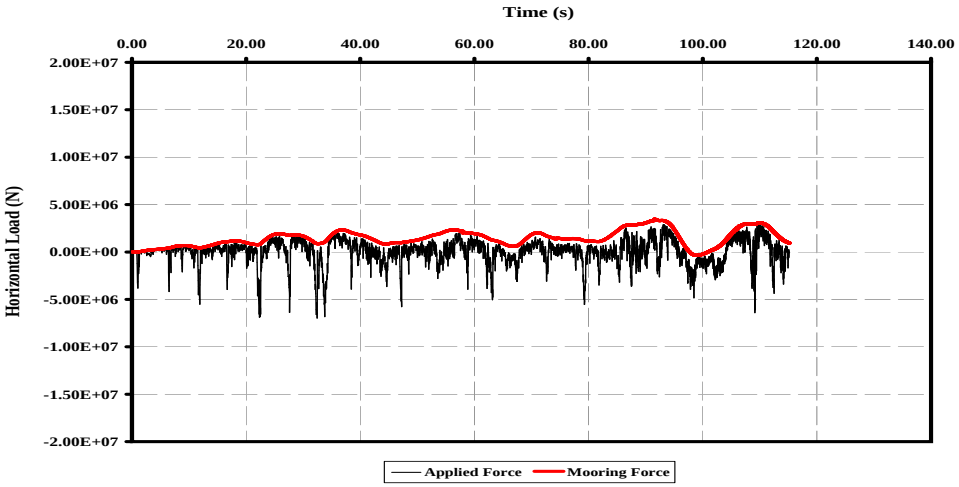

(c) $v = 1.0$m/s

Figure 7.46: Time history of applied and mooring horizontal forces for $h = 1.6$m with $\sigma_f = 800$kPa, $D_w = 35$m.

Figure 7.47 displays the current numerical results with the NRC-IOT experimental results, the previous experimental and full-scale results, and the analytical curve of Ralston (clearing force scaled by 10). The agreement between the results is con-

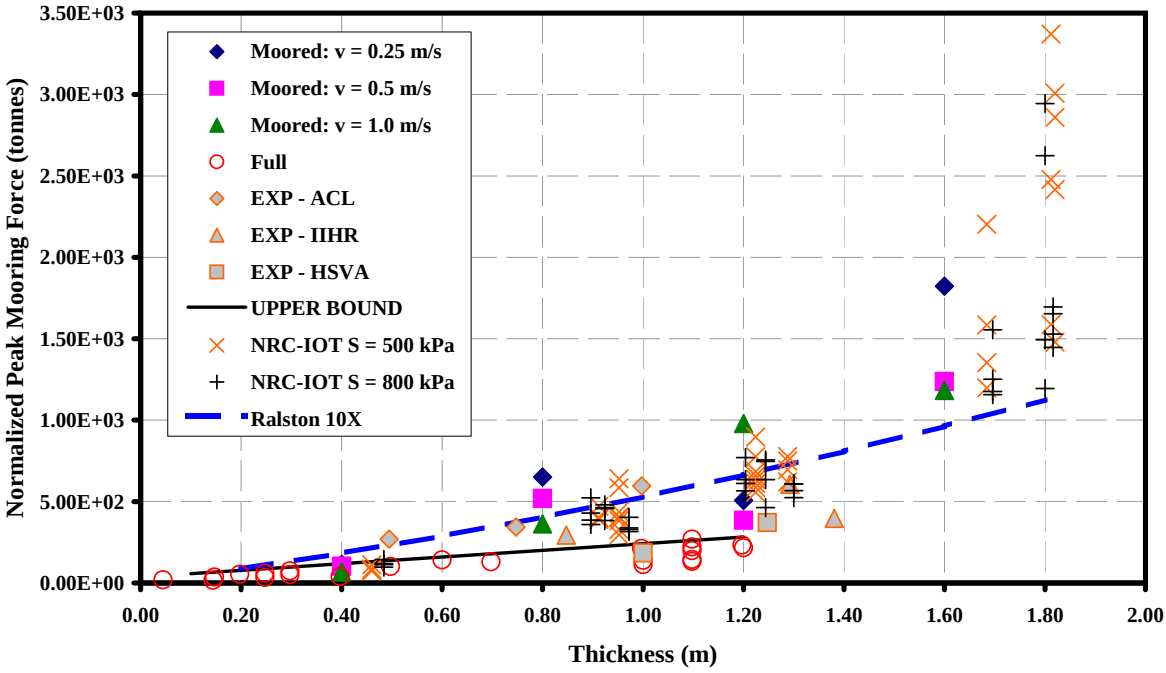

Figure 7.47: Numerical prediction of peak horizontal mooring forces versus ice thickness for $\sigma_f = 800$kPa, $D_w = 35$m together with the analytical method of Ralston (1977) (clearing force scaled by 10) and the NRC-IOT, IIHR, HSVA, Arctec, and full-scale observations.

sistent with what has been outlined thus far. The increase in the peak force at this flexural strength has moved the results for $h = 1.6$m into the range of results predicted by the NRC-IOT experiments. The maximum in the numerical data at $h = 1.6$m, $v = 0.25$m also exhibits the possibility of larger mooring forces when shear failure is encountered. This may explain the uncharacteristically high loads at $h = 1.6$m during the experiments but cannot be verified currently, since full access to the detailed images and/or videos has not been provided to the author.

Effect of velocity

The peak applied and mooring force versus velocity are shown in Figure 7.48. With the exception of the two data points noted above, there appears to be very little variation in the magnitude of the peak mooring force. The offset results for $\sigma_f =$ 800kPa indicate that there was a slight increase in peak offset for increasing velocity. In contrast, the force results at $\sigma_f = 800$kPa display a slight decrease in mooring force with velocity, indicating that there is a complex relationship between the failure mechanisms and the resultant ice forces on a platform.

7.4.6 Peak horizontal loads - $\sigma_f = 500$kPa - $D_w = 55$m

The effect of increasing the water depth from $D_w = 35$m to 55m is discussed in this section.

Effect of ice thickness and increased water depth

The peak values of the applied and mooring forces are presented in Figure 7.49 for $\sigma_f = 500$kPa, $D_w = 55$m. Both the applied and mooring forces increase with ice thickness in the range $h = 0.4 - 1.6$m with best-fit power laws of order h^2. An important observation here is that the mooring force at $h = 1.2 - 1.6$m is maximum for the intermediate velocity $v = 0.5$m/s, even though the maximum of the applied force is not maximum at this velocity. Recalling Figure 7.28, which presented the ratio of natural to forcing frequencies, the dominant frequency at $h = 1.2$m, $v = 0.5$m/s is also very close to the natural excitation frequency. Therefore, the application of a lower force resulted in a higher horizontal displacement and global mooring load. This is only possible because the particular set of problem parameters has created a loading frequency which is similar to the natural oscillation frequency of the platform.

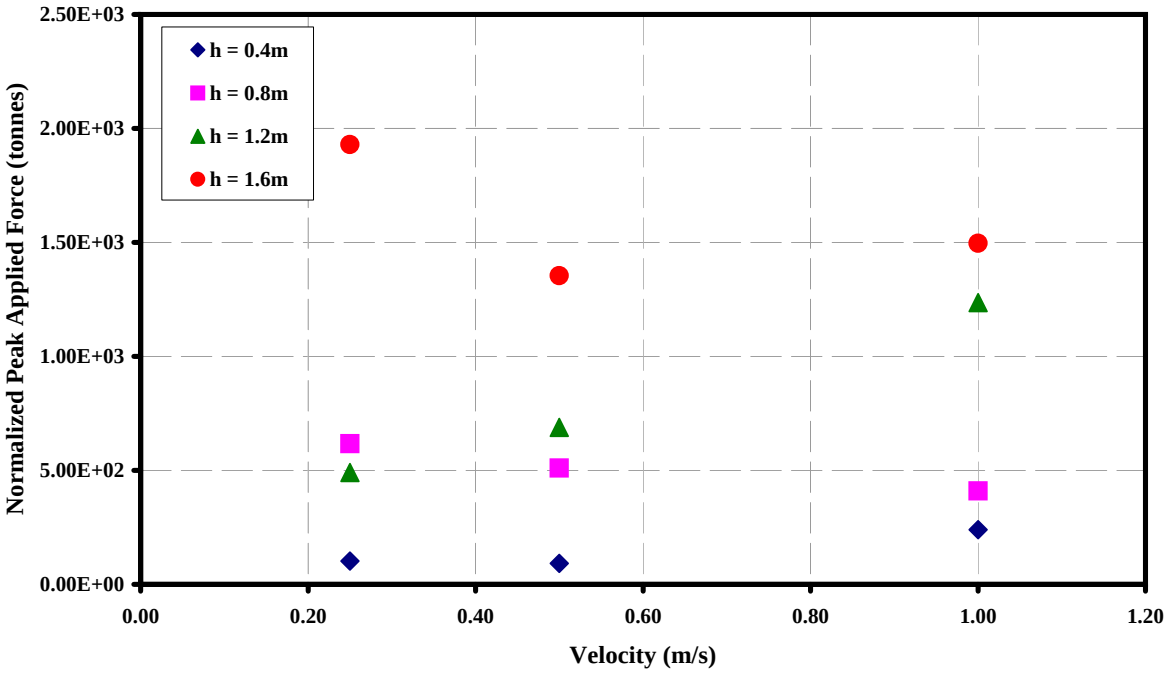

(a) applied force

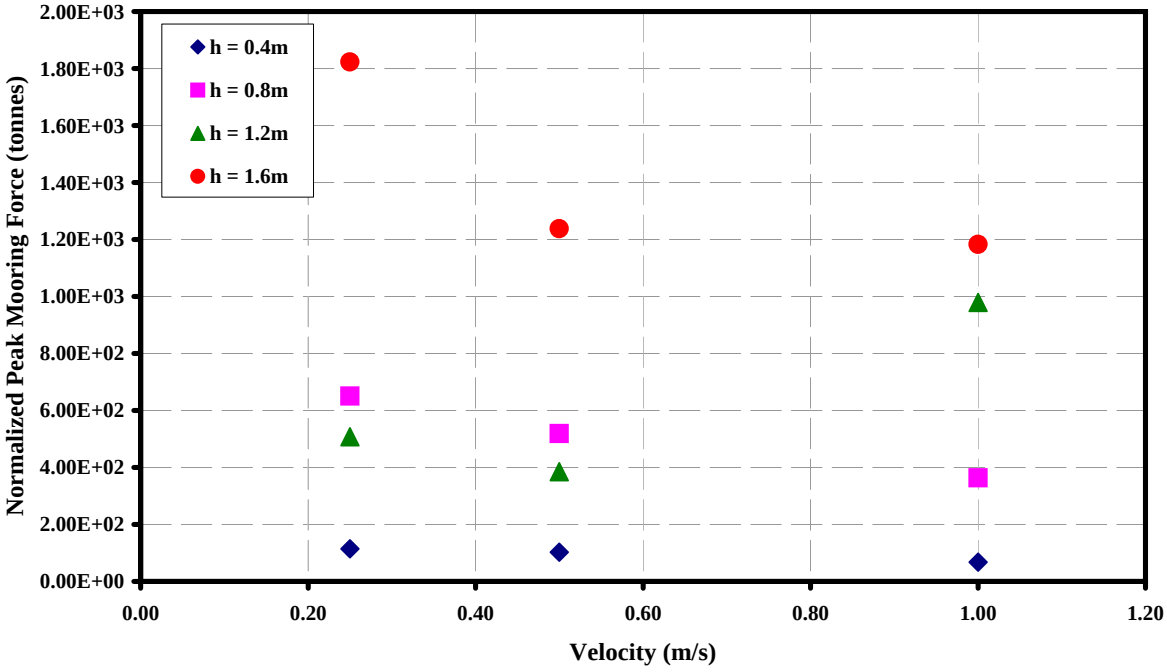

(b) mooring force

Figure 7.48: Numerical prediction of peak horizontal applied and mooring forces versus velocity for $\sigma_f = 800$kPa, $D_w = 35$m

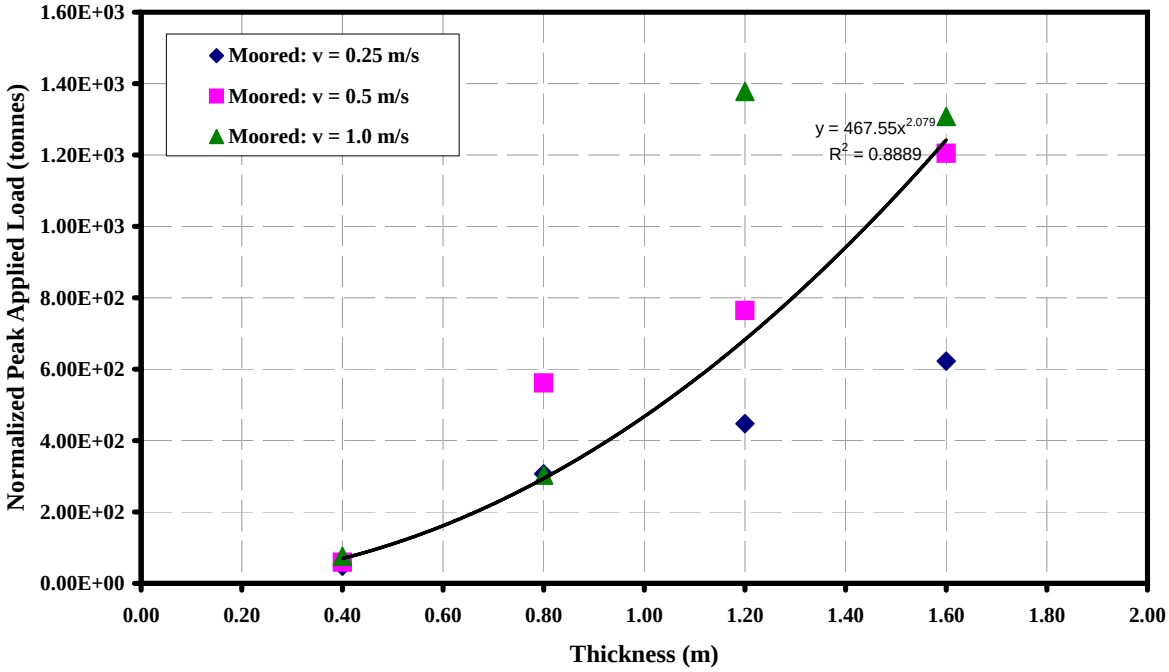

(a) applied force

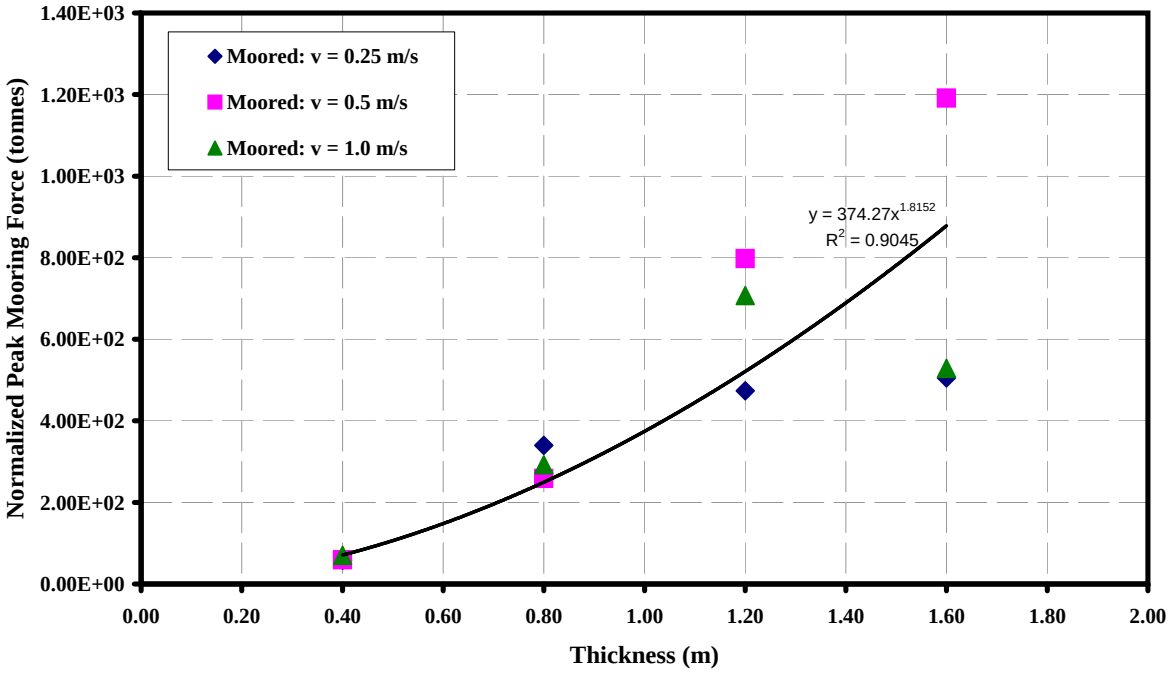

(b) mooring force

Figure 7.49: Numerical prediction of peak horizontal applied and mooring forces versus ice thickness for $\sigma_f = 500$kPa, D_w~~26~~55m.

Otherwise, it would be expected that smaller applied loads would lead to smaller offsets and mooring loads. This resonance effect was not observed at the lower water depth. This could be due to the fact that at the decreased water depth, the magnitude of the horizontal oscillations was restricted. It therefore behaved as a stiffer system than when using $D_w = 55$m, which in turn made it more difficult to control the platform motion with the application of ice forces.

Figure 7.50 presents the peak force result together with the previous observations as well as the peak load event data with $D_w = 35$m. Although the platform dis-

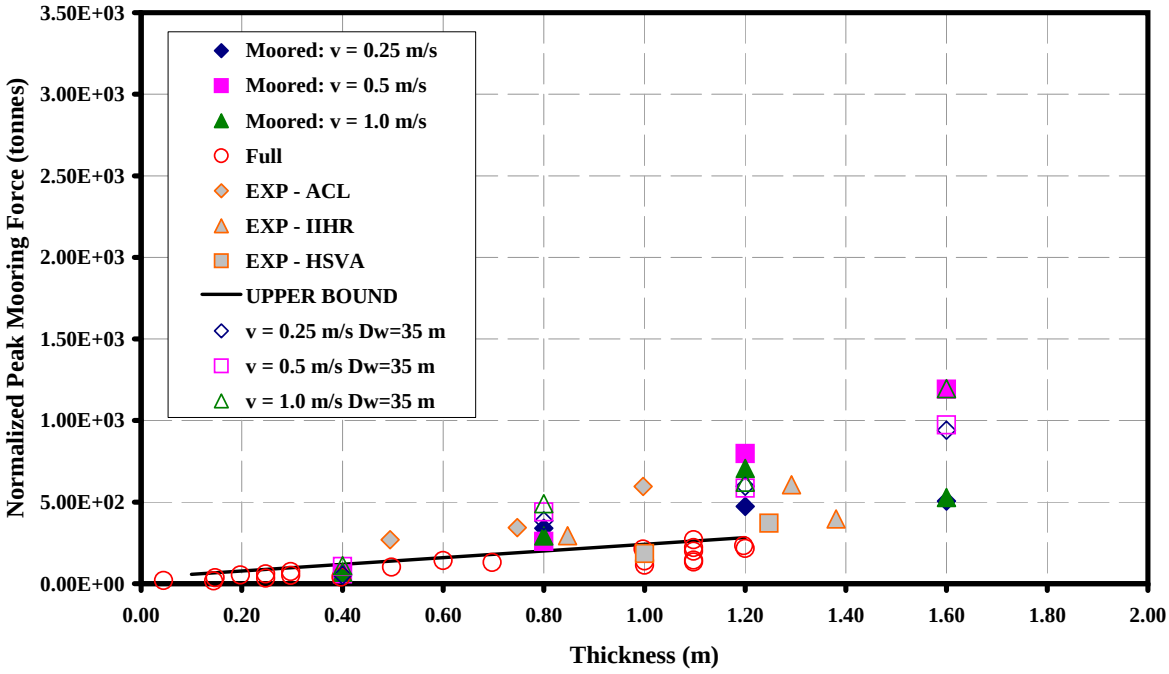

Figure 7.50: Numerical prediction of peak horizontal mooring forces versus ice thickness for $\sigma_f = 500$kPa at $D_w = 35$m and 55m together with the IIHR, HSVA, Arctec, and full-scale observations.

placements were much higher at $D_w = 55$m than $D_w = 35$m (see Figure 7.30), the peak load data at $D_w = 55$m is comparable to the data at $D_w = 35$m. In fact, in many cases, the peak load was less than that observed at the lower water depth

and closer to the full-scale data set. It appears that increasing the water depth has decreased the stiffness of the mooring system, allowing for larger overall platform displacements, which could reduce the global loads. At the increased water depth, however, the occurrence of platform excitation resonance leads to increased mooring loads (and offsets) which are approximately equal in magnitude to the results of the stiffer (shallower) system.

Figure 7.51 displays the current numerical results with the NRC-IOT experimental results, the previous experimental and full-scale results, and the analytical curve of Ralston (clearing force scaled by 10). The agreement between the results is consis-

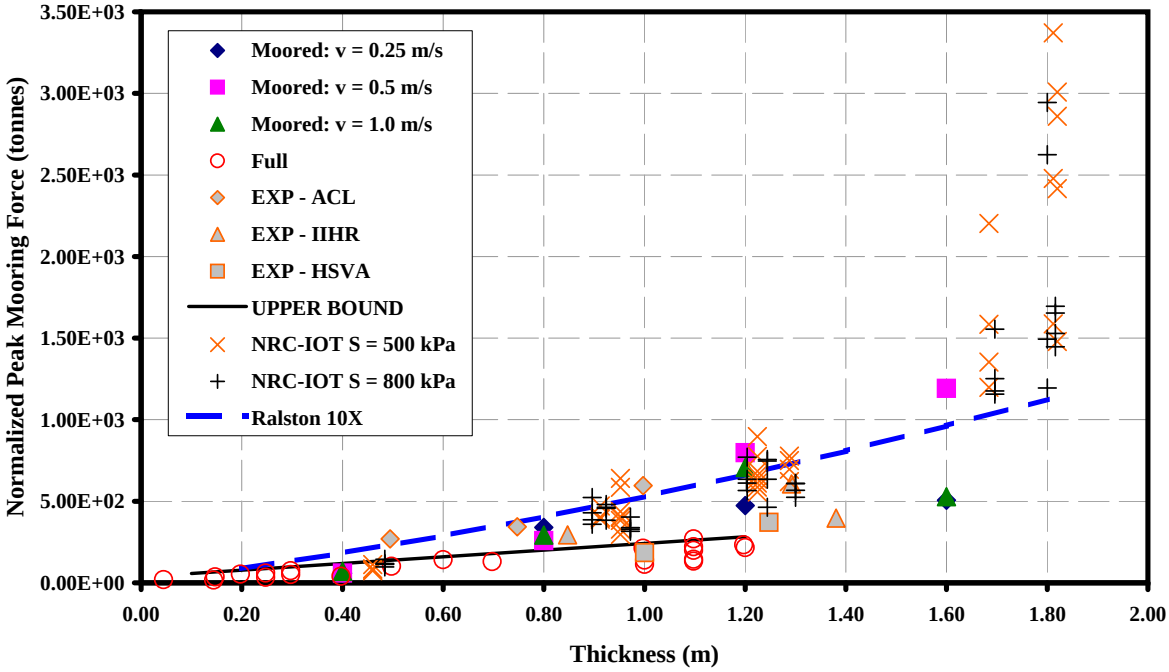

Figure 7.51: Numerical prediction of peak horizontal mooring forces versus ice thickness for σ_f = 500kPa, D_w = 55m together with the analytical method of Ralston (1977) (clearing force scaled by 10) and the NRC-IOT, IIHR, HSVA, Arctec, and full-scale observations.

tent with what has been outlined in the previous section. Increasing the water depth

does not have a significant influence on the peak forces observed but does allow for larger platform displacements. There does not appear to be any qualitative difference between operating this type of platform in water depths of 35 or 55m (with the given spread mooring system), since the larger displacements are permitted by the larger threshold values. In both instances, the threshold loads and offsets are exceeded at $h = 1.6$m.

Effect of velocity

The predictions of peak applied and mooring force versus velocity are shown in Figure 7.52. In general, the effect of velocity is less significant than the effect of thickness. The two data points at $v = 0.5$m/s ($h = 1.2 - 1.6$m) clearly do not conform to the previous trends in the peak force-velocity relationship but are explained by the platform excitation resonance.

7.4.7 Moored versus fixed structure

The same set of simulations could be conducted for a fixed conical drillship by restricting the movement of the structure in all directions. For a fixed structure, there is no mooring force so it is necessary to compare the applied force to determine the effect of mooring the platform on the peak loads. Figure 7.53 displays the time histories of the peak horizontal load on a fixed and moored structure with $h = 1.6$m, $v = 0.25 - 1.0$m/s, $\sigma_f = 500$kPa, $D_w = 35$m and Figure 7.54 shows the corresponding peak load data. The moored platform permits oscillations in the x-direction to relieve some of the applied force, whereas the fixed platform does not. Figure 7.54 indicates that, for the given set of parameters, mooring the platform instead of fixing it can result in a peak load decrease of nearly 50% (at $v = 0.25$m/s). The conclusion stated here cannot be generalized for all of the parameters investigated, but it does

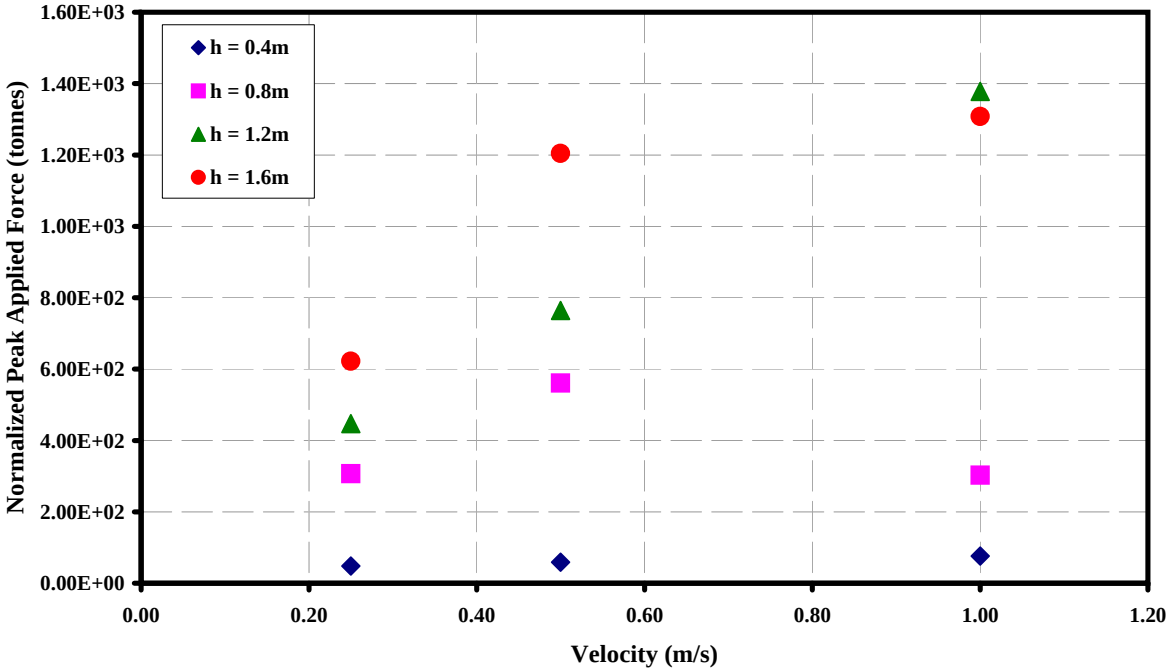

(a) applied force

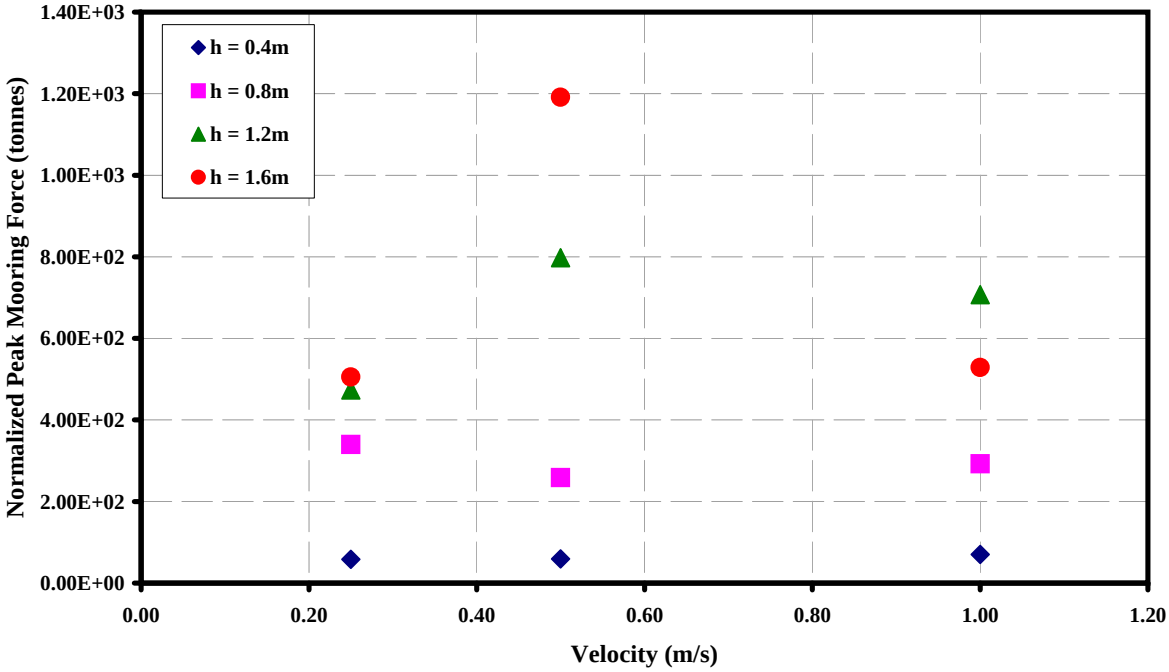

(b) mooring force

Figure 7.52: Numerical prediction of peak horizontal applied and mooring forces versus velocity for $\sigma_f = 500$kPa, $D_w = 52$m.

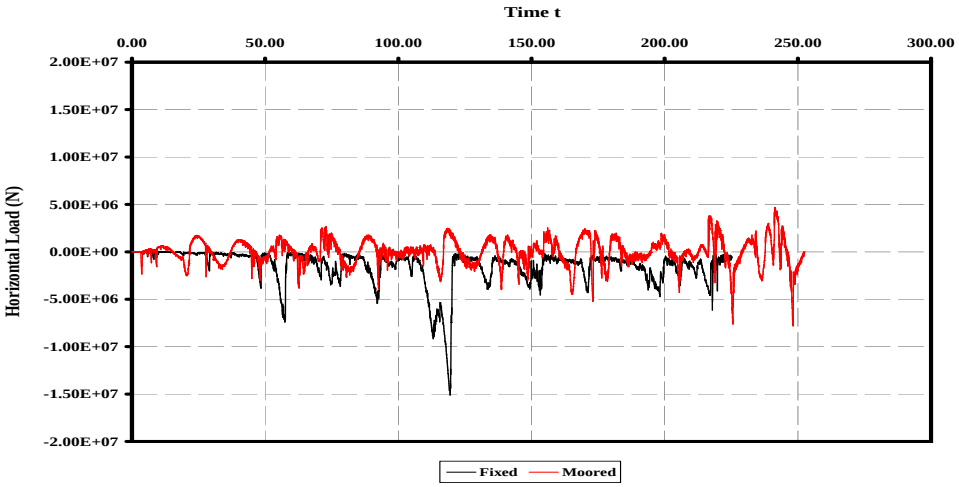

(a) $v = 0.25$m/s

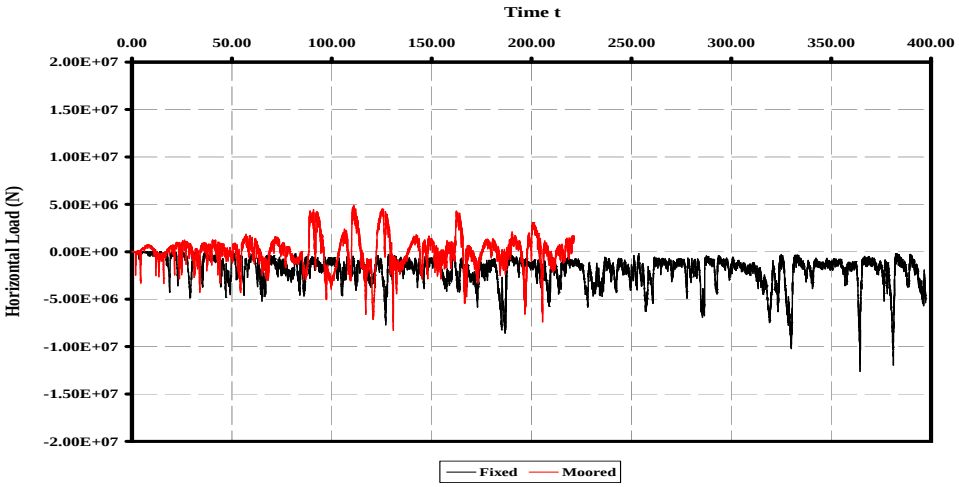

(b) $v = 0.5$m/s

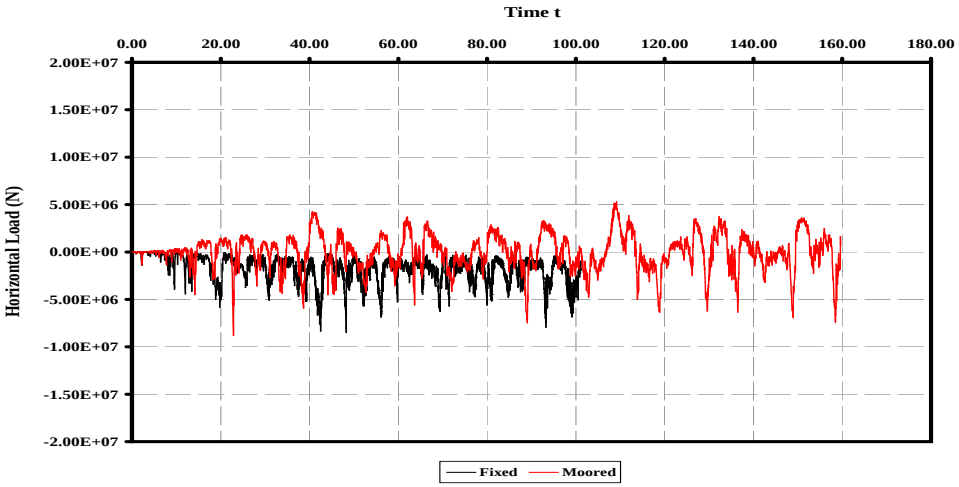

(c) $v = 1.0$m/s

Figure 7.53: Time history of applied horizontal forces on a moored and fixed structure for $h = 1.6$m, $\sigma_f = 500$kPa, $D_w = 35$m.

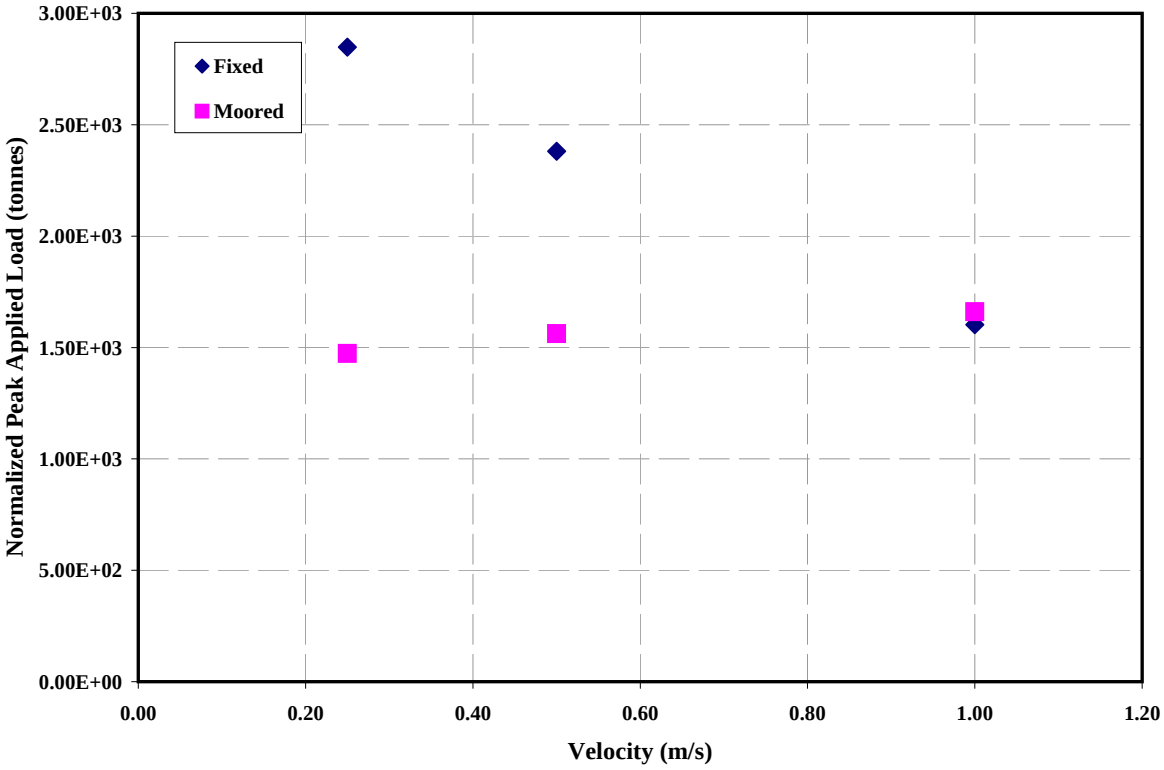

Figure 7.54: Comparison of peak applied force for a moored and fixed structure for $h = 1.6$m, $\sigma_f = 500$kPa, $D_w = 35$m.

support the claim made by previous studies (Nixon and Ettema, 1987; Wessels, 1984; Comfort et al., 1982; Abdelnour et al., 1987) that mooring the platform resulted in a significant decrease (up to 50%) in the peak force.

7.5 Ice Failure Patterns

In this section, the ice failure patterns observed in the numerical experiments are discussed. Under certain conditions, which include low ice velocities and small ice thickness (in comparison to the structure width), the dominant mode of ice sheet failure observed in previous studies on sloping conical structures is bending (with localized crushing). For narrow structures, ice typically fails along lines which extend radially from the structure. Then, as they ride along the surface of the structure, secondary failure is observed circumferentially (see Figure 7.55). For wider structures, such as the case under investigation, the curvature of the structure at the point of ice sheet impact is much smaller, which causes the ice sheet to first develop circumferential and then radial cracks. These circumferential cracks are typically formed at a distance slightly larger than the characteristic length of ice given by

$$l_c = \frac{Eh^3}{12(1-\nu^2)\rho_w g}. \tag{7.3}$$

In the numerical simulations, the characteristic length is about 5m for the thinnest ice, $h = 0.4$m, investigated and 14m for the thickest, $h = 1.6$m. These circumferential cracks, however, result from pure bending of the ice sheet only for thin ice (Wessels and Kato, 1989). As the ice thickness increases, a combination of bending and shear stresses cause the crack formation.

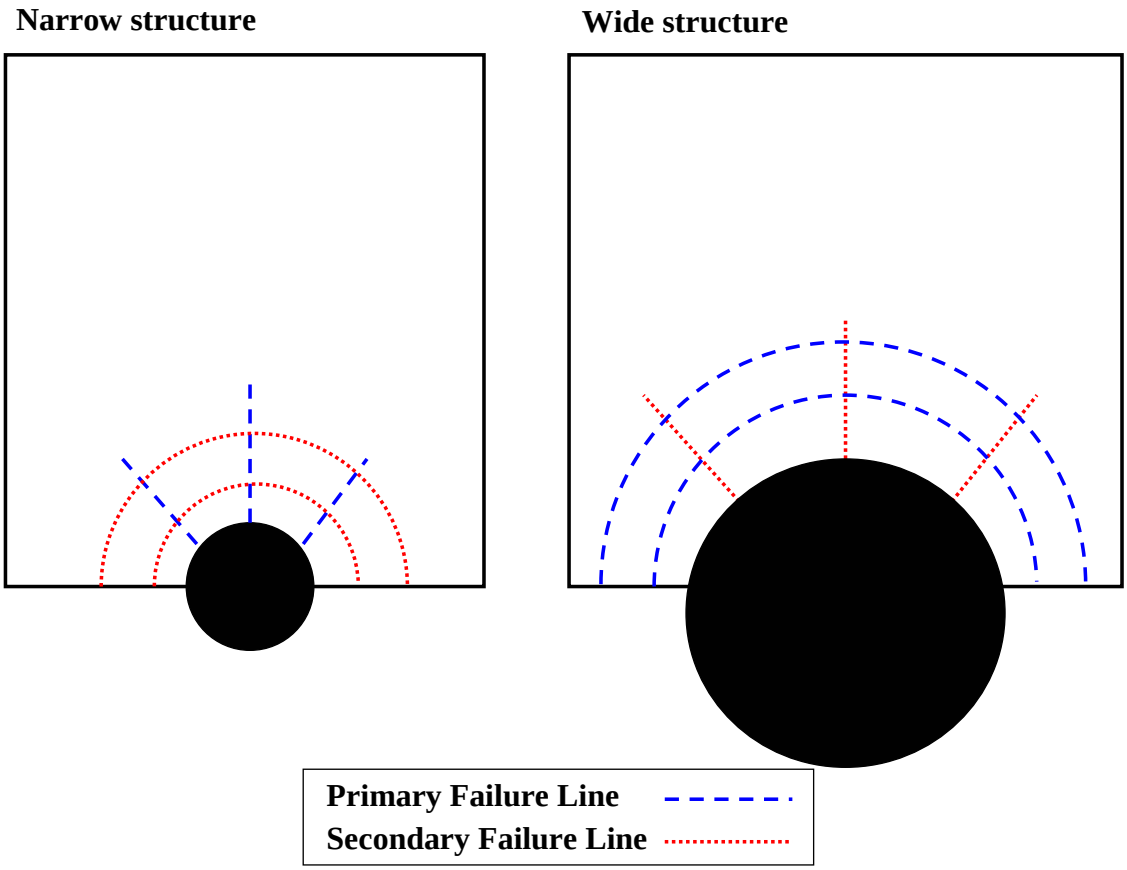

Figure 7.55: Transition of failure mode of ice sheet against conical narrow and wide structures.

7.5.1 Dominant failure modes

The percentages of the occurrence of the bending and shear failure modes during the numerical simulations are shown in Figures 7.56-7.58 for each major set of parameters.

A bar graph is presented in each figure with the horizontal axis representing the

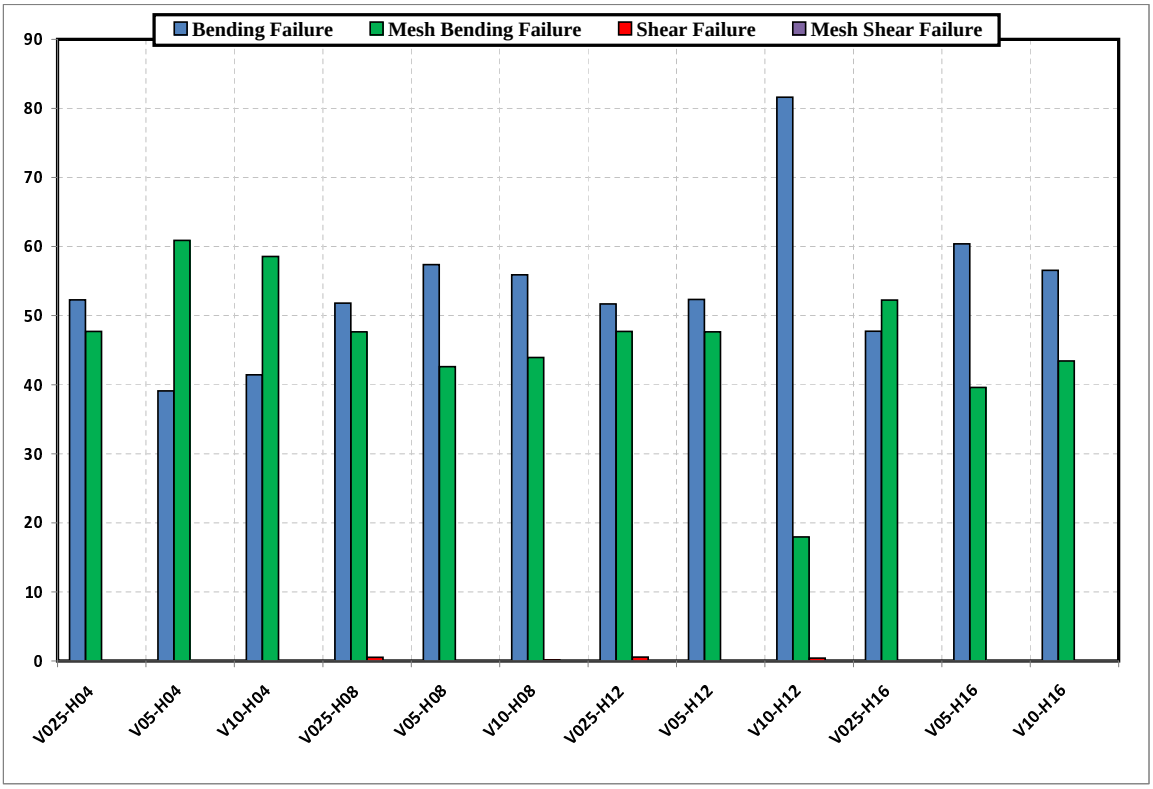

Figure 7.56: Percentage of occurrence of each failure mode during each simulation for $\sigma_f = 500$kPa, $D_w = 35$m.

varying thickness and velocity trials. The height of the bars in each trial corresponds to the percentage of that type of failure which was observed during the trial. The four failure types considered are: (1) bending failure through an element; (2) bending failure along a mesh line; (3) shear failure through an element, and; (4) shear failure along a meshline. Tensile failure is not included since it was not observed throughout the simulations. In all cases, bending failure either through the element centroid or

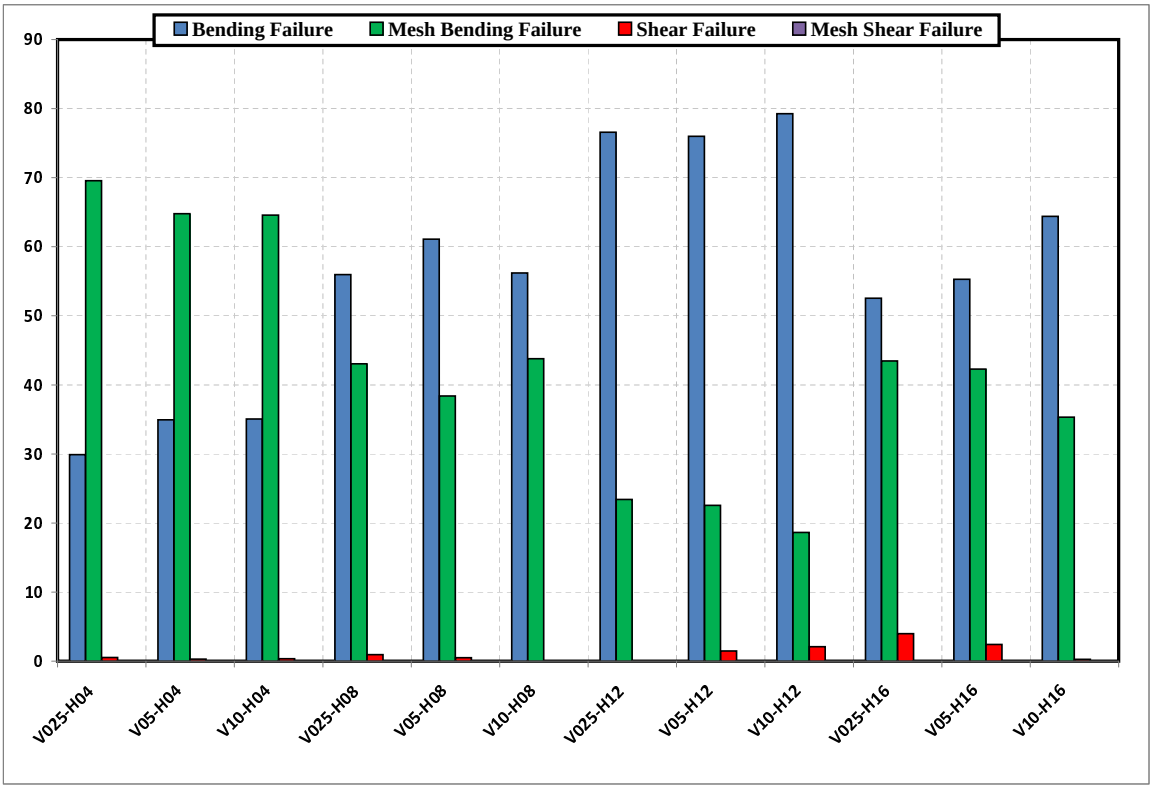

Figure 7.57: Percentage of occurrence of each failure mode during each simulation for $\sigma_f = 800$kPa, $D_w = 35$m.

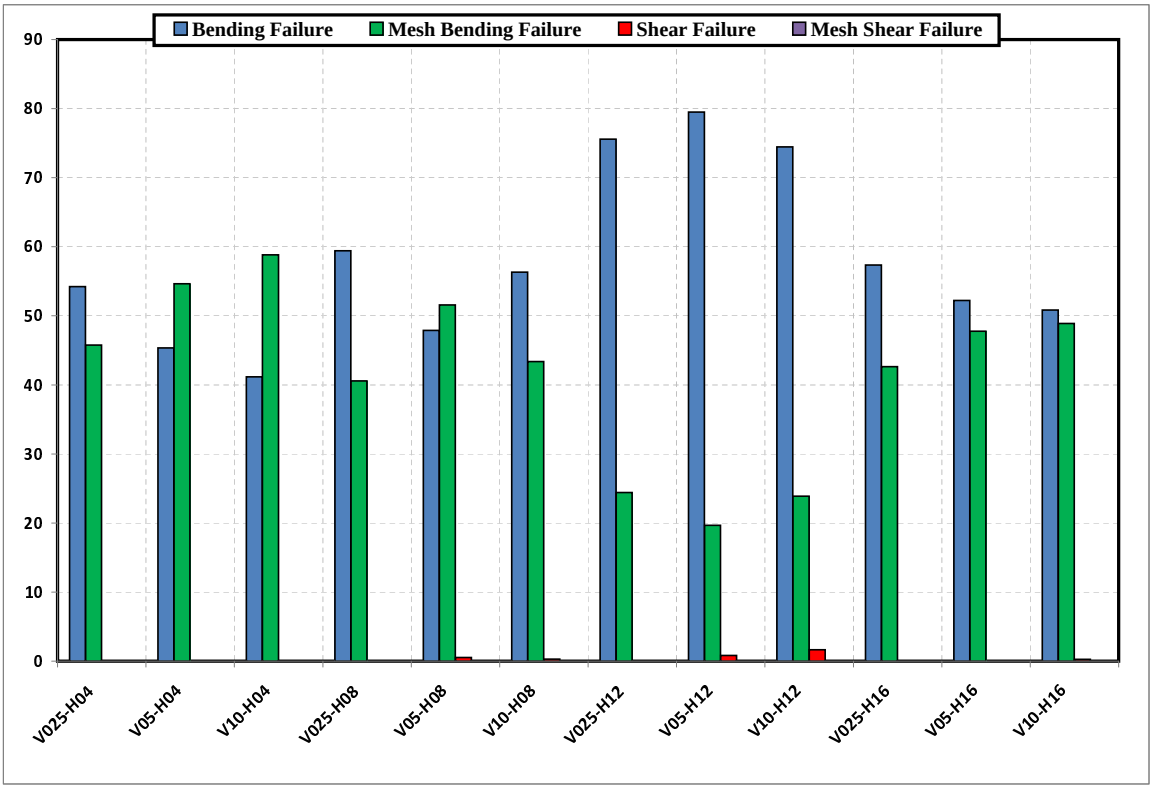

Figure 7.58: Percentage of occurrence of each failure mode during each simulation for $\sigma_f = 500$kPa, $D_w = 55$m.

along the locked element meshlines dominated the simulations (accounting for 95-100% of the failures). At $\sigma_f = 500$kPa, shear failure was almost completely absent from the simulations at both water depths investigated ($D_w = 35$m, see Figure 7.56, $D_w = 55$m, see Figure 7.58). At the increased flexural strength of $\sigma_f = 800$kPa the occurrence of shear failure increased with the largest percentage in the simulation with $h = 1.6$m, $v = 0.25$m/s. It is no coincidence then that this is also the simulation which yielded the largest magnitude for the horizontal offset and mooring force. The applied and mooring force for this case is shown in Figure 7.59 along with points along the curve where each type of failure was encountered. The amplitude of the

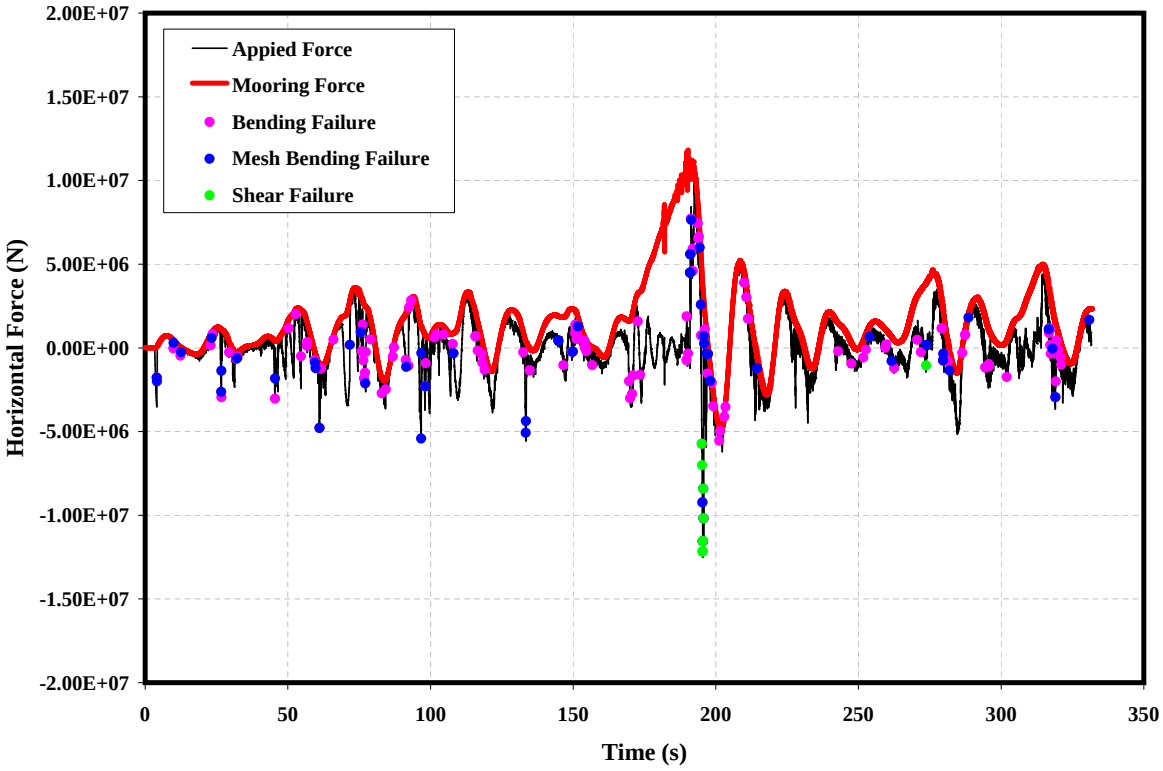

Figure 7.59: Time history of applied and mooring force for $h = 1.6$m, $v = 0.25$m/s, $\sigma_f = 800$kPa, $D_w = 35$m along with data points indicating the location of each type of failure.

mooring force is dramatically increasing in the period of time just before $t = 190$s

as the platform is pushed into the $-x$-direction (see Figure 7.60(a-b)). Instances of intra-element bending and mesh bending do occur during the climb to the peak, but the generated mooring force is not large enough propel the structure into the advancing ice sheet. At approximately $t = 195$s, the mooring lines are finally under enough tension that they create an abrupt surge in the platform displacement into the oncoming ice sheet, generating multiple instances of shear failure as a result (see Figure 7.60(c)-(d)). In this instance, the low velocity and increased flexural strength of the ice sheet and rubble pile in front of the structure created a situation in which the structure was consumed by the oncoming formation, eventually leading to a period of shear failure and increased loads/offets, as discussed in the previous section. At the higher velocities, large loads were also observed but they were large enough to keep the ice moving along or around the structure. Nonetheless, the increased flexural strength has increased the occurrence of shear failure at higher ice thickness, which resulted in increased mooring loads in this secondary set of simulations.

7.5.2 Observed failure pattern

To facilitate a discussion of the failure of the ice sheet, the elements which comprise the sheet are numbered 1 through 530. For reference, elements numbered 1 through 60 are the first row of elements, adjacent to the symmetry block, starting with the element closet to the platform. Element numbering continues in a similar pattern as you move away from the symmetry block and platform. For instance, Element No. 61 is a leading edge element, directly adjacent to Element No. 1.

The evolution of failure in the ice sheet is shown in Figures 7.61-7.64 for each ice thickness at $v = 1.0$m/s, $\sigma_f = 500$kPa, $D_w = 55$. Each figure contains a series of snapshots over the first 30 seconds of the simulation and presents the view from above and below the ice sheet. A similar pattern of bending and mesh-bending failure is

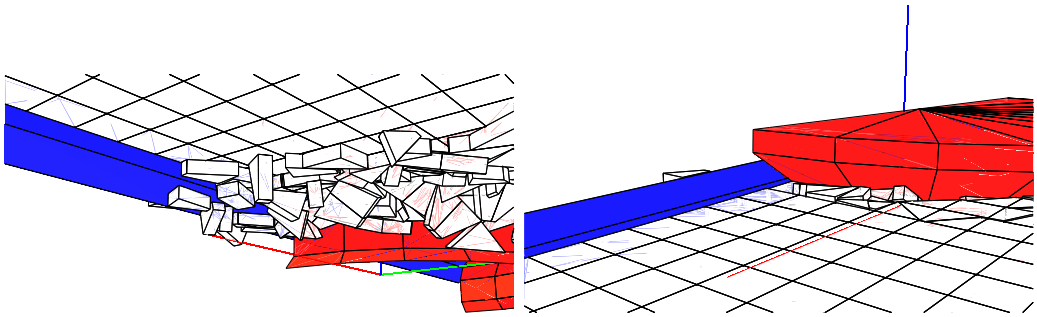

(a) $t = 188$s - ice sheet pushing the Kulluk

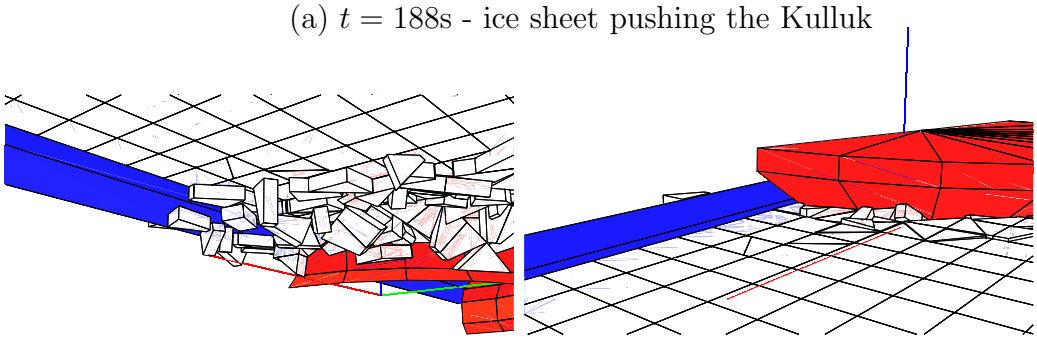

(b) $t = 192$s - mooring forces increasing

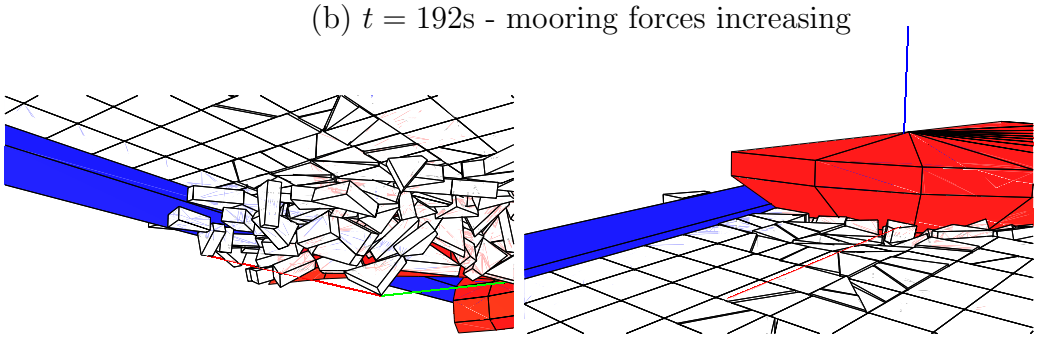

(c) $t = 196$s - Kulluk platform surges forward causing multiple shear failures

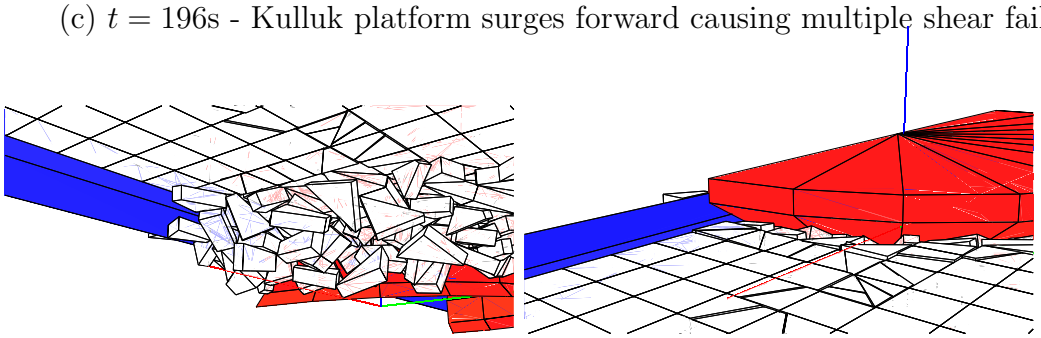

(d) $t = 200$s - platform at its maximum surge location

Figure 7.60: View from above and below the ice sheet preceding the shear failure event observed near $t \approx 195$s at $h = 1.6$m, $v = 0.25$m/s, $\sigma_f = 800$kPa, $D_w = 35$m.

observed throughout the start of the simulation. As the ice sheet approaches the platform, the leading corner of the sheet makes first contact (Element No. 1). The ice sheet then begins to bend as Element No. 1 proceeds along the 31.5° slope of the structure.

At $h = 0.4$m, the leading element is not the first to fracture. The element along the side of it, No. 61, is actually the first to fracture through its centroid at time $t = 1.83$s. Element 1 fractures shortly thereafter at time $t = 1.84$s followed by a mesh fracture along the face which is adjacent to the symmetry block at $t = 2.0$s. As the ice sheet continues to advance towards the platform, the ice sheet continues to fail in flexure along the curvature of the platform and ride down the slope of the structure. In this thinnest ice, the pieces do not tend to progress down the full height of the structure. Instead, after they break away from the oncoming sheet, the buoyant force lifts them to a position just below the approaching sheet (see Figure 7.61(d)-(f)). This process repeats itself as more ice impacts the platform, which eventually leads to a layered pile in front of the structure. As the simulation progresses, a similar failure pattern is observed, along with some clearing of the ice pieces around the structure.

At $h = 0.8$m, a similar pattern evolves with Elements No. 61 and 1 being the first to fracture at a slightly earlier time near $t = 1.81$s. As the ice sheet moves down along the structure (see Figure 7.62(a)-(d)), the fracture propagates through the oncoming ice sheet . The fractured pieces move down the structure, reaching an increased depth along the hull (see Figure 7.62(e)-(h)), until the buoyant force becomes large enough to pull the pieces upward onto the oncoming sheet (see Figure 7.62(i)-(l)), forming a layered pile as with $h = 0.4$m. The height of this pile is larger in comparison to the pile which was observed at $h = 0.4$m. During the remainder of the simulation, ice continues to fail in a cusp-like pattern and get pushed down along the structure face.

From the top view, the leading two rows of ice pieces typically fail, submerge, and the pattern is repeated (see Figure 7.62(m)-(p)). This indicates that failure is occurring 5-10m into the oncoming ice sheet, consistent with the characteristic length of 8.3m.

At $h = 1.2$m, Elements No. 1 and 2 are the first to fracture at $t = 1.35 - 1.37$s along the meshlines which they share with the symmetry block. As the ice sheet proceeds, the leading elements then fracture as contact is made with the platform (see Figure 7.63(a)-(d)). Aside from the intra-element fracturing, the ice sheet appears to stay intact as it moves down along the slope of the structure (see Figure 7.63(e)-(h)), but the buoyancy of the ice pieces, together with impact with hull skirt near the bottom of the structure, forces the pieces back upward and into the approaching sheet (see Figure 7.62(i)-(l)). This creates a much larger rubble-pile in front of the structure which interacts with the ice sheet above (see Figure 7.63(m)-(p)). Failure of ice pieces up to three rows away from the structure is observed as a result of the complex structure/rubble-pile interaction.

At $h = 1.6$m, first failure is observed at $t = 0.99$s. The failure at this ice thickness is almost sequential as elements impact the structure. The elements fracture along their centroids in the following order at the leading edge: Elements No. 1, 61, 121 181 (see Figure 7.64(a)-(d)). Then, Elements No. 2, 62, 122, 182 (see Figure 7.64(e)). Then the elements appear to fracture following the curvature of the platform as they are pushed into it (see Figure 7.64(f)-(h)). Notice that the ice moves completely down along the hull and does move back upon itself until after it impacts with the hull skirt (see Figure 7.64(i)-(l)). The height of the rubble field in front of the platform extends to the full depth of the platform beneath the waterline. Ice pieces up to three rows away from the face of the structure appear to fracture and then proceed along its contour.

Although the ice failure patterns observed above exhibit properties which are consistent with the certain trends, they do not seem to be in 100% agreement with observed patterns for sloping conical structures (or the Kulluk). The main difference is that the ice sheet was expected to fail circumferentially first and then radially. In the numerical simulations, the ice did not fail first along circumferential lines as observed in the field but it did fail within a circumferential region. The ice failure typically propagated through a circumferential region which was parallel to the curvature of the platform and located at a distance proportional to the characteristic length. If the ice sheet was constructed so that a hole was present at the leading edge of the sheet which shadowed the curvature of the platform, then perhaps such a pattern could have been observed. Nonetheless, the numerical simulations do clearly exhibit that the area of instability is the circumferential region directly adjacent to the platform.

There are several observations, however, that are consistent with the experimental and full-scale trends. As the ice thickness increased, the amount of stress in the approaching ice sheet increased proportionally leading to a decrease in the time that it took for the first element to fracture. Then, as the ice sheet the moved down along the face of the structure, a rubble pile which increased in height with ice thickness, as seen in Figure 7.65, was observed. The distance the ice was able to move down along the structure also increased with ice thickness, requiring the hull skirt to perform its primary function of deflecting the ice pieces away from the mooring lines. In the numerical simulations, the hull skirt was able to prevent the ice from moving beneath the structure for the full range of parameters investigated. The numerical results are consistent with the past and current experimental investigations which indicated that a rubble-pile formed in front of the structure. The size of this pile, as in the experiments, was larger than what was observed in the field during operation of the

platform. As a result, the peak mooring force required was much larger in comparison to the full-scale data but in agreement with the existing experiments.

7.6 Summary

In this chapter, DECICE was used to simulate the response of a moored conical drillship similar to the Kulluk. The model consisted of a 12-sided half conical structure representing the platform, a 300m-long by 100m-wide ice sheet, a symmetry and push block, and the implementation of a spread mooring algorithm. This is the first and only numerical investigation which addresses the complexities of the three-dimensional ice-structure interaction resulting from this problem. The numeric implementation of the spread mooring system allowed for the prediction of horizontal offsets, which confirmed the design goal that the Kulluk platform could withstand the impact of a 1.2m-thick level ice sheet without an emergency disconnect. The spread mooring system appears to become stiffer as larger loads were encountered so that the platform displacements could be limited. The peak mooring forces observed were also in agreement with past and current experimental model tests of the Kulluk platform and indicated an increase proportional to the square of the ice thickness (consistent with past empirical and analytical formulae).

The data from the three previous experiments outlined in Chapter 5 as well as the NRC-IOT investigation presented in Chapter 6 indicate larger mooring forces than were presented in the full-scale data set by Wright et al. (1998). An accepted analytical formula for predicting peak forces on upward- and downward-breaking cones was utilized to show that it may be possible that the full-scale values are underestimated. The numerical investigation supports this trend, although larger rubble-piles were encountered in both the experimental and current simulations, which may be the cause of the increased estimates. The numerical investigation showed that the qualitative behavior of the Kulluk platform with mooring system remained relatively unchanged in water depths from 35-55m. With increased ice thickness and flexural

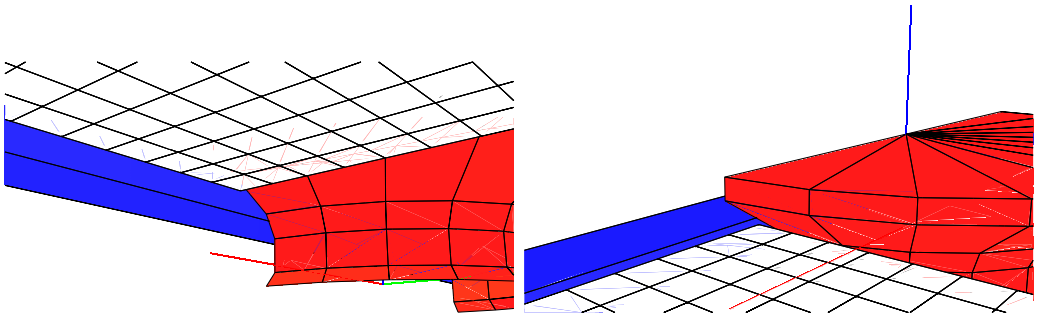

(a) $t = 0$s

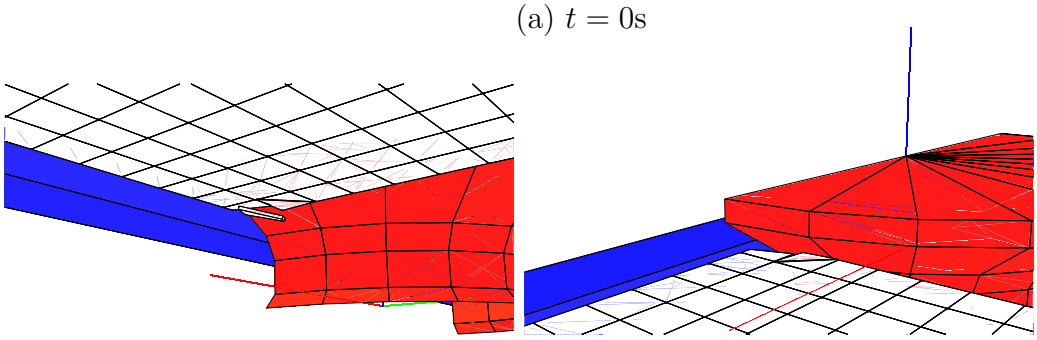

(b) $t = 2$s

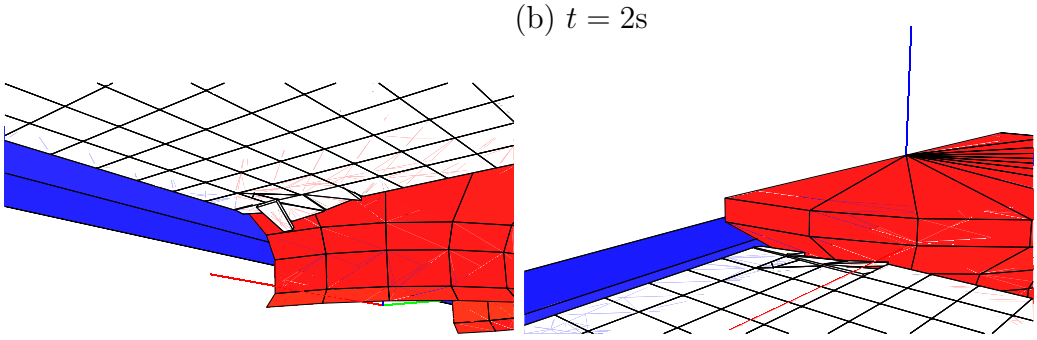

(c) $t = 4$s

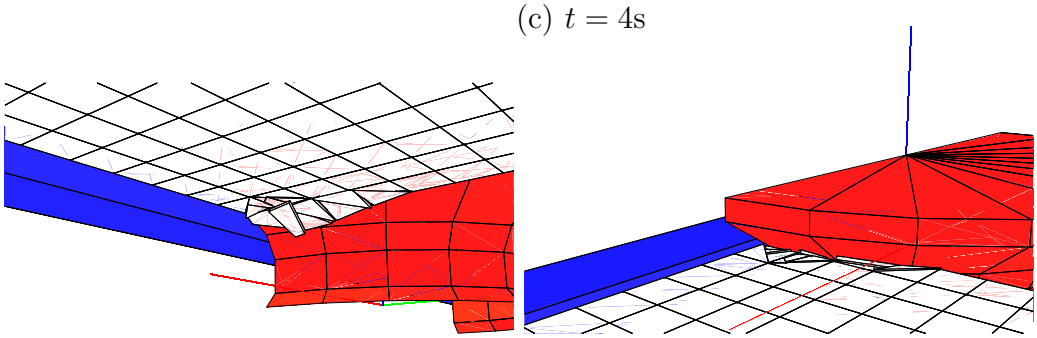

(d) $t = 6$s

Figure 7.61: View from above and below the ice sheet as it impacts the Kulluk structure for the first 30 seconds at 2-second intervals for $h = 0.4$m, $v = 1.0$m/s, $\sigma_f = 500$kPa, $D_w = 35$m.

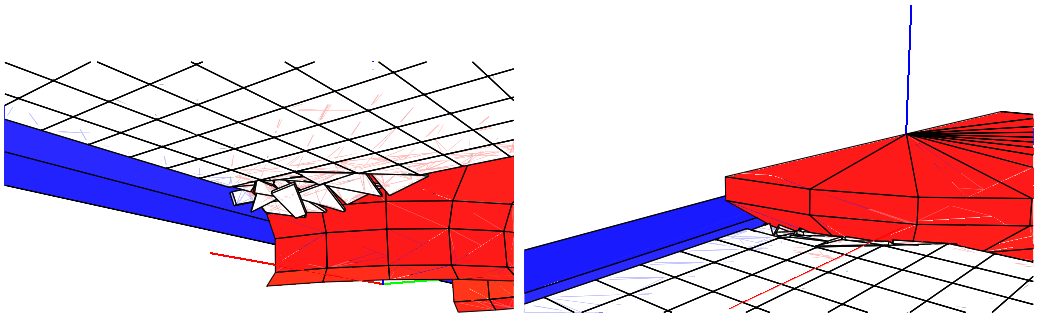

(e) $t = 8$s

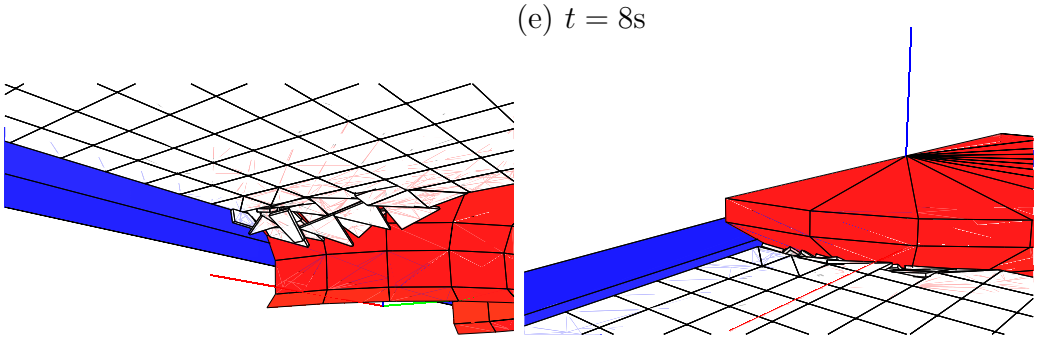

(f) $t = 10$s

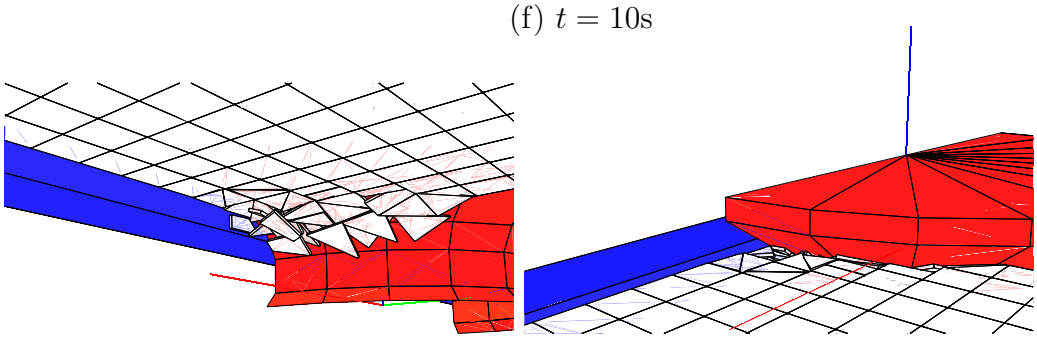

(g) $t = 12$s

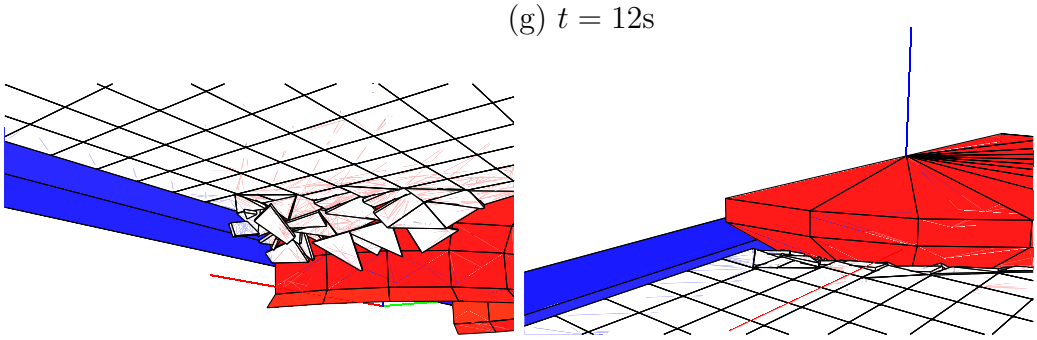

(h) $t = 14$s

Figure 7.61 (continued)

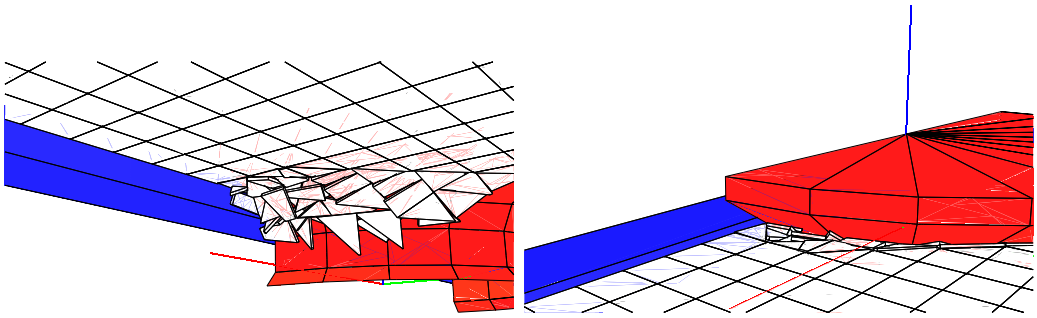

(i) $t = 16$s

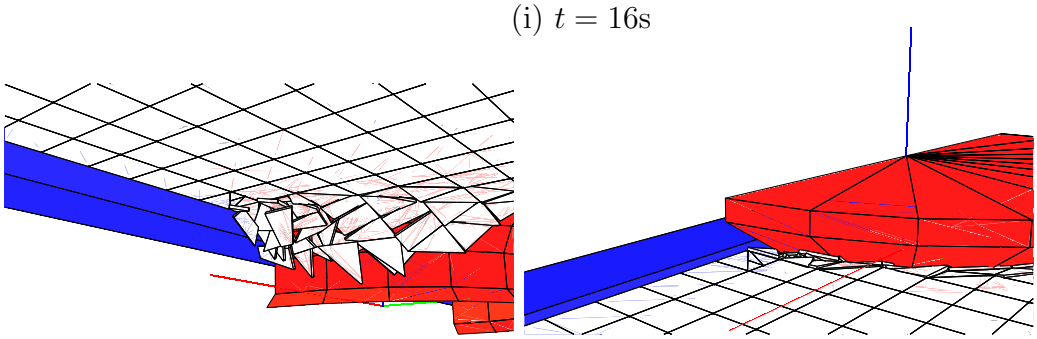

(j) $t = 18$s

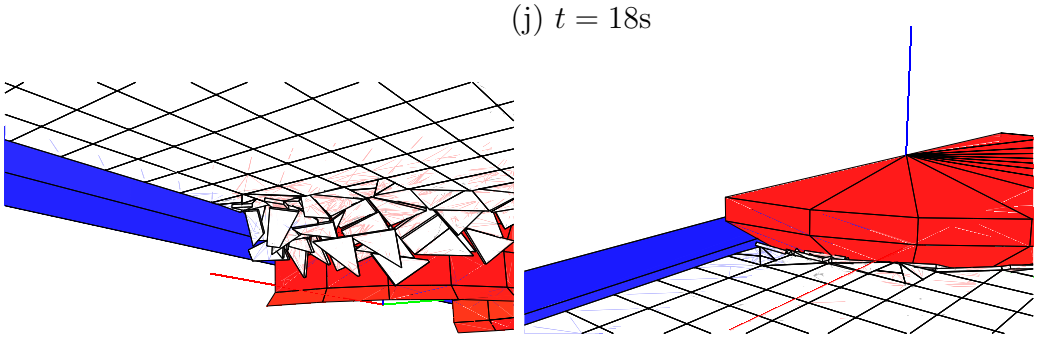

(k) $t = 20$s

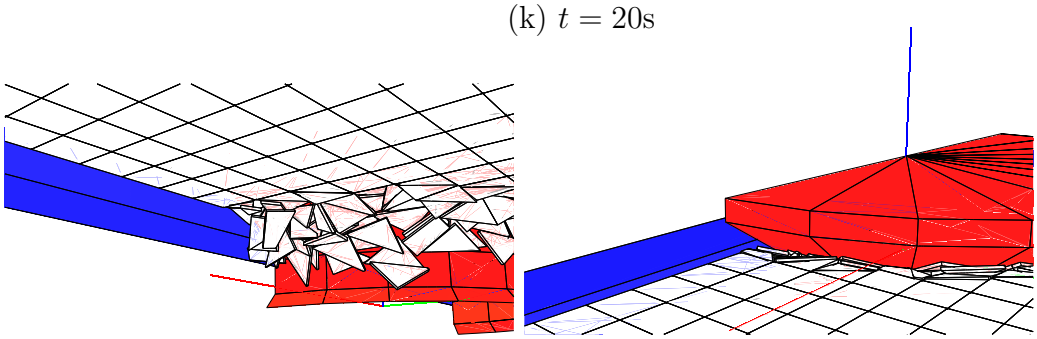

(l) $t = 22$s

Figure 7.61 (continued)

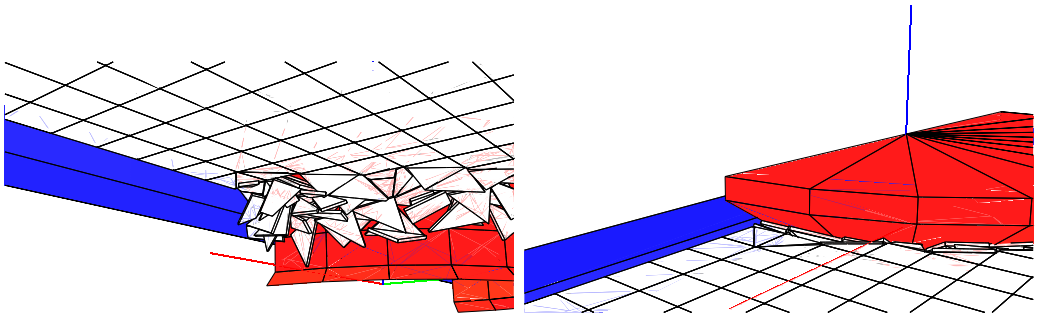

(m) $t = 24$s

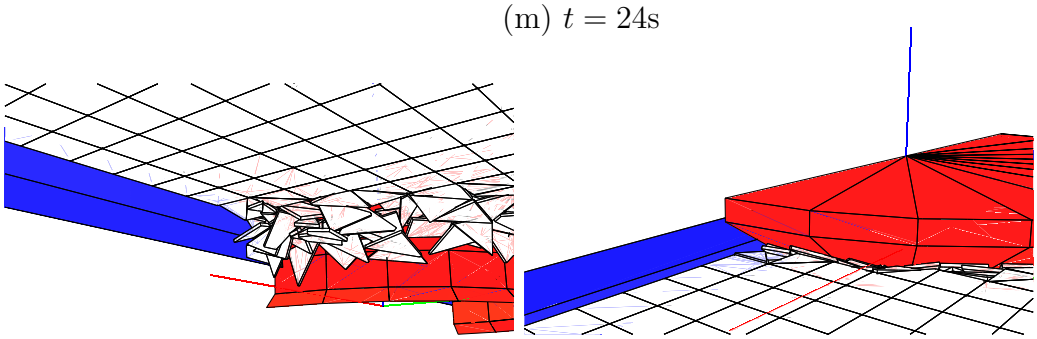

(n) $t = 26$s

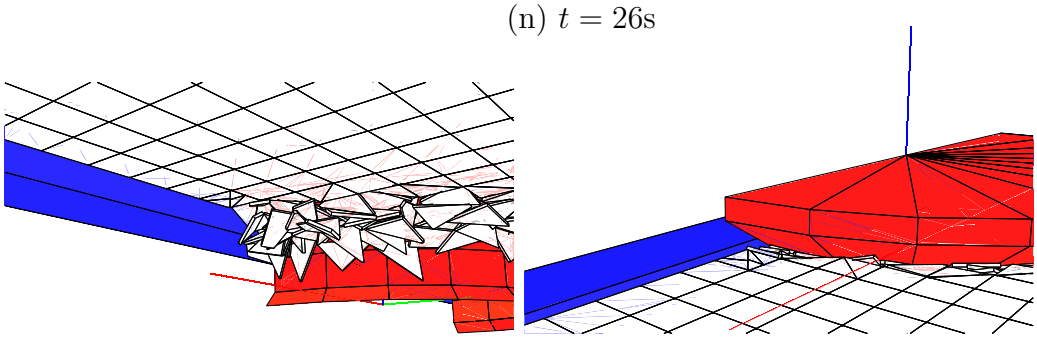

(o) $t = 28$s

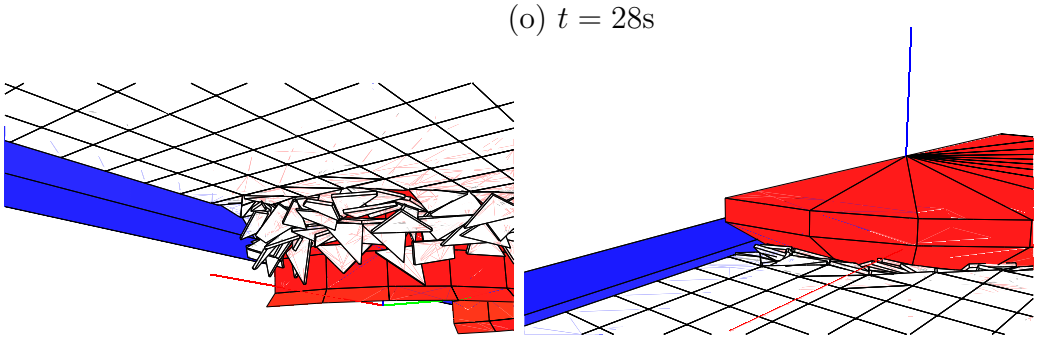

(p) $t = 30$s

Figure 7.61 (continued)

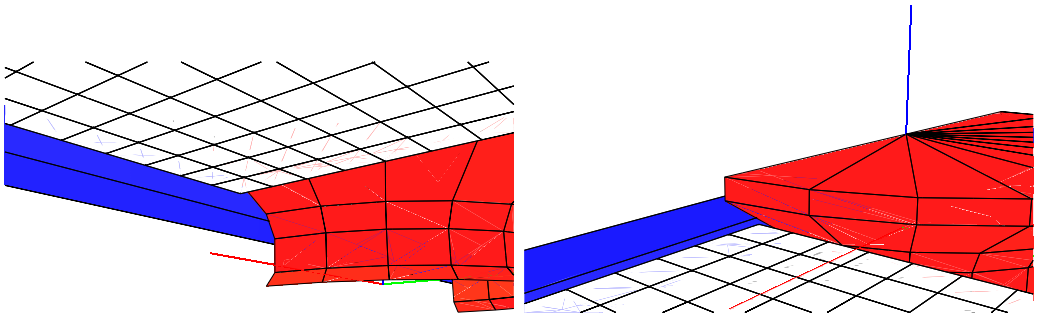

(a) $t = 0$s

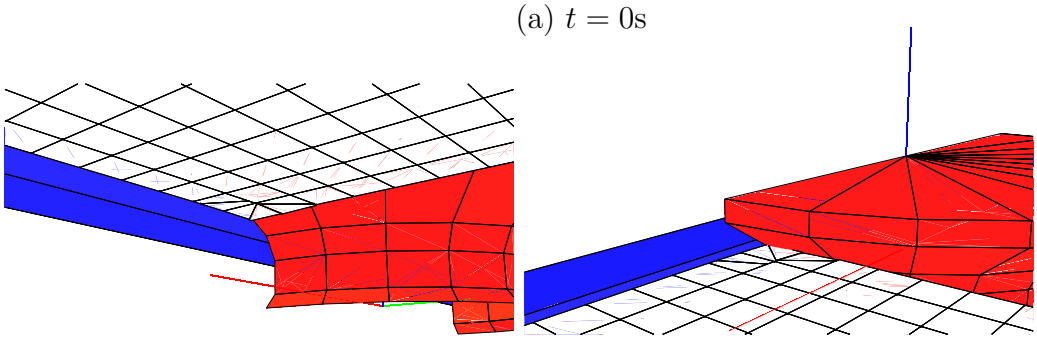

(b) $t = 2$s

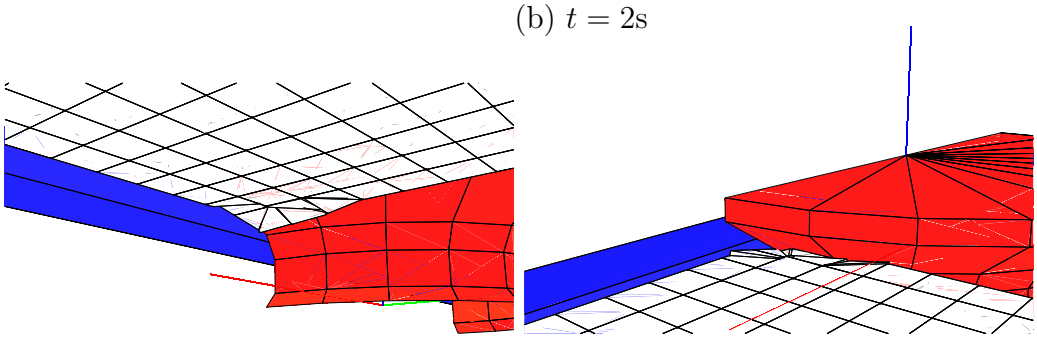

(c) $t = 4$s

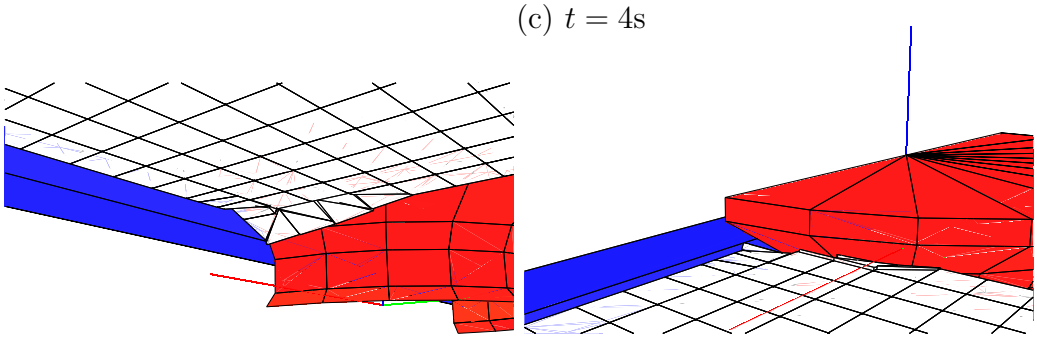

(d) $t = 6$s

Figure 7.62: View from above and below the ice sheet as it impacts the Kulluk structure for the first 30 seconds at 2-second intervals for $h = 0.8$m, $v = 1.0$m/s, $\sigma_f = 500$kPa, $D_w = 35$m.

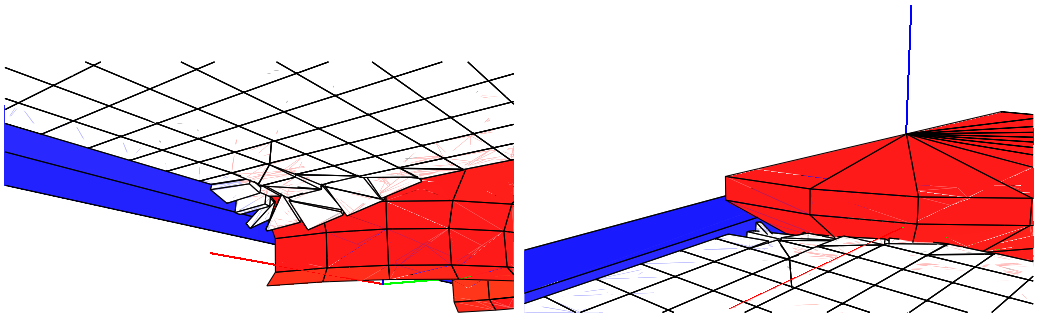

(e) $t = 8$s

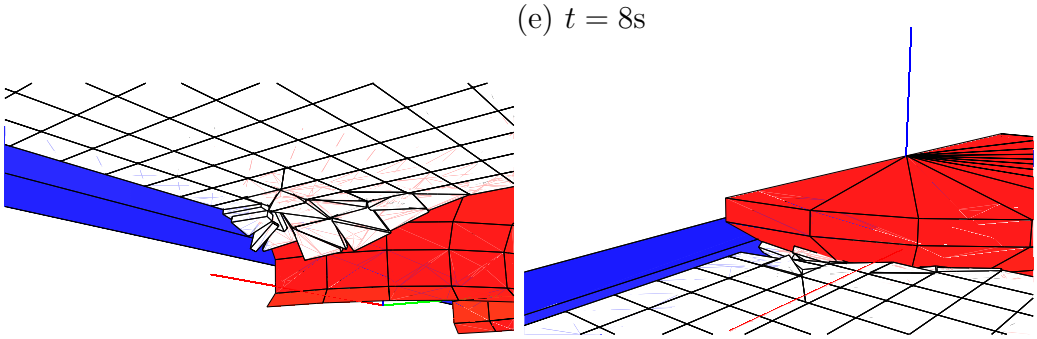

(f) $t = 10$s

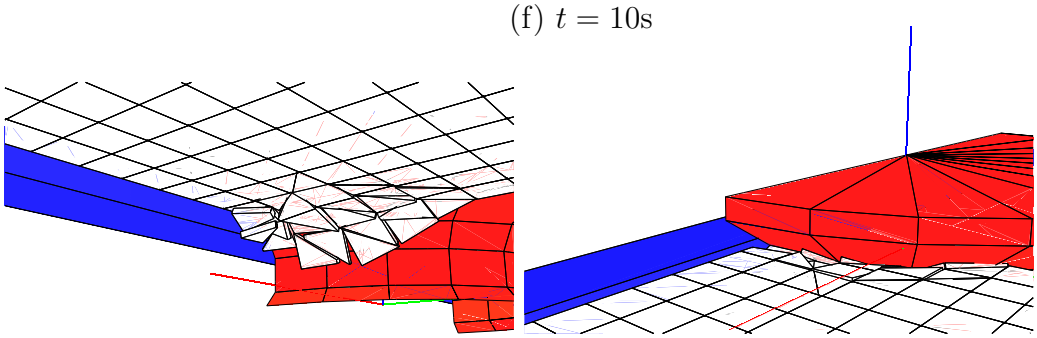

(g) $t = 12$s

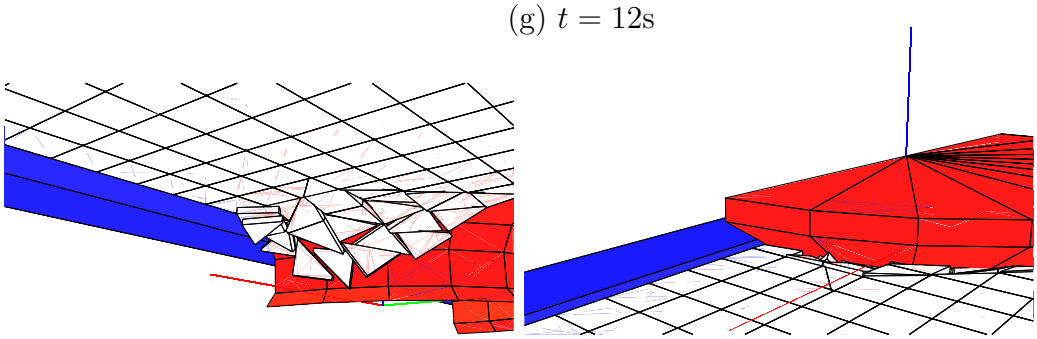

(h) $t = 14$s

Figure 7.62 (continued)

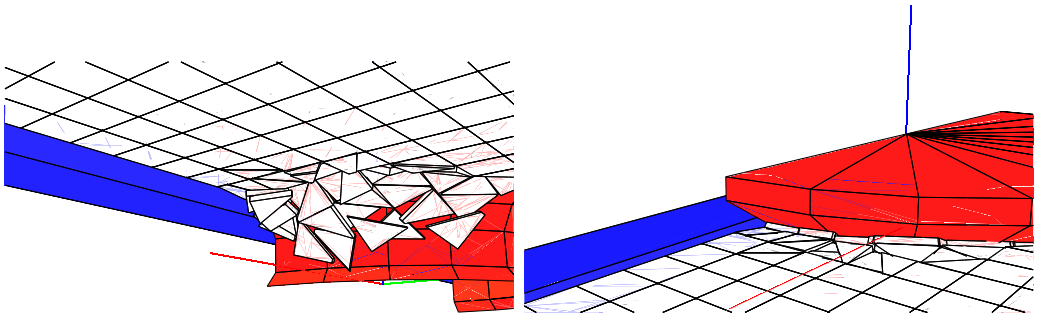

(i) $t = 16$s

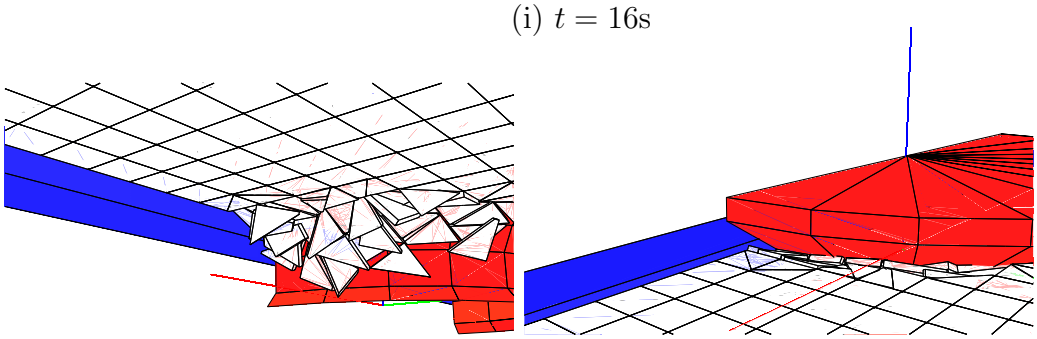

(j) $t = 18$s

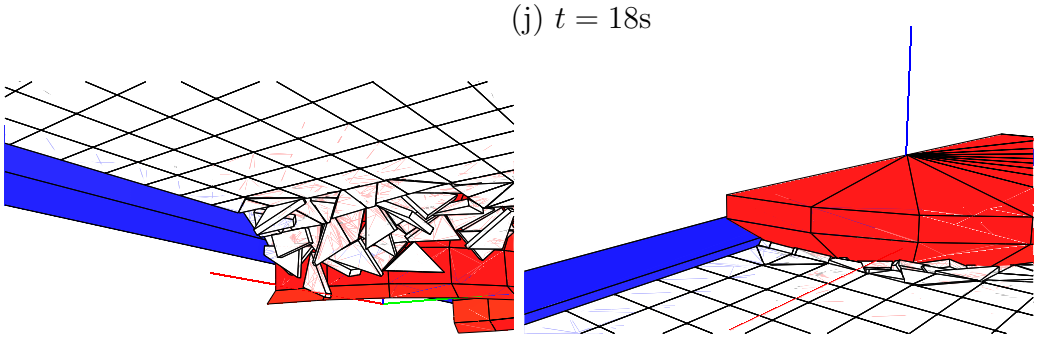

(k) $t = 20$s

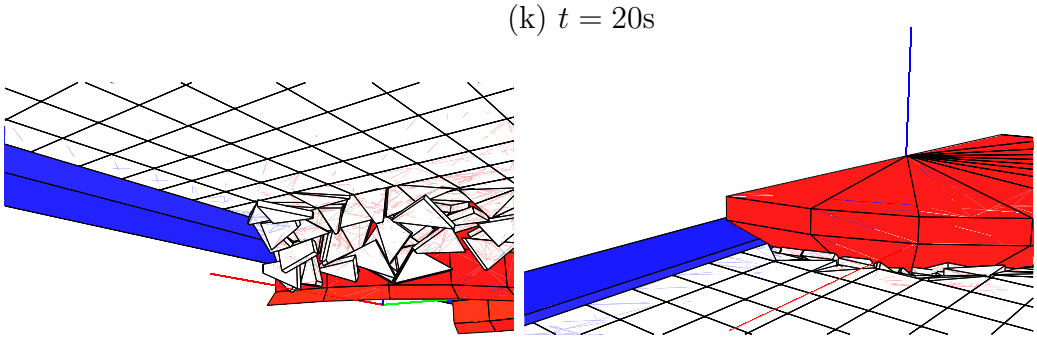

(l) $t = 22$s

Figure 7.62 (continued)

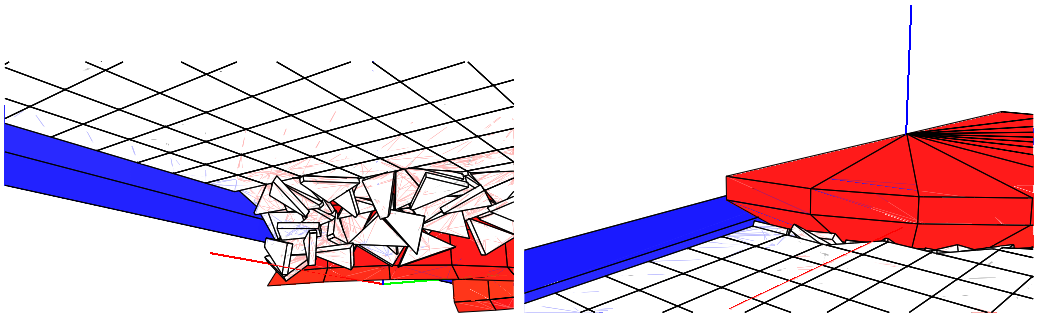

(m) $t = 24$s

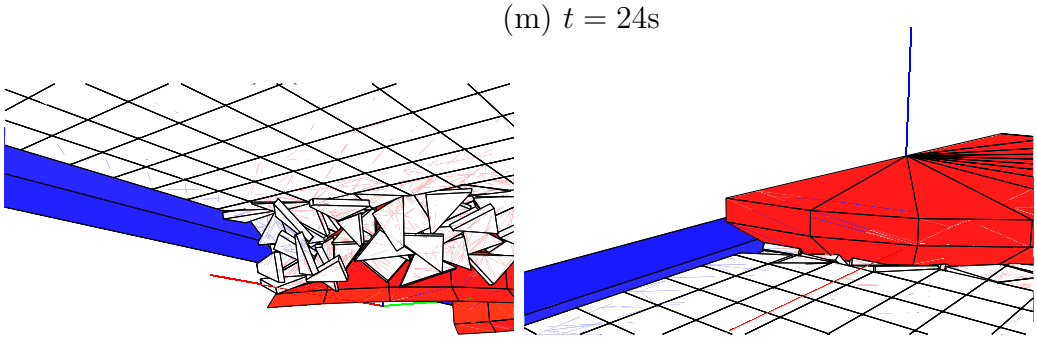

(n) $t = 26$s

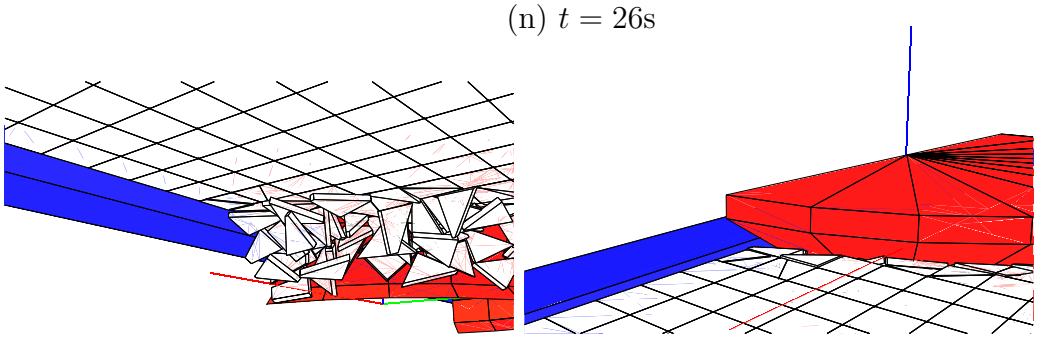

(o) $t = 28$s

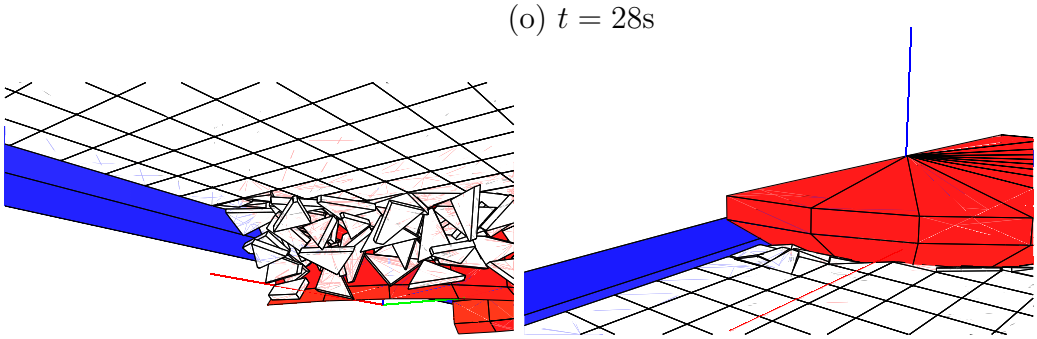

(p) $t = 30$s

Figure 7.62 (continued)

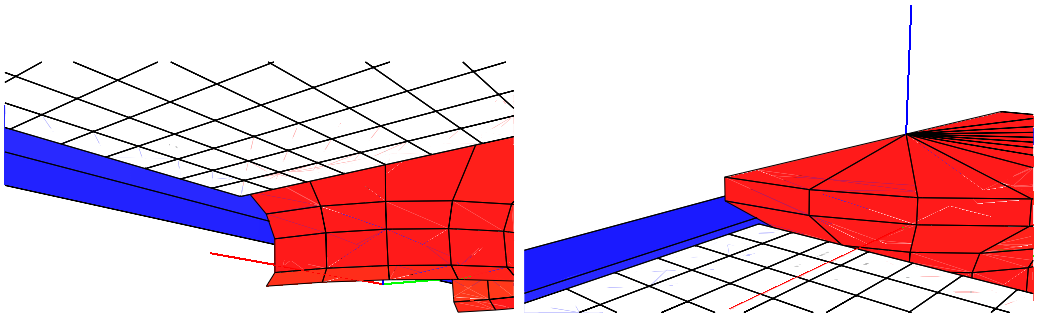

(a) $t = 0$s

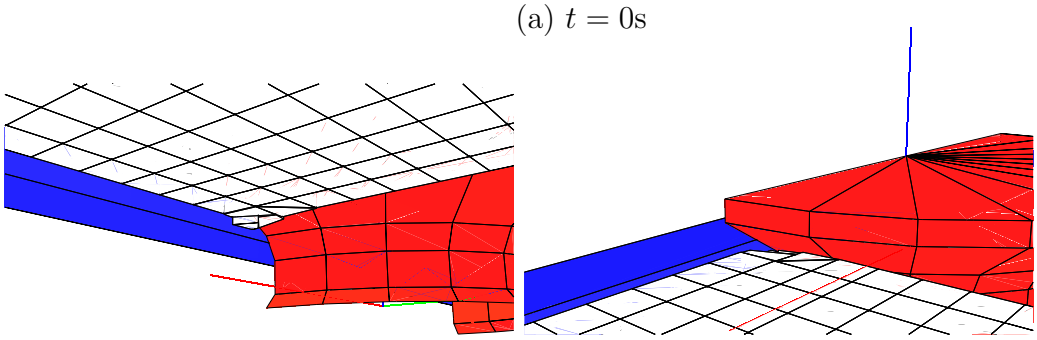

(b) $t = 2$s

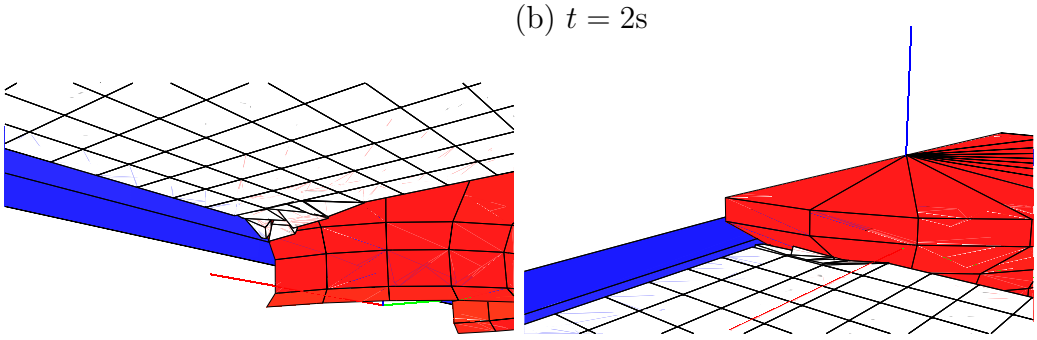

(c) $t = 4$s

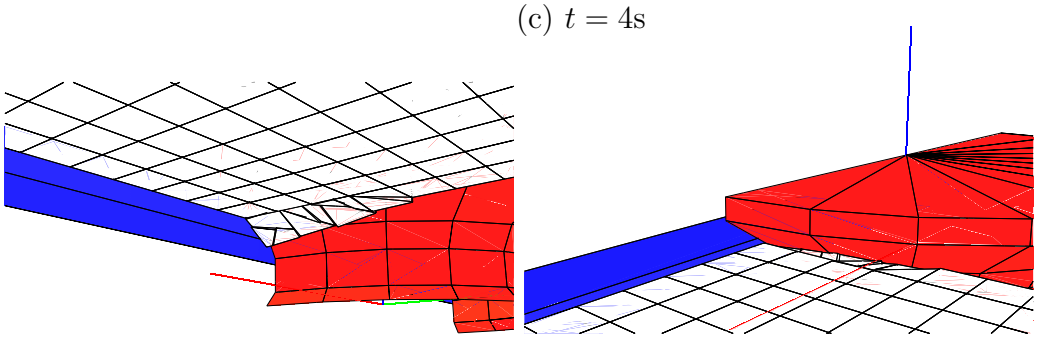

(d) $t = 6$s

Figure 7.63: View from above and below the ice sheet as it impacts the Kulluk structure for the first 30 seconds at 2-second intervals for $h = 1.2$m, $v = 1.0$m/s, $\sigma_f = 500$kPa, $D_w = 35$m.

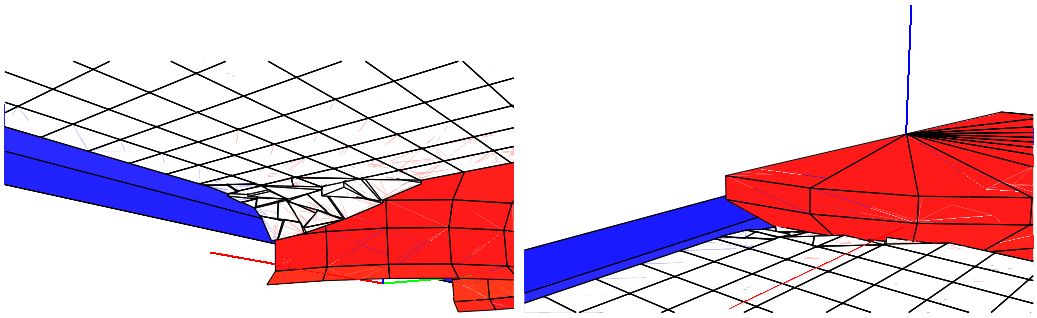

(e) $t = 8$s

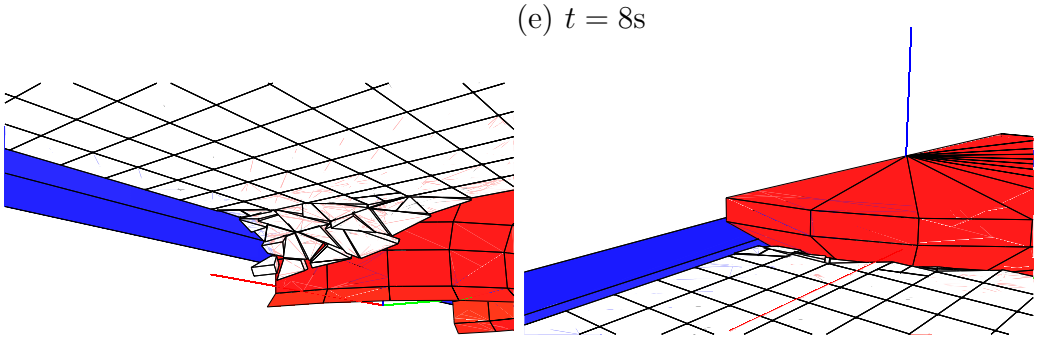

(f) $t = 10$s

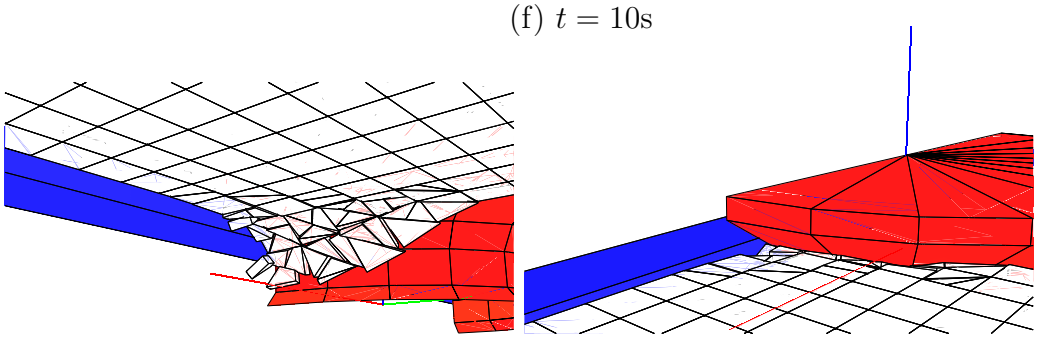

(g) $t = 12$s

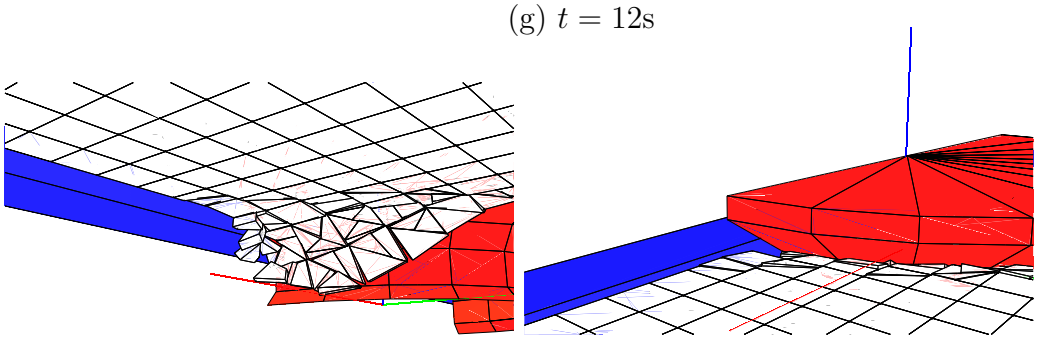

(h) $t = 14$s

Figure 7.63 (continued)

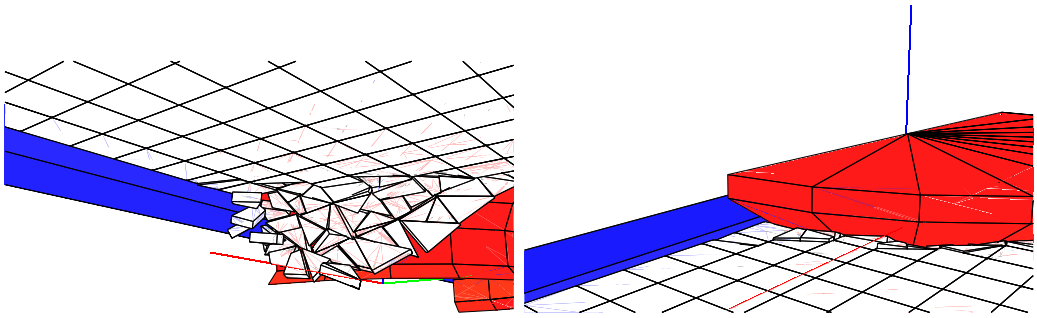

(i) $t = 16$s

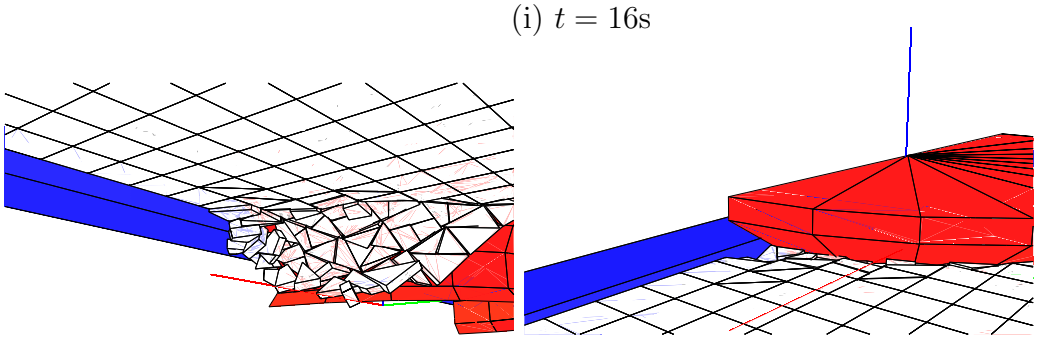

(j) $t = 18$s

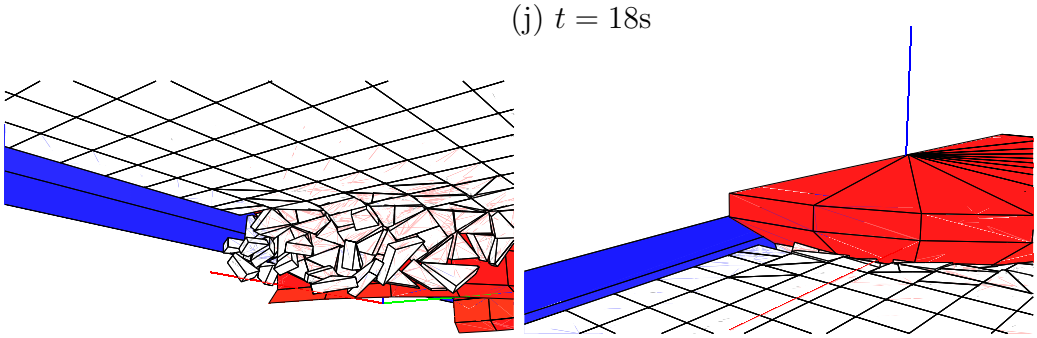

(k) $t = 20$s

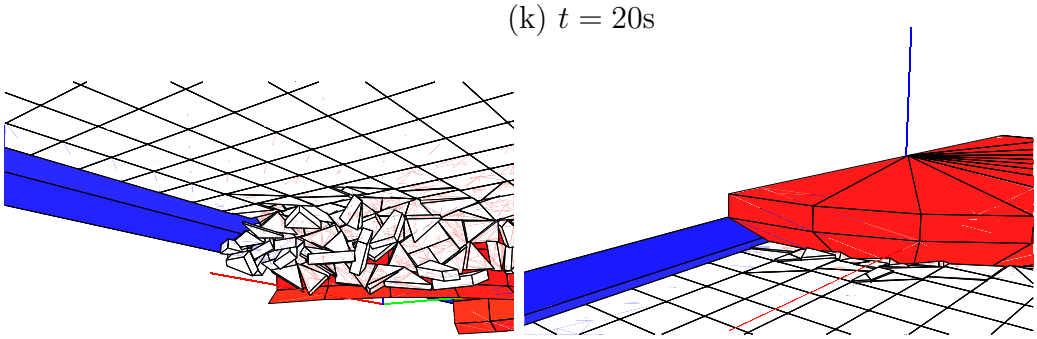

(l) $t = 22$s

Figure 7.63 (continued)

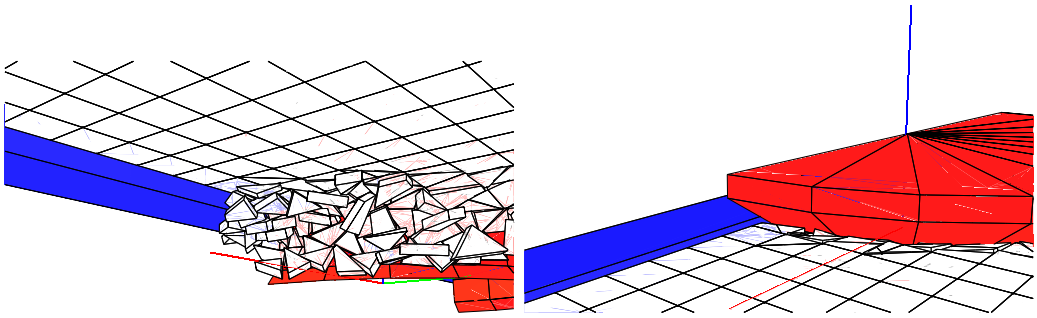

(m) $t = 24$s

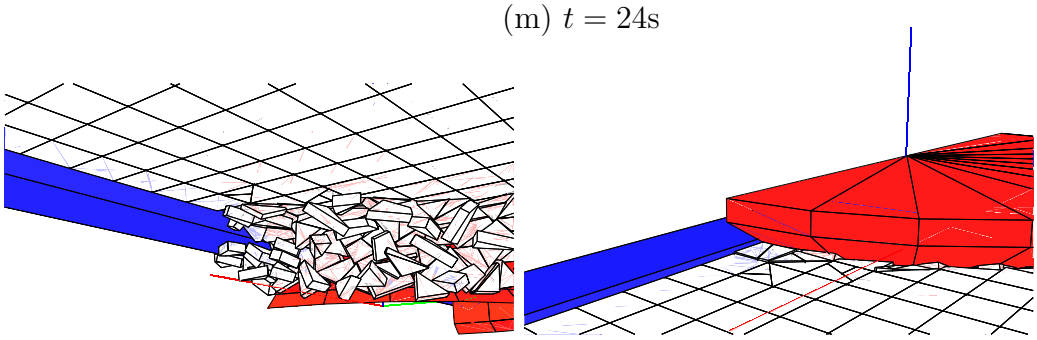

(n) $t = 26$s

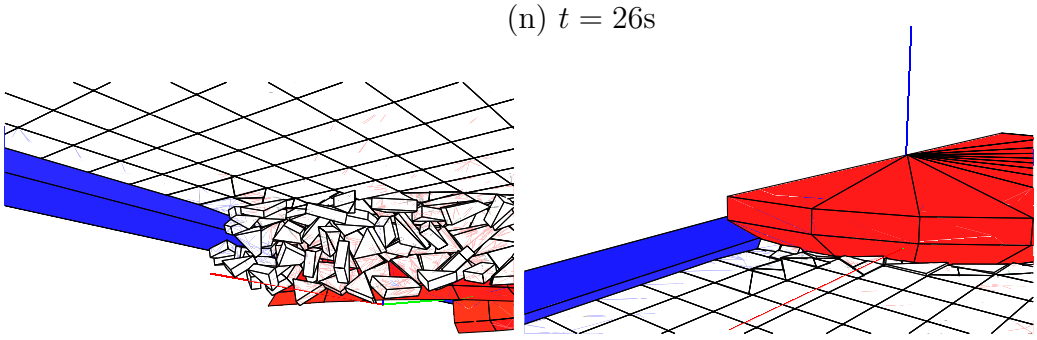

(o) $t = 28$s

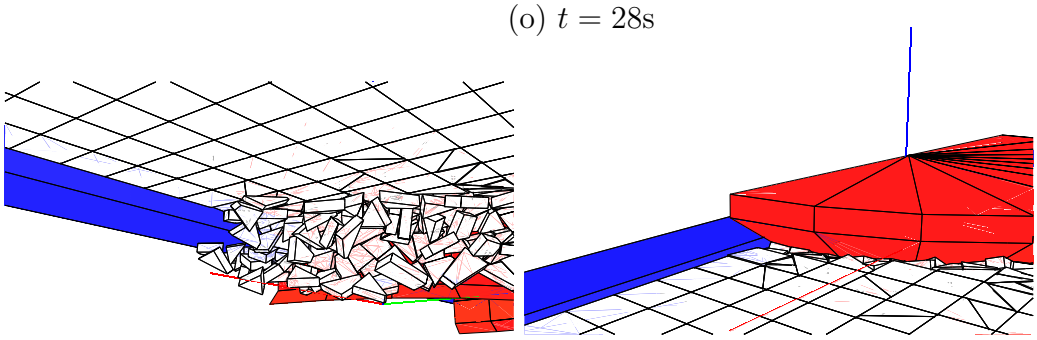

(p) $t = 30$s

Figure 7.63 (continued)

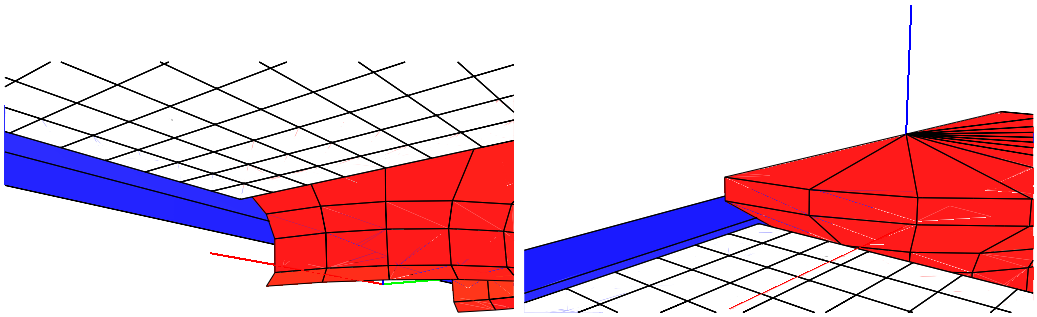

(a) $t = 0$s

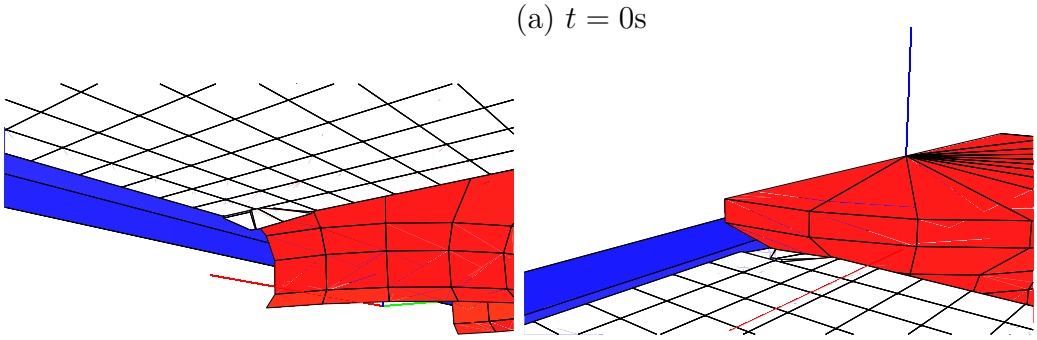

(b) $t = 2$s

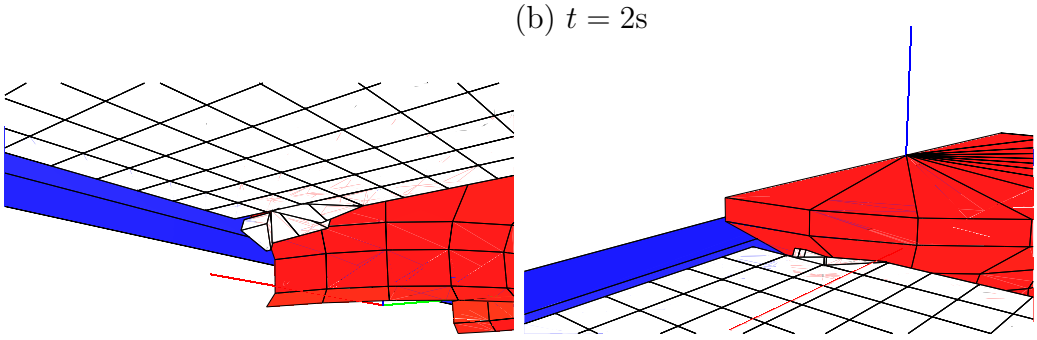

(c) $t = 4$s

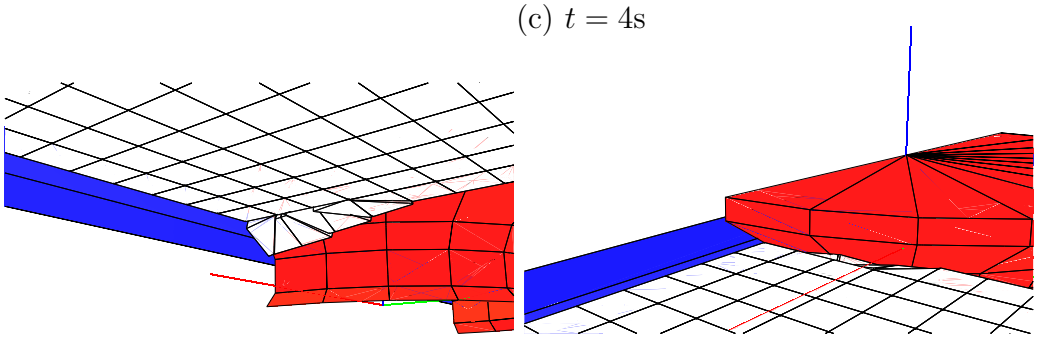

(d) $t = 6$s

Figure 7.64: View from above and below the ice sheet as it impacts the Kulluk structure for the first 30 seconds at 2-second intervals for $h = 1.6$m, $v = 1.0$m/s, $\sigma_f = 500$kPa, $D_w = 35$m.

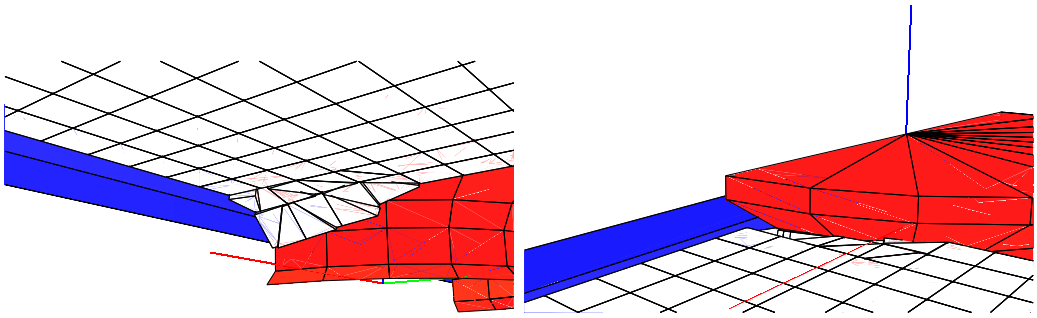

(e) $t = 8$s

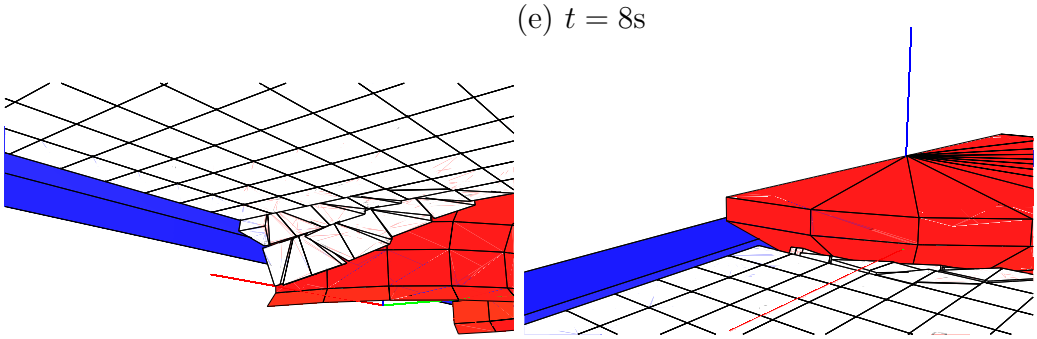

(f) $t = 10$s

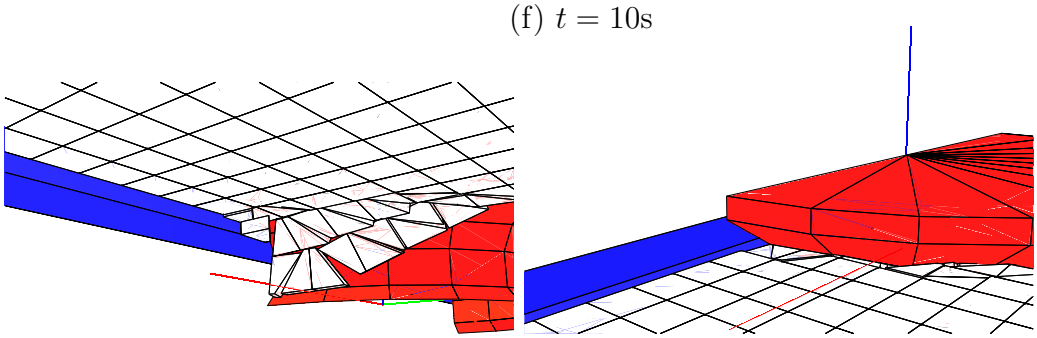

(g) $t = 12$s

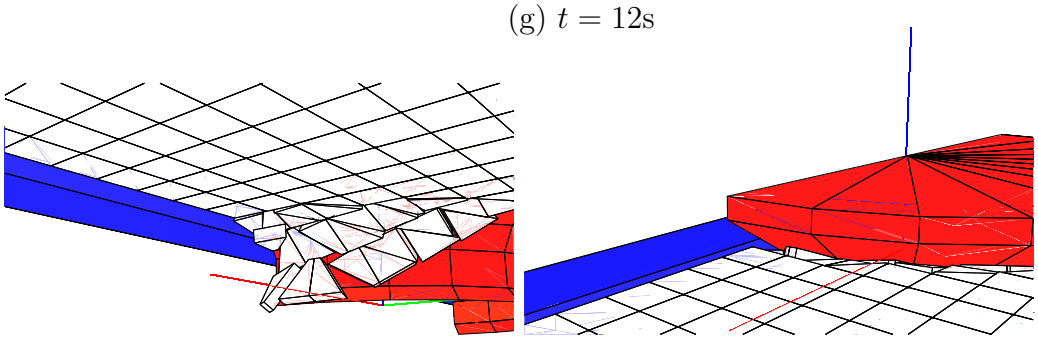

(h) $t = 14$s

Figure 7.64 (continued)

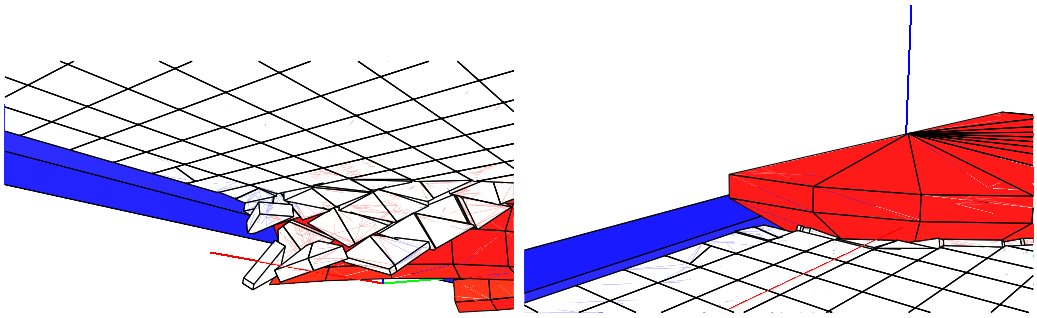

(i) $t = 16$s

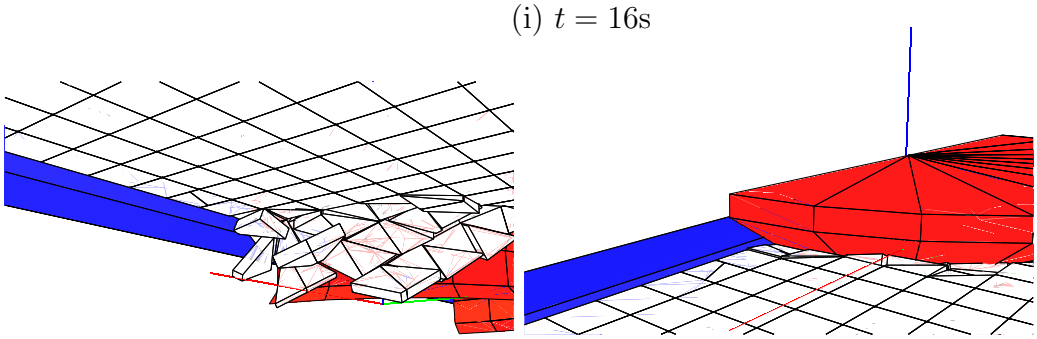

(j) $t = 18$s

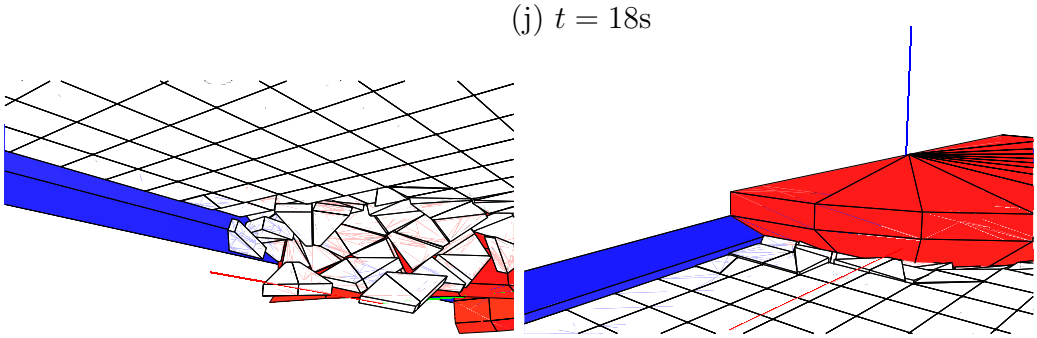

(k) $t = 20$s

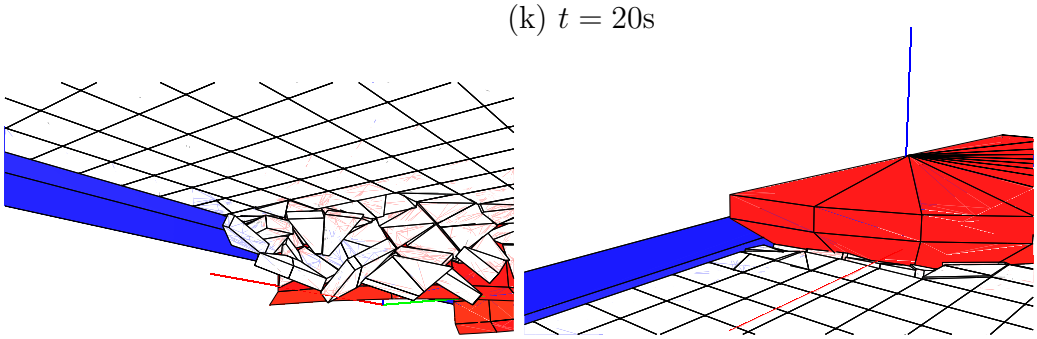

(l) $t = 22$s

Figure 7.64 (continued)

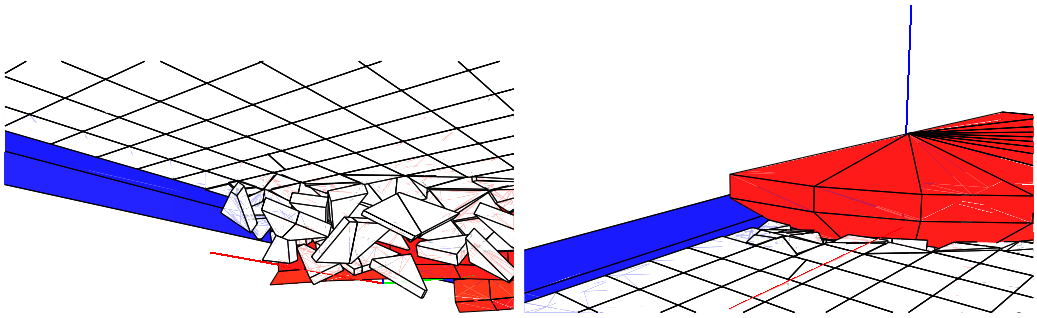

(m) $t = 24$s

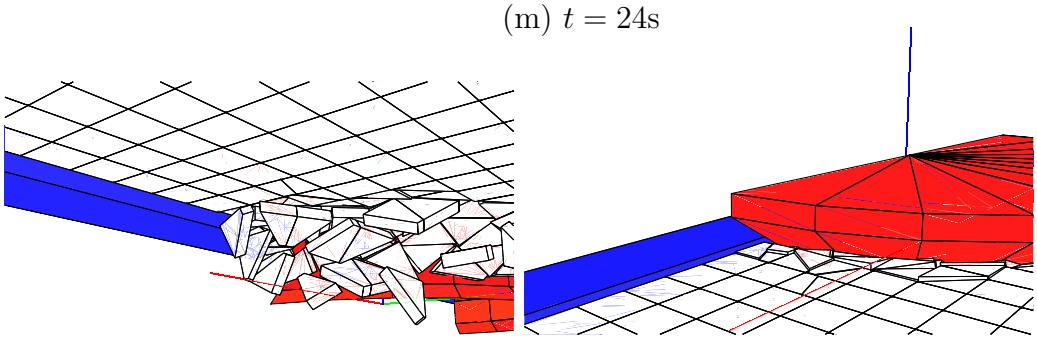

(n) $t = 26$s

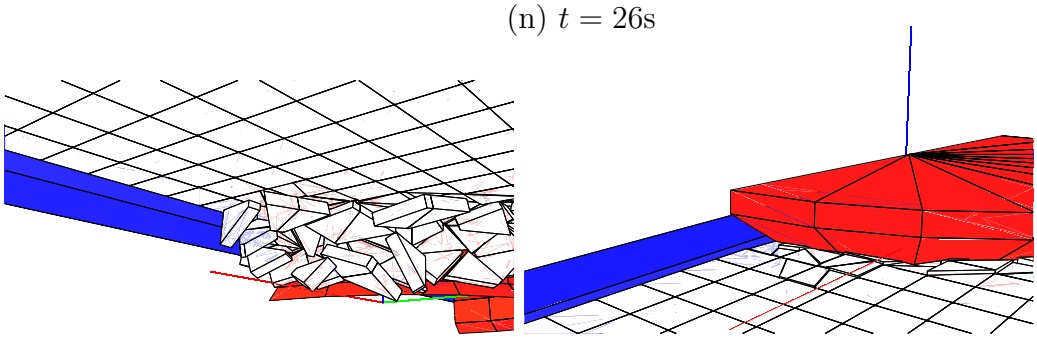

(o) $t = 28$s

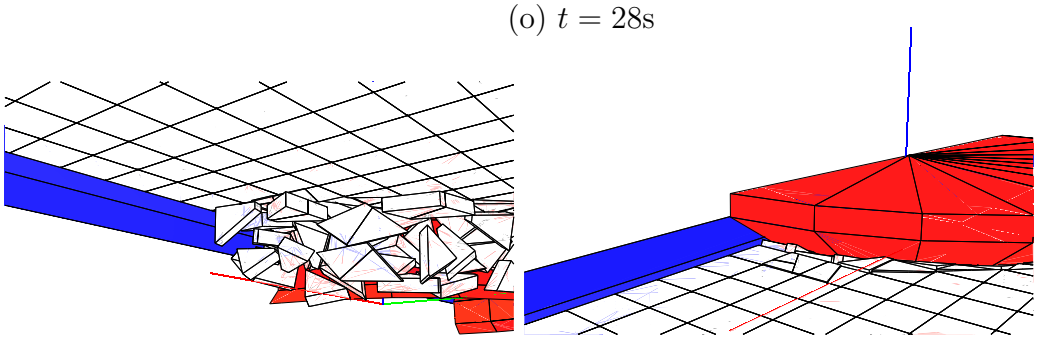

(p) $t = 30$s

Figure 7.64 (continued)

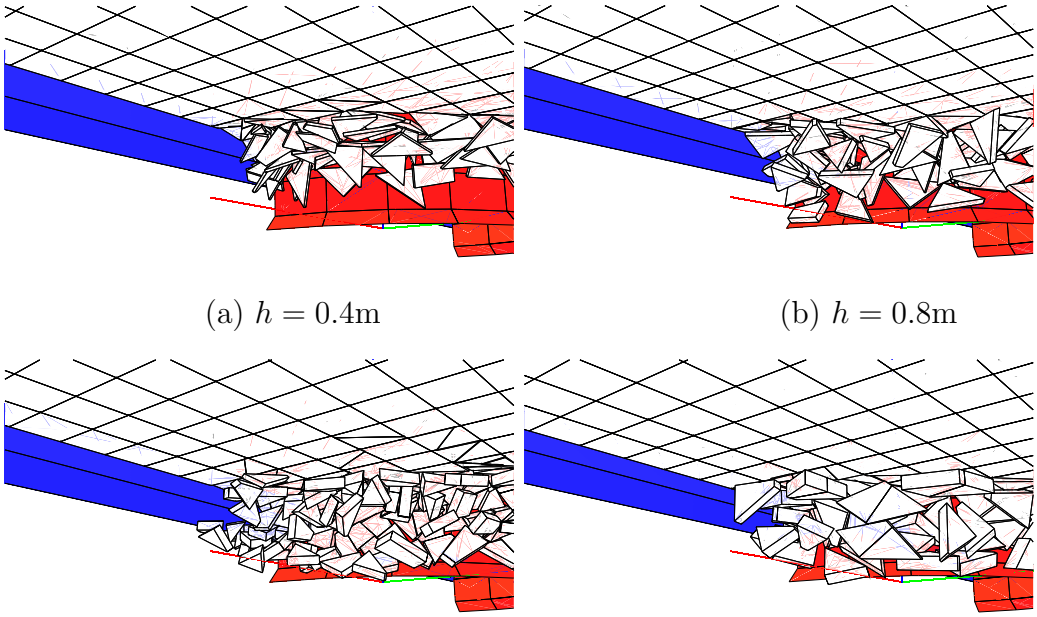

(a) $h = 0.4$m (b) $h = 0.8$m

(c) $h = 1.2$m (d) $h = 1.6$m

Figure 7.65: Simulation view from below at $t = 30$s depicting the increase in rubble-pile height with ice thickness h for $\sigma_f = 500$kPa, $D_w = 35$, $v = 1.0$m/s.

strength, however, the magnitude of peak forces/offsets could increase dramatically as the localized instances of shear failure in the ice sheet occurs. The peak force was also predicted to be maximum at intermediate velocities in certain circumstances, which supported an earlier experimental observation made by Nixon and Ettema (1987). A spectral analysis of the offset displayed that resonance of the natural mooring system frequency and ice-forcing frequency could be the cause of this phenomenon. The ice did not fail exactly as expected from previous trends but the area of instability was consistent with the tendency towards circumferential fracturing for wider structures. Even with this fundamental difference, other characteristics such as ice fracturing within one characteristic length of the platform and rubble-pile size/downride height increasing with ice thickness were present in the numerical simulations.

Chapter 8

Conclusions and Future Work

This thesis is composed of theoretical, experimental, and numerical studies. In Part I, it discusses fundamental challenges of the discrete element method, provides a set of algorithms for addressing them, and presents speed-up results of an improved algorithm on a target computer platform. In Part II, various applications of the discrete element method are reviewed with an emphasis on ice-structure interaction. The conical design of the Kulluk drillship is of particular interest. Three previous experimental studies (Comfort et al., 1982; Wessels, 1984; Nixon and Ettema, 1987) and a set of full-scale data measurements (Wright et al., 1998; Wright, 1999, 2000) form the basis for comparison. The results of a recent model scale experiment at the NRC-IOT are first analyzed and presented, followed by results of the current DEM. The numerical set-up models the full-scale platform in three dimensions, with a 24-sided rigid conical structure, ice as an elastic brittle material with plate bending elements, and the platform mooring through the implementation of a spread mooring algorithm.

8.1 Conclusions

8.1.1 Part I

DECICE is one of the few DE algorithms which utilize polyhedral elements in element modeling. In Chapter 3, a new contact detection algorithm based upon (i) the FCP algorithm of Nezami et al. (2004); (ii) using AABB's to perform a proximity search; (iii) estimating the time of collision; and (iv) accurate resolution of contact points, has led to a significant performance gain. Simulations exhibit that the execution time of DECICE has decreased by a factor of magnitude, up to 21 times faster than the original version for only 500 elements. The simulation time required for 500 elements using the new algorithm is less than half of the simulation time required for 100 using the old algorithm, and has a growth rate which is 50% less than the original algorithm.

A parallel version of DECICE was developed in Chapter 4 which, together with the new contact detection algorithm, utilized a parallel recursive coordinate bisection algorithm to sort elements into bins. Instead of completely assigning subdivisions of the physical domain of the problem to individual processor nodes, the parallel algorithm divides the work amongst processors using the inherent program data structures. This eliminates the necessity of purging large arrays, which was the main drawback of previous parallel DE algorithms. Simulations conducted on a NUMA-based SGI Origin 3000 series computer indicate that a speed-up of approximately 12 can be expected on 16 processors with proper domain binning. The parallel recursive coordinate bisection algorithm yields super-linear performance in comparison to execution times where no binning is used for a low number of processors. The remainder of the contact detection algorithm also performs well by implementing parallel refinement of the contact lists and force application on a per-element basis. The perfectly parallel regions of the algorithm achieve slightly less than optimal speed-up, but not optimal

as a result of the storage of large global data structures on the NUMA architecture. Overall, the performance of the algorithm was increased by a factor of 10-12 on 16 processors.

8.1.2 Part II

The results of Part II of this thesis can be used to aid in design and decision-making with respect to the emergency movement of the Kulluk platform. Unnecessary delays and unsafe conditions during severe ice conditions can be minimized by any design and operational improvements.

Chapter 6 presents a recent series of experiments conducted at the NRC-IOT. The peak offsets and mooring forces exhibit a pattern which displays the transition in the ice behavior from ductile to brittle, with peak values typically being observed in the ductile regime at lower velocities. Both the peak offset and mooring forces exhibit an increase with a square of the ice thickness to values which are up to 500% greater than the full-scale measurements for the largest ice thickness. The results for $h \leq 1.2$m, however, define a range which contains the data points from the three previous experimental studies. The increase of velocity in the brittle regime causes a secondary small increase in the peak loads/offsets. The stiffness of the four-point mooring system appears to have a large effect on both the offsets and forces. The stiffest system produces the smallest offsets but largest loads, and vice-versa for the least stiff system. This suggests that the use of a mooring system with an intermediate stiffness may be optimal.

Chapter 7 presents the DE numerical model of the full-scale problem together with the details of the spread mooring algorithm. A series of trials are conducted to determine the effect of ice thickness, velocity, flexural strength, and water depth. The

simulations indicate an h^2 dependency of the peak mooring force on ice thickness but only linear growth of the peak offset. This results in much lower force/offset predictions than in the experimental observations of Chapter 6, but they are still higher than those of the full-scale data set. The predictions confirm that the platform can withstand the impact of an $h = 1.2m$ thick ice sheet as was put forth in the initial design. Force and displacement time histories exhibit the "regular but stochastic" pattern and were sometimes maximum at intermediate velocities as was observed by Nixon and Ettema (1987). A spectral analysis indicated that this phenomenon may result due to resonance of the platform excitation frequency. In general, the peak values showed a slight increase with velocity, as observed in the experiments, but an increasing flexural strength showed a more dominant effect in the numerical simulations. At increased thickness and flexural strength, a period of shear failure was present, which was accompanied by a significant increase in the corresponding mooring forces and displacements, an observation consistent with past studies. The peak loads did not show any significant increase at the increased water depth but the peak offsets did increase dramatically. The qualitative behavior in comparison to the threshold value was, however, similar to the results in shallow water depth of $D_w = 35$m.

8.1.3 Major contributions

To finalize the analysis and restate for clarification, the major unique contributions of the current research are:

1. a new algorithm for contact detection and (contact point) resolution within the DE code DECICE (Chapter 3);

2. a new parallel DE algorithm which performs well on a NUMA-based SMP computer by mixing the domain decomposition, data structure, and perfectly parallel strategies of parallelism (Chapter 4);

3. an evaluation of past experimental and full-scale results on the Kulluk platform in conjunction with a new set of experiments conducted at the NRC-IOT (Chapter 5-6);

4. the implementation of an algorithm into the DECICE code which is capable of simulating the response of a spread mooring system (Chapter 8);

5. the first three-dimensional numerical model of the full-scale Kulluk drillship (Chapter 8) which produces results consistent with previous literature and exhibits the complexity of ice-structure interaction for the particular hull design.

A wide spectrum of literature from many different fields was reviewed in order to formulate and implement the above contributions. Each could separately form the basis of major research projects in the future to extend the current capabilities of both the discrete element method and DECICE.

8.2 Future Work

Although the current thesis has covered a wide range of results in relation to DECICE, there are still many issues which exist in relation to discrete element simulations. The computational algorithms developed in the thesis provide a significant speed-up over the original algorithm, but many restrictions were imposed by the original coding structure. A more efficient algorithm could be developed in the future if the methodology and complete coding structure is known a priori. The code, algorithms, and data structures could be tailored more effectively to a high performance computing

architecture.

For the parallel algorithm, first, serial portions of the DECICE code account for an additional 2-to-15% of total simulation time (not including the serial portions which exist in the parallel implementation of contact detection algorithm or the I/O routines). Second, the storage of the large data arrays in global memory and the non-uniform memory access of the target platform resulted in larger than expected execution times in perfectly parallel sections. Finally, the fracturing of elements is not permitted in the parallel algorithm at the current time, since fractured elements require significant modification to the nodal/element storage and force arrays. Using the current algorithm, fracturing should only be performed on a single processor to avoid a race condition and thus would cause significantly larger execution times. Future improvements of the parallel algorithm should focus on improving these inefficiencies.

As a tool for modeling ice-structure interaction, further studies should be undertaken to verify the accuracy of the code as well as the inclusion of more accurate modeling algorithms. A model to simulate forces during crushing or adhesion at the interface of ice-structure contact may be considered. As well, a more accurate means of calculating material and geometry-dependent characteristics such as the stiffness and mass/deformation damping parameters should be addressed. Also, the advantages of semi-implicit or iterative solving techniques should be addressed in the future so that (i) time-step which is stiffness and material dependent can be increased; (ii) damping required to reduce the oscillation in element deformation an be eliminated; (iii) parallel architectures can be exploited.

DECICE can currently be used to investigate a wide range of problems and parameters, but there are still numerical instabilities in the code when dense packings of elements and high contact forces exist. As noted by earlier researchers, the modal decomposition technique is not particularly well-suited to problems involving dense packings, since the eigenmodes are not revised to account for the contact constraints (Cundall and Hart, 1992). Any future development of DECICE should focus on removing these numerical instabilities.

The experimental results presented in this thesis over-predict the peak mooring loads on the Kulluk drillship by up to a factor of 5. Work should be completed to determine the source of the inconsistency, if any, or the reliability of the full-scale results. Whether the increased loads are a consequence of the rubble pile forming in front of the structure or a result of the four-point mooring system is a question that should be addressed. Likewise, a larger range of numerical parameters and meshes which conform to or promote ice fracturing patterns which are observed while in operation can also be addressed in the future. The effect of numerically implementing ocean currents or a constant drift velocity may produce smaller peak loads due enhanced movement of the ice pieces around the platform and should be addressed in future work. Finally, effects of variations in the geometrical properties of the Kulluk platform should be considered numerically as well as performance of the Kulluk platform in other ice conditions, including, but not limited to, pre-sawn ice, ice-ridges, and pack-ice.

Bibliography

Abdelnour, R., Comfort, G., Pilkington, R., and Wright, B. D. (1987). Ice forces on offshore structures; model and full scale comparisons and future improvements. *Oceans*, 19:24–29.

Afanas'ev, V. P., Dolgopolov, Y. V., and Shraishtein, Z. I. (1973). Ice pressure on individual marine structures. *Ice Physics and Ice Engineering*, pages 50–68. Israel Program for Scientific Translation.

Atkins, A. G. (1975). Icebreaker modeling. *J. Ship Res.*, 19(1):40–43.

Atkins, A. G. and Caddell, R. M. (1974). The laws of similitude and crack propagation. *International Journal of Mechanical Science*, 16:541–548.

Barker, A., Sayed, M., and Timco, G. (2000a). Numerical simulation of the "Kulluk" in pack ice conditions. PERD/CHC Report HYD-TR-050, Ottawa, Canada.

Barker, A., Timco, G., Sayed, M., and Wright, B. (2000b). Numerical simulation of the "Kulluk" in pack ice conditions. *Proc. 15th Intl. Symp. on Ice*, 1:165–171. Gdansk, Poland.

Belytschko, T., Yen, H. J., and Mullen, R. (1979). Mixed method for time integration. pages 259–275. Computer Methods in Applied Mechanics and Engineering, North-Holland Publishing Company.

Bercha, F. G. (1985). Ice-structure interaction: Engineering design and construction criteria. Report for Public Works, Canada, Ottawa.

Bonnemaire, B., Jenson, A., Gudmestad, O. T., Lundamo, T., and Loset, S. (2007). Oil and gas developments in arctic and cold regions: Challenges related to station-keeping in ice. pages 741–751. The 9th Annual INTSOK Conference, Houston, TX, March.

Booton, M. (1987). Segmented mooring line software. Contract report submitted to National Research Council of Canada, Institute for Ocean Technology, June.

Brooks, L. D. (1981). Ice resistance equation for fixed conical structures. *Proceedings of the* 6th *International Conference on POAC*, 1:90–99. Quebec City, QC.

Byrne, R. J. (1974). Physical and numerical model in rock and soil-slope stability. Ph.D. Thesis, James Cook University of N. Queensland, Townsville, Australia.

Calkins, D. J. (1978). Arching of model ice floes at bridge piers. *Proceedings of IAHR'78 Symposium on Ice Problems*. Lulea, Sweden.

Camborde, F., Mariotti, C., and Donze, F. V. (2000). Numerical study of rock and concrete behavior by discrete element modelling. *Computers and Geotechnics*, 27:225–247.

Cammaert, A. B. and Muggeridge, D. B. (1988). *Ice interaction with offshore structures*. Van Norstrand Reinhold, New York.

Canadian Centre for Energy Information (March 2004). Canada's evolving offshore oil and gas industry. Calgary, Alberta.

Clough, H. F. and Vinson, T. S. (1986). Ice forces on fixed conical structures. *Proceedings of the* 5th *International Conference on Offshore Mechanics and Arctic Engineering*, 4:507–514. Tokyo.

Cohen, J., Lin, M., Manocha, D., and Ponamgi, M. (1995). I-collide: An interactive and exact collision detection system for large-scale environments. *Proc. of ACM Interactive 3D Graphics Conf.*, pages 189–196.

Cole, T. (December 2005). Model tests on "Kulluk" in ice conditions. NRC Report SR-2005-27 IOT Project No. 2019.

Comfort, G., Noble, P., and Howard, P. (1982). Experimental studies of ice performance on conical drilling unit. Arctec Canada Limited Report 897, submitted to Gulf Canada Resources Ltd. (Proprietary).

Comfort, G., Singh, S., and Spencer, D. (1999). Evaluation of ice model test data for moored structures. PERD/CHC Report 26-195, Ottawa, Canada.

Croasdale, K. R. (1980). Ice forces on fixed, rigid structures. pages 34–106. A State-of-the-art Report by IAHR Working Group on Ice Forces on Structures, edited by T. Carsten, CRREL Special Report 80-26, U.S. Army CRREL, Hanover, H.H.

Croasdale, K. R., Cammaert, A. B., and Metge, M. (1994). A method for the calculation of sheet ice loads on sloping structures. pages 874–881. Proc. IAHR Ice Symposium, Trondheim, Norway.

Croasdale, K. R. and Metge, M. (1991). *Structure geometry and ice interaction in IUTAM Symposium on Ice Structure Interaction*. Springer-Verlag, New York. edited by S. J. Jones, R. F. Mckenna, J. Tillotson, and I. J. Jordaan.

Cundall, P. A. (1971). A computer model for simulating progressive, large scale movements in blocky rock systems. *International Symposium on Rock Fracture*. Nancy, France.

Cundall, P. A. (1980). Udec - a generalized distinct element program for modeling jointed rock. Report PCAR-1-80, Peter Cundall Associates Report, European Research Office, U. S. Army, Contract DAJA37-79-C-0548.

Cundall, P. A. (1987). Computer simulations of dense sphere assemblies. *Proc. of the U.S./Japan Seminar on the Micromechanics of Granular Materials*. October, Sendai-Zau, Japan.

Cundall, P. A. (1988). Formulation of a three-dimensional distinct element model. part i. a scheme to detect and represent contacts in a system composed of many polyhedral blocks. *International Journal of Rock Mechanics, Mineral Science, and Geomechanics*, 25(3):107–116.

Cundall, P. A. and Hart, R. D. (1992). Numerical modeling of discontinua. *Engineering Computations*, 9(2):101–113.

Cundall, P. A. and Strack, O. D. L. (1978). The distinct element method as a tool for research in granular media. *Report to the National Science Foundation Concerning NSF Grant ENG76-20711*. Part I.

Danys, J. V. and Bercha, F. G. (1975). Determination of ice forces on a conical offshore structure. *Proc. Int. Conf. POAC*, 2:741–751. Fairbanks.

Derradji-Aouat, A. (1994). Ice loads on conical piers - a finite element investigation. *International Journal on Offshore and Polar Engineering*, 4(1):53–61.

Edwards, R. Y. and Croasdale, K. R. (1976a). Model experiments to determine ice forces on conical structures. *Symposium on Applied Glaciology*. International Glaciological Society, Cambridge U.K.

Edwards, R. Y. and Croasdale, K. R. (1976b). Model experiments to determine ice forces on conical structures. *Journal of Glaciology*, 19(18).

Ettema, R. and Matsuishi, M. (1985a). The dynamical behavior of a floating, cable-moored platform continuously impacted by ice floes. IIHR Report 294, The University of Iowa, Iowa City, Iowa, November.

Ettema, R. and Matsuishi, M. (1985b). Ice loads and motions experienced by a floating moored platform in mushy ice rubble. IIHR Report 295, The University of Iowa, Iowa City, Iowa, November.

Frederking, R. M. W., Sayed, M., and Hodgson, T. (1985). Ice force results from the modified Yamamiche Bend Lightpier, Winter 1983-1984. *Proc. Can. Coastal Conf.*, pages 319–331. St. John's.

Garcia-Rojo, R., McNamara, S., and Herrmann, H. J. (2004). Discrete element methods for micro-mechanical investigations of granular ratcheting. European Congress on Computational Methods in Applied Sciences and Engineering, ECCOMAS, July.

Gilbert, E. G., Johnson, D. W., and Keerthi, S. S. (1988). A fast procedure for computing the distance between complex objects in three-dimensional space. *IEEE Journal of Robotics and Automation*, 4:193–203.

Gow, A. J. (1977). Flexural strength of ice on temperate lakes. *Journal of Glaciology*, 19(81).

Grest, G., Landry, J., Silbert, L., and Plimpton, S. (2001). Rheology of granular flow. Lecture at the Kavli Institute for Theoretical Physics, Santa Barbara, California.

Han, K., Peric, D., Crook, A. J. L., and Owen, D. R. J. (2000a). A combined finite/discrete element simulation of shot peening process. part i: studies on 2d interaction laws. *Engineering Computations*, 17(5):593–619.

Han, K., Peric, D., Owen, D. R. J., and Yu, J. (2000b). A combined finite/discrete

element simulation of shot peening process. part ii: 2d interaction laws. *Engineering Computations*, 17(6):680–702.

Hashash, Y. M. A. (2006). Large-scale numerical simulations via parallel computing: an application using discrete element modeling of granular material. NCSA Strategic Applications Program Status Report 03/28/2006.

Hashash, Y. M. A., Nezami, E. G., and Ghaboussi, J. (2005). Dblock3d: A 3-d discrete element analysis code for simulation of granular media and soil-machine interaction. *Workshop on Granular Materials in Lunar and Martian Exploration*. Orlando, Florida.

Haynes, F. D., Sodhi, D. S., Kato, K., and Hirayama, K. (1983). Ice forces on model bridge piers. CCREL Report 83-19, U.S. Army CRREL, Hanover, N.H.

Henty, D. S. (2000). Performance of hybrid message-passing and shared memory parallelism for discrete element modeling. *Proceedings of the 2000 ACM/IEEE conference on Supercomputing*, 15.

Hentz, S., Donze, F. V., and Daudeville, L. (2004). Discrete element modeling of concrete submitted to dynamic loading at high strain rates. *Computers and Structures*, 82:2509–2524.

Hibernia (2009). Retrieved from http://www.hibernia.ca,.

Hirayama, K. and Obara, I. (1986). Ice forces on inclined structures. *Proceedings of the 5$^{\text{th}}$ International Conference on Offshore Mechanics and Arctic Engineering*, 4:515–520. Tokyo.

Hocking, G. (1978). Analysis of toppling-sliding mechanisms for rock slopes. *Proceedings of the 19$^{\text{th}}$ US Rock Mechanics Symposium*. Reno, Nevada, U.S.A.

Hocking, G. (1987). The discrete element method of analysis of fragmentation of discontinua. *Journal of Engineering Computations*, 9:145–155. Swansea, UK.

Hocking, G. (1993). Collision impact of a ship with multi-year sea ice. *Proceedings of the* 2nd *International Conference on Discrete Element Methods*, pages 369–378. MIT Press, Boston, MA, USA.

Hocking, G., Mustoe, G. G. W., and Williams, J. R. (1985a). Dynamic global forces on offshore structures from large ice flow impacts. Arctic Conference ASCE, San Francisco, March.

Hocking, G., Mustoe, G. G. W., and Williams, J. R. (1985b). Influence of artificial island side-shapes on ice ride-up and pile up. Arctic Conference ASCE, San Francisco, March.

Hocking, G., Mustoe, G. G. W., and Williams, J. R. (1987). Dynamic analysis for generalized three-dimensional contact and fracturing of multiple bodies. *NUMETA '87, Numerical Methods of Engineering, Theory and Applications*. Swansea, UK.

Hocking, G., Williams, J. R., and Mustoe, G. G. W. (1985c). Validation of the DECICE code for ice ride-up and ice ridge cone interaction. Arctic Conference ASCE, San Francisco, March.

Hogue, C. (1998). Shape representation and contact detection for discrete element simulations of arbitrary geometries. *Engineering Computations*, 15:372–390.

Holst, J. M. F. G., Ooi, J. Y., Rotter, J. M., and Rong, G. H. (1999). Numerical modeling of silo filling. II: Discrete element analyses. *Journal of Engineering Mechanics*, 125(1):104–110.

Hustrulid, A. I. (1995). Parallel implementation of the discrete element method. Colorado School of Mines, available at http://www.mines.edu/academic/eng/research/dem/.

Intera Technologies Inc. (1984). CINE Model Validation Project, Phases I and II. Alaskan Oil and Gas Association.

Intera Technologies Inc. (1986). DECICE theoretical manual. Information Technologies Environmental Division, Denver, Colorado.

Itasca (2003a). *3DEC - 3-Dimensional Distinct Element Code Users Guide*. Minneapolis, Minnesota, USA. Itasca Consulting Group Inc.

Itasca (2003b). *PFC - Particle Flow Code in 2-Dimensions Users Guide*. Minneapolis, Minnesota, USA. Itasca Consulting Group Inc.

Itasca (2003c). *PFC3D - Particle Flow Code in 3 Dimensions Users Guide*. Minneapolis, Minnesota, USA. Itasca Consulting Group Inc.

Itasca (2003d). *UDEC - Universal Distinct Element Code Users Guide*. Minneapolis, Minnesota, USA. Itasca Consulting Group Inc.

Izumiyama, K., Irani, M. B., and Timco, G. W. (1994). Influence of a rubble field in front of a conical structure. *Proc. 4th Intl. Offshore and Polar Engineering Conference*, 2:553–558. Osaka.

Johnson, S. and Williams, J. (2002). Formation of packing structures in discrete element modeling with disks. *Proceedings of the 3rd International Conference on Discrete Element Methods*, pages 99–103. Sante Fe, New Mexico, September 23-25.

Johnson, S. and Williams, J. R. (2004). Contact resolution algorithm for an ellipsoid approximation for discrete element modeling. *Engineering Computations*, 21(2/3/4):215–234.

Jr., J. W. B. and Konduri, R. K. S. (2001). Discrete element modeling on a cluster of workstations. *Engineering with Computers*, 17:1–15.

Kato, K. (1986). Experimental studies of ice forces on conical structures. pages 185–196. Proceedings of the 8$^{\text{th}}$ IAHR Ice Symposium, Vol. 1, Iowa City.

Kawai, T., Kawabata, K. Y., Kondou, I., and Kumagai, K. (1978). A new discrete model for analysis of solid mechanics problems. *Proceedings of the 1*$^{\text{st}}$ *Conference on Numerical Methods in Fracture Mechanics*. Swansea.

Keinonen, A. J., Browne, R. P., and Revill, C. (1996). Icebreaker characteristics synthesis. *Report for Transportation Development Centre*. Transport Canada. TP 12812E. July.

Kovacs, A. (1997). Bulk salinity of sea ice. CCREL Report.

Lau, M. (1999). Ice forces on a faceted cone due to the passage of a level ice field. Ph.D. Thesis, Memorial University of Newfoundland, St. John's, NL.

Lau, M. (2001). A three dimensional discrete element simulation of an ice sheet impacting a 60° conical structure. *Proc. 16th Intl. Conf. on POAC*, pages 431–440. Ottawa, Ontario, Canada.

Lau, M. (2006). Discrete element modeling of ship maneuvering in ice. *Proceedings of the* 18$^{\text{th}}$ *International Symposium on Ice.* . Sapporo, Japan.

Lau, M., Lawrence, K. P., and Rothenburg, L. (2008). Discrete element analysis of ice loads on structures. *Proceedings of the International Conference and Exhibition on Performance of Ships and Structures in Ice.* . Banff, Alberta, Canada, July 20-23.

Lau, M., Muggeridge, M., and Williams, F. M. (1988). Model tests of fixed and free floating downward breaking cones in ice. *Proc. 7th Intl. Conf. on POAC*, pages 239–247. Houston.

Lau, M., Phillips, R., Mckenna, R. F., and Jones, S. J. (2000). Discrete element simulation of ridge keel resistance during scouring: A preliminary study. *Proc. 2nd Intl. Conf. on Ice Scour and Arctic Marine Pipelines Workshop*. Mombetsu, Hikkaido, Japan.

Lau, M. and Re, A. S. (2006). Performance of survival craft in ice environments. *Proceedings of the International Conference and Exhibition on Performance of Ships and Structures in Ice.* . Banff, Alberta, Canada, July 16-19.

Lau, M. and Stanley, J. (2005). Spread_mooring: Software for mooring system load analysis. Report Submitted to the National Research Council of Canada, Institute for Ocean Technology, LM-2005-03, April.

Lau, M. and Williams, F. M. (1991). Model ice forces on a downward breaking cone. *Proc. 11*$^{\text{th}}$ *Intl. Conf. on POAC*, 1:167–184. St. John's.

Lau, M., Williams, F. M., Molgaard, J., and Swamidas, A. S. J. (1999). Development and verification of a 3-d model for ice forces on conical structures. *Proc. 18th Conf. on OMAE*, pages 1–11. St. John's.

Lin, M. C. (1993). Efficient collision detection for animation and robotics. Ph.D. Thesis, Dept. of Electrical Engineering and Computer Science, University of California, Berkeley, December.

Lin, M. C. and Canney, J. F. (1991). Efficient algorithms for incremental distance computation. *IEEE Conf. on Robotics and Animation*, pages 1008–1014.

Lin, M. C. and Manocha, D. (1995). Fast interference detection between geometric models. *The Visual Computer*, 11(10):542–561.

Lin, M. C. and Manocha, D. (1997). Efficient contact determination between geometric models. *International Journal of Computational Geometry and Applications*, 7(1):123–151.

Lin, X., Nakagawa, M., and Mustoe, G. G. W. (1996). Simulations on hopper flow of elongated particles. *Proceedings of the* 5^{th} *World Congress of Chemical Engineering*. San Diego, CA.

Liu, L. F., Zhang, Z. P., and Yu, A. B. (1999). Dynamic simulation of the centripetal packing of particles. *Physica A*, 268:433–453.

Lobo-Guerrero, S. and Vallejo, L. E. (2005). Discrete element method evaluation of granular crushing under direct shear test conditions. *Journal of Geotechnical and Geoenvironmental Engineering*, 131(10):1295–1300.

Maattanen, M. (1986). Ice sheet failure against an inclined wall. pages 149–158. Proceedings of the 8^{th} IAHR Ice Symposium, Vol. 1, Iowa City.

Macellus, R. W., Morrison, T. B., Allyn, N. F. B., Croasdale, K. R., Iyer, H. S., and Tseng, J. (1988). Ice forces on marine structures. Volume 2 – Discussion, Department of Public Works Canada Report AES/SAG 1-2:88-5v2, Public Works Canada, Ottawa, ON, submitted by C. M. E. L. Enterprises Ltd.

Magnier, S. A. and Donze, F. V. (1998). Numerical simulations of impacts using a discrete element method. *Mechanics of cohesive-frictional materials*, 3:257–276.

McKenna, R. F. (1997). Modeling the forces exerted by pack ice consisting of small floes. *Proc. Conf. on OMAE*.

Michel, B. (1970). Ice pressure on engineering structures. U.S. Army CCREL Monograph 111-B1b, Hanover, N.H., U.S.A.

Michel, B. (1978). *Ice Mechanics*. Laval University Press, Quebec, Canada.

Mirghasemi, A. A., Rothenburg, L., and Matyas, E. L. (1997). Numerical simulations of assemblies of two-dimensional polygon-shaped particles and effects of confining pressure on shear strength. *Soils and Foundations*, 37(3):43–52.

Mirtich, B. (1998). V-clip: Fast and robust polyhedral collision detection. *ACM Transactions on Graphics*, 17(3):177–208.

Mishra, B. K. (2003a). A review of computer simulation of tumbling mills by the discrete element method. part i - contact mechanics. *International Journal of Mineral Processing*, 71:73–93.

Mishra, B. K. (2003b). A review of computer simulation of tumbling mills by the discrete element method. part ii - practical applications. *International Journal of Mineral Processing*, 71:95–112.

Munjiza, A. and Andrews, K. R. F. (1998). NBS contact detection algorithm for bodies of similar size. *International Journal for Numerical Methods in Engineering*, 43:131–149.

Murray, J. J. and Spencer, D. S. (1997). A simulation model for a turret moored tanker in pack ice cover. *Proceedings of the 14$^{\text{th}}$ International Conference on Port and Ocean Engineering under Arctic Conditions*, 4:127–140. POAC'97, Yokohama, Japan.

Mustoe, G. G. W. (1992). A generalized formulation of hte discrete element method. *Engineering Computations*, 9:181–190.

Mustoe, G. G. W., Hocking, G., Williams, J. R., and Worgan, K. J. (1987). Penetration and fracturing of brittle plates under dynamic impact. *NUMETA '87, Numerical Methods of Engineering, Theory and Applications*. Swansea, UK.

Mustoe, G. G. W., Miyata, M., and Nakagawa, M. (2000). Discrete element methods for mechanical analysis of systems of general shaped bodies. *Proc. 5th Intl. Conf. on Computational Structures Technology*. Leuven, Belgium.

Nadreau, J. P. and Michel, B. (1984). Ice properties in relation to ice forces. *Proc. Second State-of-the-art IAHR Working Group on Ice Forces*, 4:1–53. Chapter 1, Hamburg.

National Research Canada of Canada (2009). Arctic operations. Retrieved from http://www.nrc-cnrc.gc.ca/eng/programs/iot/arctic-operations.html,.

Nazeri, H. (2004). Development of a discrete element methodology for the simulation of gravity flow of ore in ore passes. Ph.D. Thesis, Colorado School of Mines.

Nevel, D. E. (1992). Ice forces on cones from floes. *Proc. 11th IAHR ice Symp.*, pages 1391–1401. Banff.

Nezami, E. G., Hashash, Y. M. A., Zhao, D., and Ghaboussi, J. (2004). A fast contact detection algorithm for 3-d discrete element method. *Computers and Geotechnics*, 31:575–587.

Nezami, E. G., Hashash, Y. M. A., Zhao, D., and Ghaboussi, J. (2006). Shortest link method for contact detection in discrete element method. *International Journal for Numerical and Analytical Methods in Geomechanics*, 30:783–801.

Ng, T.-T. (1994). Numerical simulation of granular soil using elliptical particles. *Computers and Geotechnics*, 16:153–169.

Ng, T.-T. (2004). Triaxial test simulations with discrete element method and hydrostatic boundaries. *Journal of Engineering Mechanics*, 130(10):1188–1194.

Ng, T.-T. and Lin, X. (1993). Numerical simulation of naturally deposited granular soil with ellipsoidal elements. *Proceedings of the* 2nd *International Conference on Discrete Element Methods*, pages 557–568. MIT Press, Boston, MA, USA.

Nicot, F., Cambou, B., and Mazzoleni, G. (2001). Design of rockfall restraining nets from a discrete element modelling. *Rock mechanics and rock engineering*, 34(2):99–118.

Nixon, W. A. and Ettema, R. (1987). Ice-sheet interaction with a cable moored platform. IIHR Report, The University of Iowa, Iowa City, Iowa, April.

Nixon, W. A. and Ettema, R. (1988). Ice rubble impact with a moored platform. IIHR Report No. 147, The University of Iowa, Iowa City, Iowa, April.

Nogid, L. M. (1959). Model representations of a ship going through a continuous ice field or pack ice. *Transactions of Leningrad Shipbuilding Institute*. No. 28, B.S.R.A., Translation No. 1868.

Orgill, G. and Wilson, J. F. (1986). Statis design of cable mooring arrays for offshore guyed towers. *Applied Ocean Research*, 7(3):166–174.

O'Rourke, J. (1994). *Computational geometry in C*. Cambridge University Press.

O'Sullivan, C., Bray, J. D., and Cui, L. (2006). Experimental validation of particle-based discrete element methods. *Proceedings of GeoCongress 2006*.

Palmer, A. C., Goodman, D. J., Ashby, M. F., Evans, A. G., Hutchinson, J. W., and Ponter, A. R. S. (1983). Fracture and its role in determining ice forces on offshore structures. *Ann. Glaciol.*, (4):216–221.

Pearce, J. C. and Strickland, G. E. (1979). Ice forces on conical structures. *Proceedings of the* 11th *Offshore Technology Conference*, 4:2404–2414. Houston, TX.

Perkins, E. and Williams, J. R. (2001). A fast contact detection algorithm insensitive to object sizes. *Engineering Computations*, 18:48–61.

Prochazka, P. P. (2004). Application of discrete element methods to fracture mechanics of rock bursts. *Engineering fracture mechanics*, 71:601–618.

Ralston, T. (1977). Ice force design considerations for conical offshore structures. *Proc. Int. Conf. POAC*, 2:741–752. St. John's.

Ralston, T. (1978). An analysis of ice sheet indentation. *Proc. IAHR Symp. on Ice Problems*, 1:13–31. Lulea, Sweden.

Richards, K., Bithell, M., Dove, M., and Hodge, R. (2004). Discrete-element modelling: methods and applications in the environmental sciences. *Phil. Transactions of the Royal Society of London A*, 362:1797–1816.

Riera, J. D. and Iturrioz, I. (1998). Discrete element model for evaluating impact and impulsive response of reinforced concrete plates and shells subjected to impulsive loading. *Nuclear Engineering and Design*, 179:135–144.

Rothenburg, L. and Bathurst, R. J. (1991). Numerical simulation of idealized granular assemblies with plane elliptical particles. *Computers and Geotechnics*, 11:315–329.

Sanad, A. M., Ooi, J. Y., Holst, J. M. F. G., and Rotter, J. M. (2001). Computations of granular flow and pressures in a flat-bottomed silo. *Journal of Engineering Mechanics*, 127(10):1033–1043.

Sanderson, T. J. O. (1988). *Ice Mechanics, Risks to Offshore Structures*. Graham Trotman, London.

Sawada, S. and Pradham, T. B. S. (1994). Analysis of anisotropy and particle shape by distinct element method. *Computer Methods and Advantages in Geomechanics*, pages 665–670.

Sayed, M., Frederking, R. M. W., and Barker, A. (2000). Numerical simulation of pack ice forces on structures: a parametric study. *Proc. 10th ISOPE*. Seattle.

Schachter, M. and Spencer, D. (1994). Parameters influencing ice arch formation. *Proc. IAHR Ice Symp.*, 2:847–856. Trondheim, Norway.

Schafer, B. C., Quigley, S. F., and Chan, A. H. C. (2002). Analysis and implementation of the discrete element method using a dedicated highly parallel architecture in reconfigurable computing. *Proc. 10th Annual IEEE Symp. on Field-Programmable Custom Computing Machines*.

Schwarz, J. (1977). New developments in modelling ice problems. *Proceedings of 4*$^{\text{th}}$ *International Conference on POAC*, 1:45–61. St. John's, Newfoundland.

Schwarz, O. J., Horie, Y., and Shearer, M. (1998). Discrete element investigation of stress fluctuation in granular flow at high strain rates. *Physical Review E*, 57(2):2053–2061.

Semeniuk, A. (1975). Computer program to evaluate the forces generated by a moving ice field encountering a conical structure. *APOA Project No. 87*. Calgary.

Shi, G. (1989). Discontinuous deformation analysis - a new numerical model for the statics and dynamics of deformable block structures. *First International Conference on Discrete Element Methods*. Golden, CO.

Sodhi, D. S. (1987). Flexural and buckling failure of floating ice sheets against structures. pages 53–73. 3rd State-of-the-art Report, IAHR Working Group on Ice Forces, Edited by J. J. O. Sanderson, CRREL Special Report 87-17, U.S. Army CRREL, Hanover, N. H.

Timco, G. and O'Brien, S. (1994). Flexural strength equation for sea ice. *Cold Regions Science and Technology*. No. 22.

Timco, G. W. (1984). Ice forces on structures: physical modeling techniques. *Proceedings of the 7th IAHR Symp. on Ice Problems*, 4:117–150. Hamburg, Germany.

Timco, G. W. and Johnston, M. E. (2002). Caisson structures in the Beaufort Sea 1982-1990: Characteristics, instrumentation and ice loads. Technical Report CHC-TR-003, National Research Council of Canada, Ottawa.

Ting, J. M., Khwaja, M., Meachum, L. R., and Rowell, J. D. (1993). An ellipse-based discrete element model for granular materials. *International Journal for Numerical and Analytical Methods in Geomechanics*, 17:603–623.

Toussaint, B. M. (1977). Mechanisms and theory of indentation of ice plates. *J. Glaciology*, 19(81):285–300.

Vance, G. P. (1975). A scaling system for vessels modeled in ice. *Proceedings of Ice Tech 75*. SNAME, Paper H, Montreal, Quebec, Canada.

Wait, R. (2001). Discrete element models of particle flows. *Mathematical Modeling and Analysis*, 6(1):156–164.

Wessels, E. (1984). Model test investigation of ice forces on fixed and floating conical structures. *Proc. 7th IAHR Ice Symp.*, 3:203–220. Hamburg.

Wessels, E. and Iyer, S. H. (1985). Ice loads on floating offshore structures. 80 Hauptversammlungder Schiftbautechnischen Gesellschaft, Hamburg (in German).

Wessels, E. and Kato, K. (1989). Ice forces on fixed and floating conical structures. pages 231–258. 4th State-of-the-art Report, IAHR Working Group on Ice Forces, Edited by J. J. O. Sanderson, CRREL Special Report 89-5, U.S. Army CRREL, Hanover, N. H.

White, R. M. and Vance, G. P. (1967). Icebreaker model tests. *Naval Engineering Journal*, pages 601–605.

Williams, J. R. (1992). Superquadratics and modal dynamics for discrete elements in interactive design. *Engineering Computations*, 9:115–127.

Williams, J. R., Hocking, G., and Mustoe, G. G. W. (1985). The theoretical basis of the discrete element method. *NUMETA '85, Numerical Methods of Engineering, Theory and Applications*. Rotterdam.

Williams, J. R., Hocking, G., and Mustoe, G. G. W. (1987). Dynamic contact analysis of biomechanical systems fro occupant trauma and assessment during impact. *NUMETA '87, Numerical Methods of Engineering, Theory and Applications*. Swansea, UK.

Williams, J. R. and O'Connor, R. (1999). Discrete element simulation and the contact problem. *Archives of Computational Methods in Engineering*, 6(4):279–304.

Worgan, K. J. and Mustoe, G. G. W. (1989). Application of the discrete element method to subsurface penetration of a uniform ice cover. *Proc. 1st Conf. on Discrete Element Methods*. Golden, CO., October.

Wright, B. (1999). Evaluation of full scale data for moored vessel stationkeeping in pack ice. PERD/CHC Report 26-200, Ottawa, Canada.

Wright, B. (2000). Full scale experience with Kulluk stationkeeping operations in pack ice. PERD/CHC Report 25-44 submitted to the NRC.

Wright, B., Hill, C., and Keinonen, A. (1998). Moored vessel stationkeeping in grand banks pack ice conditions. PERD/CHC Report, Ottawa, Canada.

Yan, Q., Qianjin, Y., Xiaugjun, B., and Karna, T. (2003). Random ice forces on conical structures. *Proceedings of the 17th International POAC Conference*, pages 259–270. Trondheim, Norway.

Yao, M. and Anandarajah, A. (2003). Three-dimensional discrete element method of analysis of clays. *Journal of Engineering Mechanics*, 129(6):585–596.

Zhang, Z. P., Liu, L. F., Yuan, Y. D., and Yu, A. B. (2001). Numerical study of th effects of dynamic factors on the packing of particles. *Powder Technology*, 116:23–32.

Zhang, Z. P., Zou, R. P., Yu, A. B., Langston, P., and Kafui, K. D. (1997). Dem application to the simulation of particle packing. *Chemeca '97, Particle Technology*, pages 23–29. Rotorua, NZ.

Zhao (2006). Physical and numerical model in rock and soil-slope stability. Ph.D. Thesis, University of Illinois-Champagne, Illinois, USA.

Zhao, D. (1997). Three-dimensional discrete element simulation for granular materials. Ph.D. Thesis, University of Illinois at Urbana-Champaign, Urbana, Illinois.

Index